CERN-LHCC-2004-002
TOTEM-TDR-001
7 January 2004

TOTEM

Technical Design Report

Total Cross Section, Elastic Scattering and Diffraction Dissociation at the Large Hadron Collider at CERN

Printed at CERN
January 2004
ISBN 92-9083-219-3

TOTEM Collaboration

- **INFN Sez. di Bari and Politecnico di Bari, Bari (Italy)**
  V. Berardi, M.G. Catanesi, E. Radicioni.

- **ILK, Institut für Luft und Kältetechnik, Dresden, (Germany)**
  R. Herzog, R. Rudischer, E. Wobst.

- **CERN, Geneva, (Switzerland)**
  M. Deile, K. Eggert, F. Haug, P. Jarron, D. Macina, H. Niewiadomski[1], E. Noschis[2], M. Oriunno, A.-L. Perrot, G. Ruggiero, W. Snoeys, A. Verdier.

- **INFN Sez. di Genova and Università di Genova, Genoa (Italy)**
  V. Boccone, M. Bozzo[3], A. Buzzo, S. Cuneo, F. Ferro, M. Macrì, S. Minutoli, A. Morelli, P. Musico, M. Negri, A. Santroni, G. Sette, A. Sobol[4].

- **High Energy Physics Division, Department of Physical Sciences, University of Helsinki and Helsinki Institute of Physics, Helsinki (Finland)**
  V. Avati, E. Goussev, M. Järvinen, J. Kalliopuska, K. Kurvinen, R. Lauhakangas, F. Oljemark, R. Orava, K. Österberg, V. G. Palmieri, H. Saarikko, S. Tapprogge, A. Toppinen.

- **Institute of Physics, Academy of Sciences of the Czech Republic, Praha (Czech Republic)**
  V. Kundrát, M. Lokajíček

- **Electronic and Computer Engineering Department, Brunel University, Uxbridge (United Kingdom)**
  C. Da Via, J. Hasi, A. Kok, S. Watts.

Spokesperson: **K. Eggert,** E-mail: Karsten.Eggert@cern.ch
Deputy Spokesperson: **M. Bozzo,** E-mail: Marco.Bozzo@cern.ch

[1] also at Electronic and Computer Engineering Department, Brunel University, Uxbridge (United Kingdom)
[2] also at Helsinki Institute of Physics, Helsinki (Finland)
[3] also at CERN, Geneva, (Switzerland)
[4] Visitor from the Institute for High Energy Physics, Protvino (Russia)

Several active collaborators could not yet organize a group of the size required to participate to the collaboration as an institute, but maintain their interest in the project:

- J.P. Guillaud, LAPP Annecy, (France)
- J. Kempa, Warsaw University of Technology, Plock (Poland)
- C. Kenney, Molecular Biology Consortium, SLAC (USA)
- S. Parker, University of Hawaii (USA)
- G. Sanguinetti, INFN Sez. di Pisa, Pisa (Italy)
- C. Taylor, Dept. of Physics, Case Wesetrn Reserve University, Cleveland, Ohio (USA)
- J. Whitmore, Department of Physics, Penn State University, University Park (USA)

Contents

1 Introduction

The TOTEM experiment will measure the total pp cross section and study elastic scattering and diffractive dissociation at the LHC. More specifically, TOTEM will measure:

* the total cross-section with an absolute error of 1 mb by using the luminosity independent method. This requires the simultaneous measurement of the elastic pp scattering down to the four-momentum transfer of $-t \approx 10^{-3}\,\mathrm{GeV}^2$ and of the inelastic pp interaction rate with an adequate acceptance in the forward region;

* elastic proton scattering over a wide range in momentum transfer up to $-t \approx 10\,\mathrm{GeV}^2$;

* diffractive dissociation, including single, double and central diffraction topologies using the forward inelastic detectors in combination with one of the large LHC detectors.

TOTEM was proposed in 1997 [1]. Having received favourable consideration from the LHCC and the Research Board, the Collaboration prepared a Technical Proposal [2] in 1999 in which they identified CMS as the optimal host experiment for TOTEM.

Since then TOTEM has pursued detailed studies on the integration of their detectors into the CMS environment at intersection point I5. Ongoing discussions with CMS have led to satisfactory agreements about the compatibility of the TOTEM detectors with the host experiment, the shape of the vacuum chamber, the various support structures, and the sequence of operations for the installation and the removal of the TOTEM detectors.

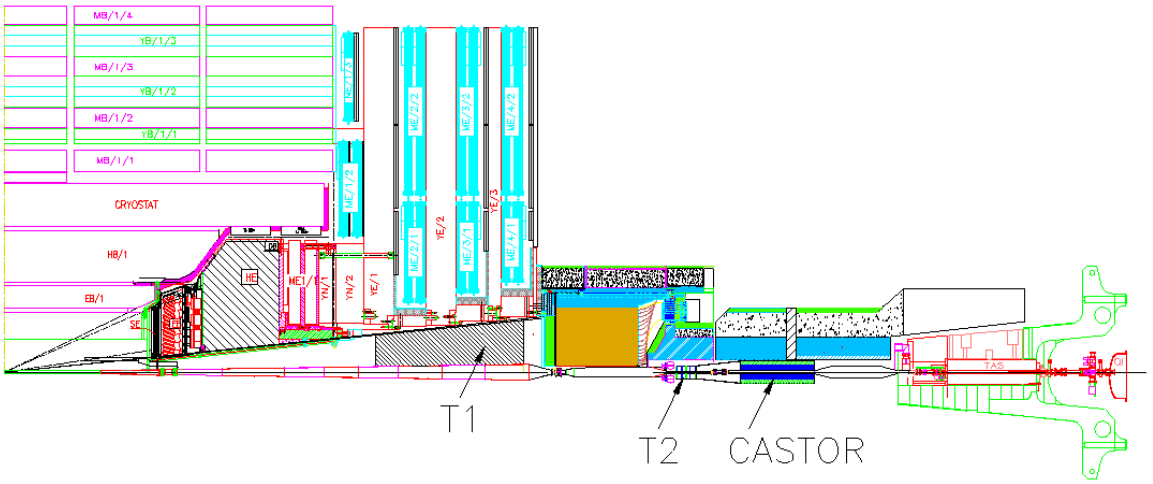

Figure 1.1: The TOTEM detectors are installed in the CMS forward region

As noted above, TOTEM has to measure the inelastic pp interaction with adequate acceptance in the forward region. Two tracking telescopes, T1 and T2, installed on each side of the IP in a manner compatible with the CMS detector, will provide this coverage (Fig. 1.1). The T1 telescope will be placed in the CMS endcaps, while T2 will be in the shielding behind the CMS Hadronic Forward (HF)

calorimeter. T1 and T2 add charged particle tracking and trigger capabilities to the CMS experiment over a rapidity interval $3 \leq |\eta| \leq 6.8$. A fully inclusive trigger, including single and double diffraction, can be provided with an expected loss in the inelastic rate of less than 5%.

The design of the T1 detectors has been finalised. It consists of five cathode strip chambers with trigger capabilities, equally spaced over 3 m along the beam. Each chamber provides a space point with a precision of the order of 0.5 mm. This permits the reconstruction of the primary collision vertex in the transverse plane within a few mm, enough to discriminate between beam–beam and beam–gas events. The T2 detector complements the T1 detector at larger rapidities, an angular range dominated by the diffractive component of the inelastic interactions. The design of T2 has been recently reconsidered since CMS foresees an additional calorimeter (called CASTOR) in the very forward cone. This has considerably reduced the available space for T2 in front of CASTOR to less than 50 cm. The spatial resolution of T2 thus has to be improved in order to provide good vertex reconstruction capability. The design of T2 is still under discussion. Two solutions are under consideration:

- A silicon tracker with detector elements identical to the ones in the outer barrel of the CMS tracker. These elements are properly arranged to form a series of disks around the vacuum pipe. For trigger purposes at least two of the planes will be made with silicon pad detectors equipped with electronics for fast trigger extraction.
- A tracker with GEM chambers has recently been operated by the Compass experiment [3]. The shape is adapted to the annular region around the beam pipe to ensure maximal acceptance. Four detector planes with a $r - \phi$ geometry are used for precise position resolution. Another four planes with a larger pad structure will deliver the trigger and facilitate pattern recognition.

Both solutions will provide the spatial resolution and good pattern reconstruction capabilities needed to cope with the high particle densities. The radiation hardness of the detectors will permit data taking up to luminosities of at least $10^{32}\,\mathrm{cm}^{-2}\mathrm{s}^{-1}$.

The precise determination of the total cross-section requires that TOTEM must also measure $d\sigma_{el}/dt$ down to $-t \approx 10^{-3}\,\mathrm{GeV}^2$. This is accomplished with two sets of silicon detectors in Roman Pots located symmetrically on each side of the IP at 147 m and 220 m (Fig. 1.2).

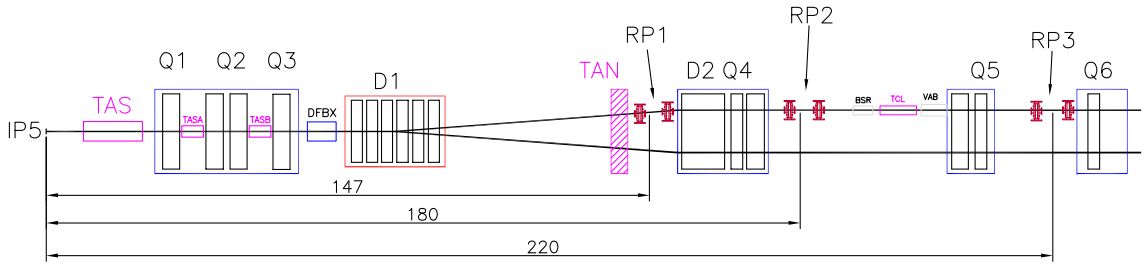

Figure 1.2: The LHC beam line and the Roman pots at 147 m and 220 m

The details of the machine optics are crucial to this measurement. The original TOTEM optics was based on $\beta^* = 1100$ m, and parallel-to-point focusing conditions in the vertical plane at the 147 m stations and in the horizontal plane at the 220 m stations. A new, superior, optics with a β^* of 1540 m has been developed. The outstanding feature of this optics is that parallel-to-point focussing can be achieved in both projections at almost the same location, dramatically improving the resolution in the momentum transfer and the azimuthal angle of the scattered protons. This optics has been accepted by the machine for the TOTEM runs. Optics with intermediate β^* values are also presently under study.

At both the 147 m and 220 m location, two Roman Pot stations separated by a distance of 4 m will permit a precise determination of the angle, even on the trigger level, thus reducing the background due to beam–gas and halo interactions. The station RP2 at 180 m might be equipped later.

It is important to note that the 147 m Roman pots are located before the D2 magnet, while the 220 m tracking station is well behind it. This geometry naturally implements a magnetic spectrometer in the standard insertion, permitting TOTEM to measure particle momenta, with an accuracy of a few parts per

thousand. This will allow the accurate determination of the momentum loss of quasi-elastically scattered protons in diffractive processes.

While the measurement of the total cross-section and the elastic scattering can be performed using only the TOTEM detectors, the integration of TOTEM into the general purpose CMS detector offers the prospect of more detailed studies of diffractive events. The TOTEM triggers, combining information from the inelastic detectors and the silicon detectors in the Roman pots 220 m upstream, will be incorporated into the general CMS trigger scheme, thus offering the ability to combine them with other CMS triggers. The digitization of the TOTEM detectors and the data acquisition system are both fully compatible with the CMS DAQ thus enabling a common read-out of both detectors, while maintaining a stand-alone read-out for TOTEM.

Good progress has also been made in the integration of the Roman pots into the machine environment. The locations of the Roman pots have been decided and reserved. The mechanical design of the Roman pots has been finalised in collaboration with the engineers of the EST division, and a first prototype will be ready in January 2004. The electronics for the detector movement and its interface to the machine will be developed in co-operation with the LHC collimator group. The accelerator division has performed extensive studies of the gas pressure in the vacuum chamber, the radiation near the Roman pots and at the location of the silicon detectors, and the collimation scheme. These results are the basis for our trigger calculations and the choice of the silicon detectors.

The beams at the LHC are rather small, with a 10 σ envelope of about 1 mm. As a consequence, the silicon detectors in the Roman pots must have a good spatial resolution and a very small dead zone at the mechanical edge facing the beam, i.e. they must be almost edgeless. Two innovative silicon detectors have been tested with good results in the beam during the year 2003:

- The 3D detector [4, 5, 6] with a detector area of about 10 mm^2 exhibits a dead zone of at most a few microns, compatible with zero, and could easily be operated.

- The silicon strip detector ($1 \times 1\,\mathrm{cm}^2$) with two miniaturised guard rings could be operated at room temperature with a signal-to-noise ratio of about 20 and a dead space at the edge of less than $50 \div 60\,\mu$m.

Both types are good candidates for the Roman pot detectors, and prototypes with the full detector area of $3 \times 4\,\mathrm{cm}^2$ will be produced and tested during 2004, allowing a detector choice in autumn 2004. TOTEM also plans to install a vertical Roman pot with the final analog detectors and the digital trigger detectors in the SPS tunnel. 270 GeV coasting beams, with proton densities of up to 10^{11} protons per bunch (similar to the LHC bunches), allow a test of the complete set-up, including possible pick-up problems due to the circulating beam. The first-level trigger can be checked and optimised in these special runs using halo particles.

TOTEM will only need a few days of running with special running conditions ($\beta^* \approx 1540$ m, 43 bunches, and zero crossing angles) at a luminosity of $10^{28}\,\mathrm{cm}^{-2}\mathrm{s}^{-1}$ in order to measure the total cross-section. Increasing the proton density per bunch and the number of bunches and lowering the β^* to a few hundred metres will allow TOTEM to run at luminosities of a few times $10^{30}\,\mathrm{cm}^{-2}\mathrm{s}^{-1}$ while still detecting most of the diffractive protons. Together with CMS, interesting diffraction physics with large transverse momentum phenomena can then be investigated at a collider for the first time over the large pseudorapidity interval of ± 7. With the injection optics ($\beta^* \approx 18$ m), large-t elastic scattering can be measured up to $\sim$10 GeV^2.

References

[1] The TOTEM Collaboration, Letter of Intent. CERN/LHCC 97-49, LHCC/I11 (15 August 1997).

[2] The TOTEM Collaboration, Technical proposal. CERN/LHCC 99-7, LHCC/P5 (15 March 1999).

[3] C. Altunbas,M. Capeans, K. Dehmelt, J. Ehlers, J. Friedrich, I. Konorov, A. Gandi, S. Kappler, B. Ketzer, R. De Oliveira, S. Paul, A. Placci, L. Ropelewski, F. Sauli, F. Simon and M. van Stenis, Nucl. Instr. and Meth. **A490** (2002) 177-203.

[4] C. Kenney, S. Parker, J. Segal and C. Storment, IEEE Trans. on Nucl. Sci. **46** (1999) 1224.

[5] DaVià et al., Nucl. Instr. and Meth. **A509** (2003) 86-91

[6] C. Kenney, S. Parker and E. Walckiers, IEEE Trans. on Nucl. Sci. **48** (2001) 2405 (2001).

2 The Physics Programme

We briefly review the physics programme of the TOTEM experiment that will be carried out in special runs during the first three years of LHC operation.

2.1 Total cross-section

The importance of the measurement of the total cross-section has already been stressed in the TOTEM Letter of Intent [1]. Recently, the COMPETE collaboration [2] has made an overall fit of the energy dependence of the total cross-section and the ratio of the real to the imaginary part of the elastic scattering (ρ parameter), taking into account all available data. Their prediction for the energy dependence of the total pp cross-section is shown in Fig. 2.1.

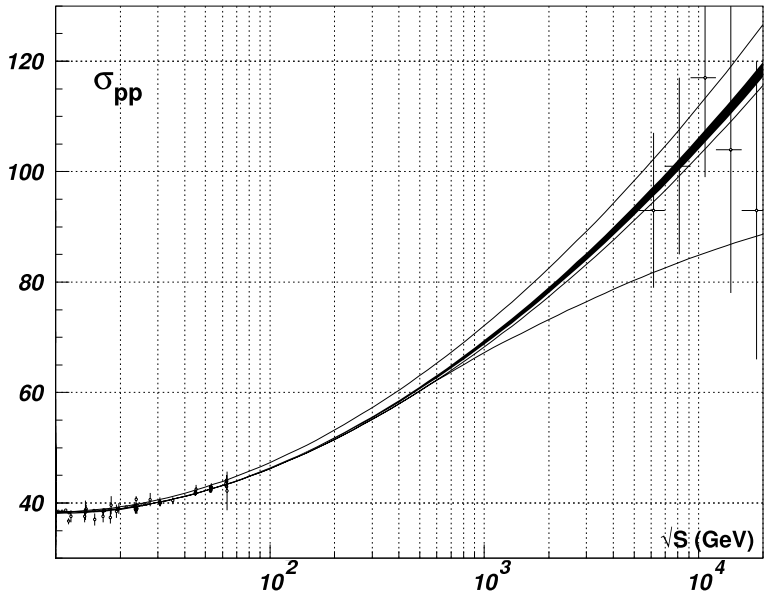

Figure 2.1: Predictions for total pp cross-sections [2], including ISR and cosmic ray data

The black error band shows the statistical errors to the best fit, the closest curves near it give the sum of statistical and systematic errors to the best fit due to the ambiguity in the TEVATRON data and the highest and lowest curves show the total error bands from all models considered.

For the LHC energy they obtain the following values for σ_{tot} and ρ:

$$\sigma_{tot} = 111.5 \pm 1.2\ ^{+4.1}_{-2.1}\mathrm{m}b \qquad\qquad \rho = 0.1361 \pm 0.0015\ ^{+0.0058}_{-0.0025}\ .$$

The first error is the statistical error to the best fit and the second one arises from the ambiguity in the TEVATRON data. In order to have an input on the selection of different models the experimental

error of σ_{tot} should be in the order of 1 mb. The total cross-section will be determined in a luminosity independent way using the optical theorem (see eq. (2.1)).

$$\sigma_{tot} = \frac{16\pi}{(1+\rho^2)} \frac{(dN_{el}/dt)_{t=0}}{N_{el} + N_{inel}} \tag{2.1}$$

Thus the optical point at $t = 0$ has to be extrapolated from the measurement of the elastic scattering at low momentum transfers.

2.2 Elastic scattering

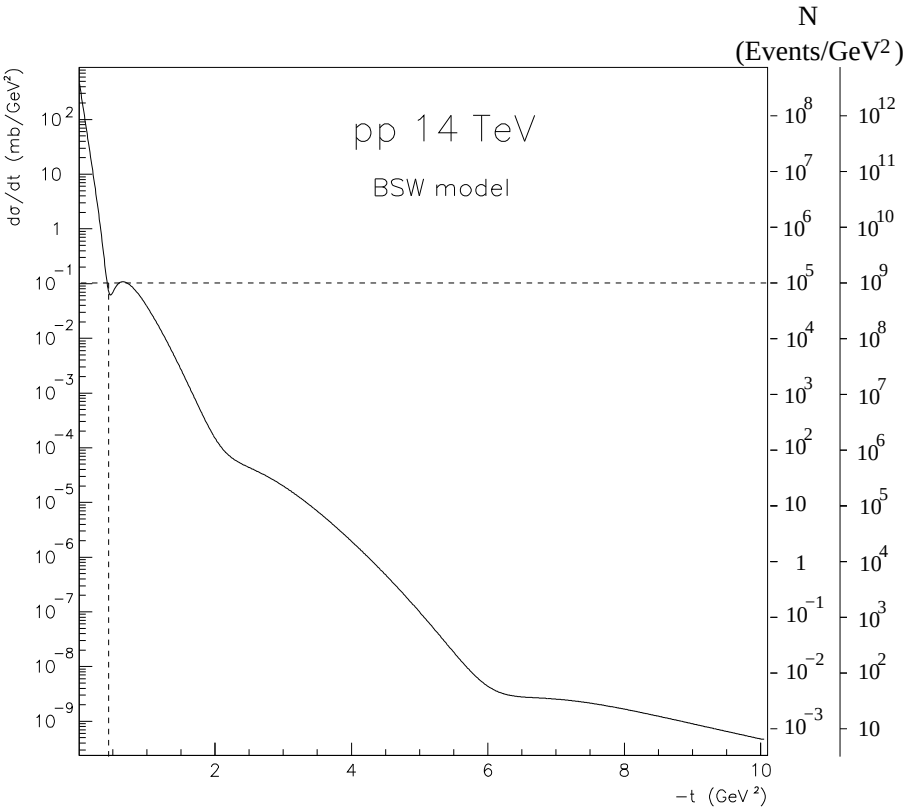

Figure 2.2: Elastic scattering cross-section, using the model from BSW [9]. The number of events at the right scale corresponds to an integrated luminosity of 10^{33} *cm*$^{-2}$ *and* 10^{37} *cm*$^{-2}$*. The dotted line indicates the highest observable t-value due to aperture limitation in the high-*β^* *optics*

High-energy elastic nucleon scattering represents the collision process in which the most precise data over a large energy range at the CERN ISR [3], the SPS collider [4] and the TEVATRON [5] have been gathered. These data have been confronted with various phenomenological models. Some information about the behavior of the phenomenological approaches at very high energies can be obtained with the help of so-called asymptotic theorems derived from first principles and only valid at asymptotic energies [6]. They tell us how models should behave in the limiting case of infinite energies and show us the trends in their high-energy behavior.

In the past, many models describing high-energy elastic hadron scattering have been formulated with different approaches [7]. In many of them the eikonal approach has been used, in analogy to optics. In other models the nucleons consist of a central core with a surrounding meson cloud or of a series of partonic clusters whose interaction is formulated with the help of Glauber's multi-scattering method.

Another class of models has started from the QCD nucleon structure and identified the partons as quarks and gluons. The hadron scattering is then described as a sum of Pomeron and gluon exchanges or as semi-hard scattering of quarks and gluons. The field model, underlying the phenomenological analysis in [8], describes the nucleon as having an outer cloud of quark-antiquark condensed ground states, an inner core of topological baryonic charge of radius 0.44 fm and a still smaller valence quark-bag of radius < 0.1 fm. These different shells of the nucleon participate in different t-regions of the elastic scattering.

To discriminate between different models it is thus important to precisely measure the elastic scattering over the whole kinematical region as the model predictions may be rather different for higher values of t. The t-distribution of the elastic scattering, assuming the BSW model [9], is given in Fig. 2.2.

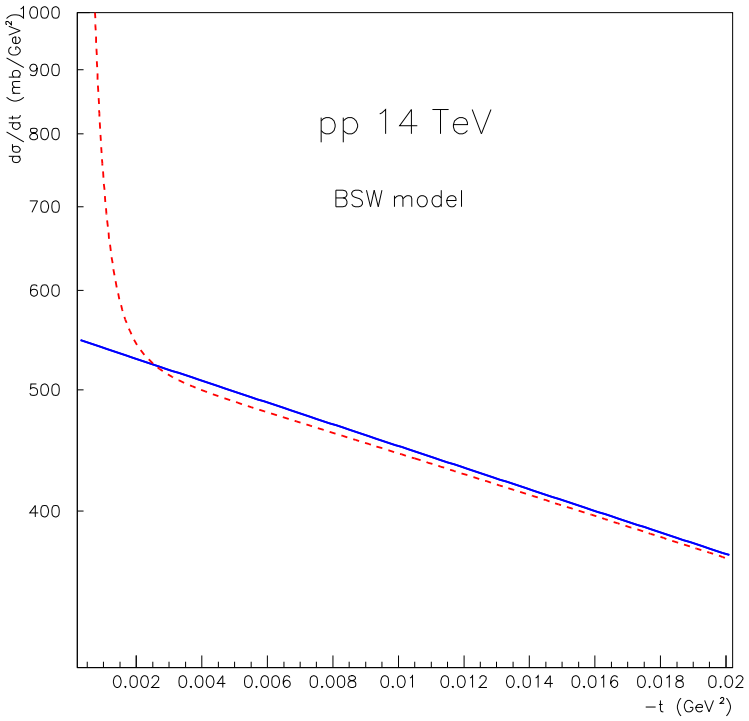

Figure 2.3: Elastic scattering distribution at low t, including Coulomb scattering (dashed line) and the hadronic part alone (solid line)

It extends over 11 orders-of-magnitude and has therefore to be measured with different optics settings. The exponential fall at low t is followed by a diffractive structure at $\sim 1\,\mathrm{GeV}^2$ and continues to large t-values where pertubative calculations suggest a power-law behaviour (t^{-8}). The number of events at the right side of the plot refers to a few days running at two conditions (scenario 1 and 4 in Chapter 10.). The maximal detectable t-value due to aperture limitations in the LHC is 0.5 ($10\,\mathrm{Gev}^2$) for scenario 1 (4) respectively.

The elastic cross-section and the total pp cross-section critically depend on the extrapolation of the low-t spectrum to $t = 0$. In the very low region of t ($\sim 2 \cdot 10^{-3}\,\mathrm{GeV}^2$) the measurement becomes exceedingly difficult. Moreover, the measured data are strongly influenced by Coulomb scattering. Indeed, the application of more general integral formula to earlier data has indicated that Coulomb scattering may play a non-negligible role in a greater interval of t up to a few times $10^{-2}\,\mathrm{GeV}^2$. The hadronic part can only be separated with the help of a model. Figure 2.3 shows the elastic scattering distribution at low t, including Coulomb scattering and the hadronic part alone.

If Coulomb scattering is not accounted for, the extrapolation will shift by 1-2 %. Furthermore, due to Coulomb scattering, the slope B ($d\sigma/dt \sim \exp(-Bt)$) is not exactly constant at low t as assumed in the extrapolation. The slope for the hadronic scattering alone and including Coulomb scattering is given in Fig. 2.4. This model dependence might add an uncertainty of several per thousand to the extrapolation.

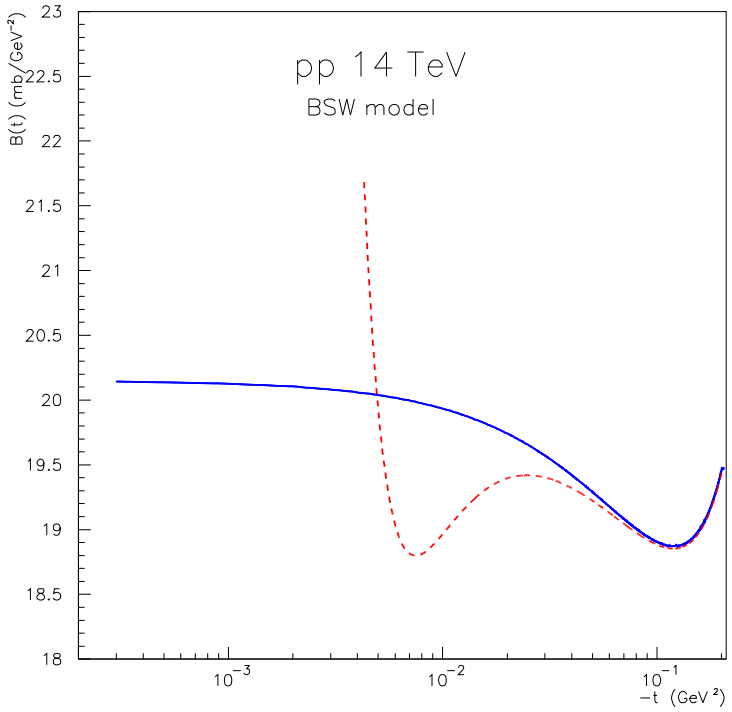

Figure 2.4: The slope parameter B, including Coulomb scattering (dashed line) and the hadronic part alone (solid line)

2.3 The Common CMS/TOTEM Detectors

While the measurement of the total cross-section and the elastic scattering can be performed using only TOTEM detectors, the integration of TOTEM into the general purpose detector CMS offers the prospect of more detailed studies of diffractive events. The TOTEM triggers, combining information from the inelastic detectors and the silicon detectors in the Roman Pots 220 m upstream, can be incorporated into the general CMS trigger scheme, thus offering the ability to combine them with other CMS triggers. The digitization of the TOTEM detectors and the data acquisition system are both fully compatible with the CMS DAQ thus enabling a common read-out of both detectors, while still maintaining a stand-alone read-out for TOTEM.

The CMS experiment extended by the TOTEM detectors into the very forward region and the Roman Pot detectors along the LHC beam line is the largest acceptance detector, ever implemented at a hadron collider. The nearly complete acceptance for charged and neutral particles (except for a gap between T2 and the Roman Pots) of such a combined experiment is shown in Fig. 2.5.

A microstation (not foreseen in the present design) placed at 18 m distance from the intersection region just in front of the TAS, would nicely fill this acceptance gap.

Figure 2.6 shows the pseudorapidity distributions of charged particles and of the energy flow at the LHC, demonstrating that with the common CMS/TOTEM acceptance almost all charged and neutral particles are detected as well as a fair fraction of the energy flow. The large coverage of such a "combined experiment" will allow for unique measurements that are also discussed in a common CMS/TOTEM physics group [14]. The wide variety of diffractive processes that can be addressed is sketched in the rapidity-ϕ plot of Fig. 2.7 (from the FELIX proposal [15]) starting with the cleanest process of elastic scattering up to the most complicated structure of multi-gap events due to multi-Pomeron exchange. Some of the processes are briefly discussed. In addition to the brief review of these processes, many accessible to CMS/TOTEM, are discussed in more detail in the above FELIX proposal [15].

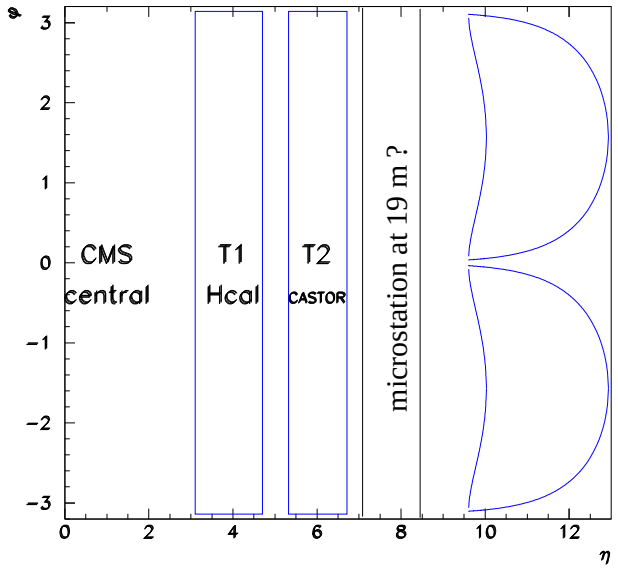

Figure 2.5: The acceptance of a common CMS/TOTEM experiment in the azimuth-pseudorapidity plane

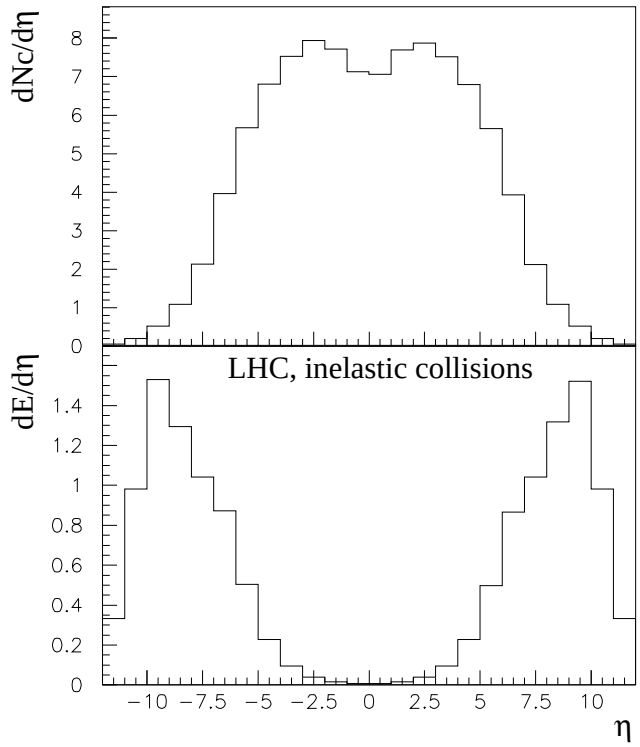

Figure 2.6: The pseudorapidity distribution of charged particles and of the energy flow at $\sqrt{s} = 14\ TeV$

2.4 Diffraction and the Pomeron

Two types of processes, the Single-Pomeron-Exchange and the Double-Pomeron-Exchange are of particular interest.

$$p + p \rightarrow p + X \tag{2.2}$$
$$p + p \rightarrow p + X + p \tag{2.3}$$

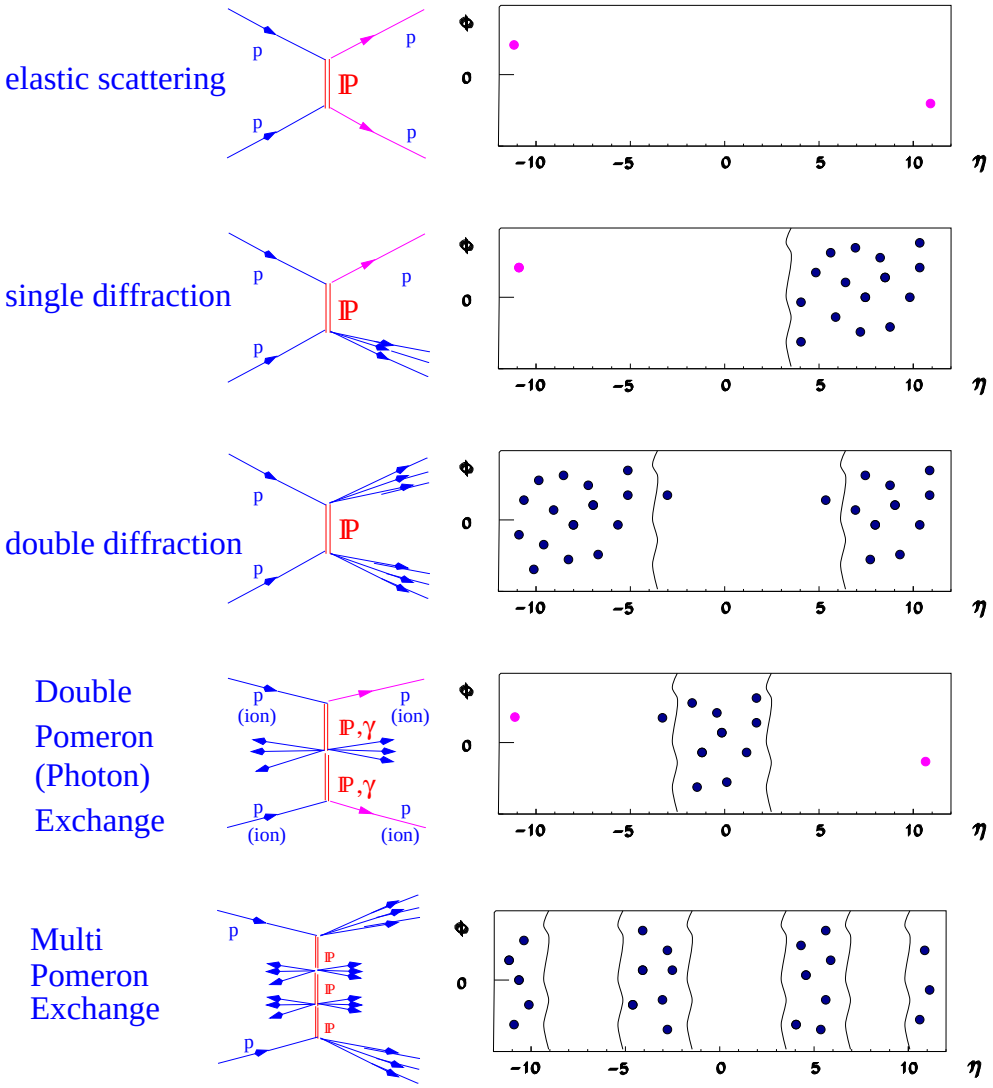

Figure 2.7: Visualization of diffractive processes in the rapidity-azimuth-plot

As a result of the UA8 experiment [10], the HERA and TEVATRON [11] experiments we now understand such diffractive events in terms of the existence of a colorless gluon-dominant cluster (Pomeron) in the partonic sea of the proton with a most likely momentum fraction of its host proton near zero. The Pomeron or its constituents interact with the constituents of the other beam proton. Two outstanding results shed light on the structure of the Pomeron: the UA8 experiment at the CERN SppS-collider observed the production of high transverse momentum jets in this class of events, demonstrating some hard partonic structure of the Pomeron. On the other hand, the H1 experiment [12] at the DESY HERA *ep*-collider studied photon interactions with rapidity gaps and showed evidence that the Pomeron has a dominant gluon structure.

It has been noted [13] that hard Pomeron-proton collisions create final states such as high-p_t jets, $t\bar{t}$ or $b\bar{b}$ in the X system (reaction (2.2)). These events can be quite spectacular, consisting of a co-planar dijet accompanied by the two unfragmented protons and nothing else. In some cases the Pomeron will give most of its momentum to one gluon (the hard structure, observed by UA8) which then interacts with a parton of the other proton creating high mass states, like e.g. the Higgs [16], in the central rapidity region. The study of the systems X in reactions (2.2) and (2.3) will answer many fundamental questions about the Pomeron structure and the Pomeron effective flux factor in the proton [17]. In particular,

detailed studies of the kinematics show that the longitudinal momentum of the mass X reflects well the Pomeron structure function. An estimate of the cross-section of reaction (2.2) at the LHC with jets $E_t > 50\,\text{GeV}$ gives 10 nb with a factor 2-3 uncertainty. This implies that one can expect to acquire about 10^3 di-jet events for an integrated luminosity of $10^{35}\,\text{cm}^{-2}$, corresponding to a few runs at large β^* with luminosities between 10^{29}-$10^{30}\,\text{cm}^{-2}\text{s}^{-1}$ (running scenario 2 and 3 in chapter 10). It should be stressed that the topology of those diffractive events is much cleaner than of ordinary non-diffractive events since the proton(s) carry more than 90 % of the initial 7 TeV beam momentum. Taking advantage of the fact that at a large β^* almost all diffractive protons will be detected in the Roman Pots and their momentum loss can be measured, an extensive program to study diffractive processes can be launched at the start of the LHC with a few days running at large β^*.

2.5 More complicated diffractive processes

By definition, diffractive phenomena are those characterized by non-exponentially suppressed rapidity gaps. Despite the fact that half of the total cross section is diffractive in nature (elastic scattering + inelastic diffractive dissociation), the processes represent a formidable challenge to theorists: how to understand the phenomena from first principles. Because of the unprecedented acceptance of the detectors, TOTEM/CMS will be able to study a wide variety of processes, previously inaccessible, that will challenge all existing ideas about diffraction, and hopefully point the way towards a better understanding of diffractive phenomena.

In the preceeding subsection we have reviewed several of the diffractive processes that will extend previous studies of diffraction to LHC energies. In discussing these processes, it has been convenient to use the language of a pomeron flux and a pomeron structure function. That is, the diffractive dijet in the Ingelman-Schlein process is thought of as arising from a pomeron-proton collision, in which a parton in the pomeron interacts with another in the proton, producing dijets in the final state. This picture provides an operational definition of the parton distribution in the Pomeron, and of the pomeron flux factor, but it is not at all guaranteed that the results can be applied to a different diffractive process.

Regardless of the theoretical framework, it is clear that the various event classes outlined in Fig. 2.2 have a logical relationship. Studying these events with TOTEM/CMS will provide stringent test of existing theoretical ideas.

2.6 Small size configurations and a new QCD regime

It has recently been noted that a trigger on hard dijet production at small rapidities provides an effective means for controlling the impact parameters in pp collisions at LHC energies [18]. Extrapolation of the HERA measurements of gluon densities to LHC energies suggest that the interaction of the "spectator" partons in the target with the strong gluon field in the projectile will be so strong as to correspond to a new regime of QCD. In this regime, multiple scattering effects are important and the interaction reaches the "Black Body Limit", that is, the maximum strength allowed by s channel unitarity. This will lead to drastic modification of the hadronic final state which can uniquely be investigated by TOTEM/CMS. Among the expected phenomena will be the strong suppression of the leading particle spectrum, and a strong suppression of correlations between the transverse momenta of the leading hadrons.

2.7 Soft diffraction and soft QCD

Complementary to the use of central dijet triggers to select small impact parameters, the use of soft diffractive triggers using the TOTEM detectors can be used to study very large impact parameters in TOTEM/CMS. There is very poor theoretical understanding of this regime, but this does not mean that it is uninteresting or unimportant. Indeed, these studies are essential if we are to better understand the processes of hadron formation, and may lead to the observation of new forms of hadron matter. For example, at LHC energies, several new phenomena may lead to a substantial change in the picture of Bose-Einstein correlations, including the presence of large long-range rapidity correlations fluctuations

in multiplicity, as well as the possible formation of large, long-lived objects such as disoriented chiral condensates or related phenomena [19].

2.8 Central diffractive production of resonances

Central double diffractive production in proton-proton collisions

$$p + p \rightarrow p + X + p$$

can be used advantageously for the study of hadronic spectra. Double Pomeron Exchange (DPE), which at the LHC is dominating over Reggeon exchanges of any kind, is predicted to be a source of glueballs or gluonic rich state. The exclusive production of scalar (0^{++}) and tensor (2^{++}) mesons via central diffractive scattering will permit the study of the dynamics of meson hadroproduction, in particular for mesons containing heavy quarks. The central exclusive diffractive production of heavy mesons could play an important role in understanding the dynamics of diffraction and improving the accuracy of theoretical predictions for new physics. The production of χ_b^0 mesons may also contribute to the understanding of the inclusive $b\bar{b}$ production cross-section at the TEVATRON, when compared to NLO QCD predictions.

Experimentally, the reaction has been studied in fixed target experiments [20] at different energies as well as at colliders, UA8 [21], at CERN SppS ($\sqrt{s} = 630\,\text{GeV}$) and CDF at the TEVATRON ($\sqrt{s} = 1800\,\text{GeV}$). CDF reported the observation of 2 jet production in DPE with a cross-section of $0.78 \pm 0.16\,\text{mb}$ [22] . Recently, they also presented results about the di-muon production in DPE with a clear J/ψ signal [11]. 10 events were found containing a $J/\psi + \gamma$ with a mass consistent with a $\chi_c^0(3415)$ resulting in an upper limit of 58 ± 18 (stat)$\pm$39 (syst) pb [23]. Estimates of the exclusive DPE cross-sections can be made using existing experimental data and different theoretical models for extrapolation. The total DPE cross-section ranges between 0.4 and 2 mbarn. The mass distribution of the central system obtained with the PHOJET simulation [24] is shown in Fig. 2.8 and individual exclusive channels are listed in Tab. 2.1 [25]. With an integrated luminosity of $10^{36}\,\text{cm}^{-2}$, corresponding to a few days running at luminosities between 10^{30} and $10^{31}\,\text{cm}^{-2}\text{s}^{-1}$, CMS/TOTEM will collect a few thousands dijet events ($E_t > 10\,\text{GeV}$) and a few hundred χ_c^0 radiative decays and perhaps a few χ_b^0 decays.

The double Pomeron topology is given by two non-collinear forward protons with activity in the central CMS detector. Whereas almost all diffractive protons are detected with high efficiency their momentum loss can only be determined with a precision of 10^{-3} and hence will not have the precision needed to determine the low masses. (A special optics is presently under consideration that may significantly improve this resolution). The azimuthal angle of the forward protons can be measured with high precision allowing the definition of the quantum numbers J^{PC} using theoretical predictions and hence simplifying the traditional partial-wave analysis.

Central system X	M_X	σ
2 jets	$E_T > 10\,\text{GeV}$	$\sim 1\,\mu\text{b}$
$c\bar{c} : \chi_c^0$	$3.415\,\text{GeV}$	$\sim 4 \div 6\,\mu\text{b}$
$b\bar{b} : \chi_b^0$	$9.86\,\text{GeV}$	$\sim 1 \div 2\,n\text{b}$
DPE total		$\sim 0.4 \div 2.1\,m\text{b}$

Table 2.1: Some DPE cross-sections [25]

References

[1] TOTEM LoI, CERN/LHCC 97-49 (1997).

[2] J.R. Cudell *et al., Phys. Rev. Lett.* **89**, 201801 (2002).

[3] E. Nagy *et al., Nucl. Phys.* **B150** (1979) 221.

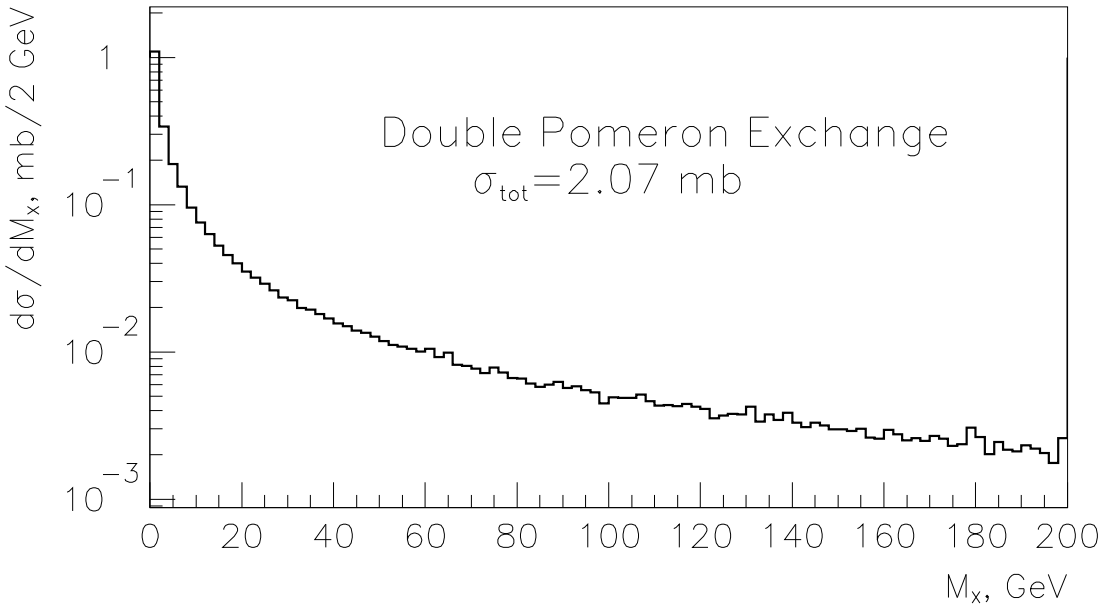

Figure 2.8: Mass distribution for Double-Pomeron-Exchange, calculated with PHOJET [24]

[4] UA4 Collaboration, M. Bozzo *et al., Phys. Lett.* **B147** (1984) 385; *Phys. Lett.* B **155** (1985) 197.

[5] N. Amos *et al., Phys. Lett.* **B247** (1990) 127.

[6] A. Martin, in proceedings of "Elastic and Diffrative Scattering at the Collider and Beyond, 1^{st} Blois 1985 Workshop, Editions Frontiers, eds. B. Nicolescu and J. Tran Thanh Van, p.153.

[7] T.T. Chou and C.N. Yang, *Phys. Lett.* **B244** (1990) 113.
S.V. Goloskokov, S.P. Kuleshkov and O.V. Selyugin, *Z. Phys.* **C50** (1991) 455.
M.M. Islam, *Z. Phys.* **C53** (1992) 253.
R.J. Glauber and J. Velasco, *Phys. Lett.* **B147** (1984) 380.
M.J. Menon, *Phys. Rev.* **D48** (1993) 2007.
J. Pumplin, *Phys. Lett.* **B289** (1992) 449.
A. Donnachiae and P.V. Landshoff, *Nucl. Phys.* **B267** (1986) 690.
B. Margolis *et al., Phys. Lett.* **B213** (1988) 221.
M.M. Block *et al., Phys. Rev.* **D60** (1999) 054024.
D. Cline, F. Halzen and J. Luthe, *Phys. Rev. Lett.* **31** (1973) 491.
L. Durand and H.Pi, *Phys. Rev.* **D40** (1989) 1436.
P.V. Landshoff, 'The two pomerons'; PSI-Proceedings 94-01, p.135.
V.A. Petrov, E. Predazzi and A. Prokudin, *Eur. Phys. J.* **C28** (2003) 525.
P. Gauron, E. Leader and B. Nicolescu, *Phys. Lett.* **B238** (1990) 406.

[8] M.M. Islam, R.J. Luddy and A.V. Produkin, *Mod. Phys. Lett.,* **A18** (2003) 743-752.

[9] C. Bourelly, J. Soffer and T.T. Wu *Eur. Phys. J.* **C28** (2003) 97. A. Ageer *et al., J. Phys. G: Nucl. Part. Phys.* **28** (2002) R117-R215.

[10] A. Brandt *et al. (UA8-Collaboration) Phys. Lett.* **B297** (1992) 417.

[11] M. Gallinaro for the CDF collaboration, FERNILAB-CONF-03-403-E, presented at 23^{rd} International Symposium on Multiparticle Dynamics (ISMD 2003), Cracow, Poland, 5-11 Sep. 2003.

F. Abe *et al.,* Phys. Rev. Lett. **80** (1998) 1156.
D. Acosta *et al.*, hep-ex/0311023
B. Abbot *et al.*,, Phys. Lett. **B531** (2002) 52.

[12] C. Adloff *et al. (H1 Collaboration), Zeit. f. Physik* **C76** (1997) 613.

[13] G. Ingelmann and P. Schlein, Phys. Lett. **B152** (1985) 256

[14] http://totem.web.cern.ch/Totem/cms/meeting.html

[15] FELIX, a full acceptance detector at the LHC, CERN/LHCC97-45 (1997).

[16] S. Erhan, V.T. Kim and P. Schlein (submitted to European Physical Journal C).

[17] D. Acosta *et al.* Phys. Rev. Lett. **88** 151802 (2002) and references therein.

[18] Frankfurt, Strikman, Weiss, hep-ph/0311231.

[19] MiniMax Collaboration, 'A Search for Disoriented Chiral Condensate at the Fermilab Tevatron', Phys.Rev. D61 (2000), hep-ex/9906026
J. D. Bjorken, 'Disoriented Chiral Condensate: Theory and Phenomenology', Acta Phys.Polon. B28 (1997) 2773-2791, hep-ph/9712434

[20] T.A. Armstrong *et al.,* CERN-SPSC-82-3, 1982.
S.Abatzis *et al.,* CERN-SPSC-90-002, 1990.
J.P. Peigneux *et al.,* CERN-SPSLC-94-22, 1994.

[21] A. Brandt *et al., Eur. Phys. J.C.* **25** (2002) 361.

[22] T. Affolder, *Phys. Rev. Lett.* **85** (2000) 4215.

[23] A. Wyatt, *Double Pomeron exchange and χ_c production at CDF,* Workshop on Physics with forward proton taggers at the Tevatron and LHC, Manchester, 14-16. Dec. 2003.
A. Wyatt, Results on Diffraction at CDF, FERMILAB-Conf-03/324-E (2003).

[24] R. Engel, PHOJET manual, version 1.05c, University Siegen preprint 95-05.

[25] V.A. Khoze, A.D. Martin, M.G. Ryskin *Eur. Phys. J.* **C23** (2002) 311.
V.A. Khoze, A.D. Martin, M.G. Ryskin *Eur. Phys. J.* **C19** (2001) 477.
V.A. Khoze, A.D. Martin, M.G. Ryskin *Eur. Phys. J.* **C20** (2001) 599.

3 Machine Optics and Parameters

3.1 Concept of the measurement

The detection of forward protons from elastic or diffractive scattering at LHC energies requires the measurement of very small scattering angles (5–10 μrad).

These particles circulate close to the beam and can be detected downstream symmetrically on either side of the interaction point (IP) if the displacement at the detector location is large enough and if the beam divergence at the IP is small compared to the scattering angle.

In order to achieve these conditions, a special high-β^* insertion is required. A large value (O(km)) of the β-function at the IP (β^*) and a smaller beam emittance reduce the beam divergence. A large effective length L^{eff} at the detector location ensures a sizeable displacement.

The trajectory of a particle at nominal momentum through the accelerator lattice can be described as:

$$\begin{pmatrix} u(s) \\ u'(s) \end{pmatrix} = T_u(s) \begin{pmatrix} u^* \\ u'^* \end{pmatrix} \tag{3.1}$$

where $u(s)$ is one of the two transverse coordinates $x(s)$ and $y(s)$, $u'(s)$ is the projected scattering angle, T(s) is the transfer matrix between the IP and the detector location and u^* and u'^* are the coordinate and angle at the IP.

From Eq. 3.1

$$u'^* = \frac{u(s) - T_{11}u^*}{T_{12}}, \tag{3.2}$$

it is clear that the best strategy for the design of the optics is:

- $T_{11} = 0$, i.e. the transverse position of the proton at the detector is independent of its transverse position at the collision point (parallel-to-point focusing optics); and
- T_{12} be as large as possible to have a deflection of the order of a millimeter.

In this special case, the element T_{12} represents the effective distance of the detectors from the IP.

For an optics symmetric around the IP, the two elements can be expressed as follows [1]:

$$\begin{aligned} &\text{Magnification} && T_{11} = v_u = \sqrt{\frac{\beta_u(s)}{\beta^*}} \cos \Delta\mu_u(s) \\ &\text{Effective length} && T_{12} = L_u^{eff} = \sqrt{\beta_u(s)\beta^*} \sin \Delta\mu_u(s) \\ &\text{Phase advance} && \Delta\mu_u(s) = \int \frac{1}{\beta_u(s)} ds \end{aligned} \tag{3.3}$$

The condition of parallel-to-point focusing is achieved by requiring the betatron phase advance $\Delta\mu_u(s) = \pi/2$ at the detector location, which also maximizes L_u^{eff}.

The minimum distance of a detector from the beam is proportional to the beam size:

$$y_{min} = K\sigma_y{}^{beam} = K\sqrt{\epsilon\beta_y(s)}, \tag{3.4}$$

where ϵ is the transverse beam emittance and K is around 10–15. Combining this with Eqs. 3.2–3.4 and assuming the parallel-to-point focusing condition, the smallest detectable angle is:

$$y'^{*} = \theta^{*}_{ymin} = K\sqrt{\frac{\epsilon}{\beta^{*}_{y}}}. \tag{3.5}$$

Assuming the nominal value for ϵ, β^{*} has to be larger than 1000 m, if scattering angles of a few μrad are to be detected. The beam divergence $\sigma^{*}_{\Theta} = \sqrt{\epsilon/\beta^{*}}$ is then K times smaller than the minimum scattering angle.

3.2 Insertion optics for elastic scattering

3.2.1 Physics optics for small $|t|$

A first optics with the properties described in the previous section was proposed some years ago [2]. It was sufficient to fulfil the above requirements but needed a special triplet powering. Since then, a new optics has been designed mainly to eliminate this drawback. It uses a symmetric triplet optics [3] (same focusing in both planes) which is possible thanks to the new triplet powering scheme [4]. The triplet powering scheme is the same as that of the nominal LHC which is another improvement compared with the old optics: it is less expensive (saving two 8kA power supplies and two high-current switches) and safer and easier to operate as it uses the standard quadrupole calibration.

In order to improve the performance, an optics with a phase advance of $\pi/2$ in both horizontal and vertical planes has been tried. In fact, the condition can be fulfilled exactly only in one plane due to the limited strength of the insertion quadrupoles, but it is almost fulfilled in the other plane. In order to maximize the effective length, the detector location had to be placed close to the quadrupole Q6.

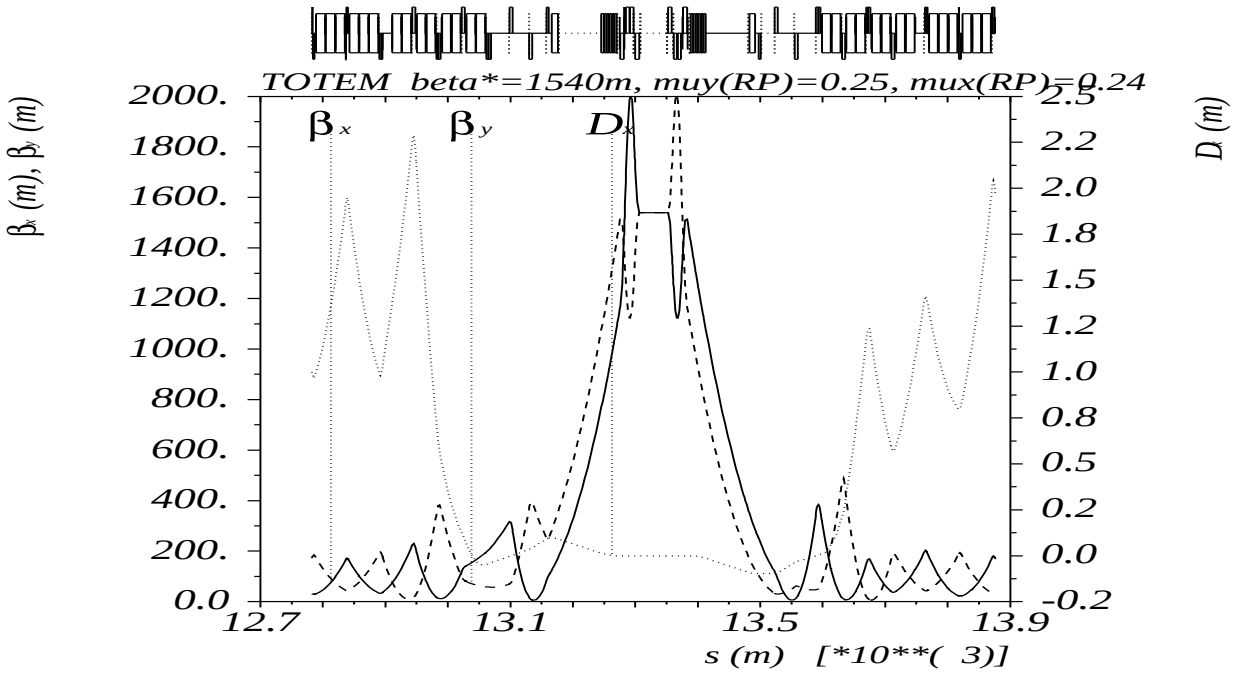

Figure 3.1: LHC high-β^{*} optics for TOTEM

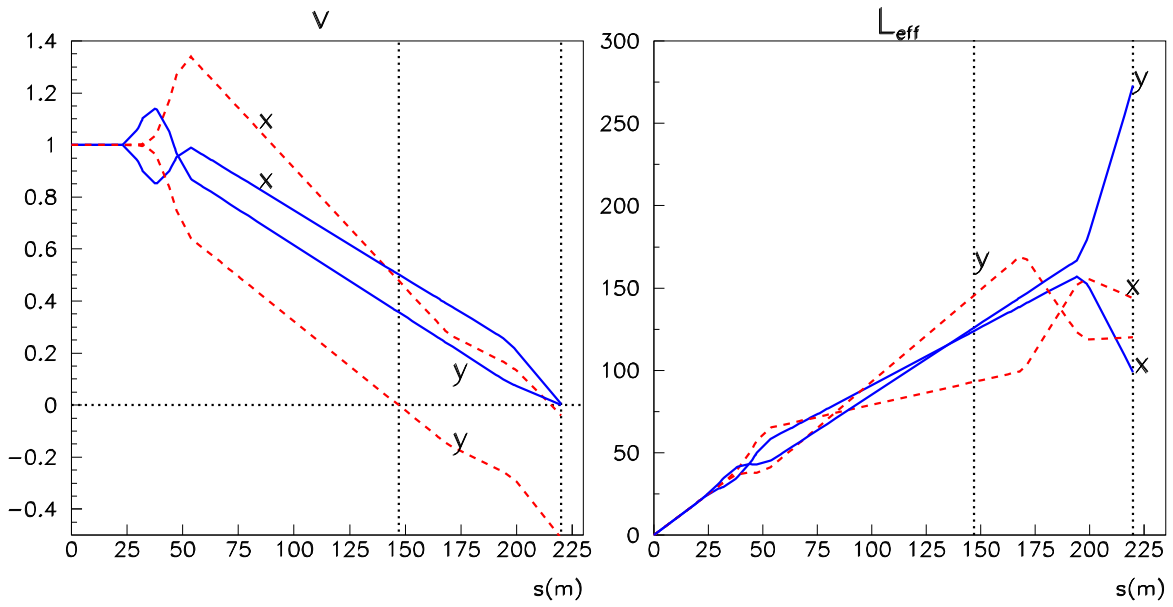

Figure 3.2: The magnification v and the effective length $L^{eff}(m)$ versus the distance to the IP along the beam (solid lines β^*=1540 m, dashed lines β^*=1100 m)

The value $\beta^* = 1540$ m is limited by the strength of the insertion quadrupoles. It is worth mentioning that by using the ultimate gradients, it is possible to obtain a value of β^* of 2500 m, while still maintaining the parallel-to-point focusing in both planes. The optics functions in the insertion are shown in Fig. 3.1.

Figure 3.2 compares the effective length and magnification of the old and new optics. For β^*=1540 m, L_y^{eff} is almost doubled and the parallel-to-point focusing condition is achieved almost precisely both in the horizontal and vertical planes at a distance of 220 m from the IP. This feature dramatically improves the resolution of the polar and azimuthal angle measurement, allowing a better resolution on the t measurement and a better determination of the colinearity of the events (see Section 11.1.3).

An effective length of 272 m can be achieved in the vertical plane (betatron phase exactly equal to 0.5π) and of 99 m in the horizontal plane (betatron phase of 0.48π). The value of β_y at the detector is 48 m giving an r.m.s. beam size of 0.08 mm at a reduced normalized transverse emittance $\epsilon_N = 1\,\mu$m$\cdot$rad (0.15 mm at nominal emittance $\epsilon_N = 3.75\,\mu$m$\cdot$rad). If a detector is placed at a distance $10\sigma_y^{beam}$+0.5 mm from the beam center, the minimum $|t|$-value (Eqs. 3.4–3.5) accessible is $1.1{\cdot}10^{-3}$ GeV^2 ($2.8\cdot10^{-3}$ GeV^2) at zero detector efficiency with a beam divergence of 0.3 μrad (0.57 μrad).

As the global betatron phases of the insertion have been left free, the tunes are far from nominal when a single insertion is introduced into the lattice. A solution to this problem consists of setting the same optics in IR1 which makes tunes equal to 64.42 in the horizontal plane and 58.19 in the vertical plane (the nominal values are 64.31 in the horizontal plane and 59.32 in the vertical plane). The difference of one integer in the vertical plane is not important as the LHC tunes have been separated to overcome a possible problem with betatron coupling (a larger tune split is more favourable). The fractional parts can be set to the nominal values by retuning the IR4 insertion [4]. This is possible provided the normalized beam emittance is smaller than 2.6 μm $\cdot$ rad due to the beam screens in the IR4 quadrupoles.

The intra-beam scattering (IBS) growth time is about equal to the transverse synchrotron damping time which is 25 h [4]. Thus no damping is expected and the 1 μm $\cdot$ rad normalized emittance can be considered as the equilibrium emittance. Actually, given these values, some scraping of the beam can be envisaged for further reduction of the emittance at special low-luminosity runs. For instance, the transverse IBS growth time goes down to 11 h if the emittances and the beam intensity are reduced by a further factor of two. Thanks to the transverse synchrotron damping, the growth time is then only 19 h, which leaves sufficient time for data taking.

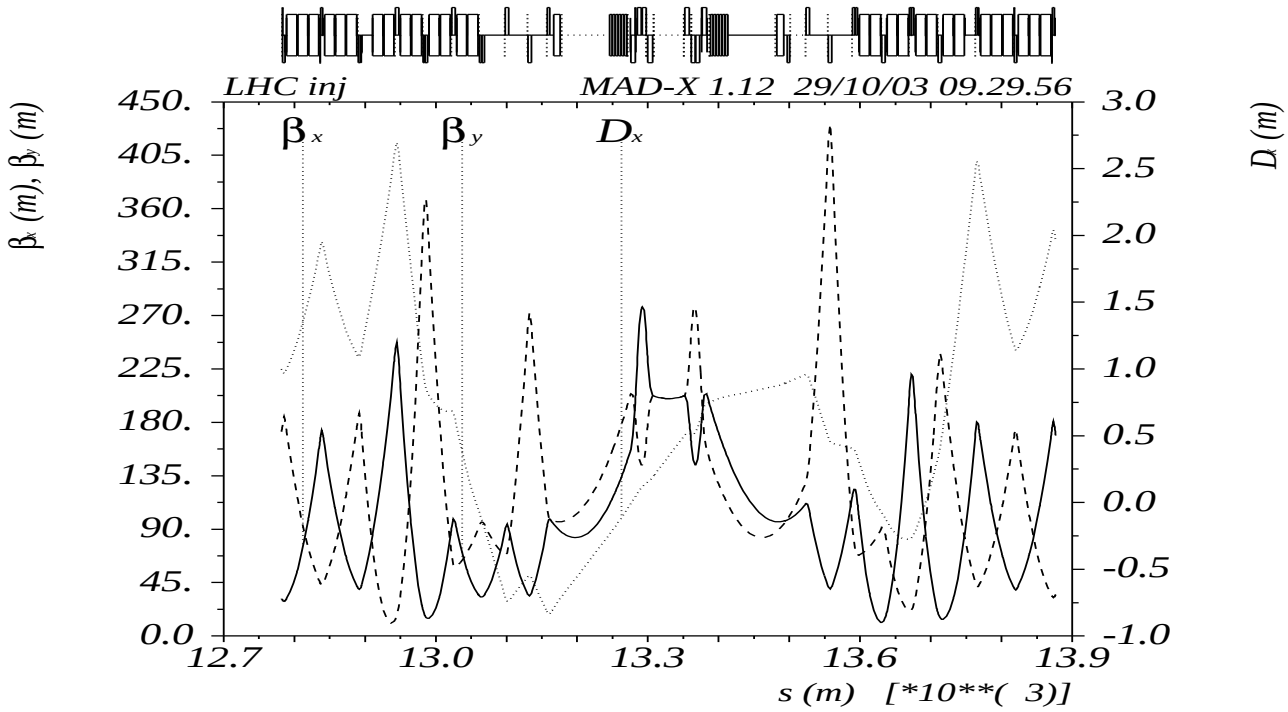

Figure 3.3: LHC injection optics for TOTEM

It is not possible to inject a beam with the physics optics because the aperture limitation in the TAS (the absorber in front of the triplet) is too tight. Thus the injection has to be done at a smaller value of β^*. It was possible to reduce β^* down to 200 m but not below, keeping the betatron phases of the whole insertion the same as for physics, but dropping the pot phases. With this value, a beam with a normalized emittance of 2 μm $\cdot$ rad can be injected safely. This is enough as the nominal emittance for TOTEM operation is 1 μm $\cdot$ rad. The optics functions are shown in Fig. 3.3.

This optics needs a special commissioning, as was also the case for the old TOTEM optics, due to the fact that the topology of the optics functions is very different from the nominal one.

3.2.2 Physics optics for large $|t|$

The large value of L^{eff} in the high-β optics and the limitation due to the vacuum pipe (and beam screens) does not allow the measurement of elastic events at $-t > 0.5$ GeV^2. Moreover, the elastic cross section decreases rapidly with t ($d\sigma/dt \sim t^{-8}$), therefore a higher luminosity is required.

Optics with values of β^* between 18 m and 0.5 m are all possible as they are included in the nominal LHC optics set. The beam emittance can be adjusted between the nominal value of 3.75 and 1.0 μm$\cdot$rad.

Consider, as an example, a scheme with the nominal LHC injection optics (β^*=18 m) and a crossing angle of 200 μrad. The value of β_y at the detector is 154 m and ${\sigma_y}^{beam}$ is 0.14 mm (0.28 mm) at $\epsilon_N = 1$ (3.75) μm $\cdot$ rad: the minimum $|t|$-value accessible is then 0.2 (0.5) GeV^2. The triplet aperture limits the maximum $|t|$-value reachable to $\sim$ 8 GeV^2. In order to have a good acceptance overlap in t between high and medium β^*, an additional detector location around 147 m is being considered. Studies on the optimization of an intermediate optics with $\beta^* = 200$–400 m are also in progress.

3.3 Machine parameters for TOTEM operation

The accuracy of the measurement of σ_{tot} and the detection of forward processes impose very demanding requirements on the beam parameters, on the accuracy of their measurements and on their stability. The TOTEM requirements on the beam parameters and on their measurement, uncertainties are listed in Table 3.1 and are compared with the expected machine performance during standard operation.

	Requested accuracy	Measurement error	Stability during a run ($\sim$ 1 hour)
β^*	1%	<1%	0.1%
β	<5%	few %	0.1%
L^{eff}	2%	2%	<1%
v	0.02	0.02	< 0.02
Emittance	1%	5%	5%
Crossing angle	0.2 μrad	0.2 μrad	0.2 μrad
Beam orbit	5–10 μm	5–10 μm	5–10 μm
Energy	$\sim$0.05%	0.1%	stable

Table 3.1: TOTEM requirements on the beam parameters

Measurement of β

In the case of the high-β^* insertion, the measurement of β^* is rather easy as it has about the same value as in Q1. This value can be measured by changing the current in the trim power supply of Q1 and recording the associated value of the tuneshifts. The value of the tuneshift ΔQ associated with an integrated gradient change ΔKl in a quadrupole of length l, when the machine β-function has the value β_Q, is given by:

$$\Delta Q = \frac{\Delta Kl \cdot \beta_Q}{4\pi}$$

As β_Q is $\sim$1.5 km and l $\sim$5 m, a change of the K of Q1 by 0.0001 (about 1% of the nominal gradient) produces a tuneshift of 0.06, which is easy to measure. The gradient setting accuracy is about 10^{-5} of the nominal, so it contributes a relative uncertainty of the order of 0.1% on the β measurement. The tuneshift can be measured within 0.0001, i.e. the relative uncertainty on a tune-shift of 0.06 is 0.2%. We see that for this particular case of the high-β insertion, the value of the β function can be measured easily with an accuracy of the order of one per cent. Actually, combining the measurements in both planes and both sides of the IP, the measurement is indeed very accurate.

The same procedure as for β^* can be applied to measure β at the detector location. The accuracy is less good as the tuneshift cannot be made larger than the above value and the value of β is smaller by a factor of about 30. The accuracy will be therefore in the range of a few per cent, provided it is not limited by the knowledge of the quadrupole transfer function.

Direct measurement of L^{eff}

The T_{12} term of the transfer matrix between the IP and the detector can be directly measured by means of a trajectory measurement. As there is one Beam Position Monitor (BPM) on each side of the IP, it can be checked that the trajectory measured from a difference between two closed orbit measurements has an angle and no excursion at the IP, and viceversa.

The procedure consists of making two sorts of local closed orbit deformations using closed orbit correctors. For a deformation with an angle and no displacement at the IP, the ratio between the displacement measured at the RP and the angle at the IP gives directly L^{eff}. For a deformation with a displacement at the IP and no angle, the displacement measured at the RP gives the magnification (it should be zero)

Assuming a BPM resolution of 5 μm the uncertainty on the angle at the IP is of the order of 0.2μrad. The displacement at the detector can probably be measured within the detector resolution by finding the

edge of the beam. As bumps of several millimeters can be made. The detector resolution is in the range of 10μm. Consequently, the accuracy on L^{eff} must be in the range of one percent.

Uncertainty on L^{eff} and magnification due to machine imperfection

As in any storage ring, there are uncertainties in the quadrupole settings as well as drifts of the power supplies during a physics run. These uncertainties introduce an uncertainty on the value of $L^{eff} = T_{12}$. This can be computed from optics perturbations in a transfer line (see for instance Ref. [5]). As we are interested in the T_{12} matrix element, only the perturbation of the phase and the β-function of the machine section between the IP and the detector taken as a transfer line, have to be estimated. As the phase at the detector is $\pi/2$, there is no contribution of the phase uncertainty, to first order, to the uncertainty on the T_{12} matrix element. An upper limit of the perturbation of the value β_t of the transferred β-function at the detector is given by a sum over the gradient uncertainties of index i, ΔK_i, integrated over their length l_i [5]:

$$\frac{\Delta\beta_t}{\beta_t} = \sum_i \Delta K_i l_i \beta_i \sin(2\mu - 2\mu_i),$$

where β_i is an upper limit of the value of the actual β-function at the place of the gradient uncertainty of index i and μ_i the phase. (Note that since the transferred β_t is involved, the machine tune does not enter into the equation. The values of β_i are the same as the machine values if the initial β at the IP is equal to the nominal, i.e. 1540m.) We assume random uncertainties or random drifts of relative r.m.s. value $\Delta K/K$. The expectation value of the uncertainty on L_{eff} is given by:

$$\frac{\Delta L_{eff}}{L_{eff}} = \frac{\Delta\beta_t}{2\beta_t} = \frac{\Delta K}{4K}\sqrt{\sum_i (K_i l_i \beta_i)^2},$$

the expectation value of $\sin(2\mu - 2\mu_i)$ being 1/2. It is clear that the main contribution to this uncertainty comes from the triplet for which: $K_i < 0.0036$ m^{-2}, $l_i < 6.35$ m, and $\beta_i < 2000$ m. An upper limit on the relative uncertainty on L_{eff} is then equal to $22\Delta K/K$. The expected random setting uncertainties are of the order of 0.001. These make a systematic relative uncertainty of the order of 2% on L^{eff}. The relative drifts of the power supplies over a physics run are of the order of 10^{-5}, which induces a drift with an expected value $2 \cdot 10^{-4}$. This drift cannot be corrected but it has a negligible impact on the measurement.

The gradient uncertainties also make a non-zero magnification. It is given by:

$$\Delta T_{11} = \sqrt{\frac{\beta}{\beta^*}}\langle\frac{\Delta\beta_t}{\beta_t}\rangle$$

where $\langle\frac{\Delta\beta_t}{\beta_t}\rangle$ is the quadratic sum of the relative uncertainties on the transferred β-functions at the quadrupoles, i.e. about equal to 1% (for the triplet contribution, the other ones being negligible). The relative increase of the beam size σ at the detector is

$$\frac{\sqrt{\sigma^{*2}\Delta T_{11}^2 + \sigma^2}}{\sigma} - 1 = \frac{1}{2}\langle\frac{\Delta\beta_t}{\beta_t}\rangle,$$

which is negligible.

Measurement of the detector phase

In principle, the phase measurement is accurate using a 1000 turn measurement as in LEP. It can be determined within one degree [6] and does not contribute a sizeable uncertainty to L^{eff}.

Emittance

Operation with low emittance has the two desirable consequences of reducing both the beam size and the beam angular spread which allows the detection of particles emitted at very small angles and reduces the

systematic uncertainty on the measurement of the angle itself. The LHC baseline normalised transverse beam emittance is 3.75 μm $\cdot$ rad. The possibility of achieving the smallest beam emittance of 1 μm $\cdot$ rad is presently under discussion. Preliminary results from the tests in the SPS during 2003 show that the injection oscillations in the SPS are under control and that normalized emittances of 1 μm $\cdot$ rad can be achieved at 450 GeV for bunch intensities up to $0.7{\cdot}10^{11}$. For higher intensities, the emittance increases due to space charge effects [7]. Moreover it has to be taken into account that such a small emittance has a quite strong implication on the collimation system since it can produce a significant transverse resistive impedance due to the small gaps which are required for a very narrow beam. In fact, assuming that the detectors will be positioned in the shadow of the collimation system to take advantage both of its cleaning efficiency and of its protection in case of accidents, the reduced emittance implies a collimator full gap opening of $\sim$ 1 mm for the nominal settings. The transverse beam emittance measurement is based on the measurement of the transverse beam size and on the optics parameters at the position of the monitors [8] and it is planned to be measured with an accuracy of 5%.

Crossing angle and beam orbit

The TOTEM running scenario foresees 43 bunches which can be increased to 156 (see Chapter 10). In these scenarios, the separation of the bunches is still sufficiently large so as to allow zero degree crossing angle. The stability of the zero crossing has to be maintained within 0.2 μrad to have no effect on the resolution. This is consistent with the BPM specifications [9] which require an instrument resolution of $\sim$ 5 μm.

Hence it can be assumed that relative orbit changes can be measured with a similar accuracy of $\sim$ 5 μm. If the position of the closed orbit is maintained with this accuracy, the beam displacement at the IP will be of this order. As the beam size is 0.45 mm, the associated relative luminosity loss is less than 0.001, i.e. negligible.

However, the measurement of the absolute beam orbit position with respect to the detectors is affected by systematic uncertainties such as, for example, the alignment uncertainties and so, in this case, the accuracy is expected to be worse than 5 μm. The possibility of minimizing these systematic uncertainties at the detector positions is presently under discussion. The closed orbit feedback allows a beam orbit stability $\leq$ 10 μm [10] while the run-to-run orbit stability can be estimated to be around 20 μm.

Energy

The absolute beam energy can be measured with the method based on the revolution frequency measurements of the proton and heavy ion beams injected into the same magnetic field [11] or via the measurement of the magnetic field integral in the LHC. The accuracy achievable with the first method is limited by the tiny frequency difference between the proton and heavy ion beams due to the very high beam energy, while the second one is limited by the accuracy of the measurement of the magnetic field integral. With both these methods it is possible to achieve an accuracy of 0.1%. However to match the required accuracy of $\sim$0.05 % other methods are presently under investigation [12].

References

[1] K.G. Steffen, H. Hultschig and W. Kern, Use of generalised amplitude and phase functions in designing beam transport systems, DESY/A 2-70 (1960).

[2] A. Faus-Golfe, A. Verdier, Optics studies for diffractive physics at the LHC. EPAC 2002 (Paris).

[3] S. Weisz, An analytic approach to a high-β insertion and possible application for TOTEM at the LHC. LHC project note 164 (September 1998).

[4] LHC 2003 design report, to be published.

[5] B. Autin and A. Verdier, Focusing perturbations in alternating gradient structures, CERN ISR-LTD/76-14, (1976).

[6] R. Bossard and W. Scandale, Measurement of the betatron phase advance and betatron amplitude ratio at the $SP\bar{P}S$ collider, PAC Washington, March 1987.

[7] Minutes of the LHC Technical Committee #2003-16 http://lhcp.web.cern.ch/lhcp/ab_ltc/ltc_2003-16.html

[8] C. Fischer, Measurement of the transverse beam distribution in the LHC rings, LHC-B-ES-0006 rev 1.0, EDMS Document No. 328147.

[9] J-P Koutchouk Measurement of the beam position in the LHC main rings, LHC-BPM-ES-0004 rev 2.0, EDMS Document No. 327557.

[10] J. Wenninger , Orbit control for machine operation and protection, Proc. of Chamonix XII, CERN-AB-2003-008 ADM.

[11] G. Arduini et al., Energy Calibration of the SPS at 450 GeV/c with Proton and Lead Ions beams,AB-Note-2003-014 OP

[12] J. Wenninger, private communication.

4 Roman Pots

4.1 Introduction

Roman Pots have been successfully designed and used for forward physics experiments at the ISR, SPS, TEVATRON, RHIC and DESY with the goal of bringing detectors very close to the beam without interfering with the primary vacuum of the machine. Nevertheless, because of the more challenging constraints imposed by the LHC, such as high beam energy, the Ultra High Vacuum, the high radiation fluxes, and the required physics performances of TOTEM, which needs to have active detectors at $\sim 1\,\text{mm}$ from the 7 TeV beam, a new Roman Pot design has been developed. Three stations of Roman Pots will be mounted on each side along the Long Straight Section at IP5 (LSS5), their positions being defined by the special optics used by TOTEM and by the space available between the LHC components. The first station is placed between 145 m and 149 m from IP5, before the dipole D2, the second station at about 180 m between the Q4 and Q5 quadrupole and the third between 216 m and 220 m behind the quadrupole Q5. The second station will be placed at a later stage. (see Fig. 4.1).

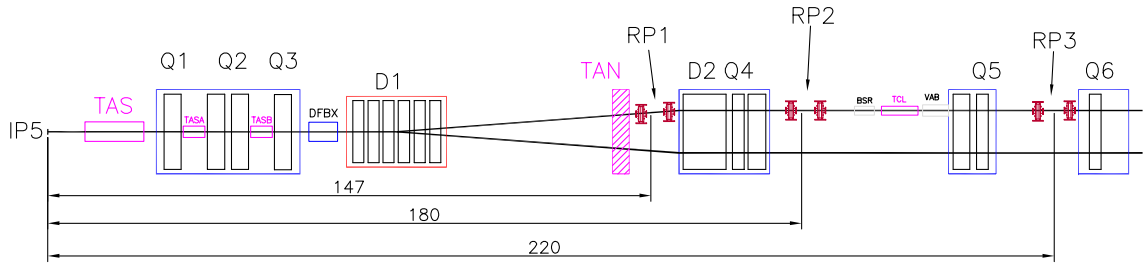

Figure 4.1: The insertion I5: location of the Roman pots stations RP1, RP2, RP3. The layout is symmetric with respect to the interaction point

Each station is composed of two units, separated by a distance of 4 m, with each unit consisting of two pots that move vertically and one that moves horizontally (see Fig. 4.3).

The design of the Roman Pots is driven by the constraints imposed by the performance and the safe operation of LHC as well as by the requirements needed to guarantee the TOTEM physics performance. The LHC needs an ultra high vacuum to guarantee a long beam lifetime and to avoid quenches in the superconducting magnets. In the warm sections of the LHC, the vacuum must be stable against ion-induced desorption. Hence the TOTEM detectors and the electronics must be physically separated from the primary vacuum of the machine to prevent an unacceptable outgassing. This physical separation between the beam and the detectors is also required to provide adequate shielding of the electronics against the radio frequency pick-up induced by the magnetic fields generated by the high intensity bunched beam structure.

The Roman Pots have to be placed in the shadow of the LHC collimators to profit both from their protection against accidental beam losses and from their cleaning efficiency to reduce the background.

In particular, the minimum distance of the Roman Pot window from the beam is defined in the vertical plane by the beam halo profile, and in the horizontal plane by the settings of the absorbers which protect the machine in case of asynchronous beam abort (see Chapter 10). Both constraints limit the approach to $10\,\sigma$ beam envelope: for the TOTEM high-β^* optics, this corresponds to a vertical distance of $\sim 1\,\text{mm}$

(Fig. 4.2). In order to meet both the physics performance and the safety requirements, the mechanical stability of the detectors and their mountings in the pot needs to be within at most $\sim$ 20 μm (see Chapter 11). For this purpose, the motors and their controls need to be chosen carefully, and in addition, they have to be radiation hard.

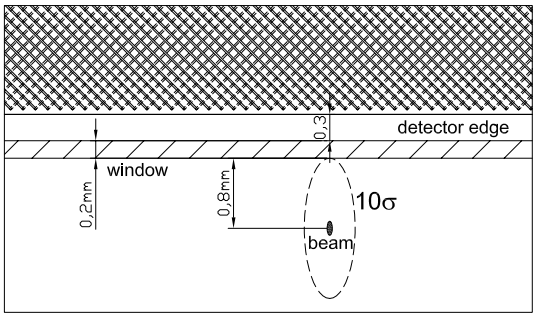

Figure 4.2: Transverse distance of detector from the beam, showing the window of thickness 0.2 mm placed at 10σ (0.8mm) from the beam

4.2 Roman Pot construction

At the Roman Pot locations, the LHC beams are physically separated in two independent vacuum chambers horizontally spaced by 194 mm. The tight space between the two beam pipes imposed a Roman Pot design with the mechanics asymmetrically placed on the side of the vacuum chamber. The TOTEM physics requires to place the detectors close to the beam both vertically and horizontally. Two different kinds of Roman Pots have been designed, vertical and horizontal ones. Two independent vertical pots allow the access of the detectors to the beam from the top and the bottom. The horizontal one can only approach the beam from one side due to the presence of two beam pipes. For both horizontal and vertical devices the mechanical features are the same.(Fig. 4.4).

At the location of the pots, an enlarged vacuum chamber provides sufficient space for the movements of the pots. This vacuum chamber (Fig. 4.5) is attached to the machine beam pipe by means of bellows.

The pots are supported and guided by a sliding mechanism which moves them relatively to the main assembly block by stepping motors with encoders placed on the top and bottom of the main block (Fig. 4.6).

Slide ball screws provide the link between the stepping motors and the pots and allow the pots to be moved precisely along these screws without any backlash. These screws also provide full pull-out of the Roman Pots in case of motor failure. The stepping motors are remotely controlled and provide a resolution of 0.9^o. When coupled with these high precision screws, they offer a positioning resolution of a few microns.The driving control system has to be designed to provide smooth positioning without undesired over-shooting. The encoder precision also plays an important role in the final positioning accuracy. The stepping motors commercially available are in general sufficiently radiation hard to withstand the radiation levels present in the tunnel. This is not the case for the control electronics which has to be placed into a shielded region.

Due to the primary vacuum of the machine, the pots are pulled into the main vacuum chamber with a force of $\sim$ 1000 Newtons. A compensation system is required to neutralize this force on the pot and to simplify its operations (Fig. 4.7). The compensation is provided by two bellows connected to the secondary vacuum pump. To be compatible with the asymmetric configuration of the Roman Pot mechanics, the force is transmitted to the sliding assembly by means of lever arms.

In this way, movement of the pots is greatly facilitated: the motors have to apply only a minimal torque for the displacement.

The Roman Pot device is fixed to the ground of the tunnel by means of a stable pedestal on which an adjusting table supports the Roman Pot. The pedestal defines the position of the Roman Pot along the

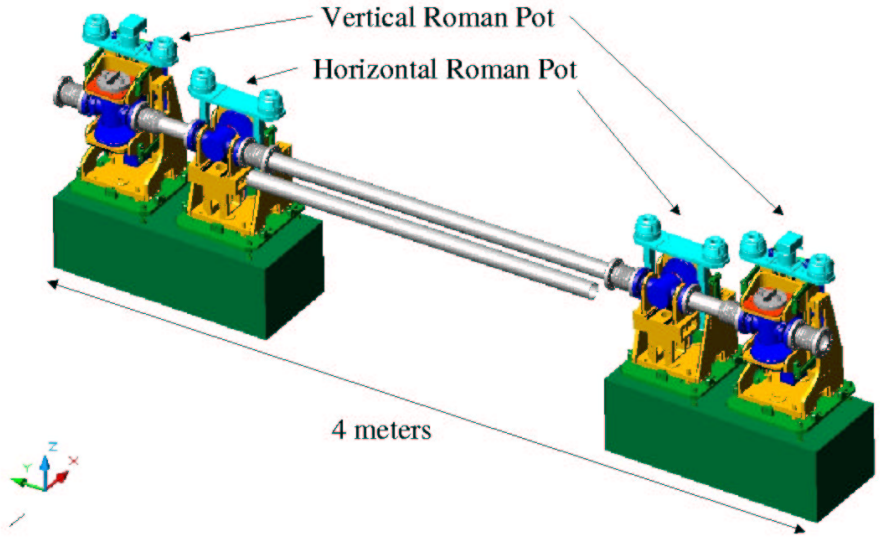

Figure 4.3: Roman Pot station composed of two units each consisting of two pots that move vertically and one that moves horizontally

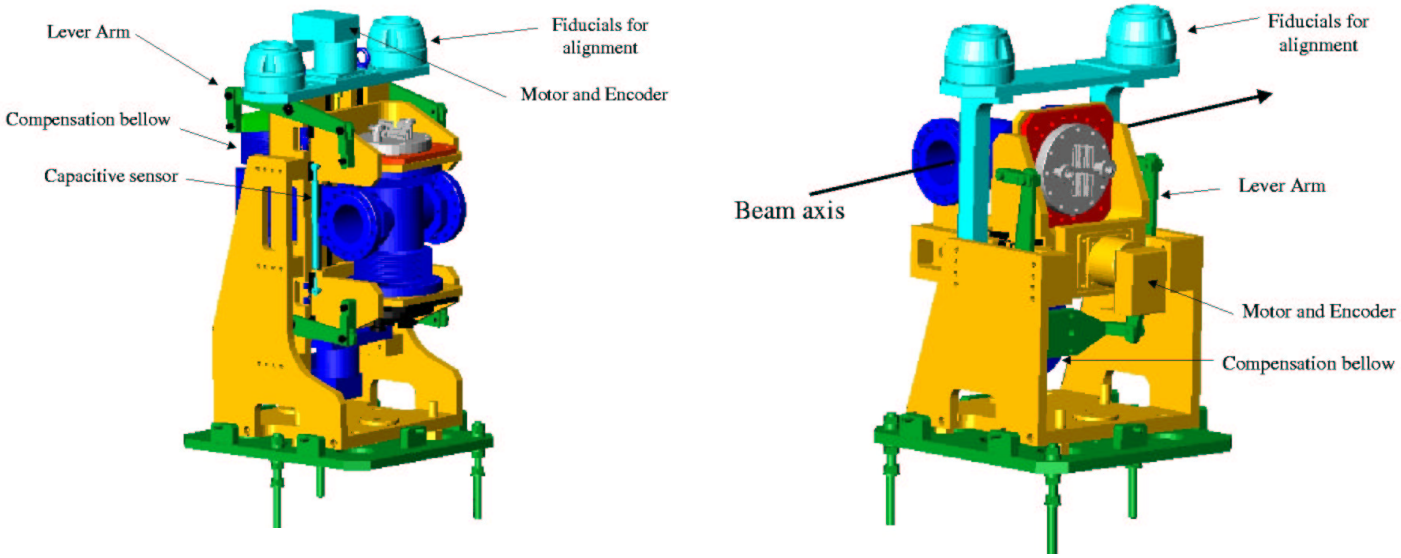

Figure 4.4: Vertical (left) and horizontal (right) Roman Pot device

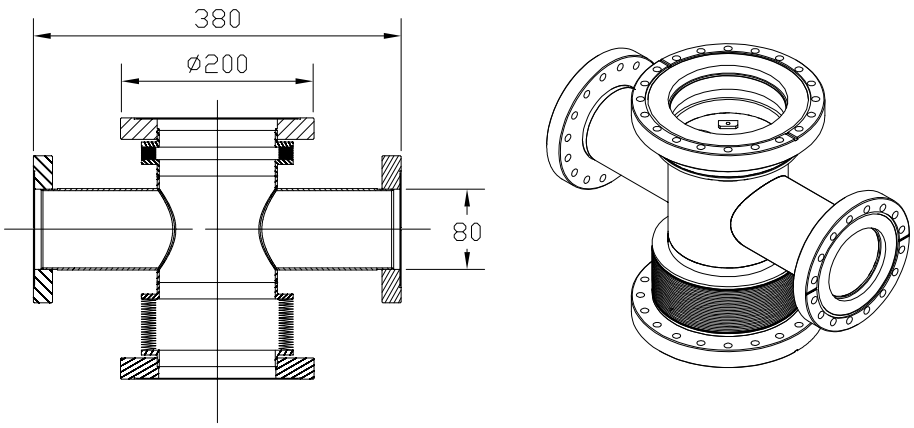

Figure 4.5: Main Vacuum Chamber Bellows

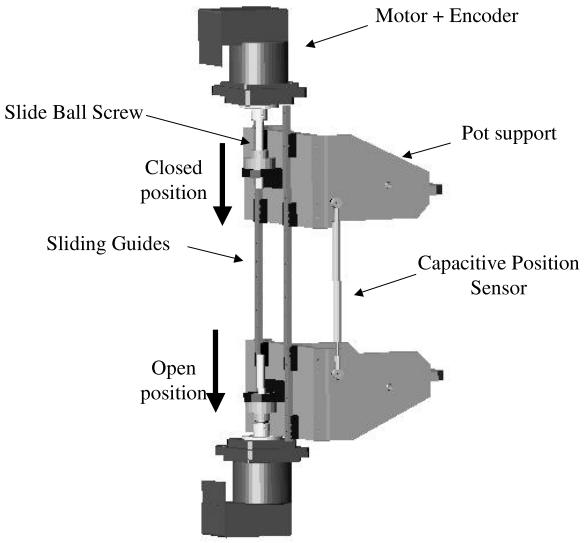

Figure 4.6: Sliding mechanism with the motors and the slide ball screws, allowing the movement of the pots. The top pot is in the data taking position at the end of the stroke of the screw, the bottom pot in the retracted position at the beginning of the stroke of the screw

beam axis (z). The table is designed to provide a fine adjustment with respect to the remaining 5 degrees of freedom (Fig. 4.8). The table is connected to the pedestal by means of three threaded rods that define the vertical position (y) and the horizontal reference plane. Four adjusting screws on the table are used to define the transverse position and orientation of the system.

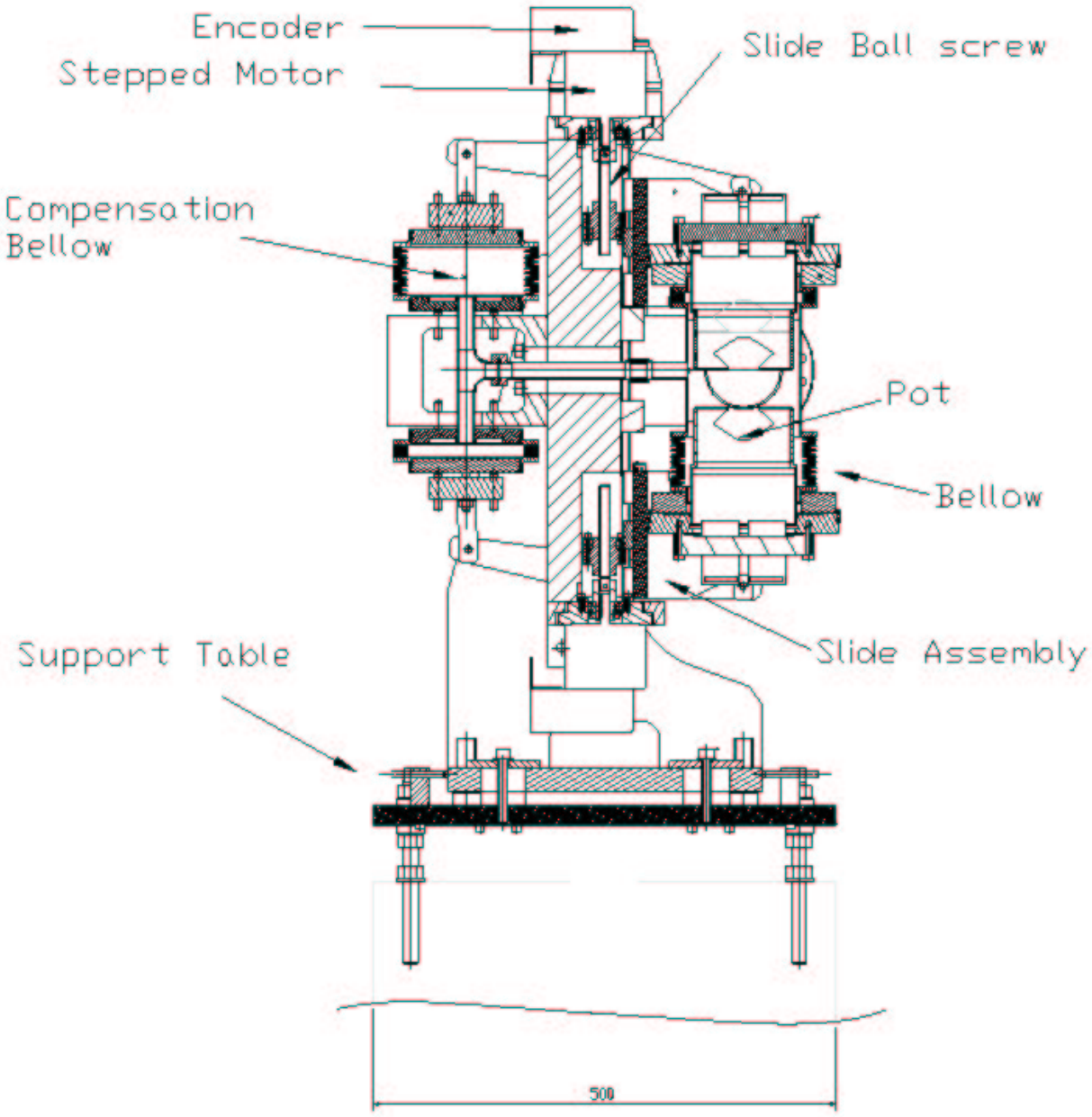

Figure 4.7: Cross Section of the Roman Pot device

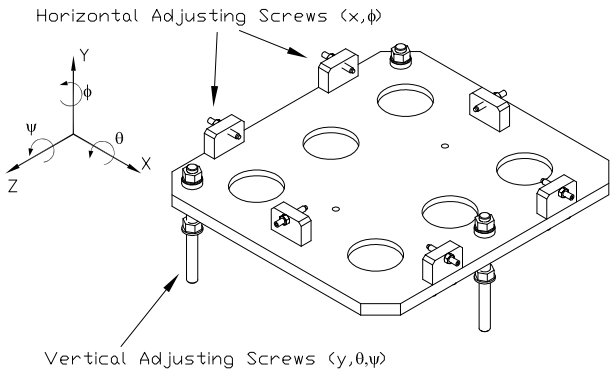

Figure 4.8: Alignment table defining the vertical and the horizontal position of the pot

4.3 The pot

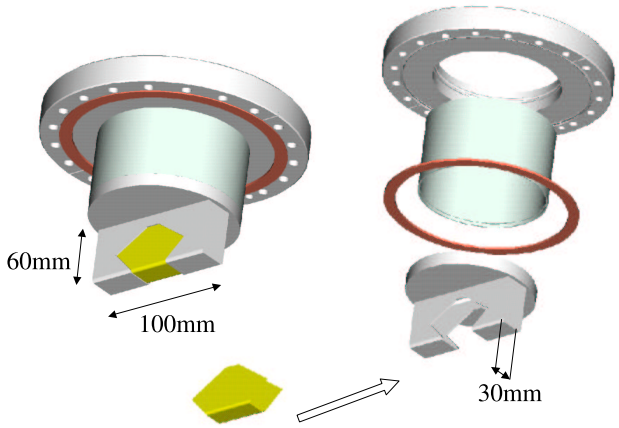

Figure 4.9: The circular pot, the protruding rectangular shape and the thin window foil

The pot has a round shape with a diameter of 115 mm and a wall thickness of 2 mm extended by an optimized rectangular shape 60 mm x 108 mm x 30 mm at the bottom close to the beam, where a thin window of 0.2 mm is placed (Fig. 4.9). This thin window provides the separation from the primary vacuum of the machine while at the same time occupying minimal space and minimizing the amount of material in front of the detectors. The rectangular shape also minimizes the interaction length along the beam and therefore the background on the detectors.

During normal operation, a secondary vacuum in the pot minimizes the deformation of the window towards the beam. During normal detector maintenance, or in the unlikely event of a secondary vacuum leak, the window is subject to a differential load due to the atmospheric pressure on the detector side and the primary vacuum of LHC on the other side. This represents a severe constraint on the strength of the window and requires careful definition of the window area and the thickness.

A finite element analysis of the bottom part has been performed to investigate the effect of this 1 atmosphere load on the window. Only the protruding rectangular part has been modelled since it is in this region where the thin window is joined to the thicker part that the higher-level stresses and deformations are located. At the interface between the protrusion and the circular region of the pot, the displacements

are fully constrained. Due to the symmetry of the structure only 1/4 has been modelled while applying the appropriate boundary condition. Shell elements with bending and membrane characteristics have been used in the model with the option of large static deformations, since the expected deformations are larger than the thickness of the shell elements. To obtain convergence in the simulations, the full load of 0.1 MPa or 1 bar has been applied incrementally. The analysis has been performed for several materials typically used in UHV applications (Table 4.1), and the results show that, for windows of Inconel R718 with a thickness of 0.2 mm, the maximum deformation at the bottom is 0.15 mm, and a maximum stress of 589 MPa occurs at the edge where the thin window joins the pot (Figs. 4.10, 4.11).

	Density (kg/m^3)	Young Modulus (GPa)	Coefficient Th. Expansion (10^{-6}ppm)	Th. Conductivity (W/mK)	Elec. Resistivity ($10^{-8}\Omega$m)	Yield Strength (MPa)
Aluminium 2063	2800	72	23	192	5.7	250
Stainless Steel 316L	8000	200	16	16	74	280
Copper	8900	110	17	398	1.7	152
Beryllium IF-1	1900	303	11	216	4.3	300
Titanium 6AL4V	4700	110	9	7	160	1100
Inconel 718R	7800	200	13	11	125	1050

Table 4.1: Materials for Ultra High Vacuum applications

The stress levels are function of the applied load and of the geometry while the deformation depends in addition on the Young Modulus of the materials. Copper, Aluminum and Titanium are poor in stiffness and would present unacceptable deformation levels, even though Titanium could stand the stress level with its high strength (1100 MPa). Beryllium and Stainless Steel have good stiffness, but do not have the required strength. Inconel graded 718R is a super alloy of nickel (60%Ni, 18%Cr, 18%Fe) with 3% Niobium added to induce the precipitation of inter–metallic compound to get the required strength. It has been developed for applications where high strength is required at elevated temperatures such as in the gas turbines of jet propellers. Inconel 718 with its high strength and stiffness presents the best characteristics for the thin window of the Roman Pot. Its cost is substantially higher than for other standard metals, but remains affordable since the amount of components needed for the final application is limited. The rest of the pot which is not subject to particularly important stress levels, is machined from Stainless Steel (316L or 304L).

Brazing can be used to join the thin window to the thick wall of the pot. The commonly–used welding methods work well with this alloy and preheating is not necessary. The direct brazing of Inconel718 on Stainless Steel is not as easy as for Inconel600, which belongs to the same family of nickel alloys but has a lower mechanical strength. For this reason, the thicker part of the pot is machined from Inconel 600. Inconel is available in sheets, so a manufacturing process has been set up with these sheets as starting material. An Inconel 718 flat thin foil (0.2 mm) shaped to the window is cut out from a sheet. This thin foil is placed in contact with a thicker (2 mm) flat sheet of Inconel 600 that has been provided with an aperture shaped like the window (Fig. 4.12). An inner rim, 5 mm wide and 0.8 mm thick, is machined to accommodate the thin flat foil. A brazing compound of Ag-Cu-Pa is deposited while the thin window is held in contact with the sheet by a brazing tool. The assembly is then folded leaving the 0.8 mm rim in the inner side of the pot. Finally, it is welded onto the lateral side with the planar rectangular element that closes the box (Fig. 4.13). The pot is finally milled to 1 mm to bring the bottom thickness to the same level to the window, thus minimizing the dead space. The bottom rectangular part is then welded to the top circular part made of Stainless Steel, where a flange with the fixture hole and the gasket for the vacuum tightness is provided.

An alternative technology based on the Electrical Discharge Machining (EDM) process is under study. It is a standard technology based on the ablation of the metal by the application of electrical discharge. EDM could offer advantages since in the brazing process the mechanical strength of the Inconel can be locally degraded due to the heating required by the process. While brazing and welding are very well known technologies for Ultra High Vacuum (UHV) applications, EDM could have the drawback of increasing the porosity of the material and making it unsuitable for UHV after the processing.

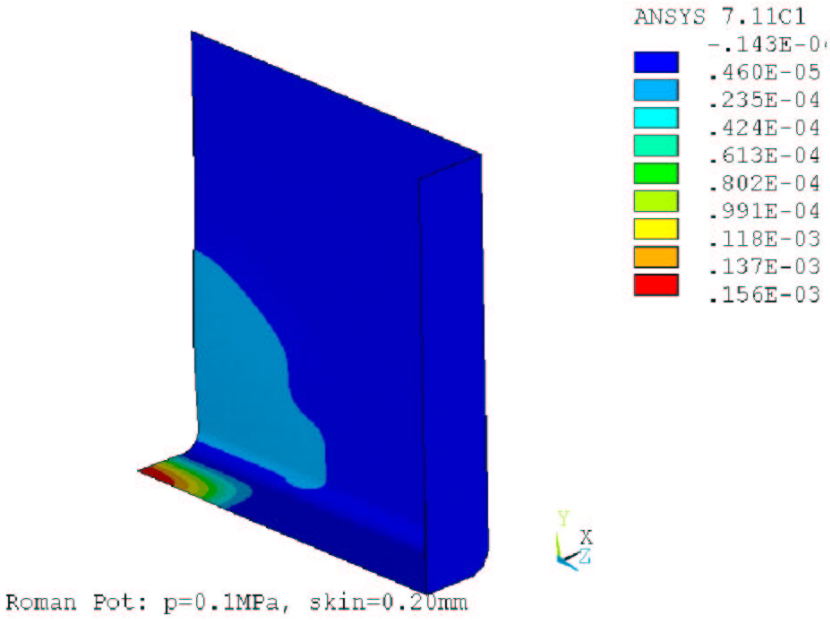

Figure 4.10: Deformation of the thin window (meters); maximum deformation at the bottom 0.15 mm

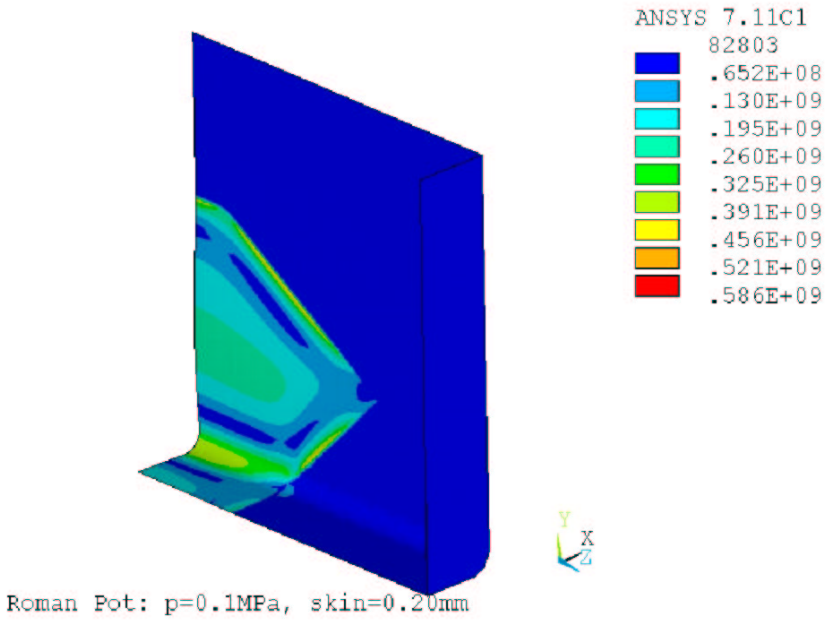

Figure 4.11: Stress level on the edge of the thin window (Pascal); maximum stress 589 MPa

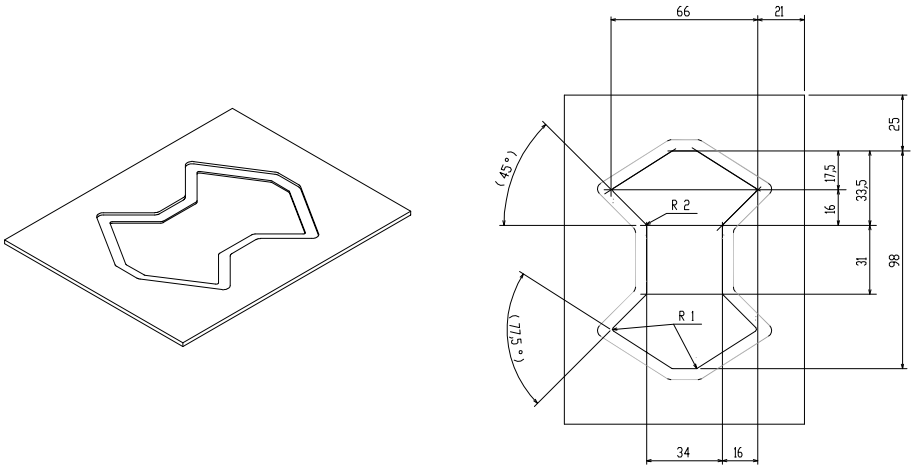

Figure 4.12: 2mm thick Inconel 600 Sheet with shaped hole for the thin window

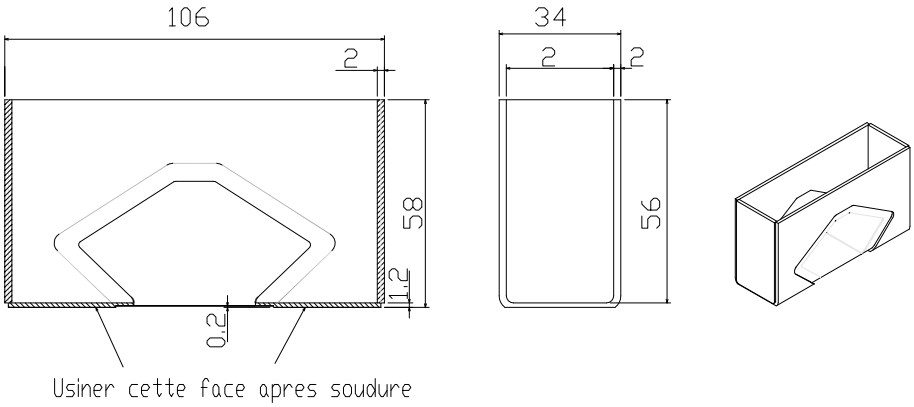

Figure 4.13: Protruded box after folding and welding of the the sheet and the window

Two prototypes with window thicknesses of 0.14 mm and 0.2 mm respectively, have been produced using a brazing process and tested under pressure, with cycles between 0 and 0.1 MPa (atmospheric pressure). For the last cycle the load was increased to 0.2 MPa. The deformations during the test as well as the residual deformations after the end of the test were measured on the bottom and on the side of the pot. The results are shown in Fig. 4.14.

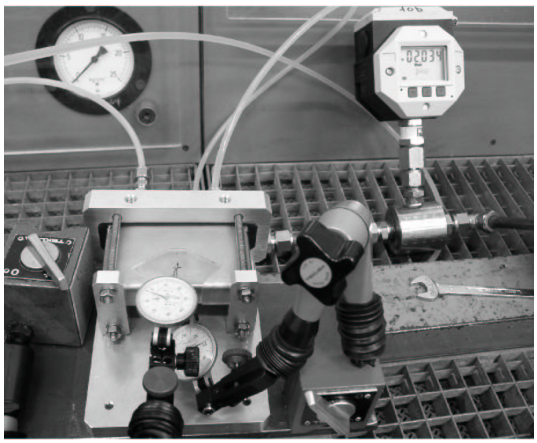

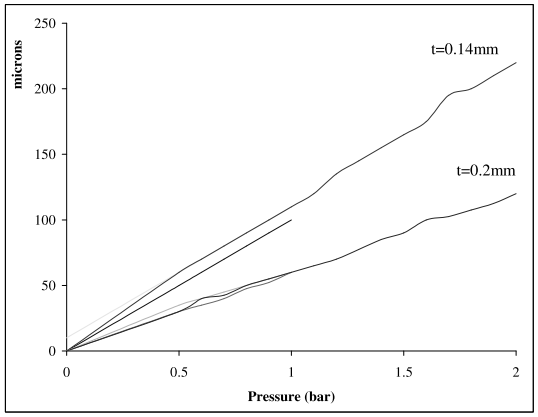

Figure 4.14: Pressure test set-up (left). Pressure test results, deformation in μm, at the bottom of the pot (right)

The maximum deformation on the bottom is 100 μm for the window of 0.14 mm and 60 μm for the window of 0.2 mm. The residual deformations at the end of each cycle were negligible since the window was always in the linear domain of the stress–deformation curve. For each pot the last cycle has been extended to higher pressure values to verify the ultimate pressure limit. For the moment the pressure has been limited to 0.2 MPa to avoid destroying the specimen since other tests were envisaged. With this 0.2 MPa value the required safety factor of 1.5 has already been reached, but further tests at higher loads are envisaged after the finalization of the production process (see below). These measurement results are better than the simulated predictions. One of the reasons might be that in the folding process the window did not remain flat but became curved increasing the membrane mechanical strength. This effect, however, increases the dead space between the detector and the beam and must be kept under control. For this purpose, a dedicated folding tool will be designed for the final production of the pot to carefully control the flatness of the window. The above tests then have to be repeated and will be carried out up to higher loads.

As for other machine components in the Long Straight Section, the pot and the vacuum chamber will be baked out in situ at 250°C, to reach the vacuum level required to store the beam. In this phase, the detectors will not be installed in the pot so as to preserve them against unnecessary heat flows. Mechanical calculations show a very high stress level on the brazing between the thin window and the pot. Thermal tests have to be performed to address this problem and also to characterize the strength of the brazing after the bake-out.

4.4 Detector arrangement

Each pot will hold a set of 10 detectors arranged in 5 double planes, where a double plane is defined by two independent and identical detectors mounted together back-to-back. On each single detector the strips are oriented at 45^o with respect to the vertical axis. When two detectors are joined to form a double plane, the strips of one side are perpendicular to the strips of the other side, defining in such way an x-y coordinate point (Fig. 4.15).

The packing of the planes inside the Roman Pot is too dense to allow an alignment in situ. Therefore, a method has been developed which provides adequate alignment by construction. The mounting relies on the stacking of the different planes by means of an optical device. On each board, where the detector

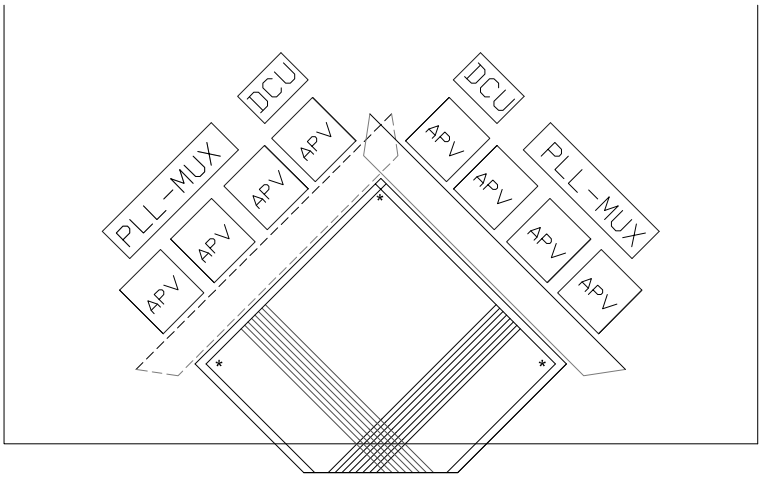

Figure 4.15: Two detectors planes are mounted back-to-back defining an x-y coordinate plane by means of the strips at a 45º angle. The stars on the detector denote the position of the alignment marks

are mounted, reference marks are provided, as well as on the support mounting on which the detector has to be fixed. Once the planes are aligned, they are successively clamped and fixed in the position, giving a self-consistent, monolithic bloc. The relative position of the detector edges with respect to the beam has to be known with an error of less than 20 μm and the edges of the aligned detectors have to be stably positioned as close as possible to the thin window at a distance not exceeding 300 μm, to minimize dead space. To fulfil these requirements, the window must be manufactured with an extreme flatness (50 μm) and should show an almost negligible residual deformation after the bake-out or the breaking of the secondary vacuum for maintenance.

The coupling between the detector assembly and the pot is crucial to control the final position and minimize the dead space. The pot is connected to the electro-mechanical device which is aligned in the reference system of the machine. The detector package is referred to the pot through the reference plane defined by the flange of the pot and the detector assembly (Fig. 4.16). Once the pots are manufactured, the distance B of the reference plane from the window can be measured with high accuracy (1 μm) for each pot. The detector package mounting can be also measured along the dimension A, the distance from the reference plane to the edge of the detector. The difference B-A gives the dead space between the edge of the detector and the window, as well as defining the error from the nominal position. If required, this distance can be adjusted by shimming or re-machining the reference plane S.

A detector plane consists of an electronics board on which the sensor and the readout electronics are mounted. A flat cable from the top of the board, with signals, and high voltage and controls, is connected to a feed-through patch panel fixed in the top flange of the pot. The passage from the vacuum to atmospheric pressure is one of the crucial items of the design of the system. This patch panel has to be vacuum tight, electrically grounded and thermally shielded. The robustness of the connection is an important feature to avoid damages to the electrical contacts and to the vacuum tightness. Two different solutions have been investigated. The first solution makes use of commercial D-sub connectors, developed for vacuum applications. These components have a high connectivity reliability and are designed for ultra-high-vacuum levels, but as drawback they need a considerable amount of space on the flange. It will be difficult to accommodate the signal lines and the services for 10 detector planes. An alternative solution is based on a PCB patch panel (Fig. 4.17), which fits into a slot machined on the flange. The vacuum tightness is then obtained by sealing the PCB with an epoxy resin. Since the vacuum level required inside the pot is not very high, the tightness through an epoxy sealing is still a reliable solution. The space needed is very limited, being just the thickness of the PCB (1 mm) and its width. The advantages of this solution are the possibility to easily customize the PCB, the rapidity of the production and the low cost. The PCB card has connectors on both sides that, if required, can be regrouped in the design. In case of failure or of an upgraded design, the PCB card can also be easily changed, just destroying

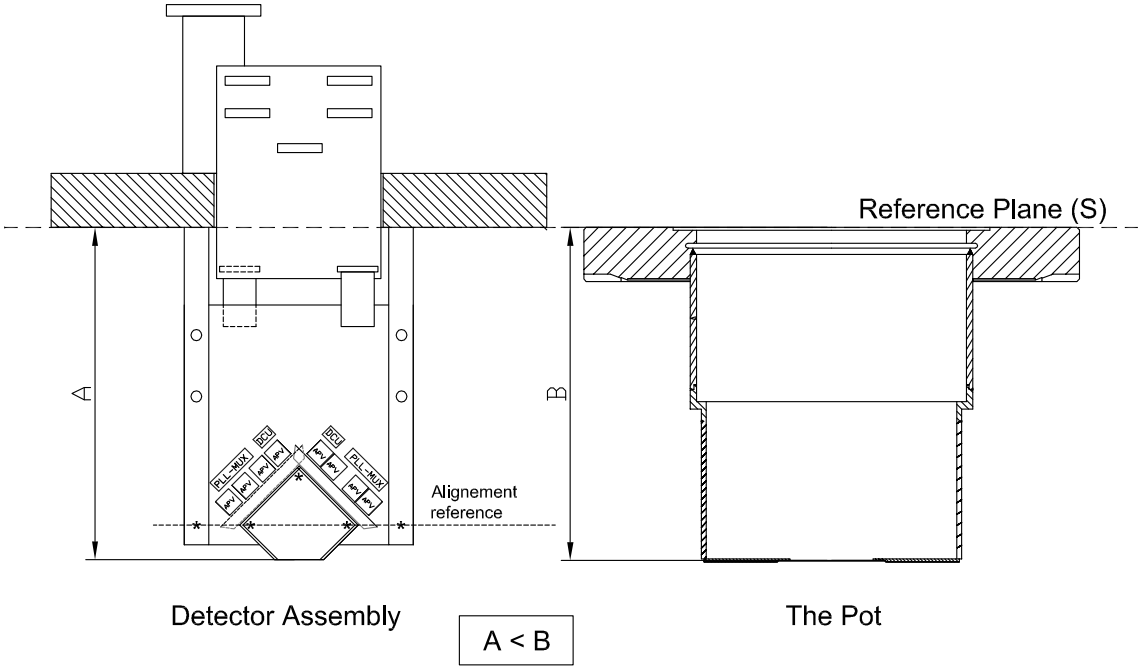

Figure 4.16: Mechanical coupling between the pot and the detector package

both the installed card and the sealing. In this case the flange in Stainless Steel is not affected at all by this operation and it would be sufficient to clean it with solvents before reusing it. The reliability of the vacuum tightness with epoxy sealing has been tested on the cryostat used for the 2003 TOTEM test beam, where an identical feed-through solution has been adopted. Vacuum levels of 10^{-6} mbar have been reached and stably maintained.

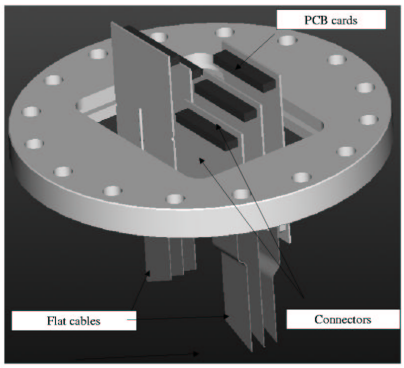

Figure 4.17: Patch panelwith PCB feed through board

4.5 Cooling

Various cooling scenarios and systems for the Roman Pot detectors have been considered. Their technical feasibility, reliability and costs implications have been investigated. For example, the potential parasitic use of part of the LHC collider cryogenics in the tunnel (LHC-QRL) or the point 5 CMS cryogenic infrastructure (helium cryoplant, LN2 surface Dewars) were considered [6]. The result indicates incom-

patibility on the following points: location and distances for transfer of cryogens from the respective cryogenic system, the cooling powers differing by orders of magnitude, different cooling temperatures, problematic operational interdependencies, potential risk of disturbances. Furthermore, modifications of the LHC cryogenics would entail excessive cost. In conclusion, the TOTEM detector areas lack of any practical cryogenic infrastructures and hence a dedicated cooling system is needed.

In addition, the hostile radiation environment at the Roman Pot stations imposes the application of radiation tolerance criteria for the cryogenic equipment that is potentially sensitive. In particular, for the electronic components of industrial instrumentation, pumps, compressors etc. Recommendations have been given in Ref. [7], which mainly result in the 'splitting' of equipment and the remote installation of radiation sensitive components.

The TOTEM cryogenic system must allow for remote operation of all functions from a common control room. All the equipment and instrumentation designed, selected and used must not require any maintenance during the physics run period. Maintenance will normally be done only during shut down times.

For all these reasons, the design of the cooling system has to minimise active components by applying passive methods whenever possible.

The silicon detector and the front-end electronics require cooling and temperature stability. The power to be extracted from a Roman Pot assembly is estimated to less than 20 W and accounts for the dissipated heat of the detectors and the electronics as well as the thermal losses of the mechanical support structure. While the temperature dependence of the energy dissipation of the detector component is negligible, the structure thermal losses increase with decreasing temperature. At the current stage of the project the detector operating temperatures are not fixed, requiring corresponding flexibility in the external refrigeration system. The system described in the following has been designed to allow a considerably large variation of the operating temperatures that also permits further investigations of detector and components performances at different temperature levels if needed. A prototype test of the Roman Pots and their detectors is envisaged at the SPS in 2004. This test installation will be equipped with such cryogenic system in ordert to validate its design. In principle, the system can cope with a temperature range from 130 K to 250 K, but the expected operation temperature will be around 240 K.

The expected useful operating temperature range is from 140 K to 250 K.

The cooling system can be subdivided by its functionalities. The generated heat load from the various sources within a Roman Pot (detector, electronics, structure) must be 'collected' and transferred to outside the Roman Pot's physical limits. In detector cryogenic engineering, this part of the detector design is generally referred to as the 'internal cryogenics'. The heat transfer and the refrigeration system itself are referred to as 'external cryogenics'.

In view of the large distances between the Roman Pot stations in the tunnel no cryogenic link is considered between them. Instead, each station will be independently equipped with a dedicated modular cryogenic system of same design. The external cryogenic system consists mainly of a common refrigerator, a cryostat and six (one per pot) heat pipes connected to the internal part of the Roman Pots (Fig. 4.18, see Ref. [8]).

The dissipated heat extracted from the individual Roman Pots is transferred via the heat pipes to a common cryostat. The cryostat contains the heat pipe terminals that are connected to the integrated cold head of the refrigerator. The corresponding refrigerator compressor will be installed in the vicinity in the tunnel. The heat pipe is a passive heat transfer device with an effective thermal conductivity several orders of magnitude higher than ordinary bulk metal. For TOTEM the geometry consists of a slim cylindrical tube of 15 mm diameter with an approximate length of 2 meters. This heat pipe will be contained in a vacuum insulated pipe. The inner wall surface of the heat pipe will be equipped with a wick structure to enhance capillarity and heat transfer. The design concept for TOTEM is versatile, allowing a large operating temperature span adaptable to the desired value provided by the refrigerator. The selected refrigerator is a 'pulse tube' type, a simple and rugged design with a thermodynamic cycle based on oscillating gas columns. In contrast to most other small-scale refrigerator machines, it does not contain any moving mechanical components close to the cold head. The vibration noise is therefore reduced to a minimum. The particular refrigerator proposed for TOTEM is based on a development for a 165 K application and its nominal refrigeration capacity is 120 W. In case of necessity, this capacity can be slightly increased by providing higher mass flows. This refrigerator has application over a large

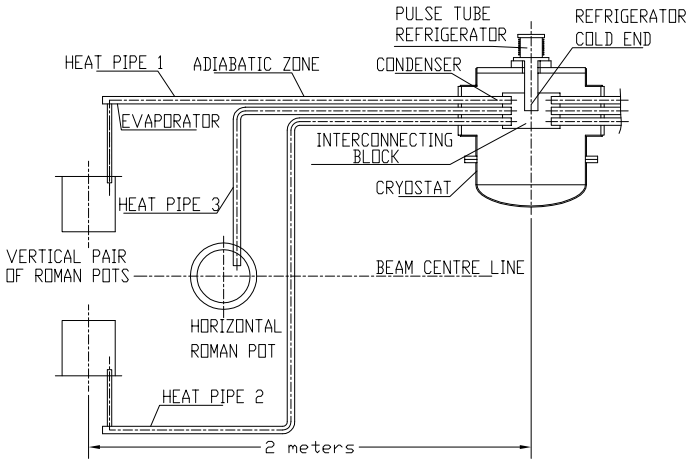

Figure 4.18: Simplified scheme of the cooling principle of a Roman pot unit (2 vertical + 1 horizontal pot) applying heat pipes for transfer of dissipated heat to the refrigerator integrated in the cryostat

temperature range from close to ambient down to 100 K and will, at later stage, be adapted to the final TOTEM requirements. The integration of the cooling system into the LHC tunnel is sketched in Fig. 4.19.

For reasons described earlier, the design principle aims to minimize the need for active elements and controls. Heat transport is done with passive elements. The refrigerator relies on a simple drive motor and the desired operating temperature is stabilized by a heater. During the operation, essential temperatures of the cooling system will be recorded. All supervision and control will be done from a distance and during normal operating conditions no personnel access is required to the equipment installed in the tunnel.

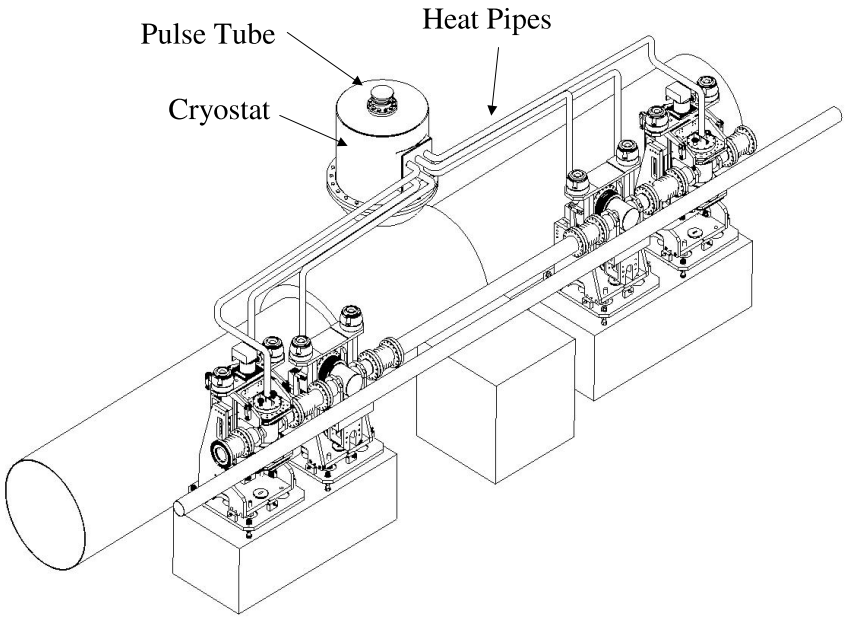

Figure 4.19: The modular cryogenic system for a TOTEM station in the LHC tunnel

The thermal design of the detector relies on the thermal conductivity of the electronic board supporting the silicon sensor and the readout chip. The silicon sensors only have to be kept at the operating temperature. Their heat dissipation is negligible, even after irradiation. The electronic readout must be cooled to minimize noise. The heat dissipated by the APV chips is around 2.35 mW per channel, which gives 1.2 W for the hybrid with 4 APVs. The internal cooling uses only high thermal conducting material elements. They provide for extraction of the dissipated heat in the Roman Pot and connect to the evaporator of the respective heat pipe. The heat pipe stabilizes the temperature and conducts the heat to the heat sink of the refrigerator.

4.6 RF Impedance and Coupling with the Beam

When the pots are close to the beam, they define an aperture limitation with characteristic longitudinal and transversal impedances, which however do not affect the beam since the cavity volume is small. The LHC beam has a high intensity bunched structure and the pots will be placed 1 mm away from the beam core where the induced magnetic field is high. The main effects are the local heating due to the image current, the resistivity impedance of high order modes and the RF pick-up in the detector electronics.

For the LHC, the total impedance budget is limited to $0.25\,\Omega$. The impedance for the pot in its data taking position is estimated to be much lower at $0.1\ \mathrm{m}\,\Omega$ [5]. In the transverse plane, the low frequency resistance term is preponderant and this term can be reduced effectively using a copper coating. The power dissipated on the surfaces of the pot is produced by the image current heating. If one assumes that the beam aperture is circular with radius b=10σ, the resistance producing the power dissipation is given by:

$$R = \varrho \frac{L}{2b\pi\delta} \tag{4.1}$$

where L is the length of the pot along the beam and δ is the skin depth parameter which gives the thickness of material where the eddy currents are generated. It is defined as

$$\delta = \sqrt{2\varrho/\mu\omega} \tag{4.2}$$

where μ is the permeability and ϱ the resistivity. The characteristic frequency ω is given by the bunch length σ_z=0.077 m ($\omega = \frac{c}{\sigma_z}$) which leads to typical skin depth of 17 μm for Inconel steel. At the LHC nominal current (0.54 A for 2808 bunches) the heat load is $\sim$13W that can be reduced to $\sim$1W if a copper coating is applied. The TOTEM optics has a reduced number of bunches and a reduced number of protons per bunch, therefore a lower beam current and consequently a lower heat load.

The RF pick-up on the electronics depends on the shielding provided by the pot. The attenuation of the induced magnetic field depends exponentially on the thickness expressed in skin depths, which is inversely proportional to the frequency. Therefore, the pot acts as a low-pass filter. As a general rule, the window shields frequencies for thickness of at least 5 skin depths. For a 0.2 mm thick window, this corresponds to frequencies $\omega > 7$ MHz.

The noise level tolerated by the electronics depends on the detector arrangement, the grounding scheme and the connections. The problem is complicated to simulate and only a real test will allow to characterize the noise level. During the SPS beam tests in 2004, a set of measurements of RF pick up is foreseen, with a proton bunch structure similar to the one at the LHC. A fully working prototype of the Roman Pot and full-scale detectors equipped with the final electronics will be installed in the SPS machine. The results of the tests should be used to validate the material and thickness chosen for the pot.

4.7 Installation in the LHC

A Roman pots station is composed of two units, separated by a distance of 4 m, each unit consisting of two pots that move vertically and one that moves horizontally. Ancillary electronics and cooling equipment are mounted very close to the station, compatible with the level of radiation. In all the Roman pot

locations, the integration with the LHC installation is straightforward and there is sufficient space also for maintenance. The position of RP1, between the TAN absorber and the bending dipole D2 is more constrained due to machine components than at the other locations. A full integration exercise has therefore been carried out in this region with 3D solid modelling (Fig. 4.20, 4.21). A refined optimization of the features and position of these components will help to decrease the background induced on the Roman Pot detectors by the neighbouring components.

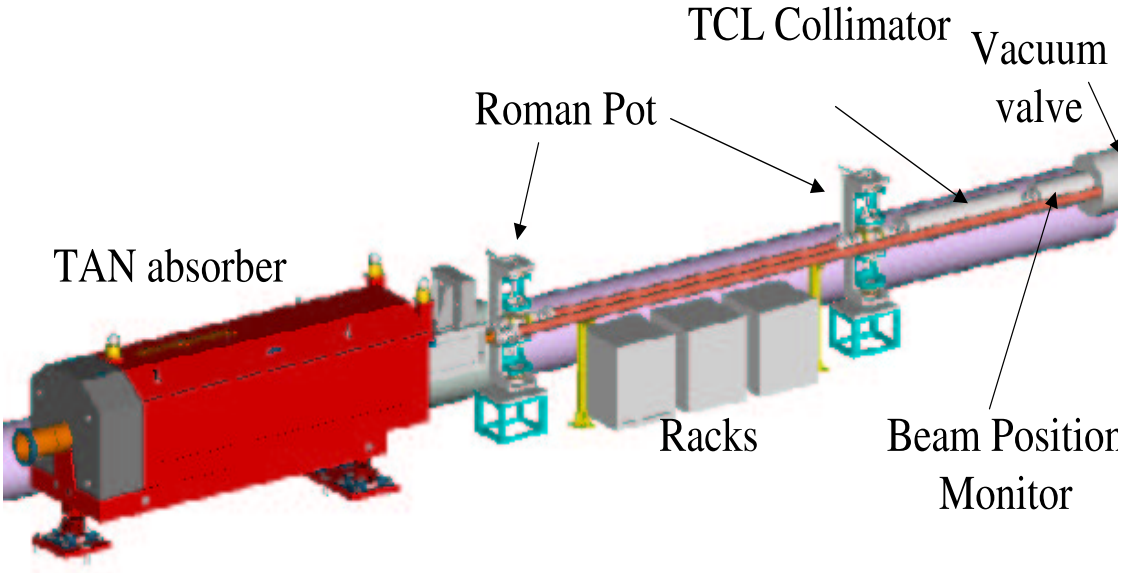

Figure 4.20: Integration of the Roman Pot in front of D2

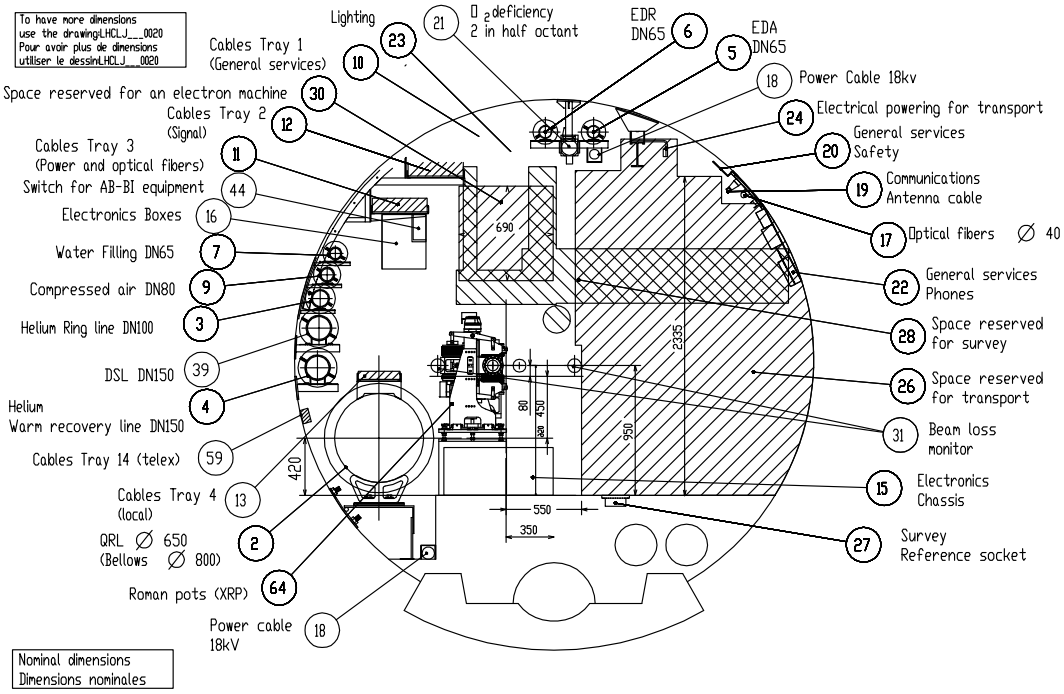

Figure 4.21: Cross section of the Roman Pot installation

In between the Roman Pot devices, there is room to place electronics racks and cooling equipment, which cannot be placed far away from the detectors. They have to stand the radiation dose present at the location and be compliant with the LHC safety requirements. Since the radiation levels in the tunnel are high for on–shelf electronics components and the space is also very limited, the main racks of TOTEM will be installed in the counting room USC55 of CMS, up to $\sim$ 250 m away from the Roman Pot installations. In order to reduce the latency of the trigger signal, the connection to the CMS counting room has to follow the shortest possible path. An overview of the services required is given in Fig. 4.22.

The routing of services can be split in three separate regions (see Fig. 4.23): Region 1: Cables leave the Roman Pot devices to join the cable trays in the tunnel allocated to TOTEM by the general services of the LHC; Region 2: The cables have to pass through the machine tunnel and then the bypass tunnel via the alcove UJ57(UJ53). Racks for the equipment have already been reserved for TOTEM in the alcoves RR57 (RR53). Region 3: The cable bundle must cross the wall between the bypass tunnel USC55 to the counting room of CMS and TOTEM to arrive at the equipment racks. Each station will contribute a certain cross-section of connections from the position in the tunnel to the counting room or the location of the service racks. The total cross section required for one Roman Pot station on a cable tray in the tunnel is estimated to $\sim$ 10 x 10 cm^2. The machine interlock and links to the Beam Instrumentation are designed together with LHC Machine Protection working group.

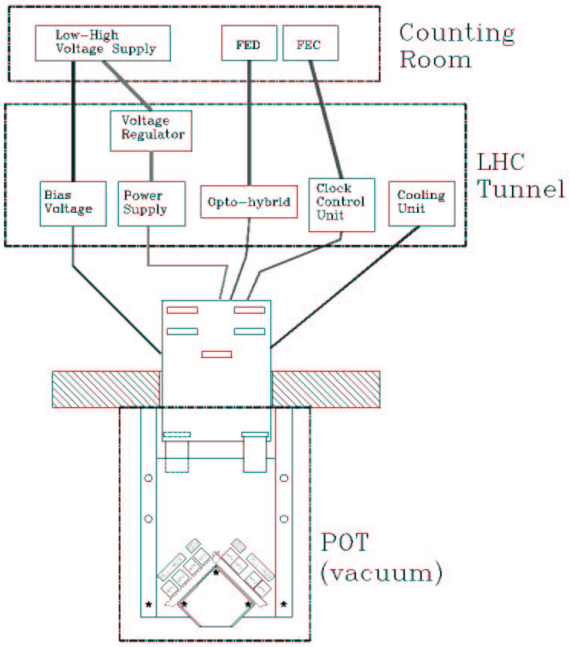

Figure 4.22: Services required for the Roman pot. See also Chapter 7

The installation of the Roman Pot in the LHC tunnel will be done according to the installation planning of the sectors 4/5 and 5/6. The cables and the racks need to be installed already in 2005 and the other infrastructure, like support blocks and local racks, before June 2006. The Roman Pot devices themselves will be installed by the vacuum group. The time needed for these operations will normally not exceed a few hours, including the survey alignment and the cabling connection to the machine protection system. The installation of the detectors inside the pot, as well as the detector maintenance, can be done in any few–hours access, very close to the start-up of the machine with the primary vacuum on. The

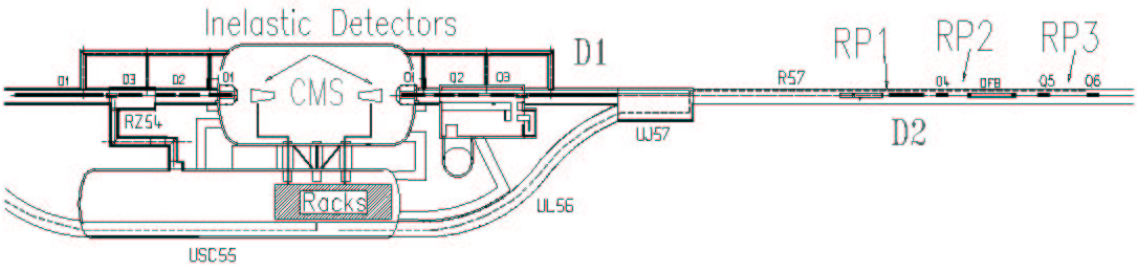

Figure 4.23: Routing of the services in the tunnel

components will be lowered through the PM56 shaft at point 5 and will reach the installation point through the underground tunnel UP56 and UL56/UL55. After the start–up of the machine, access and maintenance are granted in agreement with the LHC safety access system.

4.8 Alignment of the Roman Pot

The Roman Pots are included, as all the other machine components, in the general alignment system and their positions and orientation along the beam must be known with a high accuracy in the established geodetic reference network. The Roman pot unit is equipped with two fiducial marks installed on the top of the main body, close to the motors. The fiducials are related to the geometrical axis of the Roman Pot and provide the reference for the precision movement of the pot with respect to the reference framework. The coordinates required for the first alignment are provided by the LHC database. Each individual component can be placed at these coordinates by means of the adjustable support table. The final alignment is then done by means of smoothing operation. This smoothing operation consist of carrying out a geometrical survey of neighbouring components which is then subject to a least squares fit. The deviation of the components' positions from the fit is then compensated by fine adjustment. The accuracy with respect to the best–fit line obtained after smoothing is 0.02 mm (r.m.s.).

To maintain the precision of the mechanical alignment a periodical maintenance is carried out when the beam is off. For this purpose the magnetic elements and therefore the Roman Pot, are equipped with jacks.

The relative accuracy between two Roman Pot stations is 0.1 mm (r.m.s.) that includes only the error on the position of the fiducials and not the internal mechanical error of the system.

The alignment of the Roman Pot arms with respect to the interaction point is more challenging since the shielding and the complexity of the area block the direct view. Galleries parallel to the beam, dedicated for use of surveying, have been built and a permanent reference line, called the Offset Reference Line (ORL), is installed.

The galleries are 120 m long, and a hydrostatic network links the tunnels through the experimental cavern. The left/right inner triplets are connected to the ORL by means of a 12 m long Invar bar which transversely couples the components to the parallel galleries. In this way, the fiducials of the left inner triplet are known with respect to the right one and the Roman Pots can be related to them. The accuracy of the positioning of any fiducial mark in the experimental cavern with respect to the machine geometry is 0.5 mm r.m.s.

4.9 Operation and Control

To satisfy the physics goals of the TOTEM experiment the detectors in the Roman Pots have to be positioned very near the beam. This imposes very accurate control of the position of the Roman Pots with respect to each other and with respect to the beam. The Roman Pots are moved using stepping motors with associated encoders and precision slide ball screws. Such a system has a resolution of a

few microns.

A coarse positioning is based on a full geometrical calibration of the Roman Pots, the stepping motor system and the beam position monitoring devices. The vertical Roman Pots also make use of a capacitive sensor (a Linear Variable Displacement Transducer or LVDT) which measures the distance between them and allows in addition to detect a possible collision hazard between the two. After calibration such a capacitive sensor gives the distance between the two pots with an error less than a few microns. This sensor is mounted very close to the beam axis where the radiation level is quite high, and its readout electronics will have to be mounted at some distance in a shielded area.

At beam injection the Roman Pots will be retracted to 40 mm from the beam axis. Once the beam are colliding and stable, the pots will be moved coarsely in position based on the information provided by the beam position monitors. Then the position of the pots can be fine tuned using the on-line data from the particle detectors within the pots. The data-rate is equalized on both vertical pots in each station to ensure that the beam is centered in the gap between the two vertical pots. Then the horizontal pot can be moved in also using the data rates on its detectors.

The relative position of the Roman Pots can be determined in absolute terms using tracking data: there is some overlap of the sensitive area of the horizontal pot with that of the two vertical ones (Fig. 4.24). Since the detector strip pitch is known, this provides a way to very accurately determine the relative position between the pots with statistics determined by the number of particle tracks. This way the capacitive sensor measuring the distance between the two vertical pots can be calibrated as well. To make this accurate positioning work mechanical stability over time is essential, and therefore special care has been taken in the design of the mechanical mounting of the pots to make this possible.

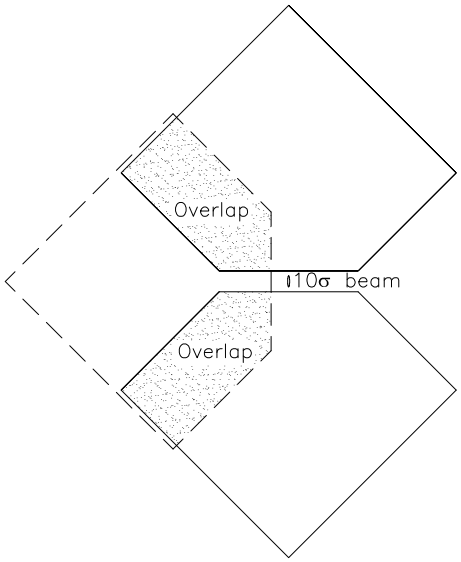

Figure 4.24: Overlap of the vertical and horizontal detector for alignment

The control system of the Roman Pots which controls their position, monitors the secondary vacuum, and provides interlock signals is currently being discussed with the machine. The current thinking is that there should be one control system for all movable elements in the machine, including the Roman Pots, and therefore a collaboration is being set up within the LHC Collimation Project.

Also the detectors within the Roman Pots and the cooling system for the Roman Pots require specific control systems. As detailed in Chapter 7, this detector control system will be fully based on the CMS control system for the tracker. The control for the cooling system is further detailed in Section 4.5.

4.10 Safety

Radiation environment The radiation environment in the IR5 tunnel due to pp collisions at center of mass energy of $\sqrt{s}$=14 TeV and luminosity $\mathcal{L} = 10^{34}$ cm^{-2} s^{-1} has been calculated with the MARS14 code ([1])for the lattice version 6.4 and the beam optics $\beta* = 0.5$ m. The absorbed dose has been integrated over a year of running (180 days) at an average luminosity of 0.5 x 10^{34} cm$^{-2}s-1$ corresponding to 5.4 x 10^{15} inelastic interactions per year. The radiation around the Roman Pot stations and the radiation level of the components of the Roman Pots has been calculated in detail. The first Roman Pot station, RP1, gets more radiation than the other stations since it is located close to the TAN absorber protecting the separation dipole D2 and the outer triplet quads. The absorbed dose at a distance of 10 cm from the beam pipe at the location of RP1 is about 1 MGy/yr (Figs. 4.25. This dose is reduced by one order of magnitude for the Roman Pot stations located further downstream. Details on the particles fluxes and energy spectra can be found in Reference [1]. The accumulated dose limits the choice of materials and electronics in the tunnel close to the Roman Pot and in the Roman Pot itself. The exact value of the accumulated dose depends on the machine integrated luminosity during the period the Roman Pots are supposed to stay in the tunnel. The values given above can then be scaled accordingly. However the exact computation of the integrated luminosity is presently difficult due to the uncertainties on the machine running conditions during the first years of the LHC operation. Anyway, it is clear that the radiation levels foreseen in the tunnel are very high and so the Roman Pots components and electronics have to be radiation hard.

Access and Maintenance The Roman Pots and all the required installation must be compliant to the safety rules of the LHC machine, defined by the French authorities Installation-Nuclaire-de-base. The radiation dose in the tunnels are high and the Roman Pot Installation will be strongly irradiated also when the pots are in retracted position. The induced radio activity on the various components in the tunnel has been also calculated in Reference [1] and the impact on maintenance activities is discussed in detail in the Ref.[3] The residual contact dose on the external body of the Roman Pots located close to the TAN calculated for 30 days of running and 1 day of cooling is $\sim 70\ \mu Sv/hr$ (see Fig. 4.26). This value does not impose severe constraints on the Roman Pot handling even if a careful planning is recommended. A program of traceability has to be set up in the framework of the LHC, adopting a unique identification code for the traceability of each component/cable/connector present in the system.

Personnel safety is defined in the LHC Access system [4], which prevents the access to the underground beam zones when the beam is running. In this case it is not possible to access the Roman Pot and the services located in the inter locked underground installation and only the racks in the USC5 cavern are accessible without restriction. When the beam has been dumped the LHC Control system defines the access to the underground area. In this phase the tunnel will be kept locked and special access to the Roman Pot installation will be granted to trained personnel only for limited interventions. The racks and the services in the USC5 cavern are accessible under the restriction of wearing a film badge.

Equipment and Machine Protection The Roman Pot equipment and the machine need to be protected from possible accidents like beam losses, loss of secondary vacuum, or stepper motor failure. The beam failure scenarios during the TOTEM runs are currently being studied in collaboration with the Machine Protection Working Group. One of the worst accident scenarios is the beam loss due to an unsynchronized abort at an accidental prefire of one of the abort kicker modules [9]. This induces coherent oscillations of the circulating bunches in the horizontal plane. As a result, the beam may not reach the beam dump absorber and may be lost instead on the limiting apertures such as the Roman Pots. To prevent such accident a special protection system has been devised [10]. This system will also protect the horizontal Roman Pot. Nevertheless, we have calculated the warming up of the window of the Roman Pot due to the incidence of one bunch. The window is only 200 μm thick, which is about one percent of the interaction length. The thermal diffusion length is much smaller than the length of the bunch and therefore the energy deposition of a bunch of 7 TeV protons can be assumed adiabatic. Under these conditions the net temperature increase ΔT can be calculated as follows via the internal energy of the material:

$$\Delta T = \frac{0.68\, N_p\, dE/dx}{\pi \sigma_x \sigma_y\, \varrho\, C} \tag{4.3}$$

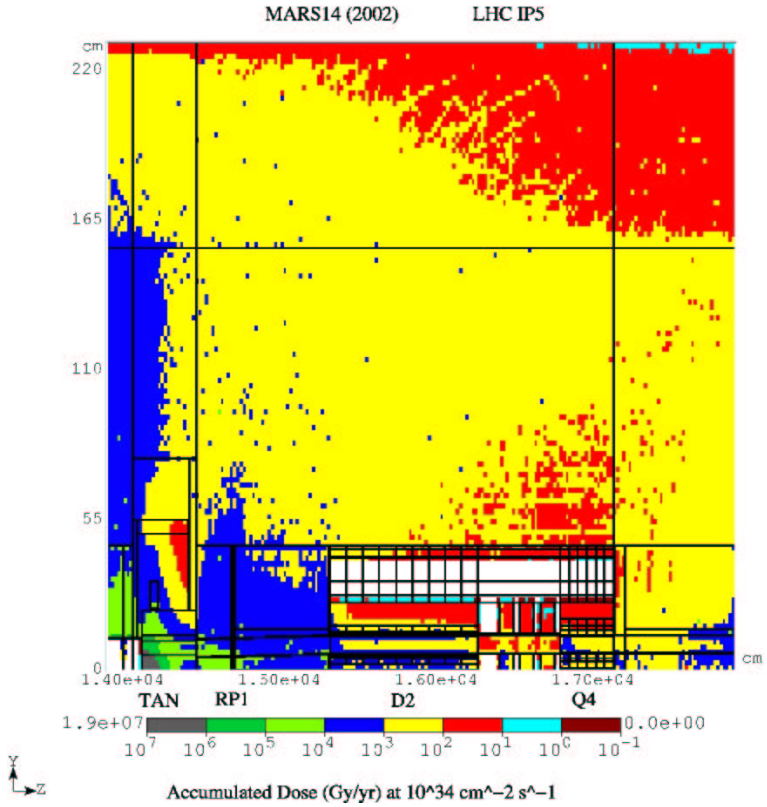

Figure 4.25: Azimuthally averaged yearly absorbed dose in the RP1 region

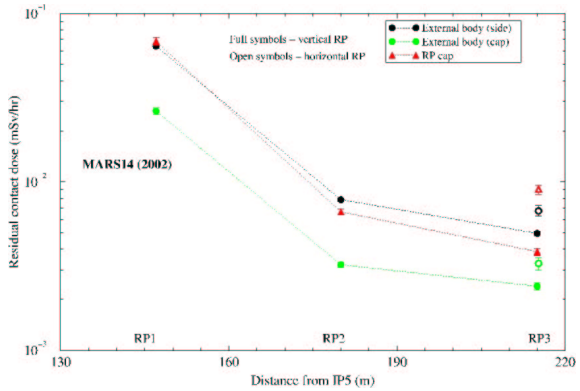

Figure 4.26: Residual Contact Dose after 30 days irradiation and 1 day cooling in mSv/hr at the luminosity of 10^{34} cm^{-2} s^{-1}

where dE/dx is the energy loss, σ_x, σ_y the transverse beam dimensions, ρ is the material density, C is the heat capacity, and where N_p is the number of protons contained in one bunch. The number of protons is reduced by a factor 0.68 to take into account that we consider a beam area corresponding to one sigma.

In the case of the running scenario 2 (see Chapter 10), $N_p = 0.6 \cdot 10^{11}$, $\sigma_x = 0.029$ mm, $\sigma_y = 0.08$ mm. For a window made of Inconel 718, the temperature increases by 360^o. This value is well below the melting temperature of the Inconel which is by the way a super-alloy used for very high temperature applications.

However, if the beam traverses the window at the bottom of the pot over its full length of 40 mm, the above calculation does no longer hold since the Inconel interaction length is 160 mm. In this case the shower development must be taken into account with more refined models like Fluka. However, given the short length, we do not expect a temperature increase bigger than twice the value given in Eq. 4.3.

At the LHC a beam loss monitoring system will be installed to continuously survey particle losses due to fast beam movement or hardware failures. Beam loss monitors will then provide fast signals to trigger a beam dump to protect the machine. Being the Roman Pot an aperture limitation, beam loss monitors will also be located close to each station.

In case of stepping motor failure the Roman Pots should automatically be retracted from the beam in a similar way as the collimators. As mentioned before, the vacuum force compensation system for the Roman Pots has been designed such that the Pots can be removed without having to overcome the force induced by the vacuum.

The study on the thin window of the Roman Pot showed that the window can stand a 1 atmosphere pressure difference without difficulty. Therefore the window will maintain isolation for the primary machine vacuum in case the secondary vacuum is lost. However, such loss will deform the window towards the beam. The first study indicates that the deformation is limited to less than 1σ, but this will be further verified when the full fabrication process for the window is finalized. Proper interlock signals will be provided when such vacuum loss occurs.

4.11 Prototype test in the CERN SPS

A test of the first Roman Pot prototype in the CERN SPS ring during summer 2004 has been recently proposed [11]. This test offers us the opportunity to check the following points before final installation in the LHC tunnel:

- thorough tests of the Roman Pot mechanics, of the local control and of the interface to the SPS (later to the LHC) control system;
- test of the radiation hard edgeless silicon detectors and the associated readout chain;
- test of the performance of the first level trigger;
- study of the influence of the passing proton bunches on the silicon detectors and its related electronics installed inside the pots (RF coupling).

It is therefore an excellent multi-purpose test of the Roman Pot which will be integrated into the LHC vacuum chamber and operated in collaboration with the LHC control room. The RF coupling due to the passing proton bunches is a very important issue and quite difficult to simulate because of its complexity. Hence a test with a real circulating beam with properties as close as possible to the LHC beam is highly recommended. In addition, the CERN SPS test results can be used to cross check the results from simulation programs and from tests in the laboratory. Finally, the SPS beam halo protons are a perfect simulation of elastically scattered protons. Therefore they will be used to check the efficiency of the trigger system. The prototype consists of a vertical Roman Pot fully equipped from both the mechanical and the functional point of view including the interface to the CERN SPS control system and silicon detectors. The Roman Pot will be installed in the SPS LSS5 low radiation area 3.5 m upstream of the quadrupole QD51910 close to the ECX5 (old UA1) experimental cavern. The Roman Pot installed at this location, with its 80 mm inner diameter vacuum pipe, provides, in its retracted position, enough aperture for the very wide beam foreseen at injection for the fixed target runs. In fact given the transverse beam size of $\sigma \sim 4.3$ mm in the horizontal plane and ~ 7 mm in the vertical one, the Roman Pot aperture

amounts to about 10 σ in the horizontal plane and about 6 σ in the vertical one which is considered to be suffcient for the injection of the fixed target runs [12].

This means that the Roman Pot, apart from the period dedicated to the test, will not interfere with any of the SPS operations foreseen in 2004. During the special runs requested by TOTEM, the Roman Pot will be moved to its data taking position at $\sim$ 10 σ from the beam which, at this location, corresponds to $\sim$ 3 mm (horizontal plane) or 6 mm (vertical plane) for a normalized beam emittance of $\epsilon_N = 1$ μm $\cdot$ rad. This distance is thought to be sufficient for this test. The integration at the above location is rather easy and has been discussed with the AT/VAC group (SL section). The vacuum group will supply the dummy vacuum chamber which will be used until the Roman Pot is installed and will assure its dismantling and the connection of the Roman Pot to the SPS vacuum chamber. The two vertical pots will be equipped with edgeless silicon detectors previously characterized in the CERN X5B beam. Since this test is a unique opportunity for the study of the RF coupling, it is important to test both silicon detector technologies under evaluation. Thus one pot will be equipped with planar silicon detectors and the second one with 3D silicon detectors. A Beam Position Monitor, equipped with LHC electronics, is placed sufficiently close to the Roman Pot to provide information on the beam position.

The contribution of the Roman Pot to the total impedance budget of the SPS machine is negligible. It has been calculated [5] that the additional impedance due to the presence of the Roman Pot at about 6 mm from the beam is about 1 $m\Omega$ to be compared to a total SPS impedance in the range of 7-9 Ω.

The installation of the Roman Pot in the SPS will be done in three steps. The cables and the mechanical infrastructure will be installed during the SPS shutdown period before the end of February 2004.

The Roman Pot system will be installed later during the SPS running period without interfering with the SPS schedule, at any time during an 8 hours access to the SPS tunnel.

This ensures enough time to vent the vacuum sector, to install the Roman Pot, to make the survey and to pump the sector again. According to the SPS schedule, suitable dates for the Roman Pot installation are the PS technical stop in week No. 26 or one of the PS Machine Development periods with no beam in the SPS (week No 27 or 30). The silicon detectors, previously characterized in the CERN X5B beam during the weeks 29-30, will be installed in the Roman Pot during one of the following SPS Machine Development periods (week No 33 or 36). Once installed, the Roman Pot will be kept in the retracted position and the setup will be checked and tested with halo particles during normal SPS operation.

The test proposed requires a coasting beam and beam parameters as close as possible to the ones presented in Table 10.1 for the LHC run. The machine will need a special setting which may require a set-up time of $\sim$ 12 hours for the first run while for the successive runs the set-up time will be shorter and evaluated in 3$\div$ 4 hours [12].

We believe that 3 or 4 hours coasts will be necessary to make and check the measurement proposed, i.e. 3 to 4 shifts of 8 hours including the machine set-up. The initial machine development of 12 hours to tune the SPS for coast will profit also from the already foreseen test of the LHC Collimators presently under discussion.

The definition of the detailed list of the beam parameters needed for the test is at the moment under evaluation. However, according to a first discussion with the machine, it seems that the range of parameters requested, i.e. up to 8 bunches with a normalized beam emittance of $\epsilon_N \sim 1$ μm $\cdot$ rad and intensities up to $0.6 \cdot 10^{11}$ protons per bunch (or up to 8 bunches with nominal emittance and bunch intensity), is within the SPS present capabilities.

4.12 Microstations

4.12.1 The Microstation Concept

The Microstation (MS) was developed to detect leading 'beam-like' protons in the LHC environment with high efficiency and minimal disturbance to the machine and close-by detectors. The concept is based on compact and modular design, which separates the detector element and its moving mechanism from the vacuum chamber (Fig. 4.27). The detector element is moved by a precision motor, which is placed within a secondary vacuum enclosure built within the microstation. With this arrangement, small high precision solid state (ultrasonic), non-magnetic motors can be used. The microstation provides an ideal geometric acceptance and accuracy and - with its light-weight structure - minimizes the backgrounds and material activation caused by incoming particles. Due to its compactness and robust construction, a microstation requires minimal space for installation. Microstations are integrated to a section of the beam vacuum chamber to allow easy access in case of failure or change of running mode of the machine.

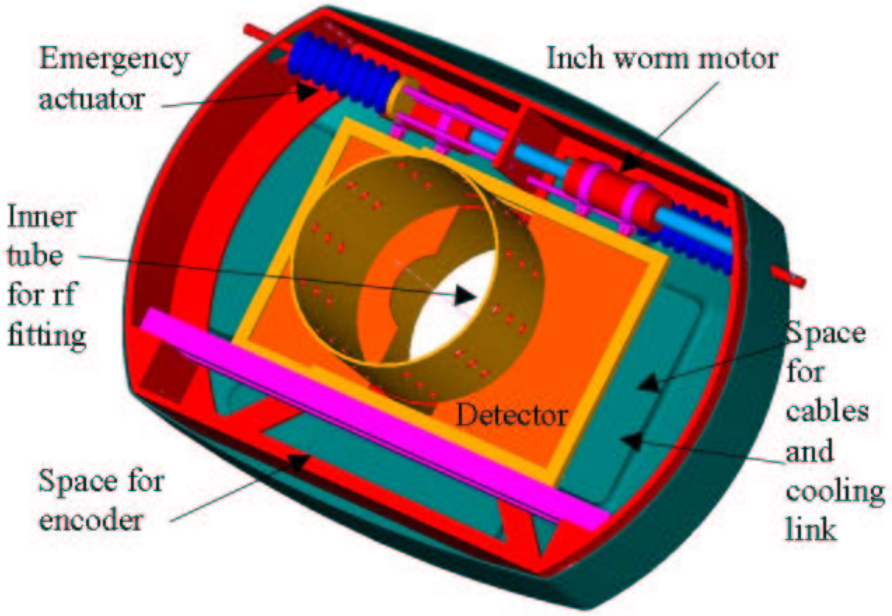

Figure 4.27: The over-all layout of the microstation (the secondary vacuum arrangement is not shown)

4.12.2 Constraints and requirements

The LHC environment and TOTEM requirements for the leading proton detection set a number of basic constraints for the microstation design:

- limited space and limited access for installation and services
- light compact structures with materials with low radiation and nuclear absorption lengths for reducing backgrounds and multiple scattering
- the ultra high vacuum which has to be preserved within the beam pipe and the vacuum insertions; low out-gassing and 24 hours bake-out at 250° C is required

Overall dimensions	Diameter $< 20\,\mathrm{cm}$
mass (transparency for particles)	$< 3000\,\mathrm{g}$ (stainless steel)
Outgassing	10^{-11} atm (restricted use of materials)
RF-impedance	$< 1\,\mathrm{m}\Omega$
radiation dose	$< 10\,\mathrm{Mrad/year}$
max temperature during bake-out	250° C
temperature during operation	20° - -20° C (200 K optional)
max power dissipation of detectors	10 W per detector plane
precision of detector movements	$< 10\mu$m

Table 4.2: General requirements for the microstations

- the detector elements that can approach the beam up to 10 times the beam r.m.s. size during the low luminosity runs; the detector movement is accurately controlled (accuracy < 10 μm) and an independent detector enclosure relative to the beam is provided, an emergency detector retraction is enabled
- the detector enclosures, which are placed close to the beam that carries high currents of protons shaped into bunches of about 1 ns (r.m.s.) length with a periodicity of 25 ns, imply that the detector sensors will be exposed to a strong RF field which induces noise and eddy currents. This requires careful shielding of the sensitive detector elements. Detector geometry has to be designed for minimum impedance to the RF waves inside the beam pipe
- to avoid flanges, it is preferable to manufacture the microstations of the same material as the beam pipe and weld them directly to the beam pipe
- the heat produced by the detectors and read-out electronics inside the microstations has to be dissipated outside the secondary vacuum enclosure
- the high radiation levels expected at the locations where the microstations are installed, require the use of radiation hard materials and technologies for all detector elements to ensure their robust operation during the LHC runs.

The requirements for the microstations are summarised in Tab. 4.2.

4.12.3 Description of the microstation

General

The mechanical structure of a microstation is depicted in Figs. 4.27-4.29. Fig. 4.27 illustrates the overall design with all the components and functions included. A microstation can be divided into five subsystems: the vacuum chamber, the support structure, the detector element, the driving mechanism and the cooling system (Fig. 4.29). The detector element is similar to the one in the Roman Pot and is described in detail in Chapter 5. In addition there are the issues related to the secondary vacuum. The basic design principle has been to make the vacuum chamber independent of the precision mechanics and other components located inside. The vacuum chamber is constructed of stainless steel sheet and all seams are welded to avoid vacuum leaks. All the components are mounted to a support structure which is fixed directly to the beam pipe. With this arrangement, any deformation of the vacuum chamber during the welding process or pump-down does not affect the rest of the system. The vacuum chamber can now be designed to be light without jeopardizing the overall operation of the microstation. The estimated total mass of the structure is 3000 g.

The Vacuum Chamber

The vacuum chamber is made of stainless steel. The chamber consists of three parts (two 180 mm domes and a short section of the 60 mm beam pipe), which are welded together as the final step of the assembly

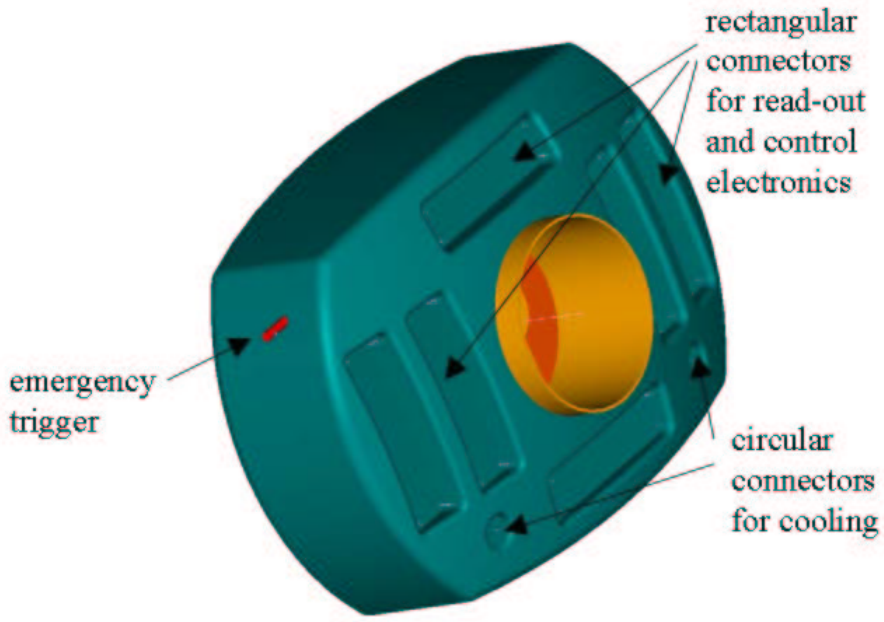

Figure 4.28: The interface side of the microstation with feed-throughs for read-out and control electronics (rectangular) and cooling (circular). The emergency trigger is based on the pressure difference between the vacuum chamber and the atmospheric pressure outside the microstation. In this version of the microstation, the two sides are flattened to facilitate services (cooling and electronics) of a cluster of devices

procedure. Based on a number of tests and considering the ease of manufacture, we prefer laser beam welding. The feed-throughs of the system are confined to the right hand side (see Fig. 4.28) of the chamber. As a default option, standard D-type connectors are selected for the signal read-out connections. The final target design is based on optical connection between the front-end electronics, which is located within the secondary vacuum enclosure, and the read-out system outside the vacuum camber. The two motors (see Fig. 4.27) require an electrical feed-through which is shared by the two optical encoders used for measuring the absolute detector position (Fig. 4.27). Finally, two additional feed-throughs are needed for the cooling system based on flexible solid state cold finger system (see Fig. 4.29). In order to avoid condensation and formation of ice on the surface, these feed-throughs are vacuum insulated.

The beam pipe wall seen by the particle beams is a smooth continuation of the standard vacuum chamber except for the two smoothly shaped slots through which the detectors move into the beam region. Since they interrupt the longitudinal continuance of the envelope they will create a discontinuity in the RF impedance seen by the wake field. It is not probable that this has any effect on the stability of the high-energy particle beams, but local eddy current heating might occur. This is being checked by computer simulations and tested in the laboratory.

If it is demanded that the final version needs a flange that can be opened, it will be located on the cylinder section of the vacuum chamber. Because of the separation of the precision mechanics from the vacuum chamber this option does not make a big difference on the basic structure. The lighest device will anyhow be all welded with only a gas feed through for secondary vacuum pumping.

The Support Structure

The support structure consists of components which are used to connect the detector driving mechanism (see Fig. 4.27) rigidly to the beam pipe. The mechanism is assembled on a machined steel plate, which is welded to a fixed ring welded to the beam pipe. The supports for the motor shafts and brackets for linear guides are integral parts of the support plate but isolated from both the beam and secondary vacuum enclosures. The assembly can be made and independently tested outside the vacuum chamber. The support plate will be mounted in its place just before the final assembly (welding) of the vacuum chamber.

The two detector modules of a microstation are to be moved with respect to the proton beam. This movement is realized as translation of about 30 mm. Each module moves independently to allow adjustment with respect to the beam trajectory, which may not be exactly centred in the vacuum tube. The transverse repeatability and stability of translation movement is better than 10 μm.

Detector Moving Mechanism

Ultra High Vacuum (UHV) inch worm motors are used for the detector movement. The slider material is PZT-ceramics, a perovskite structured ceramic of typically barium, bismuth or lead-zirconium titanate composition, while the stator rod can be made of any compatible ceramic material. Although the density of the PZT material can be fairly high (up to 7.5 g/cm^3) the total amount is very small (about 10 g per motor) and would thus absorb very little radiation. Ceramic materials are typically not affected by radiation doses up to 108 Gy and are thus suitable for this application.

The design is based on the commercial type UHVM-400 of UHV-compatible inchworm motors available from Burleigh Instruments Inc., USA. Fig. 4.27 shows the layout of the mechanical construction. The detectors are hanging from the slides of two inchworm motors mounted side by side. A simple linear guide at the bottom, consisting of a thin fin moving in an axial slot, prevents rotation around the stator shaft. The detector plates are supported by copper frames, which cover the three edges that are not adjacent to the proton beams. In addition to supplying mechanical support and attachment interfaces these frames serve as primary heat sinks for cooling of the detectors. Flexible heat conductors connected to the vertical sides of the frames remove the heat from the frames to the stationary primary heat sinks. It should be noted that the motor slide is always firmly gripping the stator, so the structure can be mounted in any position without being affected by gravity.

The inchworm motors can be moved in sub-micrometer steps and stopped firmly at any position without acceleration or deceleration ramps, which are required in normal motor operations. The repeatability of the step-wise movement is not well defined and an auxiliary linear encoder is required for ensuring accurate positioning. The encoder consists of a scale mounted on the detector frame and a stationary optical measuring head for non-contact readout of the position. For this, miniature scales with 10-20 μm pitch are commercially available. By interpolation techniques an incremental positioning resolution of 1 μm can be achieved. The measuring head is custom made for compatibility with the specifications of UHV, temperature and radiation hardness. The inchworm motors will be refreshed with orientation electric field after the bakeout. If this appears to be too difficult in the coming tests, the motors will be cooled during the beam pipe bakeout.

Optical fibre connections are used in order to avoid light sources, photo sensors or electronics.

Detector Cooling

The detector plates are cooled during the two different operational modes: (1) normal operation with power switched on (power dissipation of 10 W/plate as a design value) and (2) vacuum bake-out with the ambient temperature of 250° C (MS chamber) and 200° - 0° C (detector element). The most practical cooling arrangement is based on flexible solid state cold finger system.

The baseline design for the cooling system is illustrated in Fig. 4.29. The heat transfer from the detector frame is arranged by flexible copper or diamond like carbon based cold finger system. The cold finger is cooled down by heat pipes outside the MS chamber. The arrangement is very similar to the one described in section 4.5 for the Roman Pots. In the following analysis it is assumed that the heat pipes can provide two heat sinks at 78 K capable of absorbing 20 W.

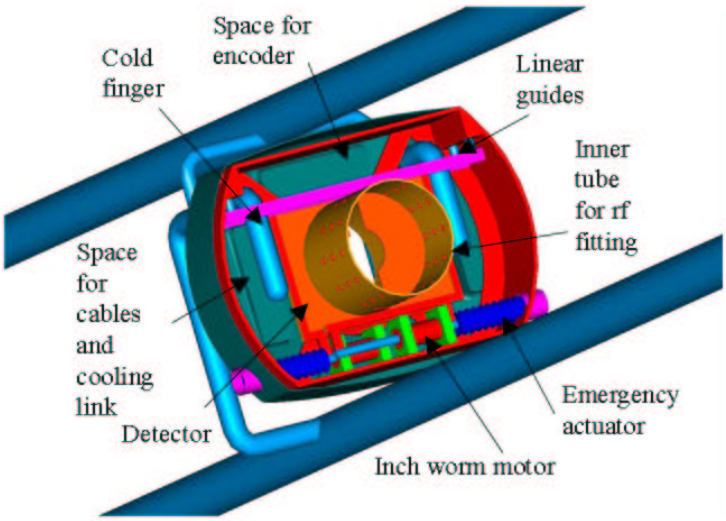

Figure 4.29: Cooling arrangement for the microstation

The flexible thermal bridge is made of copper or diamond-like carbon. The temperature difference across the bridge is obtained by:

$$\Delta T = \frac{P \cdot l}{A \cdot k}, \tag{4.4}$$

where
P = power = 10 W
l = strip length = 0.06 m
A = cross-section (m^2)
k = thermal conductivity ($\frac{W}{Km}$).

If we assume $T_{sink} = 78\,\mathrm{K}$ and $T_{detector} = 273\,\mathrm{K}$, then $\Delta T = 195\,\mathrm{K}$. In this temperature range only few materials have a constant value for k and therefore in (Eq. 4.4) $k \cdot \Delta T$ has to be substituted by the true thermal conductivity integral for this temperature interval. These numbers give a necessary cross-section of $7.5\,\mathrm{cm}^2$ for Cu.

The cross-section for copper is quite small and e.g. thin sheets can be used for the construction of the thermal bridge. The particular type of copper or copper alloy selected for this application depends also on the tensile strength and flexibility of the material.

The analysis above is based on the assumption, that the detectors are heated only by electrical power dissipated in plates. During bake-out mode the plates are heated also by radiation from the vacuum chamber wall: this power can be obtained from:

$$P = \sigma \cdot \epsilon \cdot A \cdot (T_1^4 - T_2^4) \tag{4.5}$$

where
P = power absorbed (W)
σ = Stefan-Boltzmann's constant = $5.67 \cdot 10^{-8}\,(\frac{W}{m^2 K^4})$
ϵ = emissivity (0.0 ... 1.0), worst case appr. = 1
A = detector area (m^2) = $2 \cdot 0.045 \cdot 0.060\,\mathrm{m}^2 = 0.0054\,\mathrm{m}^2$
T_1 = chamber wall temperature (K)

Operating mode	T_1 (K)	T_2 (K)	P (W)
Normal	273	273	0
Bakeout 1	523	473	8
Bakeout 2	523	273	21

Table 4.3: The worst case approximations for the absorbed power in normal operation and in bake-out condition

T_2 = detector temperature (K)

Tab. 4.3 lists the worst case approximations for the absorbed power. During normal operation, no extra power is absorbed and the values of Tab. 4.3 for the bridge are valid. During the bake-out process, when ofcourse the electrical power is switched off, the cooling load needed is at similar level as during operating mode, even in the worst case approximation, if the detector element can be heated to 150-200° C without causing damage to the further operation of the detector. Such a scenario would carefully have to be tested and possible necessary modifications on e.g. material choices taken into account in a re-design of the detector element. Even if this would not be possible and the detector would have to be kept 0° C during bakeout, this would imply not more than double the cooling load as during normal operational period in the worst case scenario. All this indicates that the two operating modes are possible with a single configuration.

The heat sink and the conducting bridge only ensure, that the warm end is at the selected operating temperature (273 K or 0° C in the calculation above). For the calculation of the temperature distribution of the detector plate, we first assume that the power dissipated (10 W for each plate) is evenly distributed on the surface. Two types of detector plates have been analyzed, one with a diamond coating - to increase thermal conductivity - and another one without any coating. The analysis is based on the following detector parameters, which, in our opinion, characterize one detector type reasonably well. The 0.1 mm diamond coating may not be practical in a real detector plate, but it has been included to demonstrate the effect of a good thermal conductor.

Detector dimensions:	45×65 mm
Detector thickness:	0.3 mm
Detector material:	silicon (thermal conductivity 150 $\frac{W}{Km}$)
Coating material:	diamond (thickness 0.1 mm, thermal conductivity 1200 $\frac{W}{Km}$)
Detector frame:	3×4 mm (cross-section)
Frame material:	Copper (thermal conductivity 400 $\frac{W}{Km}$)

The Secondary Vacuum

Secondary vacuum is introduced to secure a proper beam vacuum. This architecture also widens the selection of materials, motors and position encoders, if wanted. The original beam pipe size will go through the secondary vacuum chamber that is seen in Fig. 4.28. The chambers form a coaxial firm structure. The bellows are welded on smooth openings of the beam tube and the cups for the detectors are welded on the other end of the bellows. In the cups that will approach the beam during the measurements, there are thin superalloy windows for the active area of the detector element. The positioning and moving mechanics of the detector element are independent so that the bellow assembly is not critical. The surface areas of the bellows are such that if there is vacuum in the beam pipe and atmospheric pressure in the secondary vacuum chamber, the detectors will be drawn out from the beam pipe because of the pressure difference. If there is room on the sides of the MS chamber in the direction of the movement of the detector element, single standard welded bellows will be used but in such locations where space is restricted, coaxial bellows will be used. With coaxial bellows the total device diameter will be 20 cm.

4.12.4 Prototyping and plans

The design is made so that the development can be done with an open structure to have functional components freely accesible without the secondary chamber. The bellow surface areas are such that strong forces coming from normal pressure on the moving are partly internally compensated with dummy bellows opposite to the moving detector chamber. The air pressure force is balanced with extra weights during the development. The device is fully functional and vacuum tight in this form without the secondary vacuum.

References

[1] N.V. Mokhov, I.L. Rakhno, J.S. Kerby, J.B. Strait, 'Protecting LHC IP1/IP5 Components Against Radiation Resulting from Colliding Beam Interactions' CERN-LHC Project Report 633

[2] R. Assmann *et al.* 'Requirement for the LHC collimation system', CERN-LHC Project Report 599

[3] S. Roesler*et al.*, 'Constraints from induced radio activity on design and maintenance', Proceedings of '12th LHC Performance Workshop – Chamonix XII', Chamonix 3-8 March 2003, CERN-AB-2003-008-ADM.

[4] 'Systeme generaux de securite du LHC', CERN-LHC Project Document LHC-P-ES-0002 v 1.1. EDMS No 346512

[5] Lucien Vos, Private Comunication

[6] G. Passardi, F. Haug, J.M. Rieubland, L. Tavian, AT, private communication

[7] F. Haug, W. Kubischta, M. Dentan, "Memorandum on radiation hardness assurance for the ATLAS cryogenic instrumentation", CERN, 2001

[8] F.Haug, "Studies on cooling of th TOTEM particle detector at the LHC", to be submitted ICEC 20, Beijing

[9] A.I. Drozhdin, N.V. Mokhov, M. Huhtinen, Proc. of the 1999 Part. Accel. Conf., New York, 1999, p. 1231.

[10] A.I. Drozhdin, M. Gyr, N.V. Mokhov, I.L. Rakhno, E. Weisse, 'Protecting LHC Components Against Radiation Resulting From an Unsynchronized Beam Abort', CERN-LHC Project Report 478

[11] 'Proposal for a measurement with a Roman Pot in the SPS', The TOTEM Collaboration, CERN/LHCC 2003-061

[12] Gianluigi Arduini, private communication

5 Leading Proton Detectors

5.1 Main physics requirements for the silicon detectors

The leading proton detectors are installed into special beam pipe insertions (Roman Pots) and have therefore to fulfill stringent requirements set by the machine and the TOTEM experiment (see also Chapter 4). A 200 μm window separates the detectors from the primary beam vacuum and the high intensity proton bunches. During operation the detector edge is positioned at a distance of about 1 mm from the beam axis which poses a challenge concerning radio frequency pick-up in the detector and the close-by front-end electronics. The detector system has to be robust, its position has to be aligned and also accurately maintained within 20 μm.

Silicon strip detectors present an attractive choice for the leading proton detectors of typically $3 \times 3\,\mathrm{cm}^2$. Their production technology is well developed. With a strip pitch of 50-100 μm and an analog read-out the spatial resolution of 10-20 μm is adequate.

Silicon devices can easily be aligned and closely staggered with high precision. With a different front-end electronics and digital read-out these detectors will also have the required trigger capability (see. Chapter 7). Despite the numerous advantages and well known tracking properties of silicon detectors, two stringent requirements, arising from their use close to the beam, call for an extensive Research and Development:

1) For optimal performance, the active edge of the detector has to approach the $10\,\sigma$ envelope of the beam as close as possible. Consequently, the detectors should be active up to their physical edge. It is desirable that they are edgeless to a level of less than $50 \div 60\,\mu$m. In general, planar silicon detectors have a wide (0.5 – 1 mm) insensitive border region around the sensitive area that is occupied by a sequence of guard rings. This ring structure, called 'voltage terminating structure', controls the potential distribution between the detector's sensitive area and the cut edge in order to reduce the electrical field maxima at the detector periphery and thus the surface leakage current. In particular, detectors designed for a heavy radiation environment or generally for operation at high bias voltages, contain multi-ring structures with up to 20 rings. In the framework of TOTEM, two new approaches to fabricate edgeless silicon detectors have been developed: the planar detector with a minimized guard-ring structure and the 3D detector.

2) The second issue concerns the required radiation hardness of the detectors. Fig. 5.1 shows the charged hadron and neutron fluxes over the detector area for a luminosity of $10^{33}\,\mathrm{cm}^{-2}\mathrm{s}^{-1}$ [1] simulated with the MARS code [2]. The flux of charged hadrons, dominantly protons, averaged over the detector, amounts to $6.7 \cdot 10^5\,\mathrm{cm}^{-2}\mathrm{s}^{-1}$, a factor 4 larger than the neutron flux. The highest flux with $5 \cdot 10^7\,\mathrm{cm}^{-2}\mathrm{s}^{-1}$, narrowly focused horizontally and close to the beam originates from diffractive protons which are bent outside due to their momentum loss. To get a realistic idea about the radiation we consider two scenarios: the detector will be close to the beams during the TOTEM runs and retracted by 4 cm during the higher luminosity runs. In order to obtain an upper limit on the radiation we assume a maximum running time, integrated over 3 years, with a TOTEM participation of 10^6 s at an average luminosity of $2 \cdot 10^{30}\,\mathrm{cm}^{-2}\mathrm{s}^{-1}$ and a running time with our detectors retracted of 10^7 s at an average luminosity of $0.5 \cdot 10^{33}\,\mathrm{cm}^{-2}\mathrm{s}^{-1}$. For the TOTEM runs the maximal integrated proton flux stays below $10^{11}\,\mathrm{cm}^{-2}$ while for the high luminosity runs the flux is below $10^{12}\,\mathrm{cm}^{-2}$ since the detectors are retracted. These radiation levels are well below standard radiation tolerances of silicon detectors. We must, however, keep

in mind that accidents and unforeseen partial or total beam losses in the neighbourhood of the detectors could lead to drastically enhanced radiation levels. Furthermore, the beam halo has large uncertainties. We therefore aim at a radiation hardness of the Roman Pot detectors to withstand up to 10^{14} n(equivalent)/cm^2.

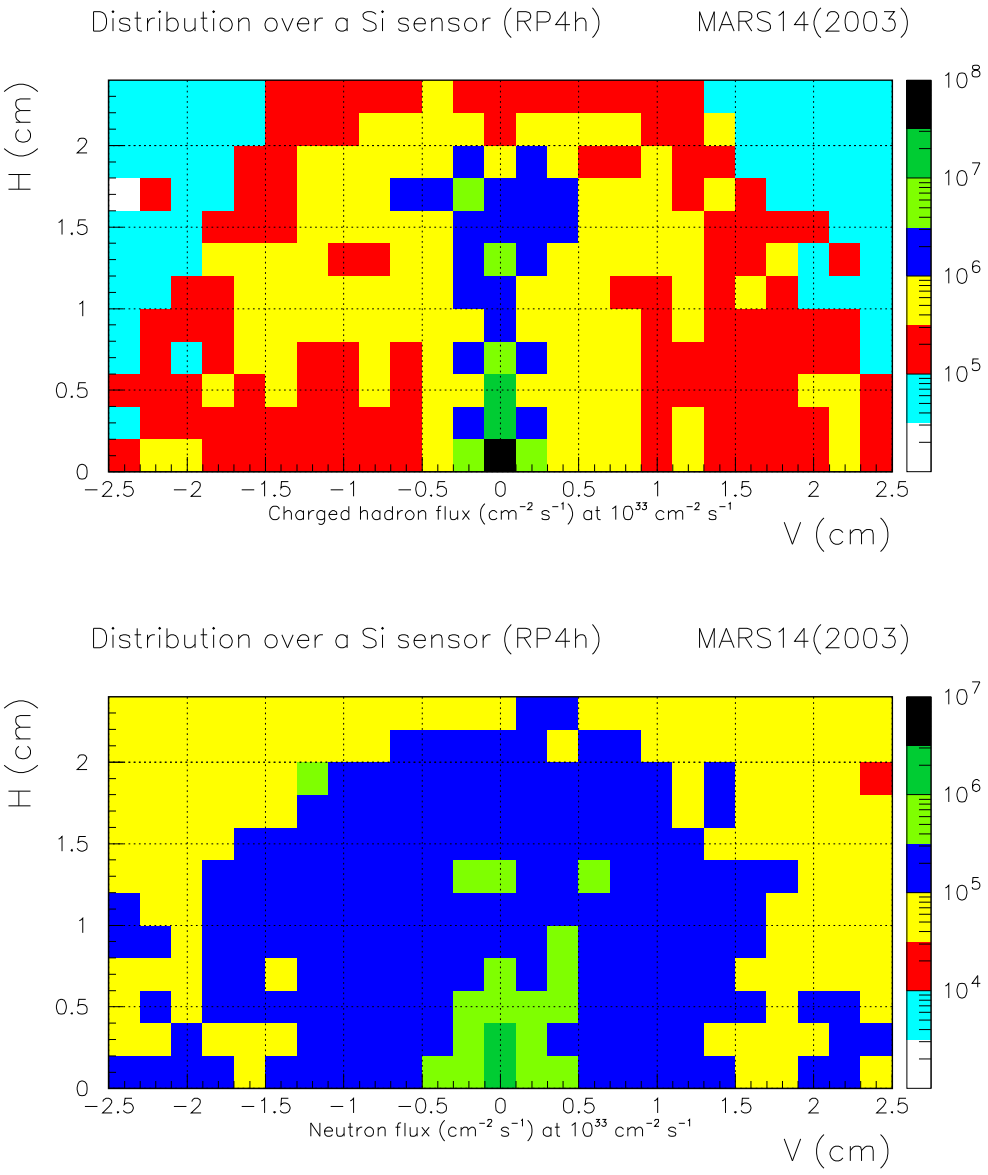

Figure 5.1: For a luminosity of 10^{33} cm^{-2} s^{-1}, the charged hadron (top) and neutron (bottom) fluxes for the horizontal detector at 220 m, placed 10σ away from the beam center. Note that H and V are the horizontal and vertical coordinates

5.2 Detector geometry

5.2.1 General considerations and detector layout

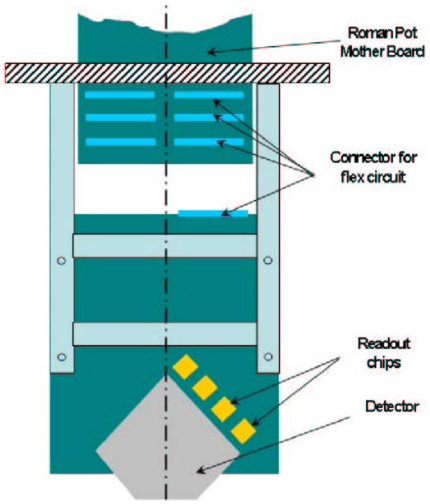

Figure 5.2: Principle of the placement of the silicon detector on the printed circuit board inside the Roman Pot and the connection to outside

The silicon detectors will be mounted (glued) on a printed circuit board, and will be placed into the Roman Pot as shown in Fig. 5.2. The lower edge of the detector is near the beam and should be 'edgeless', i.e. have an insensitive part which is as small as possible. The definition of the geometry was essential not only for the experiment itself but also for the proper coordination between the manufacturers developing detectors for the experiment, to make all detectors mutually compatible. The purpose is to define a standard with respect to the geometry, sensitive area, bonding pads, etc.

The following constraints have led to the set–up sketched in Fig. 5.3:

- The limiting aperture has a diameter of 6 cm and the sensitive part of the detector should be located inside this envelope to avoid any showers from interactions.

- A fully symmetric shape is desirable to be able - just by flipping the full card around its central vertical axis - to obtain the other coordinate in the plane. The strips are at a 45° angle from the vertical axis, from bottom left to top right, flipping around the vertical axis will yield strips oriented at 90° with respect to the situation prior to flipping. Moreover, the occupancy distribution over the ±45° strips is identical for the two orientations and is spread more uniformly over the detector strips.

- The Roman pot limits the lateral size of the board to less than 10 cm.

- The space in the Roman Pot parallel to the beam is not very large – at most 3-4 cm to receive all planes. Therefore it is desirable to only occupy the right side of the board with electronics, so that when another board is flipped along the vertical axis and sandwiched with the first one, the electronics of first and second plane sit side by side and do not add up for the thickness of the full assembly.

- For the same reason an additional area of about 1 mm^2 is used to move the detector pads (and therefore the bonding wires) away from the central line so that bonding wires from planes mounted face to face do not interfere with each other.

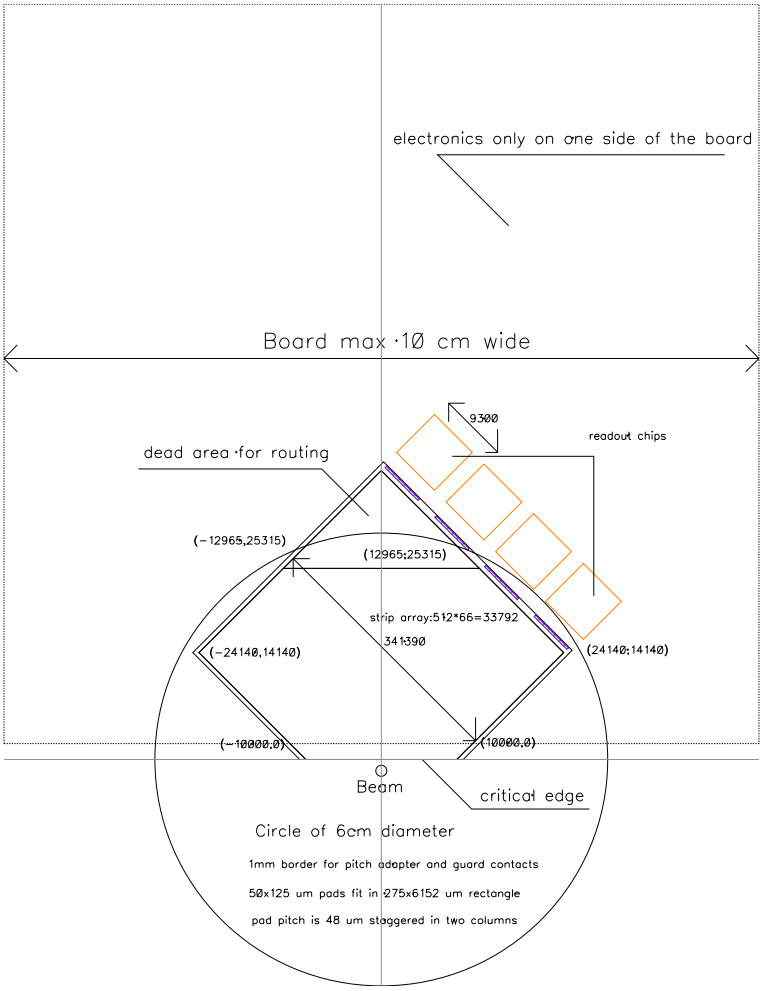

Figure 5.3: General overview of the setup, the numbers between brackets denote (x, y) coordinates in μm

– The detector strip pitch and readout chip channel pitch are not identical and some pitch adaptation is necessary to facilitate the bonding. The extra silicon area added to the top right can be used for this pitch adaptation. Doing the pitch adaptation on the detector silicon offers several advantages: it avoids the use of a dedicated pitch adapter, or the use of very fine line pitch on the card for the same purpose, both of which would represent a significant cost increase. The drawback is that it would be necessary then to incorporate the circuitry of the CMS hybrid for the APV25 chip [9] on the readout board.

These constraints lead to a hexagonal shape of the sensitive area of the detector shown in Fig. 5.4, The distance between the upper left and lower right edge of about 34.2 mm is covered by 512 strips spaced at a pitch of 66 μm. The top triangle of the detector is made unsensitive (so diffusions defining the detector sensitive area should not continue in this triangle). The metal routing should continue over this region towards the readout pads. Fig. 5.5 gives some details on the pad layout discussed below.

5.2.2 Connections to the readout chips and pad layout

The detector is read out by 4 chips each containing 128 readout channels. The two chips presently considered are the APV25 developed by CMS and the VFAT chip [10] developed by the MIC group at CERN. The former provides analog readout, but no trigger, and needs AC coupled detectors, the latter provides the trigger and a digital readout, and can be used for both DC and AC coupled detectors.

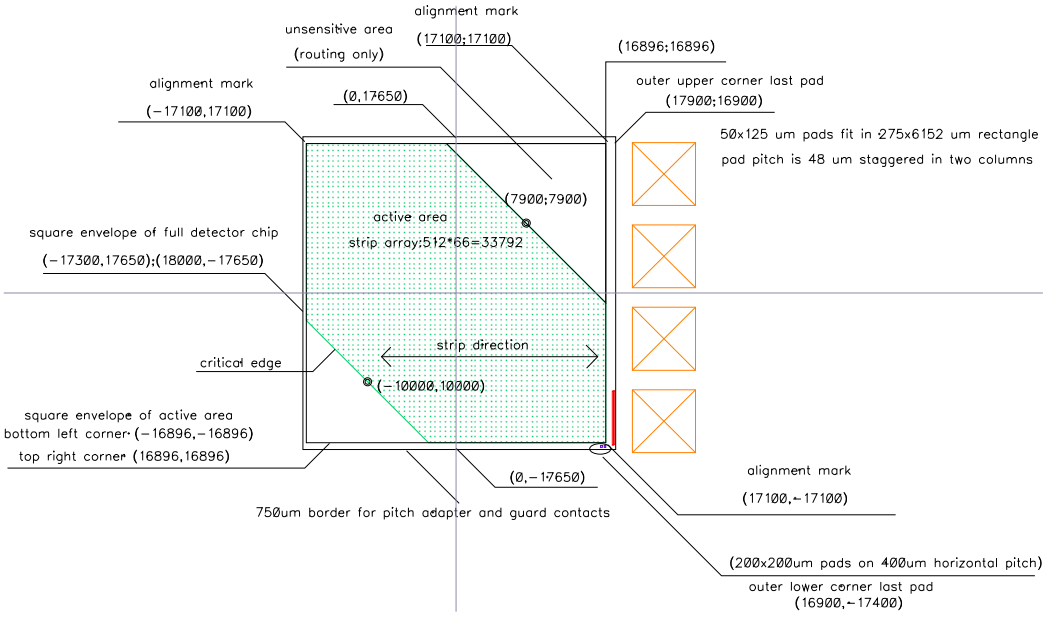

Figure 5.4: Details of the detector layout. The squares represent the readout chips

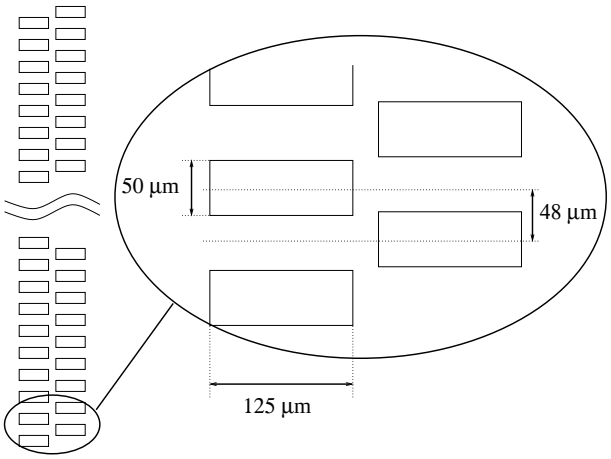

Figure 5.5: Details of the pad layout on the detector for each set of 128 strips. The pads are located in two columns. The vertical pitch is 48 µm. The four sets of 128 pads are placed along the detector edge near the readout chips with a pitch of 9.3 mm. The pads measure $125 \times 50\,\mu m$*, and the distance between the two columns (not the pitch) is 25 µm*

The pads' pitch on the APV25 is 44 μm, with an interruption of the pad row in the middle for extra power supply and ground contacts, the gap is roughly 350 μm. The VFAT chip has a pad pitch of 48 μm. In both chips these pitches are obtained by staggering the pads in two columns (see Fig. 5.5). To simplify production and avoid extra cost the two readout chips were designed to be compatible with the same detector. For this purpose a pad pitch on the detector of 48 μm was adopted to allow a direct adaptation for the VFAT, but which would still ensure bonding to the APV25 as well.

The VFAT chip has bonding pads on all four sides, thus imposing a minimum space between the chips. A readout chip pitch along the detector edge of 9.3 mm was chosen, leaving a space of more than 2 mm between the chips and enabling bonding to pads located on the board in between the readout chips with the automated bonding machines at CERN.

The APV25 which does not have bonding pads on the sides perpendicular to the side facing the detector could in principle be placed on the board with a smaller distance between the chips. However, the ground and power connections in the middle of the detector pads impose a displacement of at least 2 mm away from the detector edge, to reduce the angle of the bonding wires due to the slightly different pad pitch on detector and readout chip.

The significant advantages of being able to bond readout chips directly to the detector are: 1) an additional pitch adapter can be avoided, with considerable cost savings, and 2) the number of wire bonds can be reduced, increasing the reliability of the assembly. In this way some dead area should be foreseen on the detector, which would not add too much additional capacitance to the metal lines carrying the strip signal to the bonding pad, and which should not induce signal charge onto these electrodes if an ionizing particle traverses this dead region.

Pad Positions

Fig. 5.4 shows the details of the detector layout (rotated by 45°) and the pad positions. The numbers between brackets denote the (x, y) coordinates. The sensitive area of the detector is centered at the origin, and takes - at a strip pitch of 66 μm - 33792 μm, and therefore fits in the square drawn in the figure with corner points at (-16896,- 16896) and (16896, 16896). The edge of the detector close to the beam is at a 45° angle and crosses its central point at (-10000,-10000). The sensitive area stops at the other side at the same distance from the origin, but there the silicon continues beyond the sensitive edge as explained to accommodate the routing of part of the strips.

Apart from the pads connecting the sensitive strips to the readout chips, some pads have been foreseen on the bottom right. These are square in shape (200 μm by 200 μm), now on a horizontal pitch of 400 μm. The first one is supposed to be connected to the ground of the detector (at the same potential as the strip), the second (more to the left) should be used to absorb the leakage current at the detector edge, if any, and a third one could be introduced if a front side contact for the backside voltage needs to be provided. The location of the pads is indicated in Fig. 5.5. The pads are somewhat removed from the edge of the sensitive area of the detector as explained above to cleanly separate the bonding wires of two different planes if they are sandwiched together.

In principle the pads for the ground, guard and high voltage of the detector could have been placed closer to the sensitive area of the detector and some silicon area could have been gained. However, that would complicate the cutting of the detector wafer since the piece of silicon containing the detector would no longer have a square as delimiting envelope. A square has the advantage that, if four detectors would be placed on a 4 inch wafer each having a different orientation, they would be separated maintaining the saw cut straight (see Fig. 5.6).

Alignment issues

For the best positioning, it would be desirable to glue the detector to the readout card and afterwards to finely align the detector card within the frame holding the card. Since the alignment should be carried out with respect to the detector, alignment marks on the detector are required. One obvious place to put an alignment mark is at the very top of the detector, as indicated in Fig. 5.4. An example of an alignment mark is shown in Fig. 5.7. It has been designed using 5 μm wide geometry and measures 175 μm across. Note that one set of legs of the alignment cross should be parallel to the detector edge near the beam thus it should be oriented at 45° in Fig. 5.4.

At the beginning it was considered to place an alignment mark near the sensitive edge which, however, revealed to be too complicated for many reasons. Therefore two alignment marks are foreseen in the left and right corner of the sensitive area, as shown in Fig. 5.4. Together with the top alignment mark good alignment in x, y and θ should be possible.

Some details on the alignment are explained in the chapter describing the mechanics of the Roman Pots, and further details on the board on which the detector is mounted are explained in the electronics chapter.

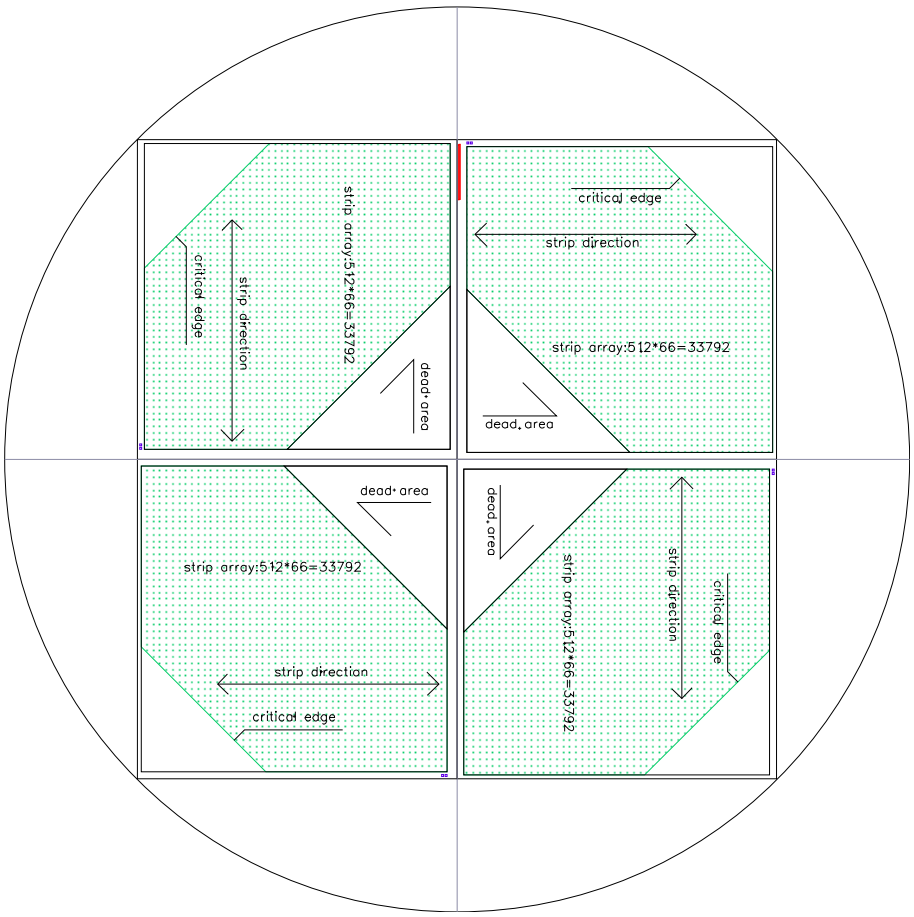

Figure 5.6: Possible layout configuration for a detector wafer containing 4 detector units each oriented in a different direction. The detector edge close to the beam is near the wafer edge. The key point is that the area containing each detector is square to be compatible with dicing

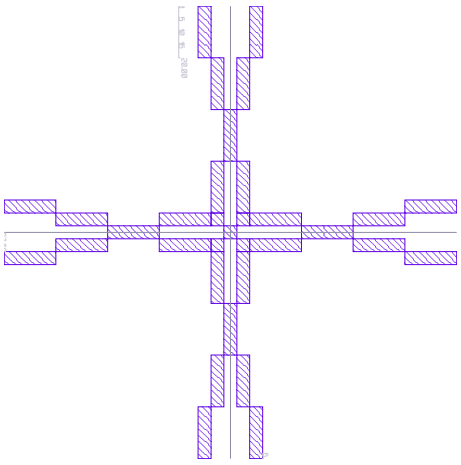

Figure 5.7: Example of an alignment mark to be put at the top of the detector

5.3 Edgeless Planar Detectors

Modern planar technology for integrated circuits, one of the cornerstones of the current semiconductor industry, has also been adapted to reliably fabricate radiation silicon detectors with very fine segmentation pitch. These silicon detectors used as tracking devices can achieve spatial resolutions of the order of few microns and perform reliably under different ambient conditions.

These detectors are typically *p-n* junctions operated under reverse bias to deplete and set up an electric field in their bulk that allows the collection of the charge generated by ionizing radiation.

To improve stability and performance of these devices, the electric field present in the detector bulk is reduced at the die cut edge by mean of voltage terminating structures, i.e. a sequence of concentric rings of implant surrounding the sensitive area on the detector side with higher electric field. These implants are of the opposite type of conductivity of the detector substrate to generate many junctions over which the detector bias voltage is dropped in small steps. This voltage terminating structure therefore controls the potential distribution around the detector sensitive area and also makes sure there is no voltage drop across the chip cut. Such a structure in particular for detectors operated in a heavy radiation environment or at a high bias voltage, can contain up to 20 rings and take up hundreds of microns between the active area and the detector chip cut edge. Since almost edgeless detectors are mandatory for TOTEM, Research and Development Projects were started with the aim to achieve edgeless planar detectors:

- The 'cut through' approach [3] combined with low temperature operation.
- New approach with 'current terminating structure'.

5.3.1 Detectors with 'cut through' edge operated at low temperature

The 'cut through' approach is based on the simple idea that the detector sensitive area may be limited by the detector chip cut through the sensitive p^+-n junction. Investigations of this approach have shown that:

- The detector leakage current is not stable in time and reduces with time if the detector is stored at the ambient conditions.
- The leakage current depends on the technique used for cutting, on a possible subsequent chemical treatment, and also from which side of the wafer the cut was made (the current is lower when the cut is made from the non-sensitive Ohmic side of the detector). In general the leakage current remains too high for standard operation and needs to be reduced by some other means.

The high and unstable leakage current which also depends on the cut procedure can be drastically minimized by reducing the working temperature of the detector. Under these conditions, an acceptable signal-to-noise ratio can be achieved, if the leakage current across the cut edge is reduced, such that the instability does not affect the detector performance. A successful test of the 'cut through' detectors has been performed at 110 K [4].

Results from the test beam activity of 2002 using 'cut through' edge detectors

The successful measurement of the efficiency up to the edge of the silicon sensor has been performed with a microstrip detector cut through the sensitive area. Scribing the backplane of a planar silicon detector with a laser beam and then bending it to crack produced a clean edge perpendicular to the strips. No further treatment was applied to the cut edge (see Fig.5.8).

The tracking effciency near the cut edge was then checked with a 120 GeV pion beam. For this measurement, the detector under test was cooled to 110K with a resulting leakage current of only 15 nA at full depletion voltage (45 V), then placed between two pairs of similar microstrip detectors mounted with their strips horizontal and vertical, V3 and H4 with V7 of and H8 in Fig. 5.9.

The recorded hits on the reference planes and on the test detector allowed a fine study of the behaviour at the edge. The results (reproduced in Fig. 5.9(right)) show that the efficiency is uniform and reaches a maximum at 25 μm from the physical edge. The data show that the position where the maximum is

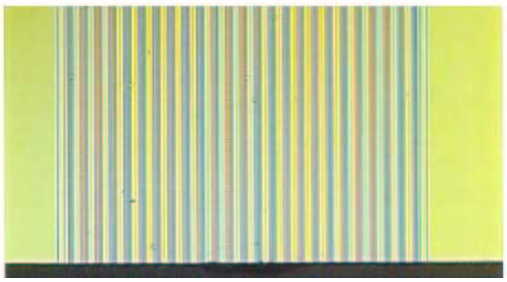

Figure 5.8: Enlarged picture of the edge of the microstrip detector. The scale is given by the pitch of the 24 strips, which is 50 μm

reached does not vary for different cuts on detector noise. The uncertainty is dominated by the knowledge of the position of the detectors. It is worth noting that the beneficial effect of the low temperature operation also guarantees higher radiation hardness [5, 6, 7].

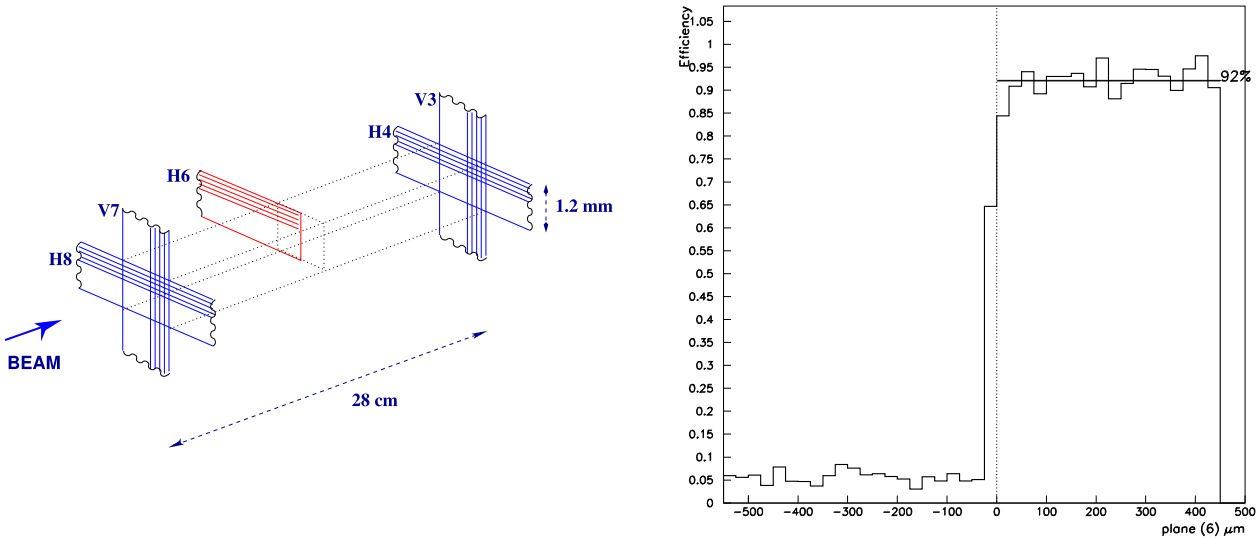

Figure 5.9: Setup of the test beam showing the planes of the telescope (V7 with H8 and V3 with H4) and the cut detector (H6) (left). Plot for the efficiency of the cut silicon detector (right). The dashed line in the plot corresponds to the position of the physical edge of the detector measured with metrology

While the performance of these 'cut through' detectors is satisfactory at cryogenic temperatures, cooling to these temperatures is not ideal for the tight assembly of the TOTEM Roman Pots. In addition, the readout electronics cannot be operated at these low temperatures. Requiring thermal insulation between the readout electronics and the detectors results in additional capacitance seen by the readout, and therefore additional noise. To avoid these disadvantages and to operate close to ambient temperature, an improvement of the 'cut-through' detector has been developed.

5.3.2 Detectors with current terminating structure (new approach)

As mentioned before, standard planar detectors contain a voltage terminating structure which smoothly reduces the potential from the highly biased detector sensitive area to the potential of the back ohmic contact. The detector chip cut does not contribute to the detector leakage current as there is no potential drop across this cut.

The conceptual idea of the new approach is to allow the full detector bias to be applied across the detector chip cut, and to collect the resulting current on an implanted ring, which surrounds the active area and is biased at the same potential as the detecting strips (see Fig. 5.10).

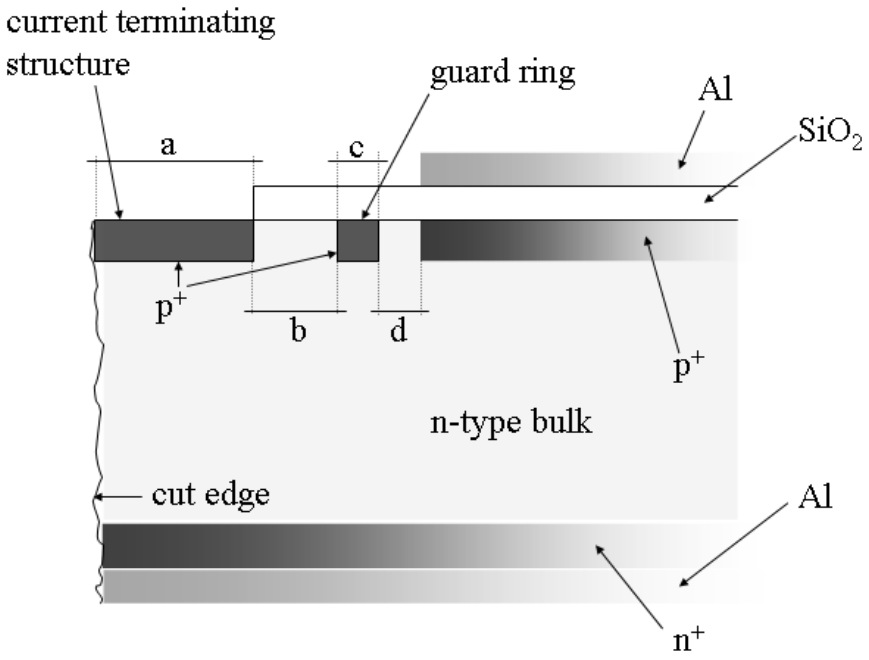

Figure 5.10: Simplified cross-section of the detector with the sensitive edge at the left side

This ring is separated from the detector biasing ring (the strips are biased by means of a punch-through structure between this biasing ring and the strips). Separating this current correcting ring from the bias ring strongly reduces the influence of the current generated at the detector edge on the active area of the detector. In fact, by collecting the current on a separate electrode, this current does not contribute to the noise.

At full depletion, the detector leakage might be too high at room temperature, but the limitation here is excessive power dissipation and not the noise.

Detectors with current terminating structure have been developed within a joined effort between the TOTEM group at CERN and Megaimpulse, a spin-off company from the Ioffe PT Institute in St. Petersburg (RUSSIA).

Electric field at the edge of the detector

This new detector development started by modelling the potential distribution in the detector, using different boundary conditions at the cut edge. It was considered that the chip cut surface contains a high density of lattice defects, dangling bonds and disordered regions. As it is known, a significant fraction of these defects are electrically active, i.e. produces energy levels in the silicon forbidden gap. Given the wide variety of the defects, their energy levels can be considered almost continuously distributed between the valence and conduction bands. Their high concentration is responsible for a high conductivity of the cut surface producing an effective screening of the electric field in the layers adjacent to the chip cut. On the other hand in the presence of an oxidizing atmosphere a naturally grown layer of SiO_2 appears on the cut surface reducing its conductivity. All this makes the prediction of the properties of the cut surface

difficult, therefore two possibilities for the surface boundary conditions were considered to simulate the potential distribution in the new detectors [8]:

- Highly conductive surface of the cut.
- Non-conductive surface with low concentration of lattice defects and the reverse biased junction on the front side.

This leads to two types of boundary conditions to apply along the cut to solve the 2D Poisson equation for the detector bulk: a linearly and quadratically distributed potential with their maximal value equal to the applied bias voltage.

The numerical calculations of the potential distribution have been done over a section of a p^+-n-n^+ pad detector with the sensitive area limited by the current terminating ring at the cut edge and then the biasing ring as shown in Fig. 5.10. The bulk resistivity used for the calculation is 8 kΩ cm. The potential applied on the back plane is 35 V, while the two implanted rings are set to ground. The distribution of the equipotential lines for these two approaches are shown below: Fig. 5.11 illustrates the case of the non-conductive condition over the edge (right) and the case of conductive surface (left).

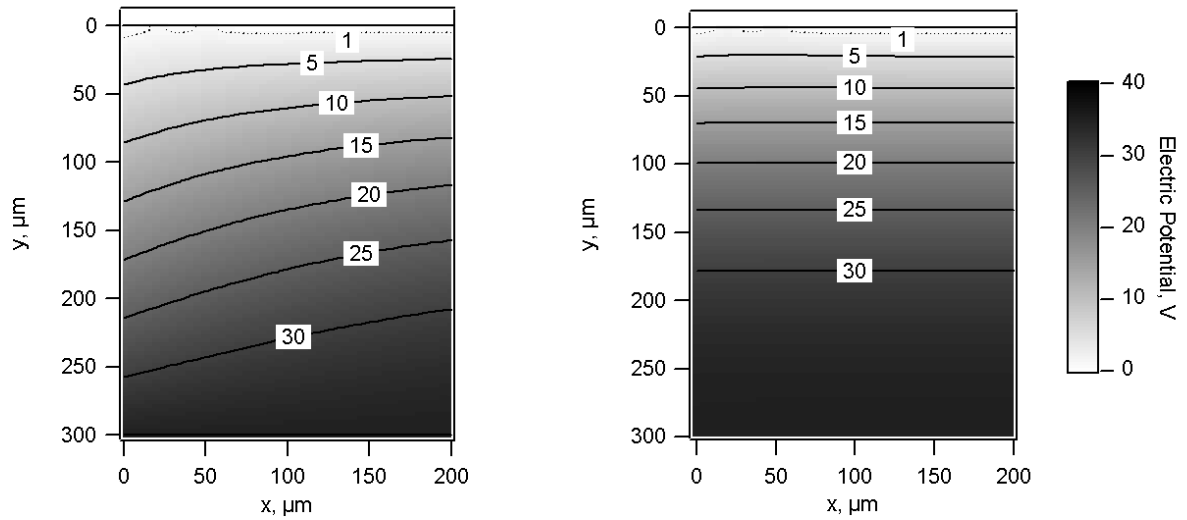

Figure 5.11: Portion of the potential distribution calculated for a sample 1000 µm large (along direction x) and 300 µm thick (direction y) with rispectively constant (left) and linear (right) electric field at the edges which are at x=0. In both cases the current terminating structure is on the front side (y=0) and starts at the edge with a,c=10 µm and b,d=20 µm where a,b,c, and d are defined in Fig. 5.10

The presence of the electric field at the cut edge for both cases meets the goal of developing a sensor with minimal dead edge. In particular, for the case of linear electric field boundary the charge generated at the cut edge drifts only along the surface and then is collected by the current-terminating ring. Moreover, the grounded inner p^+ ring used for the punch through biasing cleans up the current generated at the cut edge which cannot be collected by the outer current terminating ring due to diffusion to the detector bulk from the cut.

The briefly overviewed results of the detector simulation show that the detector configuration with the outer current terminating structure can be applied for the sensitive edge detectors. Edge sensitive detectors conceived as in this model are not only promising but also realistic with respect to detector fabrication with standard planar technology.

Electric characterisation of edgeless detectors

Current/Voltage Characteristics A matter of concern for detectors with the current terminating structures is the influence of the current generated at the cut surface on the detector active region. To

address this question and to better understand the applicability of the approach based on the current terminating structure, a set of $1 \times 1\,\mathrm{cm}^2$ microstrip detectors with several topologies at the edge has been processed on a $300\,\mu$m thick wafer. Their simplified cross-section at the sensitive edge is presented in Fig. 5.10

The different topologies given by variations at the cut edge, in terms of a, i.e. the width of the outer p^+ ring implant, b, i.e. the distances between the rings, c, i.e. the width of the bias ring and d, the distance between the strips and the bias ring are listed in Tab. 5.1.

Detector type	a (μm)	b (μm)	c (μm)	d (μm)
A	20	10	5	6
B	20	20	5	6
C	40	10	5	6
F	60	20	5	6

Table 5.1: Definition of the different detector types with respect of the characteristic widths at the sensitive edge

To study the fractions of the surface current flowing in the active region, each detector was kept on a sample holder with the inner biasing ring and the outer current terminating ring both bonded to allow current/voltage (I-V) and current/temperature (I-T) measurements.

Two schematics were used for the I-V investigations at room temperature (see Fig. 5.12):

- Scheme 1: current measured from the biasing ring and the outer ring kept floating.
- Scheme 2: current measured from the biasing ring with the outer ring grounded.

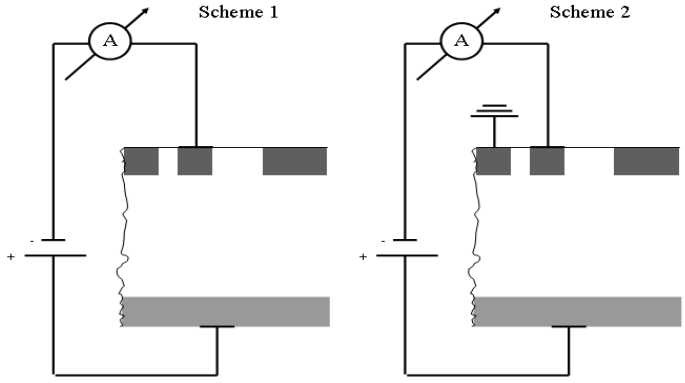

Figure 5.12: The two schemes for the measurement of the detector current at the inner ring

The I-V characteristic dependence measured for scheme 1 for the different topologies is shown in Fig. 5.13. The current measured in such scheme is strongly dominated by the current generated at the surface. This current flows at least partially in the active region and renders the operation of the detector impossible.

The variation of this current for the different samples does not seem to be correlated with the changes in their ring structures at the edge, but seems to be more an effect of the differences that can arise at the surface after the cut. In any case, given the cutting technique (diamond saw) some variations are expected. This is not the case anymore if the outer ring is grounded as seen in Fig. 5.14 for the same

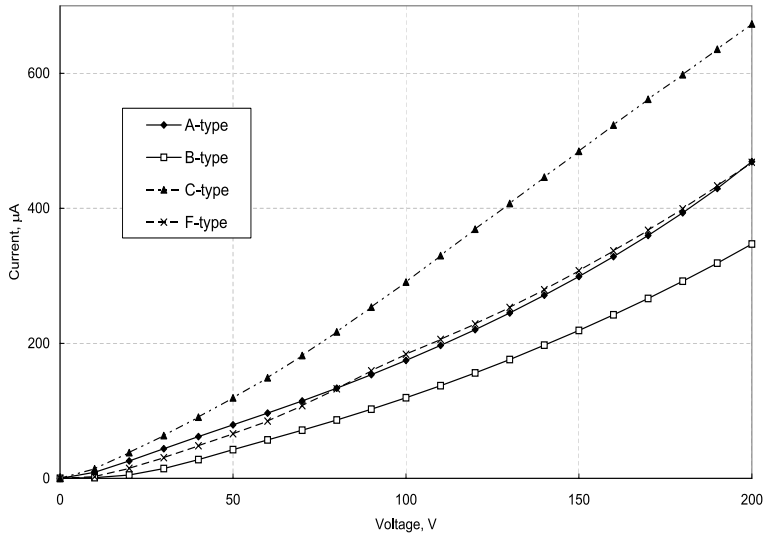

Figure 5.13: Current–Voltage characteristics measured with the scheme 1 for the different topologies

samples: the current on the bias ring is reduced by up to four orders of magnitude compared to scenario 1. This confirms the validity of the current termination approach: only a very small portion of the detector edge leakage is collected by the bias ring, practically all current is collected by the outer ring. Moreover the difference between the different topologies seems to be negligible.

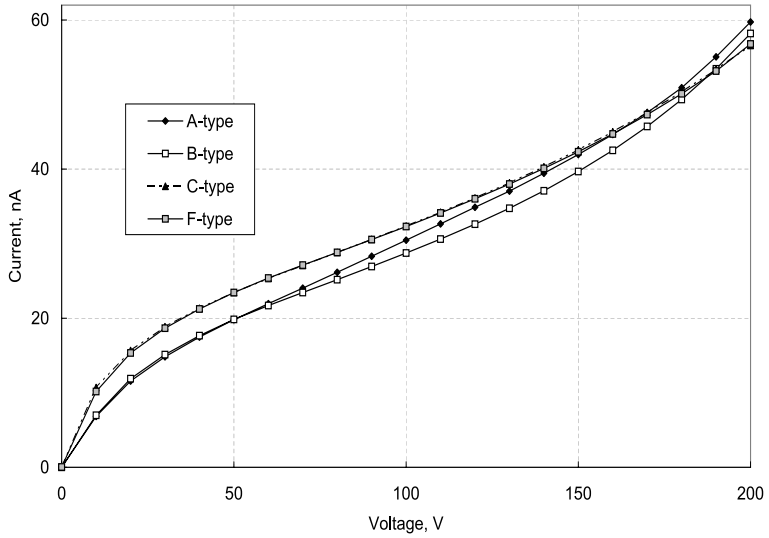

Figure 5.14: Current–Voltage characteristics measured with the scheme 2 for the different topologies. The current reduction is evident, and illustrates the effectiveness of grounding the outer ring

A common feature presented by these current-voltage characteristic dependences is the similar progressive rise. Each I-V curve clearly shows that in the range of 0-20 V the rising slope is higher than in the following range. The knee of the curves between the two slopes is the sign that the full depletion has been reached. Further increase of the current with voltage can be associated to the increase of the electric field at the cut edge that enhances the injection of the current from the surface to the bulk.

In conclusion, this investigation of I-V characteristics shows that, in presence of a biased current terminating ring, a narrow gap between the chip cut and biasing ring is sufficient to control the leakage

current. Even at room temperature the biasing ring current is almost exempted by the current generated at the surface, moreover a further reduction is expected at the strips. However, if required, the high value of the current collected by the current terminating ring can be further reduced by lowering the working temperature.

Current/Temperature dependence The well-known exponential temperature dependence of the reverse current of a p-n junction is due to the thermal excitation mechanism of electrons transferring from valence to conduction band. The activation energy of this process is controlled by the spectrum of deep levels in the semiconductor band gap. For the high resistivity silicon used to process these detectors, the concentration of the deep traps is such, that it generates a reverse current of only a few tenths of nA/cm^2. Therefore the cut edge current will fully dominate the bulk current and determine the current temperature dependence. Fig. 5.15 presents the Arrhenius plot for the current flowing through the current terminating ring in a sample of $0.5 \times 0.5\,cm^2$ biased with 100 V and its exponential approximation that has the form of:

$$I = A \cdot \exp\left(-\frac{E_j}{kT}\right) , \tag{5.1}$$

where E_j is the effective activation energy, A is a constant that depends on thermal velocity of the carriers, the recombination cross-section, the density of defects and the extension of the surface.

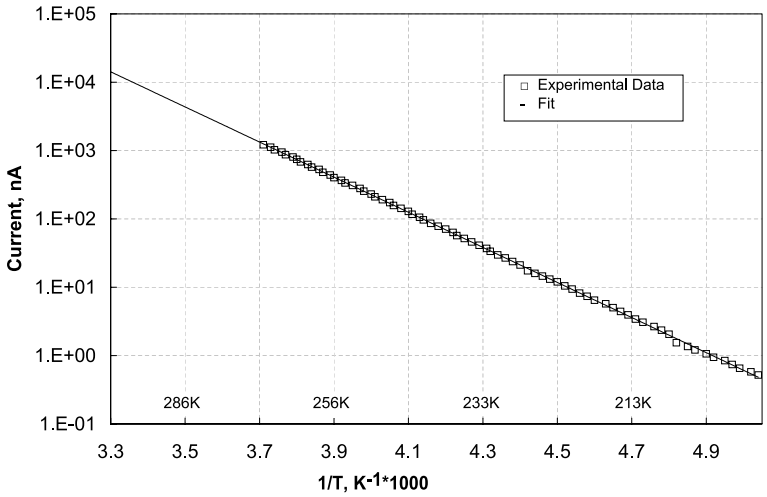

Figure 5.15: Arrhenius plot: experimental data and fit with E_j of 0.51 eV

The effective activation energy derived from this fit is 0.51 eV and is very close to the mid gap energy for silicon. This correlates with the fact that the sensitive edge contains a high concentration of defect levels continuously distributed over the band gap, with the mid gap levels being most effective for current generation. Moreover, this observation allows to practically predict the effect of the detector cooling: at -20° C the current decreases of two orders of magnitude with respect to room temperature.

Test beam results from 2003

Silicon detectors with the above guard-ring structures have been tested in September 2003 with a muon beam in the X5 area at the CERN SPS. Several samples were used for this test, with guard-ring geometries defined in Table 5.1.

The test set-up is given in Fig. 5.16 and Fig. 5.17. Two test detectors (TD) were mounted on a side of a board next to each other, with the cut edges facing each other and being parallel. The detectors were aligned under a microscope and the mechanical distance between the detectors was measured with

a precision of better than 10 μm. A reference detector (RD) was mounted on the back side of the board with the strip direction perpendicular to the ones of the test detectors, i.e. parallel to the sensitive edges of the two TD's. Thus, due to the high spatial resolution of the RD (strip pitch of 50 μm), the insensitive distance between the two TD's can be measured precisely and can be compared with the mechanical distance enabling a precise determination of the efficiency drop at the edges of the test detectors.

The silicon devices were coupled with the electronics foreseen for the Roman Pot detectors in the TOTEM experiment, i.e. the APV25 chip, developed within the CMS collaboration for the readout of the silicon tracker. A special board was developed to assemble two TD's and the RD together with the readout electronics. The board, made of a G10 plate, 600 μm thick, was laminated with a kapton foil on which the signals from the detector were routed to the readout chip. The routing of the signals was accomplished by 25 μm wide, 17 μm thick copper lines covered by a gold layer. This technology allows to safely bend the Kapton with metallised lines. In fact, for the channels associated to the TD's, the lines were bent to follow the kapton to continue to the back plane of the G10 board. Laminating the G10 with the Kapton allowed to define all lines on both sides only with one metal layer. On this board the detectors were 6 cm away from the APV25 to provide sufficient thermal resistivity to allow temperature differences between detector and electronics of more than 50 K. The choice of technology used for the board was the result of an optimisation for the thermal performance, the cost and the production time. The pictures of the back and front of the board with the electronics and the detectors are shown in Fig. 5.16.

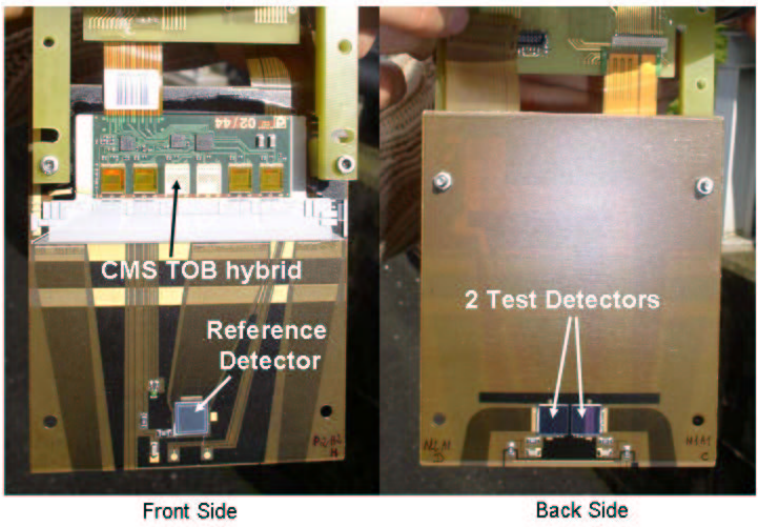

Figure 5.16: Pictures of the board developed for the test beam

As can be seen from Fig. 5.16, the readout chips were mounted already assembled on a package, the CMS TOB hybrid that also hosts electronics for other readout features.

In order to optimise the common-mode-noise rejection on the front-end electronics, each detector was coupled to an individual APV25 with 128 input channels. The board was also equipped with two couples of PT100 thermometers and heating resistors to implement two temperature control loops, one at the level of the detector and one at the level of the electronics.

To allow measurements with cooled detectors, the boards were also mounted in a cryostat (see Fig. 5.17), which was an open loop cryostat cooled with liquid nitrogen and based on the principle of the cold finger, i.e. cooling down via thermal conductivity without liquid transfer. This solution follows the same principle foreseen for the cooling in the Roman Pots (see Section4.5).

Results were obtained for two edges, the types A and B (see Tab. 5.1), placed on two different modules sitting back-to-back with the reference detectors arranged along the beam line, as sketched in Fig. 5.17. All the detectors were operated over-depleted with a bias voltage above 120 V; while the full depletion was evaluated to be around 20 V (see Fig. 5.14). The measurements were performed at room temperature

and at $\sim -4^\circ$ C.

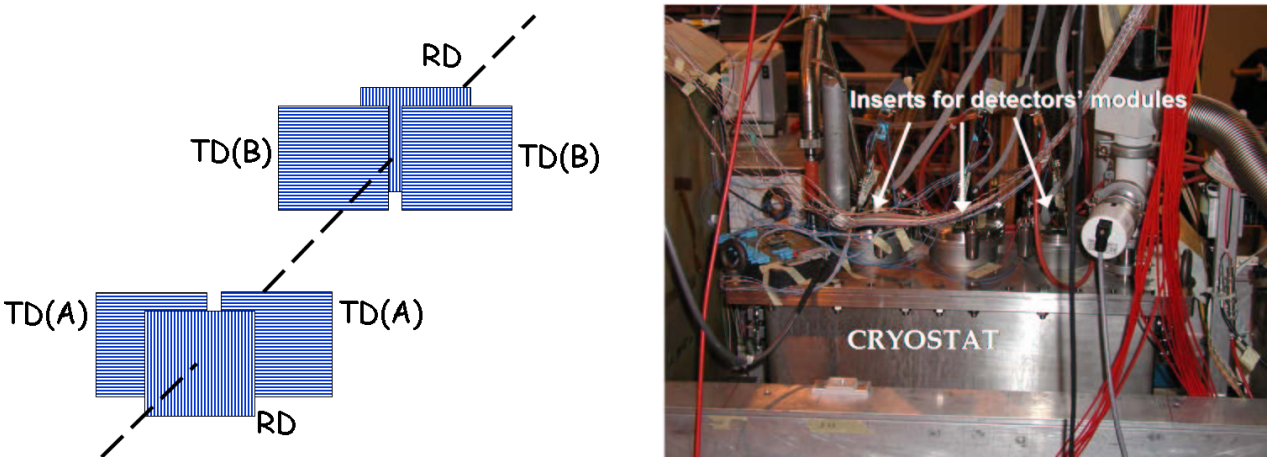

Figure 5.17: Arrangement of test detectors (TD) of type A and type B and their reference detectors with respect to the beam direction (dashed line) on the left and picture of the cryostat in the beam area on the right

The detectors were triggered by a $10 \times 10\,\mathrm{mm}^2$ scintillation counter, placed 2 m away from the detectors downstream in the beam line.

A track was defined by the two reference detectors in coincidence either with the two left or the two right test detectors. For this coincidence condition, the correlation between the hit strips of the two reference detectors is plotted in Fig. 5.18. The four-fold coincidence cleans the data well as can be concluded from the low background in the plot. The diagonal correlation indicates that the two detectors were well aligned and that the tracks were perpendicular to the detector planes. The divergence of the beam was less than 0.5 mrad. The gap in the middle reflects the insensitive region between the test detectors.

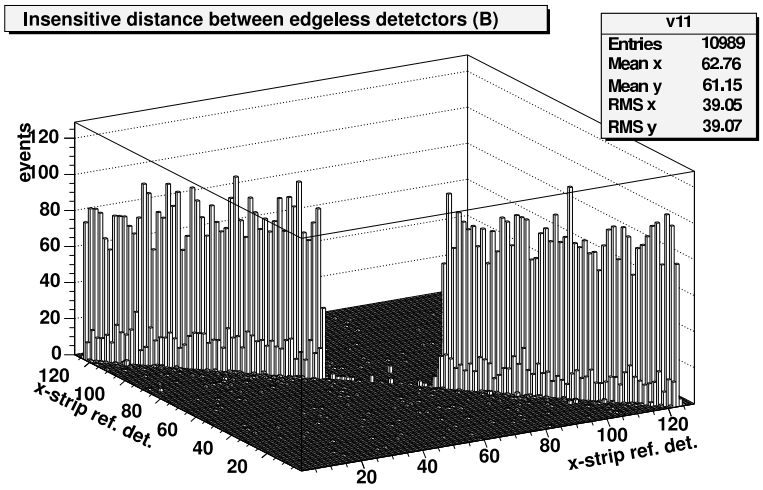

Figure 5.18: Coincident hits in the two reference detectors with the condition of having a hit only on one of the two test detectors of type B

A sharp decrease of the efficiency close to the cut detectors' edge is observed on both sides. To study this effect further with better precision, the distribution of the reference detector mounted on the other side of the test detectors is plotted in Fig. 5.19 and in Fig. 5.20 for the two guard-ring configurations. The end of the strips at the cut edge of each detector was measured with micrometric precision ($10\,\mu$m) with respect to the $50\,\mu$m strip of the corresponding reference detector. The dashed lines in the plot give

the position of the strip ends where the detector is supposed to be fully efficient.

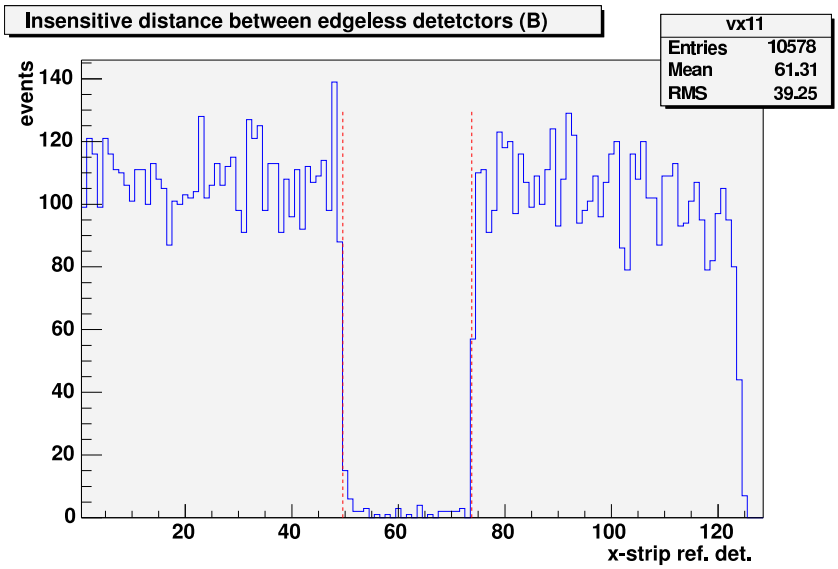

Figure 5.19: Distribution of hits in the reference detector in coincidence with hits in the two test detectors of type B. The dashed line corresponds to the beginning of the sensitive area of the two TD's

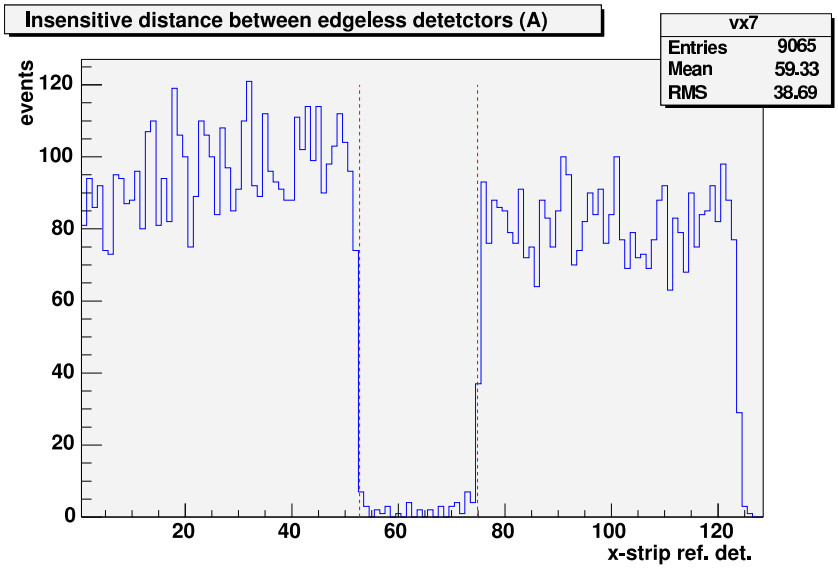

Figure 5.20: Distribution of hits in the reference detector in coincidence with hits in the two test detectors of type A. The dashed line corresponds to the beginning of the sensitive area of the two TD's

In principle, with good statistics these edges can be determined with high precision from the distributions in Fig. 5.19 and in Fig. 5.20. We estimate a combined statistical and systematic error of 20 μm. Since the strips start at 40 and 50 μm away from the physical edge respectively, the detectors exibit an insensitive edge region of 60-70 μm.

The detectors were operated in a cryostat at a temperature of $-4°$ C. The characteristics of the detectors were unchanged, but the current in the grounded outer guardring changed from $\sim$ 160 μA to $\sim$ 40 μA. This reduction is only the half of the one expected (see Fig. 5.15).

The detector efficiency is difficult to estimate due to an incomplete overlap of the detectors and a too small number of planes. Instead, the pulse height distributions are given in Fig. 5.21 for a test and a reference detector. Since the noise pedestal was evaluated to be 1 count, the comfortable signal-to-noise ratio (as expected from calculations) ensures a high detection efficiency.

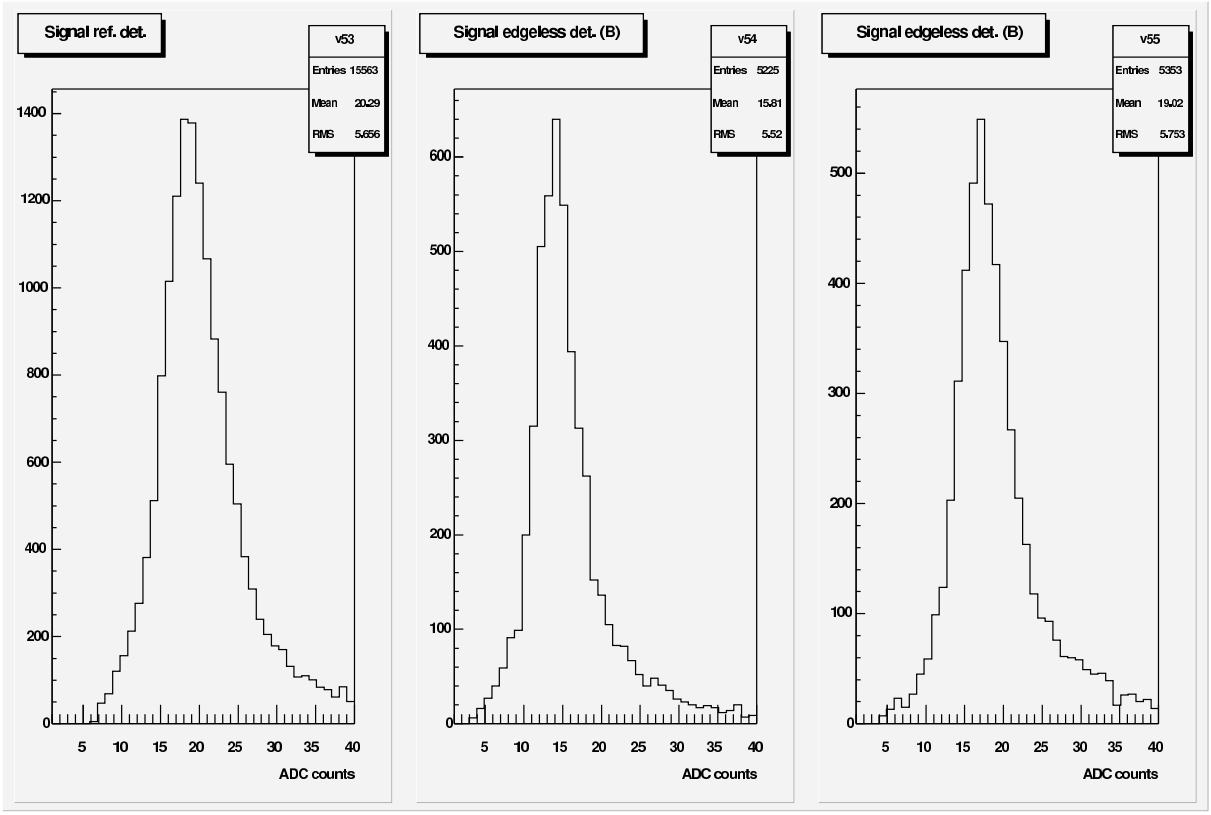

Figure 5.21: Signal in the test detectors B and their associated reference detector

In conclusion, almost edgeless detectors with a current terminating structure were successfully tested with the CMS read-out via the APV25 chip. They showed an excellent and stable performance at room temperature with an insensitive border of less than 60 μm. This result meets the experimental requirements for Roman Pot detectors making the current terminated microstrip silicon detector an excellent candidate for the leading proton detectors at the LHC.

5.4 3D and Planar/3D Detectors

5.4.1 Concept and Overview of 3D Detector Characteristics

S. Parker proposed 3D detectors in 1995 [11] and C. Kenney active edges in 1997 [12]. This technology, which combines micro-machining and standard VLSI (Very Large Scale Integration) processing, takes full advantage of the development of high precision etching techniques in silicon. Since the publication of the 3D detector idea, several prototypes with different dimensions and electrode configurations have been fabricated and fully characterised [12, 13, 14].

Fig. 5.22 sketches the main features of this novel detector design. Contrary to the standard planar silicon configuration, in the 3D design the electrodes are processed inside the bulk of the silicon wafer instead of being implanted on its surface. The consequences of this approach are manifold:

1. collection distance as short as 50 μm or less while using the full charge generated by the traversing

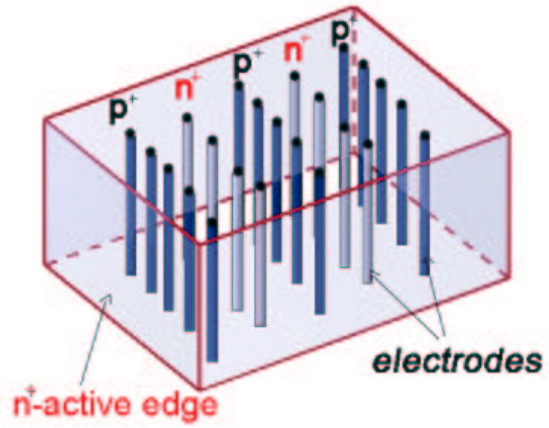

Figure 5.22: Sketch of a pure 3D detector where the p^+ and n^+ electrodes are processed inside the silicon bulk. The edges are trench electrodes (active edges) and surround the sides of the 3D device making the active volume sensitive to a few µm from the physical edge

particle in a thick substrate (normally 24000 e^- for a 300 µm thick substrate);

2. a factor 10 faster pulse speed, due to the shorter drift distances, the higher average field for any given maximum applied field and the small differences in arrival time for the charges arrayed parallel to the electrodes;

3. increased radiation tolerance due to the shortened drift distances and a still moderate full depletion voltage;

4. capability for room temperature operation after heavy irradiation (see Fig. 5.23).

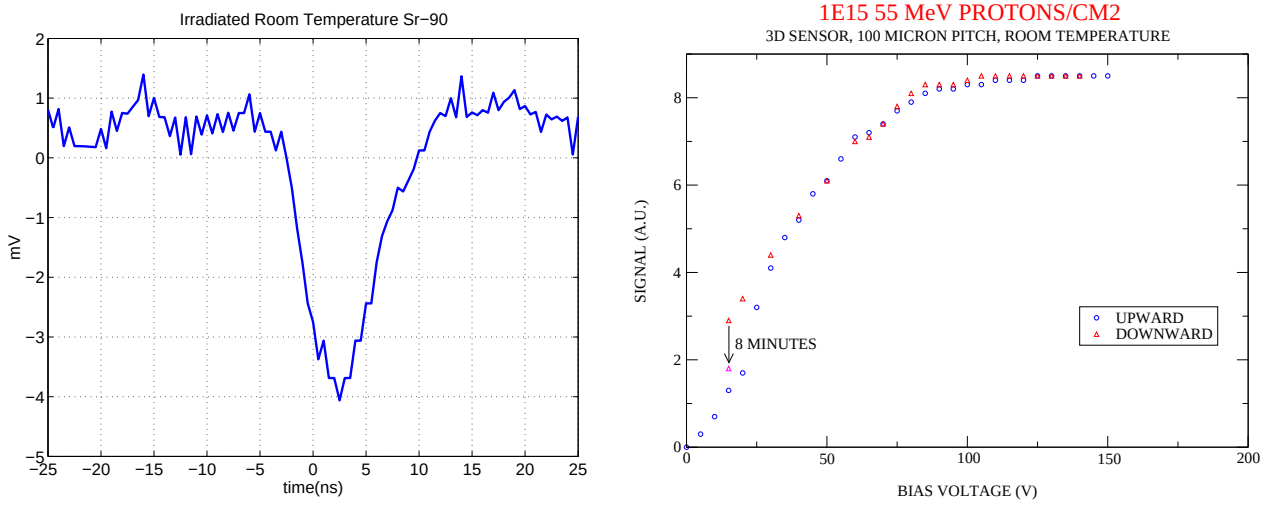

Figure 5.23: Left: oscilloscope trace of a minimum ionising particle detected with a 3D detector irradiated to 10^{15} protons/cm^2 and fully reverse annealed. The test was performed at room temperature. Right: signal of a 3D device irradiated with 10^{15} 55 MeV protons (equivalent to $1.8 \cdot 10^{15}$ n/cm^2) measured at room temperature but stored at low temperature with minimal beneficial and reverse annealing. The 8 min pause at one point was allowed to show the apparent hysteresis due to the time required for (presumably surface) charge settling

At present, the charge collection efficiency has been measured to be 60 % for a detector irradiated up to 10^{15} protons/cm^2 with a detector bias of 40 V. The irradiation and the characterisation of some samples have been performed at room temperature. An example of a signal from a minimum ionising particle (MIP) after such a fluence is shown in Fig. 5.23 (left). A full depletion bias voltage of 105 V (Fig. 5.23, right) has been measured for a device irradiated with 10^{15} 55 MeV protons/cm^2, corresponding to $1.8{\cdot}10^{15}$ n/cm^2. 3D detectors are expected to resist beyond 5×10^{15} n/cm^2, in particular if oxygen enriched substrates and electron signal readout are employed [15, 16, 17].

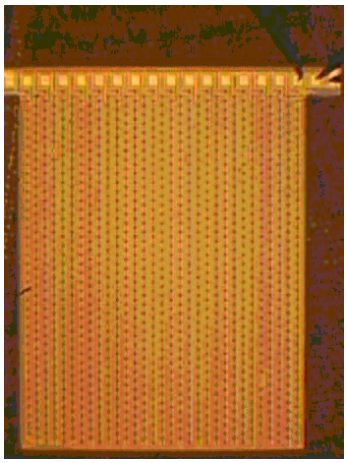

Figure 5.24: Pure 3D detector with microstrip readout configuration. The electrodes and the aluminium strips, which tie the rows of p^+ and n^+ electrodes, are clearly visible. The p^+ strips end at the bonding pads (top)

3D geometry has shown great flexibility in the use of readout electronics. Since both electrodes are accessible from the front and back side of the wafer, it is possible to process the readout electrodes to be compatible with both pixel and micro-strip readout electronics chips for both input polarities and on either side of the wafer. An example of a micro-strip compatible readout is shown in Fig. 5.24, where aluminium strips have been used to tie together electrodes of the same type. Another important feature, crucial for TOTEM and characteristic to 3D detectors, is the possibility to minimise to no more than few microns the dead area of the sensor by etching a trench along the full surface of the physical edge and diffusing in dopant to make an electrode. The electric field lines, which are parallel to the wafer's surface, can then be properly completed at the edge electrode. An exampe of an "active-edge" electrode is shown in Fig. 5.25.

The same processing technique used to fabricate full 3D (3D interior and 3D-active edges) has been used to produce planar/3D devices (planar interior and 3D-active edges). In this configuration, the free edges of a planar detector are again deep etched and n^+ dopant diffused in. Then a final dicing etch instead of sawing (as in traditional planar structures) separates the sensors. In this way the edges of the sensor become an extension of the back-side n^+ electrode to the front side, as shown schematically in Fig. 5.26. In this configuration the electric field lines will not need to be kept far from the edge but will be controlled by what is now an active electrode. The advantages of this approach are the following:

1. The surface leakage current, usually present after the device has been saw-cut, is suppressed.
2. The dead area which would be otherwise needed for guard rings and to control the bulge of the electric field in planar detectors is reduced to no more than a few microns.
3. There should be no insensitive volume in the central region.
4. Fewer fabrication steps are needed.

The disadvantages are the loss of speed and radiation tolerance.

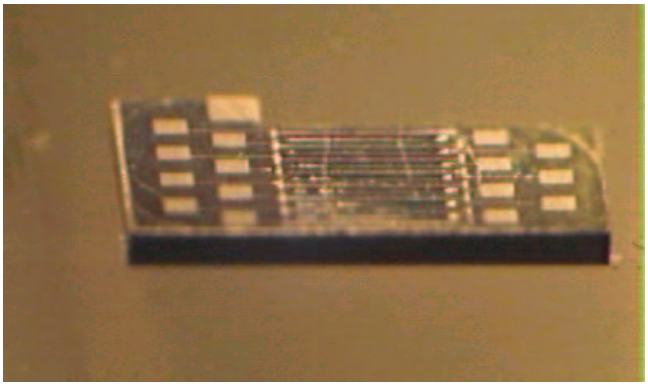

Figure 5.25: Example of an "active-edge" 3D detector (pure 3D) where the edge electrode is visible at the front of the picture

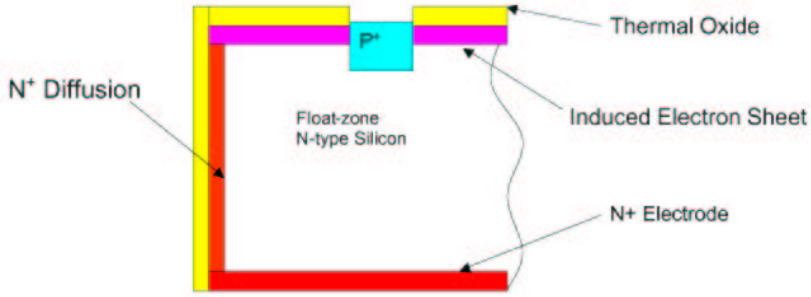

Figure 5.26: Schematic representation of a planar/3D device (planar interior and 3D active edges). In this configuration the free edges of the detector are deep-etched and an n^+ dopant diffused in. Then a final dicing etch separates the sensors

5.4.2 Testbeam Results in 2003

3D and planar-3D detectors, both provided with active edges, have been fabricated at the Stanford Nanofabrication Facility (SNF), USA. In 2003 they have been tested with X-rays at the Advanced Light Source (ALS) at the Lawrence Berkely Laboratory, Berkeley, California, and with a high-energy particle beam at CERN SPS.

X-ray Tests at the Advanced Light Source, Berkeley

An X-ray micro-beam was used to characterise the detector response with high precision. The beam had a width of 6-10 μm, an energy of 12 keV and an intensity of $\sim 10^9$ particles/s. The readout was performed in current mode. Fig. 5.27 shows a scan of a part of the surface of a 3D device. The sensor, made of n-type high-resistivity silicon with n-type active edges, had 16 rows – parallel to the x-axis – each having 38 p^+ signal electrodes spaced by 100 μm. They had an active edge of n^+ electrodes surrounding the four edges of the device. Rows of n^+ electrodes were between the p^+ rows, separated in y from them by 100 μm. Each n^+ electrode was midway in x between the p^+ electrodes. Neglecting the end under the bonding pads, each sensor had a total width in y of 3.195 mm, a length of 3.948 mm, and a thickness of 180 μm. All the features of the detector are clearly visible in the scan: the sharp edge signal turn-on and the response to the low-energy X-rays across the centre of the device. Due to the fine beam dimensions it is possible to resolve the expected reduced response of the central part of the electrodes. With the present

technology, the diameter of the electrodes is about 8 % of the thickness of the substrate. This corresponds to about 2 % of the total detector area which would not be fully sensitive to particles impinging along the electrode itself. For detection of minimum ionising particles this should not represent a limitation, since a slight tilt of the detector with respect to the impinging particle direction would be enough to guarantee energy deposition in the active volume. However, the implementation of new state-of-the-art instrumentation at SNF, which took place this year, should provide a better processing performance of fabrication runs in 2004.

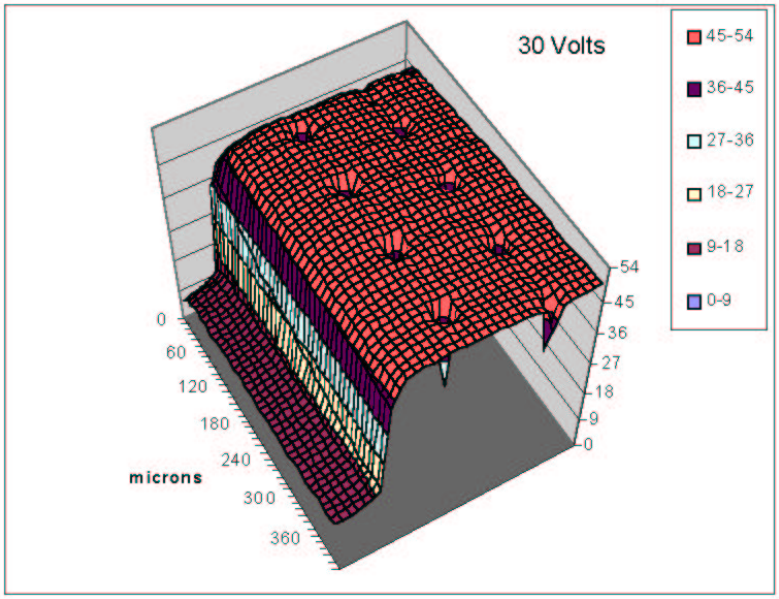

Figure 5.27: Scan of a part of a 3D detector performed with a 12 keV, ∼ 6 µm wide, X-ray beam. The edge signal turn-on is visible on the left. The vertical scale represents the current pulse height in arbitrary units (also colour-coded), and the distance between electrodes is 100 µm

Fig. 5.28 shows a detail of the edge response of the 3D device under test. The $10-90\,\%$ transition distance is measured to be $(6 \pm 2)\,\mu$m.

The I-V curve of both edge and central rows of electrodes shorted with aluminium strips is shown in Fig. 5.29. The reverse leakage current is the same for all the measured electrodes and is limited to an average of 7 nA at 80 V bias. Full depletion is reached at about 30 V.

Planar/3D sensors 100 µm thick and with 150 µm planar strip pitch were also tested at the Berkeley ALS. Fig. 5.30 shows a picture of one of the detectors with clearly visible readout pads and wire bonds to the readout electronics.

Fig. 5.31 shows the signal on the first and the second channel recorded during the 12 keV X-ray beam scan. The mid point between the two strips is determined by the strip signals' crossing point. The sensor is mounted on a translation stage with 0.2 µm step size and 0.1 µm accuracy. The distance between the sensor inter-strip mid point to the physical edge is known from lithography to an accuracy of 1 µm, and can be compared with the stage shift from the point of equal signal size to the corresponding drop-off position at the edge. The width of the dead edge, determined from that difference, is $(5 \pm 2)\,\mu$m. The I-V curve of this detector is shown in Fig. 5.32. At 220 V, the leakage current of the full device, including the edge, is measured to be 6 nA. This demonstrates that the combination of etching and doping implantation correctly controls the electric field lines and can suppress the generation of surface leakage current in planar detectors. The radiation hardness of this type of devices has not been tested at present. While the radiation-induced bulk leakge current and the increase of the full depletion voltage should follow well-proven laws [18], the active edge behaviour after heavy irradiation is still to be studied; the overall radiation hardness is expected to be similar or higher to the one of standard planar devices with multiple guard ring structures.

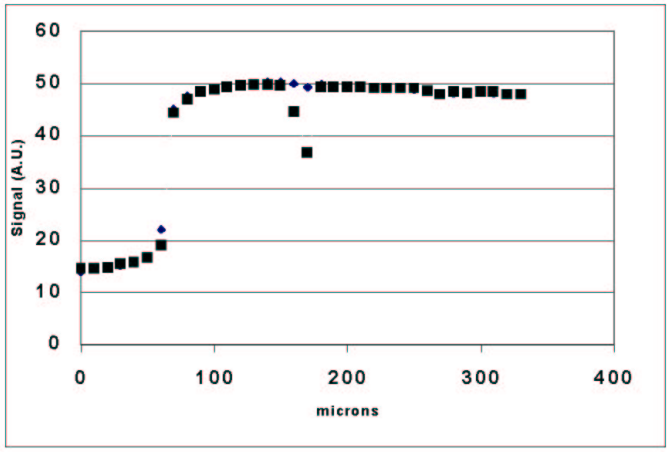

Figure 5.28: Detail of the edge response of the 3D detector. The 10−90 % transition distance is measured to be $(6 \pm 2)\,\mu m$*. The dip between 100 and 200* μm *occurs when the beam cuts across an electrode. The 12 keV X-ray beam was scanned with 0.2* μm *steps and had a dimension of roughly 6* μm

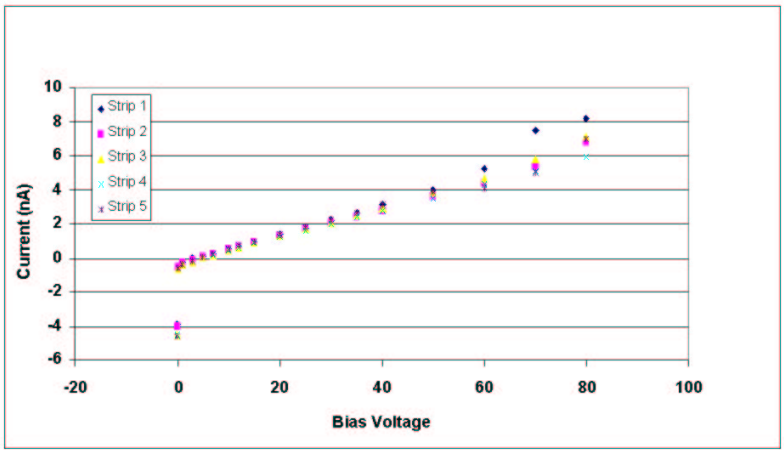

Figure 5.29: I-V response of the edge (strip 1) and some of the central strips of the 3D detector under study. The average leakage current at 80 V is 7 nA. For these devices full depletion is reached at 30 V

The SPS Testbeam Measurements

The aim of the muon testbeam experiment in the SPS beamline X5 in summer 2003 was to test the operation and edgelessness of 3D detectors in a high-energy particle beam. The system efficiency was measured with reference to a beam telescope (Fig. 5.33) consisting of six silicon microstrip detectors with a strip pitch of 50 μm and a typical hit cluster size between 2 and 3 resulting in a resolution of about 8 μm per plane if the charge sharing is taken advantage of. Four of these planes had their strip horizontally oriented like the 3D prototype detectors in the focal plane of the telescope. Hence the vertical track intercept at the 3D detector was predicted with a precision of about 4 μm. The second (horizontal) coordinate of the tracks was measured by the remaining two telescope planes whose strips were oriented vertically.

The 3D devices under study were the ones already tested at the ALS as discussed above. Three of these detectors were bonded to ATLAS SCTA128VG readout electronics chips [20] developed for the SCT silicon tracker. Details of the hybrid boards carrying the detectors and the front-end chips are shown in Fig. 5.34 together with an overview photograph of the detector boxes aligned in the centre of the reference

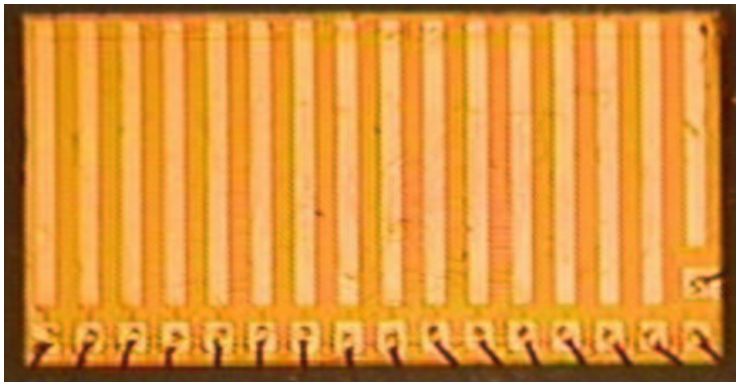

Figure 5.30: Picture of one of the planar/3D (planar inside, 3D edges) devices tested at the ALS (Berkeley) with a 12 keV X-ray beam

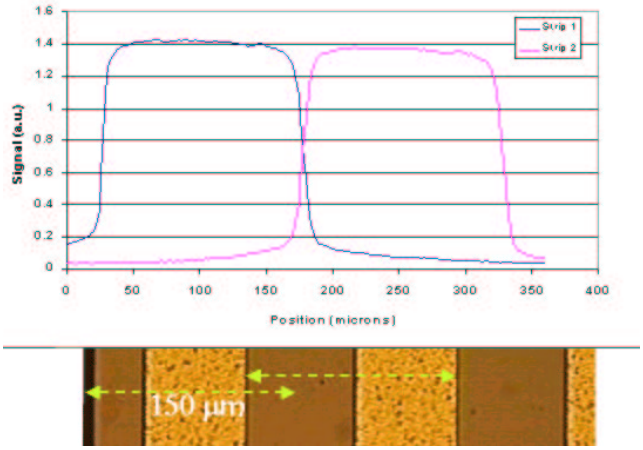

Figure 5.31: Signal of the first and second channels of a planar/3D device where the midpoint between the two strips is clearly determined. This point is used to measure the sensitive region of the edge strip. The dead edge is in this case $(5 \pm 2)\,\mu m$

telescope.

The analogue SCTA circuit has 128 channels (16 of which were used) of front-end amplifiers with an rms noise level of 720 electrons, a peaking time of 20 ns, a 128-cell × 128-channel analogue pipeline, and a multiplexed output. In its intended application, strip detector readout for the LHC, the instantaneous pulse height from each amplifier was to be stored in successive cells every 25 ns, i.e. the beam-crossing interval, and read out if a trigger was received several μs later. Here, with particles coming in at random times with respect to the 40 MHz provided by SEQSI sequencer modules, a trigger signal defined by a 1 × 1 cm^2 scintillator is used to start a time-to-digital converter (TDC), and a signal that is time-coherent with the clock is used to stop it. The content of a pre-selected cell for each channel of the analogue pipeline is read out to a SIROCCO Flash-ADC. The time window within which a trigger pulse had to arrive in order to coincide with the peak of the corresponding 3D detector pulse needed careful adjustment, which made the system susceptible to timing problems. Fig. 5.35 (left) shows the typical dependence of the signal-to-noise ratio (and hence of the sampled pulse height) on the TDC timing. Only events occurring between the two TDC cuts drawn were in-time and could be accepted for the analysis.

In order to avoid radio frequency pick-up and light-induced noise, a light-tight metal box was constructed to cover the 3D detectors and to ensure a proper ground definition. Since no cooling was available the temperature rose considerably above 20° in the course of long data taking. While a labo-

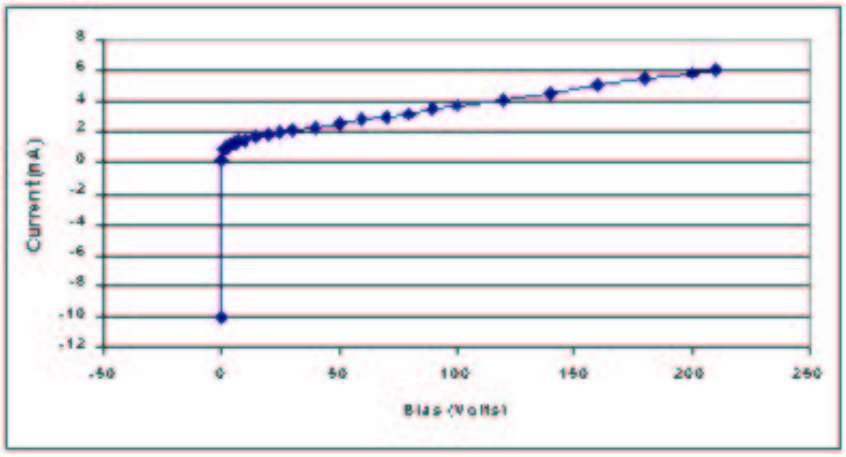

Figure 5.32: I-V curve of the planar/3D detector tested with the 12 keV X-ray beam at the ALS. The total leakage current at 220 V (including the edge) is measured to be 6 nA

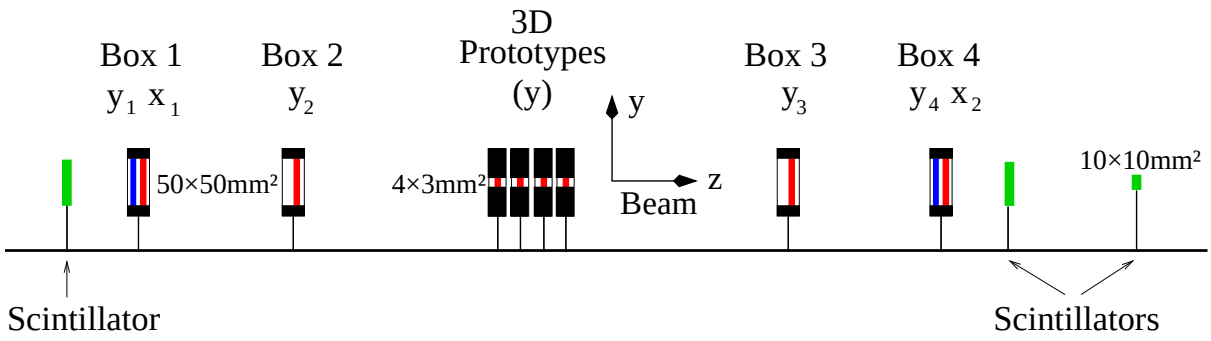

Figure 5.33: Schematic drawing of the X5 testbeam layout in August/September 2003. The boxes 1-4 constitute the silicon reference telescope "ODYSSEUS" [19] with four detectors measuring the y projection and two detectors measuring x. The 3D detectors measure y coordinate

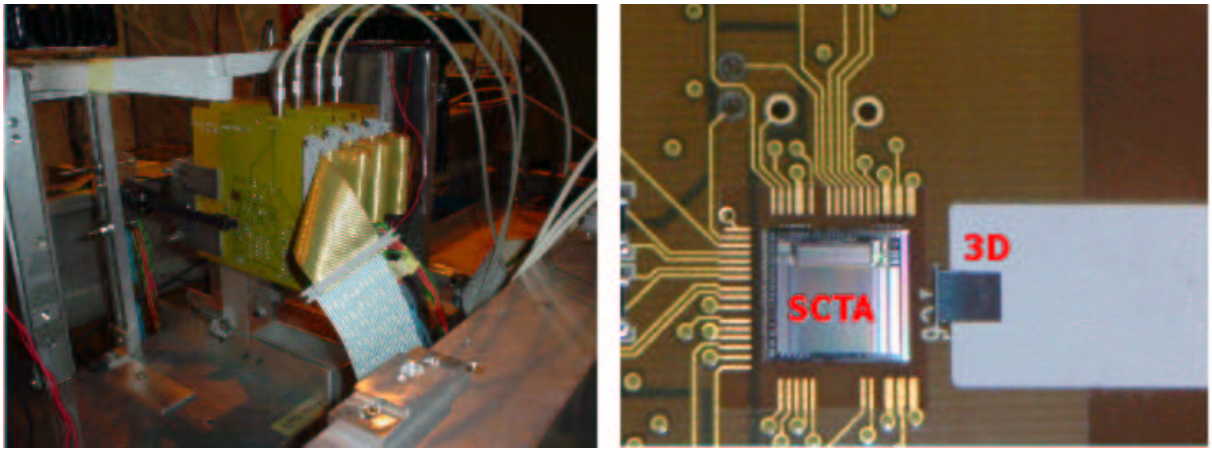

Figure 5.34: Left: the 3D detector boxes in the focus of the beam telescope. Right: the hybrid board carrying the 3D detector and the SCTA readout chip

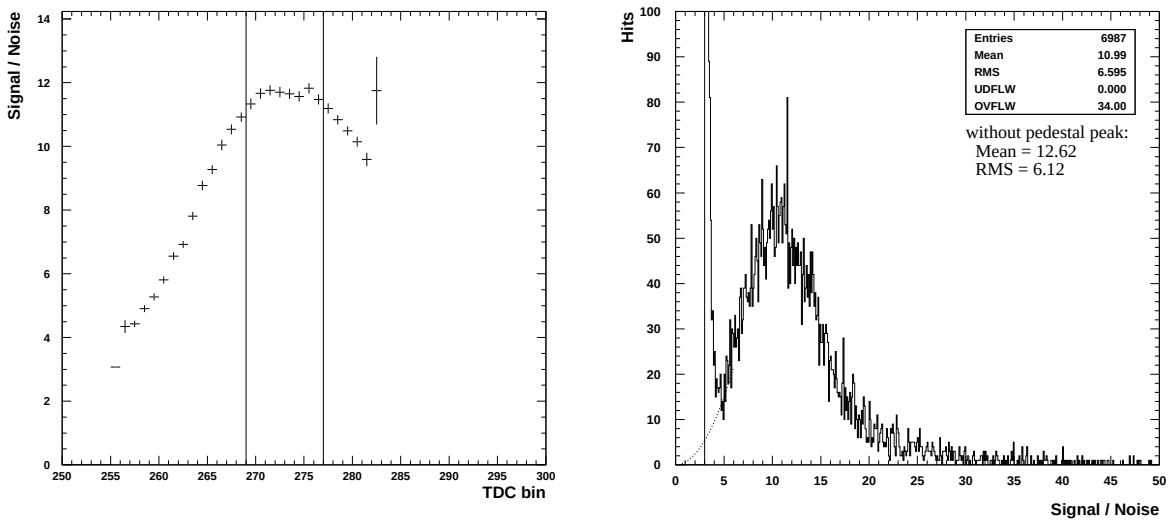

Figure 5.35: Left: Signal-to-noise of a 3D prototype detector as a function of the trigger time with respect to the internal clock of the 3D readout electronics (with a constant offset). The cuts excluding out-of-time events are displayed as vertical lines. Right: Signal-to-noise distribution of the 3D detector for events within the time window shown in the left figure. A pedestal cut $S/N > 3$ was applied. The spike near 3 is the tail of the pedestal peak. The dotted line drawn for $S/N < 5$ approximately continues the Landau distribution to 0 and serves for a rough estimate of the expected detector efficiency

ratory test with β-particles from a ^{90}Sr source had yielded a mean signal-to-noise ratio of S/N = 14:1, the corresponding result from the muon beam measurement was only 12:1 (Fig. 5.35, right), which can be explained partly with the leakage current induced by the higher temperature, and partly with noise caused by problems from the data transmission in 30 m long cables that were not optimised for fast signals. The theoretically expected signal for 180 μm thick silicon is 14400 electrons, corresponding to S/N = 14.6:1 for the nominal electronics noise of 986 electrons, including the detector and the bonding wires input capacitances. The final detector will be 300 μm thick; hence the expected S/N will be about 23.

The correlation between the predicted y-coordinates of tracks at 3D detector plane 3 and the hit positions reconstructed from the 3D detector is shown in Fig. 5.36 (left). The residuals $y(3D) - y(STEL)$ are distributed box-like (Fig. 5.36, right) with a width well in agreement with the 3D detectors' strip pitch of 200 μm. The small quadratic difference between the distribution's rms and the expected value of 200 μm/$\sqrt{12}$ comes from the small but finite resolution of the telescope.

Using the telescope predictions for both track projections, the two-dimensional efficiency maps of the 3D detectors were recorded. The example plot in Fig. 5.37 renders well the detector shape. It shows the track points (x, y) at the z-position of the 3D detector predicted by the reference telescope under the condition that the 3D detector itself has also had a hit.

The normalised efficiency map is obtained by dividing this two-dimensional 3D detector hit map by the hit map of the telescope alone.

To simplify the quantification and visualisation of the efficiency, an x-band well within the plateau region was projected upon the y-axis (Fig. 5.38) and fitted with the function

$$\eta(y) = b + \frac{1}{4}\eta_0 \left[1 + \mathrm{erf}\left(\frac{y - y_l}{\sigma_l \sqrt{2}}\right)\right] \left[1 + \mathrm{erf}\left(\frac{y_u - y}{\sigma_u \sqrt{2}}\right)\right] \tag{5.2}$$

describing a box distribution with Gaussian smearing. The results for one of the detectors are listed in Table 5.2.

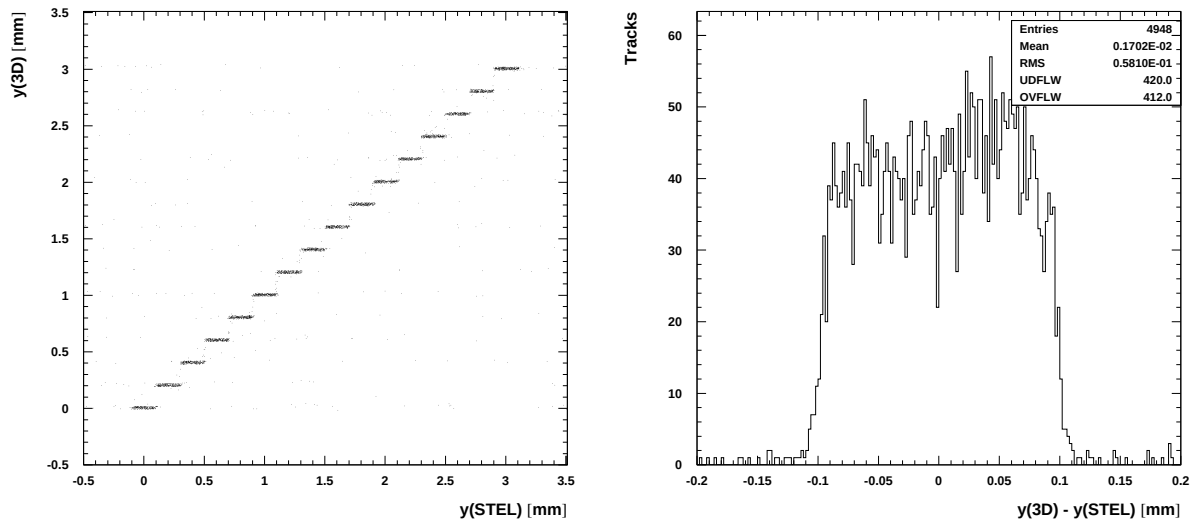

Figure 5.36: Left: Correlation between the hit positions $y(3D)$ measured by the 3D detector and the predicted track position $y(STEL)$ in this plane (detector 3). Right: Residuals $y(3D) - y(STEL)$. The box distribution resolves well the strip pitch of 200 µm. As expected, the rms is close to 200 µm/$\sqrt{12}$=57.7 µm

Parameter	Fit result	Expectation
Width $y_u - y_l$	(3.203 ± 0.004) mm	3.195 mm
Lower edge: σ_l	$(4.3 \pm 4.2)\,\mu$m	–
10 % – 90 % interval	$(11.0 \pm 10.8)\,\mu$m	–
Upper edge: σ_u	$(9.7 \pm 3.0)\,\mu$m	–
10 % – 90 % interval	$(25 \pm 8)\,\mu$m	–
Plateau η_0	(80.8 ± 0.6) %	–
Background b	(1.8 ± 0.1) %	–
χ^2/ndof	1183 / 994	–

Table 5.2: Results of the efficiency fit (Eqn. 5.2) shown in Fig. 5.38

The table demonstrates that the sensor width known from the photolithography process is reproduced by the efficiency curve within two statistical standard deviations, which confirms the "edgeless" nature of the 3D detector technology. This property is further underlined by the steep efficiency rise from 10 % to 90 % within only $(18 \pm 7)\,\mu$m on average. The measured plateau efficiency of 81% (plane 3) however is surprisingly low. The second 3D detector system used in this study (plane 1) had a very similar efficiency of 78 %. Given the signal-to-noise distribution shown in Fig. 5.35 (right), one would expect a much higher efficiency. An expectation can be estimated by continuing the measured Landau distribution $\Lambda_{meas}(S/N)$ from the waist at $S/N = 5$ back to 0 and taking the ratio

$$\eta(\text{from S/N}) \approx \frac{\int_5^{50} \Lambda_{meas}(x)\,dx}{\int_5^{50} \Lambda_{meas}(x)\,dx + \int_0^5 \Lambda_{cont}(x)\,dx} \tag{5.3}$$

which amounts to 96 % for detector 3 and 98 % for detector 1. To the latter however a correction factor of 0.97 has to be applied because half of one strip was damaged, which results in an expected efficiency of 95 %.

Considering the geometry of 3D detectors immediately suggests the electrode pillars as potential culprits. However, this idea does not withstand a simple quantitative consideration: the 3D detectors

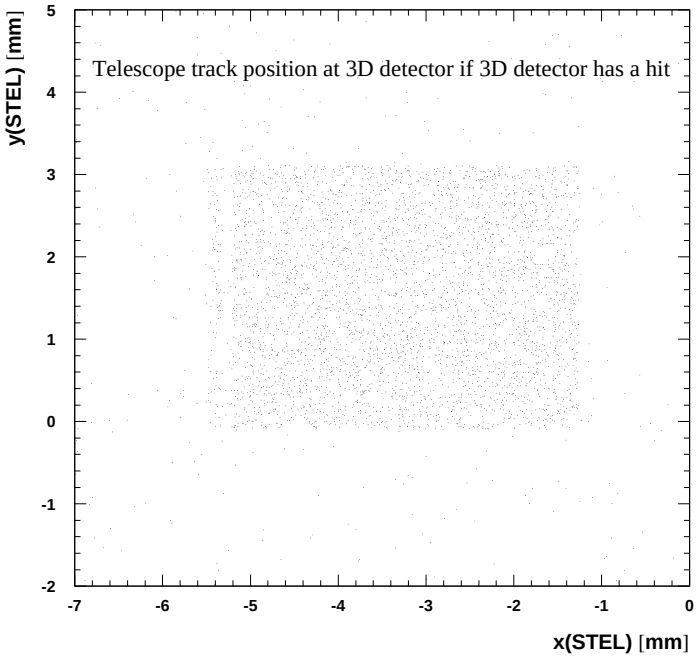

Figure 5.37: Two-dimensional efficiency map of one of the 3D detectors (plane 3). Whenever the telescope predicts a track and the 3D detector has a hit, a point is plotted at the (x, y) coordinates given by the track at the z-position of the 3D detector. The inefficient band near the lower x edge lies under the bonding pads. The details of this structure depend on the complicated field configuration in that region and is currently under investigation. The sensitive edges are the upper, lower and right-hand ones

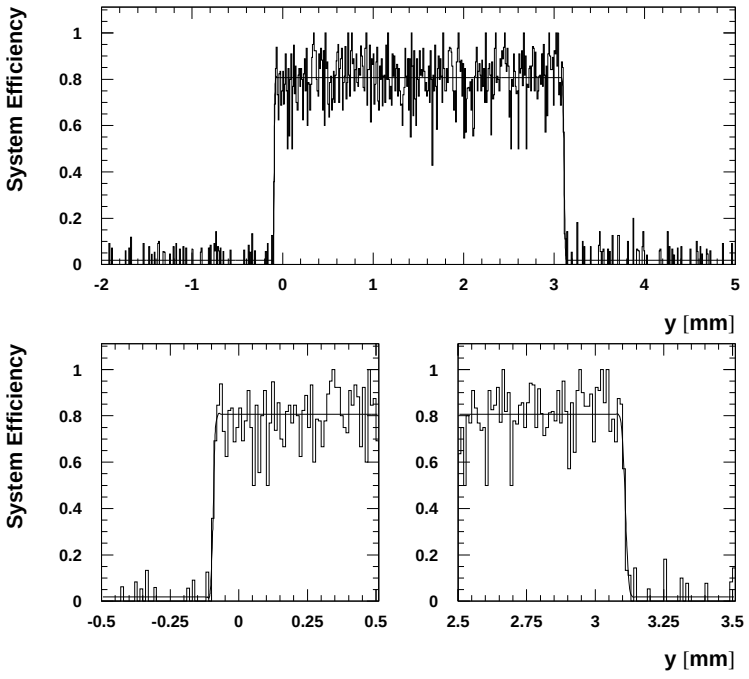

Figure 5.38: The projection of the band $-5\,\mathrm{mm} < x < -1.5\,\mathrm{mm}$ in Fig. 5.37 on the y-axis yields the vertical efficiency curve. The fit superimposed is explained in the text. Its parameters are given in Table 5.2. The efficiency obtained with this analysis characterises the full system comprising the 3D detector, its read-out electronics and the DAQ

employed for this test, consist of rectangular cells, each with an area of $100 \times 200\ \mu\text{m}^2$. Each cell has two electrodes with a radius of $7.5\,\mu$m. Hence a fraction of 1.8 % of the cell area is occupied by electrodes. Assuming that the electrodes are totally insensitive and the particles are passing through the detector perpendicularly to its surface, a sensor efficiency of about 98% is expected.

To shed some more light on this efficiency puzzle, efficiency correlations between two different detectors were investigated. It has to be kept in mind that the efficiencies determined above do not characterise the isolated detectors but the entire system including the read-out electronics whose problematic timing with respect to the rest of the setup (in particular the telescope) was already mentioned. Finding a correlation between inefficient events in both planes would hint at a fault in the data-processing chain.

$P(1) = 78\,\%$ and $P(3) = 81\,\%$ are the efficiencies of detectors 1 and 3 respectively, as they were determined by the fits discussed above. If the two detectors are entirely independent, their combined hit probabilities factorise. Four cases are distinguished:

1. No hit in both detectors: $P(\bar{1} \times \bar{3}) \stackrel{\text{indep}}{=} P(\bar{1}) \cdot P(\bar{3})$.
2. No hit in D1 but a hit in D3: $P(\bar{1} \times 3) \stackrel{\text{indep}}{=} P(\bar{1}) \cdot P(3)$.
3. A hit in D1 but no hit in D3: $P(1 \times \bar{3}) \stackrel{\text{indep}}{=} P(1) \cdot P(\bar{3})$.
4. Hits in both detectors: $P(1 \times 3) \stackrel{\text{indep}}{=} P(1) \cdot P(3)$.

Owing to a transverse misalignment the geometrical overlap between the two detectors was rather poor, limiting the statistics of this test to 752 out of the about 5000 tracks recorded for this particular run configuration. Fig. 5.39 shows the calculated hit statistics (dashed histogram) and compares it with the actual observation (continuous histogram).

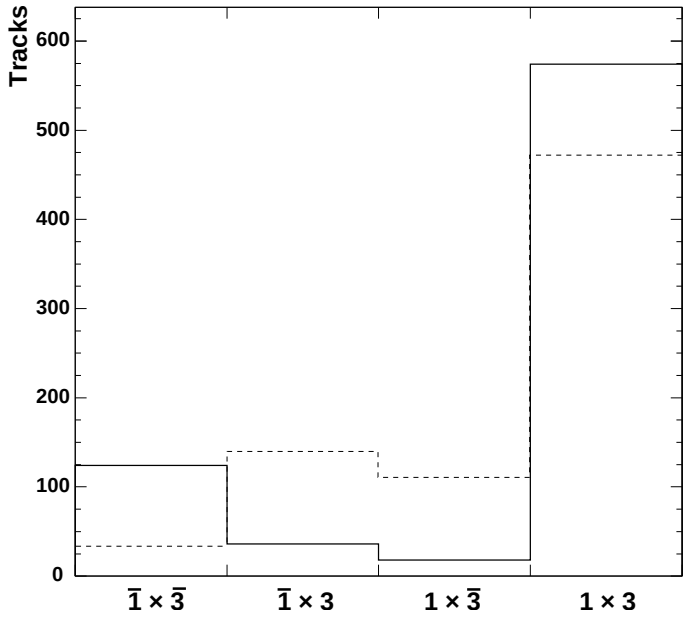

Figure 5.39: Hit correlations between 3D detector planes 1 and 3. The continuous histogram shows how often tracks (predicted by the telescope) passing through the sensitive areas of both detectors 1 and 3 created hits in neither plane, in only one plane or in both planes. The dashed histogram shows the hit statistics expected if the responses of the two planes are assumed to be independent and if the efficiencies 78 % (det. 1) and 81 % (det. 3) obtained from the plateau fits are used

The numerical results are given in Table 5.3. The statistical significance of the discrepancy between observation and expectation is evident.

Combined Probability	Predicted assuming independence	Measured
$P(\bar{1} \times \bar{3})$	$(4.2 \pm 0.8)\,\%$	$(16.5 \pm 1.2)\,\%$
$P(\bar{1} \times 3)$	$(14.8 \pm 1.4)\,\%$	$(4.8 \pm 0.6)\,\%$
$P(1 \times \bar{3})$	$(18.2 \pm 1.6)\,\%$	$(2.4 \pm 0.4)\,\%$
$P(1 \times 3)$	$(62.8 \pm 2.9)\,\%$	$(76.3 \pm 1.5)\,\%$

Table 5.3: Combined hit probabilities as calculated from the observed system efficiencies and the values from direct observation

There seems to be a strong correlation between the efficiencies of detectors 1 and 3. From the values shown in Table 5.3 one can infer that a missed hit in plane 3 entails a probability of $16.5/(16.5{+}2.4) = 87\%$ for missing the hit in plane 1 as well. For independent systems, the probability of a miss in plane 1, given – or not given – a miss in plane 3, is just the measured miss rate in plane 1, i.e. $16.5\,\% + 4.8\,\% = 21.3\,\%$. Analogously, 78% of the tracks missed by plane 1 are also missed by plane 3, in contrast to the prediction of 18.9 %.

Apparently, the observed system efficiencies include a common factor η_e pertaining to read-out or DAQ of the 3D system. With this model the combined hit probabilities can be written as

$$
\begin{aligned}
P(\bar{1} \times \bar{3}) &= P(\bar{1}) \cdot P(\bar{3}) \cdot \eta_e + (1 - \eta_e) && (5.4)\\
P(\bar{1} \times 3) &= P(\bar{1}) \cdot P(3) \cdot \eta_e && (5.5)\\
P(1 \times \bar{3}) &= P(1) \cdot P(\bar{3}) \cdot \eta_e && (5.6)\\
P(1 \times 3) &= P(1) \cdot P(3) \cdot \eta_e && (5.7)\\
& && (5.8)
\end{aligned}
$$

Resolving this equation system yields the bare efficiencies

$$P(1) = 94\,\%, \quad P(3) = 97\,\%, \quad \eta_e = 84\,\%\,, \tag{5.9}$$

which are not far from the expectations. In particular, these numbers agree well with the estimates from the signal-to-noise distributions.

In conclusion: the tests performed so far on 3D detectors demonstrate that these devices can track minimum ionizing particles with very high efficiency (98 %) at $\leq 10\,\mu$m from their physical edge. These results, together with their radiation tolerance and signal speed characteristics, make 3D detectors strong candidates for the TOTEM Roman Pot detectors. Planar/3D (Planar with 3D edges) devices also demonstrated similar edge response as 3D detectors. However, more tests are still required to prove their performance after irradiation and with high energy particle beams. Both technologies are being processed to fulfil the TOTEM Roman Pot design and will be tested in high energy particle beams in 2004.

References

[1] N. V. Mokhov et al., 'Accerator related backgrounds in the LHC forward detectors', Proceedings of the Particle Accelerator Conference PAC 2003, Paper ID TPPBO63.

[2] http://www–ap.fnal.gov/MARS

[3] Z. Li et al., 'Electrical and TCT characterization of edgeless silicon detector diced with different Methods.', IEEE NSS Proc., San Diego, Nov. 2001.

[4] V. Avati et al., 'First test of cold edgeless microstrip detectors'. Conf. Proc. of 9^{th} Pisa Meeting on Advanced Detectors - Frontier Detectors For Frontier Physics, May 2003, La Biodola, Isola d'Elba, Italy. NIM A, to be published.

[5] V. G. Palmieri et al., Nucl. Instr. and Meth. A 413 (1998) 475.

[6] K. Borer, et al., Nucl. Instr. and Meth. A 440 (2000) 5.

[7] G. Ruggiero et al., 'Silicon detectors irradiated "in situ" at cryogenic temperatures', Nucl. Instr. and Meth. A 476 (2002) 583-587.

[8] I. Eremin, Private Communication.

[9] L. Jones. 'APV25-S1 User Guide Version 2.2'. http://www.ins.clrc.ac.uk/INS/Electronic_Systems/Microelectronics_Design/Projects/High_Energy_Physics/CMS/APV25-S1/index.html.

[10] R. Szczygiel and J. Kaplon "The VFAT-128 Test Chip User Guide", CERN (2003).

[11] S. Parker, C. Kenney and J. Segal: 3D - A proposed new architecture for solid state radiation detectors, Nucl. Instr. Meth. in Phys. Res. A 395(1997) 328-343

[12] C. Kenney, S. Parker and E. Walckiers: Results from 3D silicon sensors with wall electrodes: near-cell-edge sensitivity measurements as a preview of active-edges sensors, IEEE Trans Nucl Scie Vol.48 n 6 Dec 2001, 2405-2410.

[13] C. Kenney et al: Silicon deetectors with 3D electrode arrays fabrication and initial test results, IEEE Trans Nucl Scie Vol.46 n 4 August 1999, 1224-1236.

[14] C. Kenney et al: Observation of beta and x-rays with 3D architecture silicon microstrip sensors, IEEE Trans Nucl Scie Vol.48 n 2 April 2001, 189-193.

[15] S. Parker and C. Kenney: Performance of 3D architecture silicon sensors after intense proton irradiation, IEEE Trans Nucl Scie Vol.48 N 5 Oct 2001, 1629-1658.

[16] C. DaVià and S. Watts: Can silicon detectors survive beyond 10^{15} n/cm^2?. Nucl. Instr. Meth. in Phys. Res. A501(2003) 138-145.

[17] C. DaVià et al: Advances in silicon detectors for particle tracking in extreme radiation environments, Nucl. Instr. Meth. in Phy. Res. A509(2003) 86-91.

[18] G. Lindstrom et al: The ROSE/RD48 Collaboration. Nucl. Instr. Meth. A466 (2001) 308.

[19] M. Deile et al.: ODYSSEUS: A Silicon Telescope for Test Beam Experiments, ATLAS Communication ATL-COM-MUON-99-015.

[20] J. Kaplon et al: Progress in development of the analogue read-out chip for silicon strip detector modules for the LHC experiment, Proc of the 7th Workshop on Electronics for the LHC experiments, Stockholm, Sweden, 10-14 Sept 2001, CERN/LHCC/ 2001 -034, Geneva 22 October 2001.

6 The Level-1 Proton Trigger

The Roman Pot detectors have two purposes. Firstly a precise tracking of single protons has to be performed. The second task is to provide a fast level-1 trigger decision and timing information based on leading protons. Since the TOTEM data acquisition system has to be synchronised with its CMS counterpart, the event selection has to be done within a tight latency time. Hence it will be limited to the separation of a general event topology from the most dominant background processes in order to reduce the event rate to the level of at most 100 kHz as accepted by the DAQ. Refined logical decisions need to be reserved for later trigger stages.

This section discusses the requirements for the level-1 trigger system and options for its realisation.

6.1 Physics Processes Targeted

The task of the first trigger level is the identification of events with isolated protons on one or both sides of the interaction point.

- Elastic scattering events have two collinear proton tracks, one on each side (arm) of the interaction point and no activity in the central detectors.
- Central diffractive events ("Double Pomeron exchange") are also characterised by one proton track on each side of the interaction point. However, they are non-collinear and can have different momenta. In addition, there is activity in the central detectors.
- In single diffractive events there is only one proton track on one side of the interaction point. In addition, particles from the dissociated proton are seen by the central T1 or T2 detectors on the other side.

Two running scenarios are foreseen:

1. $k_1 = 43$ bunches, $N_1 = 0.29 \times 10^{11}$ protons per bunch and normalised emittance $\varepsilon_{n,1} = 1\,\mu\text{m}\,\text{rad}$ for a luminosity $\mathcal{L}_1 = 1.6 \times 10^{28}\text{cm}^{-2}\text{s}^{-1}$.
2. $k_2 = 156$ bunches, $N_2 = 1.15 \times 10^{11}$ protons per bunch and normalised emittance $\varepsilon_{n,2} = 3.75\,\mu\text{m}\,\text{rad}$ for a luminosity $\mathcal{L}_2 = 2.4 \times 10^{29}\text{cm}^{-2}\text{s}^{-1}$.

In both cases $\beta^* = 1540\,\text{m}$.

The calculated trigger rates for the event classes given above and for the two running conditions are listed at the end of the chapter in Table 6.5 together with background estimates.

6.2 Trigger Strategy

6.2.1 Trigger Detector Layout

For the Roman Pot detector configuration two options are under study:

- Use the same detectors for the trigger and for tracking.
- Equip the Roman Pots with separate tracking and trigger detectors.

The choice will mainly be a function of the front-end electronics which have to meet different conditions for tracking and triggering (Chapter 7.9.2). While for precision tracking an analog output with pulse height information is advantageous, fast triggering requires a digital output. If a front-end chip with both functionalities can be designed, then the first option will be favoured because it avoids additional detector development and makes more planes available for both tasks.

In the rest of this chapter we shall assume that each Roman Pot will house three dedicated trigger detectors for which a suitable coincidence condition will be defined.

To achieve an optimal background rejection for a limited total number of channels, the detectors will be segmented in strips rather than pixels (see Section 6.4.2). It was found to be adequate to divide the detectors into 32 strips of 1.056 mm width. All trigger planes will have their strips oriented in the same direction. Given that the precision tracking detectors will have their strips oriented at $\pm 45^{\circ}$ to the beam, it is advantageous to have the trigger strips perpendicular or parallel to the beam, thus obtaining a measurement in a third projection. The criterion of equal illumination of all strips then leads to the choice of strips perpendicular to the beam. This orientation also facilitates the geometrical arrangement of the read-out electronics and cables in the Roman Pots.

The choice of technology for separate trigger detectors has not been made yet. One manifest solution minimising additional detector development is to use the same technology as for the precision tracking detectors: edgeless planar silicon detectors (Section 5.3) or 3D silicon (Section 5.4). The coarser segmentation for the trigger detectors can be obtained by combining 16 basic strips of 66 μm width to 1.056 mm wide groups at the logics level, i.e. after the preamplifiers. A dedicated front-end chip is being designed (Section 7.7.2) which not only fulfills the trigger-specific fast tasks based on the coarse segmentation, but also keeps digital hit information from the basic 66 μm strips.

A potential problem with metallised silicon strip detectors very close to the beam may arise from RF coupling. This issue needs to be studied in future test beams. If it turns out to be serious, a fall-back solution for the trigger detector technology would be scintillating fibers of about 1 mm diameter. Detector development for scintillating fibers in Roman Pots is being pursued by the ATLAS collaboration.

6.2.2 Local Decisions per Detector and per Roman Pot

In each Roman Pot a preselection of events will be made:

- Events with a hit multiplicity exceeding an adjustable limit (of the order 3) in each trigger plane of a Roman Pot will be discarded. This cut reduces shower events from beam-gas scattering (see Section 6.4.3).

- Events with a pattern of tracks almost parallel to the beam are selected with a collinear coincidence requirement as shown in Fig. 6.1. To avoid inefficiencies at the strip boundaries, the coincidence between detector planes requires hits either in the corresponding segments or in the direct neighbours. Furthermore, small detector inefficiencies are taken into account by requiring hits in only 2 out of all 3 detector planes. This concept also allows to monitor the efficiencies of the single detector planes (see Section 6.3.3). The coincidence condition reads:

$$\text{(RP, strip i)} = \text{(D1, i)} \times \sum_{j=i-1}^{i+1} \text{(D2, j)} + \text{(D1, i)} \times \sum_{j=i-1}^{i+1} \text{(D3, j)} + \text{(D2, i)} \times \sum_{j=i-1}^{i+1} \text{(D3, j)} \qquad (6.1)$$

- If instead of 3 dedicated trigger planes the 6 tracking planes can be used for triggering, the coincidence requirement will be (2 out of 3 detectors along $+45^{\circ}$) $\times$ (2 out of 3 detectors along -45°).

6.2.3 Decisions per Detector Arm

The track candidates given by the individual Roman Pots on one side of the interaction point are taken into collinear coincidence with an angular cut, defining a track in the respective "arm" of the experiment. To decide how tight the angular cut can be without discarding physics events, we have to consider the

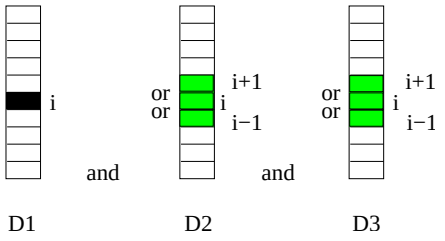

Figure 6.1: Collinear coincidence requirement for three trigger detectors in a Roman Pot. For each hit in one plane, the other planes must have a hit in either the same strip or in one of its neighbours. Out of the three planes only two are required to have a hit

track slope in the projection perpendicular to the strip direction. In the most general case with diffraction it is given by

$$\frac{dx}{dz} = \frac{dL_x}{dz}\frac{\sqrt{t}}{p}\cos\phi + \frac{dv_x}{dz}x_0 + \frac{dD_x}{dz}\xi + \frac{dL_x}{dz}\theta_{\text{beam}}\cos\phi_{\text{beam}} \tag{6.2}$$

A safe upper limit for x' is obtained by evaluating it at the limiting values $-t = 1\,\text{GeV}^2$, $\phi = 0$, $\xi = 0.1$. For the slopes of the optical functions, the values $L'_x = 2.55$, $v'_x = 10.2\times10^{-6}\,\text{mm}^{-1}$ and $D'_x = 1.98\times10^{-3}$ were used. The displacement of the interaction point and the beam angle were assumed to be four times their standard deviations, i.e. $x_0 = 4\sigma(x_0) = 4\times0.45\,\text{mm}$ and $\theta_{\text{beam}} = 4\sigma(\theta) \le 4\times0.57\,\mu\text{rad}$. This results in $|x'| < 586\,\mu\text{rad}$. Within the 4 m distance between the two Roman Pots of a station, x can change by $4\times586\,\mu\text{m} = 2.33\,\text{mm}$ which is slightly bigger than twice the strip pitch of 1.056 mm. Hence, for the collinear coincidence between the two Roman Pots it is not sufficient to include the immediate neighbours like in Fig. 6.1. The coincidence road has to be extended to the third neighbours:

$$\text{(arm, strip i)} = \text{(RP1, i)} \times \sum_{j=i-3}^{i+3} \text{(RP2, j)} \tag{6.3}$$

To have some flexibility in the angular selection, the road width in the coincidence logics will be programmable.

6.2.4 Combined Decision

At the interaction point the single arm triggers are combined with each other and with the information from the central trackers T1 and T2. The resulting global trigger then has to be distributed to all subdetectors and CMS.

Elastic Trigger:

The basic trigger criterion identifying elastic events is:

$$\text{Elastic Trigger} = \text{(left arm)} \times \text{(right arm)} \times \overline{\text{(T1 or T2)}}. \tag{6.4}$$

To reduce background, an additional collinearity cut on the tracks in the two arms is applied. In the ideal case with perfect resolution, each hit in an upper Roman Pot in one arm must have a matching hit in the corresponding strip in the lower Roman Pot in the other arm. Although the intrinsic detector resolution is much better than the strip width of 1.056 mm, strip edge effects and deviations due to misalignments and the uncertainties of interaction point and beam angle have to be allowed for by loosening the collinearity cut. The x-coordinates measured by the right and left Roman Pots are given by

$$x_r = L_x(\theta\cos\phi + \theta_{\text{beam,r}}\cos\phi_{\text{beam,r}}) + v_x x_0 + \delta x_{RPr} + \delta x_{res,r} \tag{6.5}$$

$$x_l = -L_x(\theta\cos\phi + \theta_{\text{beam,l}}\cos\phi_{\text{beam,l}}) + v_x x_0 + \delta x_{RPl} + \delta x_{res,l}\,, \tag{6.6}$$

where $\delta x_{RPl/r}$ are displacements of the left and the right Roman Pots and $\delta x_{res,l/r}$ are shifts due to finite intrinsic detector resolution. Allowing for a deviation of 4 standard deviations in all contributions and adding them coherently, leads to

$$||x_l| - |x_r|| < 4 \times 2v_x\sigma(x_0) + 4 \times 2\sigma(x_{RP}) + 4 \times 2\sigma_{res} + 4 \times 2\sigma(\theta_{\rm beam})L_x \ . \tag{6.7}$$

Using $\sigma(x_{RP}) = 20\,\mu$m and $\sigma_{res} \approx 20\,\mu$m, we obtain $||x_l|-|x_r|| < (0.36{+}0.16{+}0.16{+}0.49)\,$mm $=1.17\,$mm. Hence, accepting hits in a road around the corresponding strips and extending up to the second neighbours comfortably accomodates these uncertainties. Thus the refined coincidence requirement is written as

$$\begin{aligned}&\text{Collinear Elastic Trigger} = \\ &\quad \text{(left RP1, } i_{l1}) \times \sum_{j=i_{l1}-2}^{i_{l1}+2} \text{(right RP1, } j) \times \text{(left RP2, } i_{l2}) \times \sum_{j=i_{l2}-2}^{i_{l2}+2} \text{(right RP2, } j) \\ &\times \quad \overline{\text{(T1 or T2).}}\end{aligned} \tag{6.8}$$

Like at the Roman Pot level, the width of the accepted coincidence road will be programmable.

Central Diffractive Trigger:

The trigger condition is given by:

$$\text{Central Diffractive Trigger} = \text{(left RP)} \times \text{(right RP)} \times \text{(left T1 or T2)} \times \text{(right T1 or T2).} \tag{6.9}$$

Single Diffractive Trigger:

The trigger condition is written as:

$$\begin{aligned}&\text{Single Diffractive Trigger} = \\ &\quad [\,\text{(left RP)} \times \overline{\text{(right RP)}} \times \text{(right T1 or T2)} \times \overline{\text{(left T1 or T2).}}\,] + \text{vice versa}\end{aligned} \tag{6.10}$$

6.3 Performance Requirements

6.3.1 Trigger Latency

For combined running with TOTEM triggering CMS, the TOTEM level-1 trigger – generated by physics events up to 220 m from the cavern – has to arrive at the CMS counting room within the CMS DAQ latency time of 91 standard bunch-crossings (bx = 25 ns) or 2.275 μs. A calculation of the latency budget (Sections 7.1.3 and 9.2.3) shows that after subtraction of the proton travelling time from the interaction point to the Roman Pots (29 bx) and the signal propagation time back to the counting room (52 bx), the remaining processing time for the TOTEM level-1 trigger including signal generation in the VFAT is at most 10 bx or 250 ns.

6.3.2 Time Resolution

The targeted trigger time resolution is driven by the need of identifying the correct bunch-crossing. Since the bunch separation will range between 25 ns and 2.0 μs, this requirement is not very tight. An easily achievable resolution of a few nanoseconds is adequate.

6.3.3 Efficiency

The measurement of elastic events down to the smallest achievable momentum transfer $t_{min} = 1.1 \times 10^{-3}\,\text{GeV}^2$ implies "edgeless" trigger counters with efficiency plateaus extending to about 20 μm from the physical edges of the detectors. This criterion narrows the choice of suitable detector technologies; possible solutions are the specially developed silicon detectors used for the precision trackers or scintillating fibers.

A single 300 μm thick silicon detector plane has a plateau efficiency of at least η =99 %. Requiring a coincidence of $n_d - 1$ out of n_d planes in each Roman Pot results therefore in an efficiency of

$$\eta_{pot} = \eta^{n_d} + n_d \eta^{n_d - 1}(1 - \eta) \tag{6.11}$$

per pot. Furthermore, for elastic events a coincidence of 4 Roman Pots (2 per arm) is required, which yields a total efficiency of

$$\eta_{tot} = \eta_{pot}^4. \tag{6.12}$$

In the case of $n_d = 3$ we obtain η_{tot} =99.9 %.

For the measurement of the elastic cross-section and its extrapolation to $t = 0$ it is not only important to have a high efficiency, but also to know its value precisely. It is straightforward to monitor each detector plane continuously during data taking, using the other planes in the same Roman Pot. To achieve the required precision of about 0.1 % in the efficiency, at most 10^3 events are needed.

6.3.4 Background Rejection

At the first trigger level, the main task of background rejection is to keep the event rate below the DAQ sampling capability of about 100 kHz, and to keep the background rates as low as possible compared to the physics event rates.

A detailed discussion of the different background processes and their rejection will be given in the next section.

6.4 Background Processes and their Rejection

Background in the Roman Pots is mainly produced by the following mechanisms:

1. Protons hitting collimators and other machine elements.
2. Beam-gas scattering.
3. Inelastic proton-proton scattering in the interaction point.
4. Intra-beam scattering.

Phenomenologically, these four processes produce three kinds of background:

- Beam halo created by (1), the elastic part of (2), and (4).
- Photons created by (1), the inelastic part of (2), and (3). They are seen as isolated hits.
- Shower particles (hadrons and electrons) created by (1), the inelastic part of (2), and (3). They are seen as tracks with a wide range of angles.

At present, background estimations are based partly on simulations of the production processes, and partly on simulation results for the total particle fluxes where information about the underlying production processes is no longer available. Hence a certain level of double counting is unavoidable and results in rather conservative limits.

For each kind of background, Tables 6.3 and 6.4 give the rates for the single-pot, for the arm with two pots and for the two-arm coincidence with and without collinearity cut.

6.4.1 Beam Halo

Due to machine imperfections, intrabeam scattering, proton-proton scattering at the interaction point and scattering of beam protons off rest gas molecules or aperture limitations, protons are lost from their design orbit with a rate of

$$f_{loss} = \frac{k\,N}{\tau} \tag{6.13}$$

at injection time. N is the number of particles per bunch, and k is the number of bunches. The values have been given in the definition of the two running scenarios (Section 6.1). The beam lifetime τ has the following components:

$$\tau^{-1} = 2\tau_{vacuum}^{-1} + \tau_{IBS}^{-1} + \tau_{bb}^{-1} \tag{6.14}$$

According to the LHC specifications [5], the vacuum lifetime $\tau_{\mathrm{vacuum},\,1} = \tau_{\mathrm{vacuum},\,2} = 100\,\mathrm{h}$, the intrabeam scattering lifetime $\tau_{\mathrm{IBS},\,1} = 300\,\mathrm{h}$ and $\tau_{\mathrm{IBS},\,2} = 105\,\mathrm{h}$. For the TOTEM luminosities the beam-beam interaction contribution is negligible. The resulting lifetimes are $\tau_1 = 42.9\,\mathrm{h}$ and $\tau_2 = 33.9\,\mathrm{h}$.

The protons lost by the mechanisms discussed above will constitute a halo which will be cut by a two-stage beam cleaning system [3]. The primary and secondary collimators will be placed at 6 and $7\,\sigma$ (Gaussian beam width) from the beam centre. Despite collimation a rather flat tertiary halo will remain, extending from the secondary collimators out to the aperture limitation defined by the TAS. For run scenario 1 (2) with $\varepsilon = 1\,\mu\mathrm{m\,rad}$ ($3.75\,\mu\mathrm{m\,rad}$), this limit will be at $38\,\sigma$ ($20\,\sigma$) horizontally and at $36\,\sigma$ ($19\,\sigma$) vertically.

Figure 6.2 shows the probability of finding a lost proton outside a given radius after one turn around the ring. During the first turn, about 70 % of the lost protons have already been absorbed by the collimators. At the second turn, the remaining $\sim 30\,\%$ are found at radii greater than $6\,\sigma$ where the primary collimators are positioned. The probability of finding a lost proton at a radius greater than the inner edge of the Roman Pot detectors, i.e. $16.7\,\sigma$ ($13.4\,\sigma$), is expected to be $P(r > 16.7\,\sigma) \approx 10^{-3}$ ($P(r > 13.4\,\sigma) \approx 4 \times 10^{-4}$) with a large uncertainty of about a factor 3 due to imperfections in the collimation.

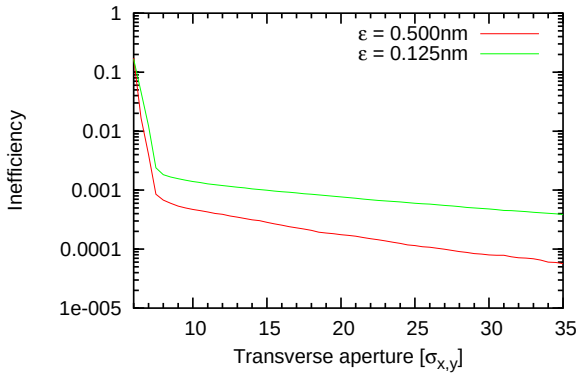

Figure 6.2: Collimation inefficiency for TOTEM running conditions [4] as a function of the distance from the beam in units of the r.m.s beam width. The 'inefficiency' shown is defined as the probability to find a lost proton after one turn around the ring at a radius greater than the abscissa value. The primary and secondary collimators are positioned at 6 and 7σ respectively. The Roman Pot detector edges will be located at 16.7σ (scenario 1) or 13.4σ (scenario 2). The absolute emittance ϵ =0.125 nm (0.503 nm) corresponds approximately to scenario 1 (2) with normalised emittance ϵ =1 (3.75) $\mu m \cdot rad$

Beam halo protons are problematic for the Roman Pot system because their direction is almost parallel to the beam and hence undistinguishable from the direction of the elastically or diffractively scattered protons to be detected. Only a global trigger coincidence between the two arms of the experiment – if necessary with a collinearity cut – can suppress beam halo background.

To obtain a conservative limit on the beam halo rate in a Roman Pot we assume a full azimuthal coverage of the beam periphery with $r > r_{inner\ edge}$ and $r < r_{outer\ edge}$. This results in a rate of

$$f_{\mathrm{halo}} = [P(r > r_{inner\ edge}) - P(r > r_{outer\ edge})] f_{\mathrm{loss}} \quad . \tag{6.15}$$

Since the detectors extend to much greater radii than the TAS aperture limits mentioned above, $P(r > r_{outer\ edge}) = 0$. Inserting the numerical values into Eq. (6.13) yields the loss rates $f_{loss,\,1} = 11.1\,\mathrm{MHz}$

and $f_{loss,\,2} = 147\,\mathrm{MHz}$. Using Eq. (6.15), $f_{\mathrm{halo},\,1} = 11\,\mathrm{kHz}$ and $f_{\mathrm{halo},\,2} = 59\,\mathrm{kHz}$ in each arm, with an uncertainty of a factor 3.

For the elastic and central diffractive trigger the background rate will be reduced by requiring a coincidence between the pots on one side of the interaction point with either the pots on the other side. The two-arm halo coincidence rate is given by

$$f_{\mathrm{coinc}} = f_{\mathrm{halo}}^2 \Delta t_{\mathrm{bunch}}. \tag{6.16}$$

For run condition 1 with a bunch separation of $\Delta t_{\mathrm{bunch}} = 2.021\,\mu\mathrm{s}$, $f_{\mathrm{coinc},\,1}$ is 245 Hz. For run condition 2 with a bunch separation of $0.570\,\mu\mathrm{s}$, the coincidence rate is 1.97 kHz.

For the elastic trigger, a further reduction can be achieved by applying the collinearity cut. With a tolerance of ± 2 strips for the collinearity deviation between the two arms, the probability of getting a collinear coincidence from a flat halo is $(5\,\mathrm{strips})/(2 \times 32\,\mathrm{strips}) = 0.078$, reducing the coincidence rates to 19 Hz and 154 Hz for the two run scenarios respectively.

6.4.2 Photons

Simulations [2] for a luminosity of $10^{33}\,\mathrm{Hz/cm^2}$ yield a flux $R_\gamma = 8.1\,\mathrm{MHz/cm^2}$ of photons above 100 keV, averaged over the area of a detector. The peak flux is about 5 times higher, i.e. about $40\,\mathrm{MHz/cm^2}$. Scaling this value to the TOTEM luminosities of $1.6 \times 10^{28}\,\mathrm{Hz/cm^2}$ or $2.4 \times 10^{29}\,\mathrm{Hz/cm^2}$ depends on the origin of the photons. At $\mathcal{L}_0 = 10^{33}\,\mathrm{Hz/cm^2}$ a fraction p_0 between 0.1 % and 1 % of all photons is produced by beam-gas scattering and collisions between the beam halo and machine elements. The rest is related to beam-beam collisions in the interaction point. Considering that the beam-beam component scales with the luminosity $\mathcal{L}$ whereas the halo-machine and the beam-gas components[1] scale with the beam current or $k\,N$, the total rate at a luminosity $\mathcal{L}_T$ is given by

$$R_\gamma(\mathcal{L}_T) = R_\gamma(\mathcal{L}_0) \left[\frac{k_T\,N_T}{k_0\,N_0} p_0 + \frac{\mathcal{L}_T}{\mathcal{L}_0}(1 - p_0) \right]. \tag{6.17}$$

Thus we obtain peak fluxes $R_\gamma(1.6 \times 10^{28}) = (0.55 \div 2.0)\,\mathrm{kHz/cm^2}$ and $R_\gamma(2.4 \times 10^{29}) = (10.5 \div 30.5)\,\mathrm{kHz/cm^2}$. A pair of detector planes (above and below the beam) with an area of $2 \times 3 \times 3\,\mathrm{cm^2}$ and a typical photon detection efficiency of 1 % would suffer from a background rate of up to 6 kHz. However, since photons create uncorrelated hits, this rate is drastically reduced by the collinear coincidence requirement laid out in Section 6.2.2. Furthermore, since the residual gas densities during TOTEM running will be significantly lower than at full luminosity, the values calculated are very conservative upper limits.

The probability for a fake track from photons was calculated with simple combinatorics as a function of the number of planes and of the number of segments per plane. The following kinds of detector segmentation were considered (see Fig. 6.3):

- Pixel detectors:
  The fake track frequency is given by

$$f_p = \frac{2}{\Delta t_b} \frac{n_p}{9} \left[P^{n_d} + n_d\,P^{n_d - 1}(1 - P) \right]$$
$$\text{with}$$
$$P \equiv 9 R_\gamma \eta \frac{l^2}{n_p} \Delta t_b \tag{6.18}$$

  where n_d is the number of planes and n_p is the number of pixels.

- Strip detectors, all planes having their strips parallel to each other:

$$f_\parallel = \frac{2}{\Delta t_b} \frac{n_s}{3} \left[P^{n_d} + n_d\,P^{n_d - 1}(1 - P) \right]$$
$$\text{with}$$
$$P \equiv 3 R_\gamma \eta \frac{l^2}{n_s} \Delta t_b \tag{6.19}$$

[1] For a given gas density.

- Strip detectors with perpendicular strip orientations:

$$f_\perp = \frac{2}{\Delta t_b}\frac{n_s^2}{9}\left[P^{n_d} + n_d\, P^{n_d-1}(1-P)\right]$$
$$\text{with}$$
$$P \equiv 3R_\gamma\eta\frac{l^2}{n_s}\,\Delta t_b \tag{6.20}$$

  where $n_d = n_{dx} + n_{dy}$, $n_{dx} \geq 1$, $n_{dy} \geq 1$. Note that it doesn't matter how the n_d planes are distributed in planes measuring x and y.

In view of keeping the coincidence calculation in the read-out logics as simple as possible, the total number of detector segments has to be kept small.

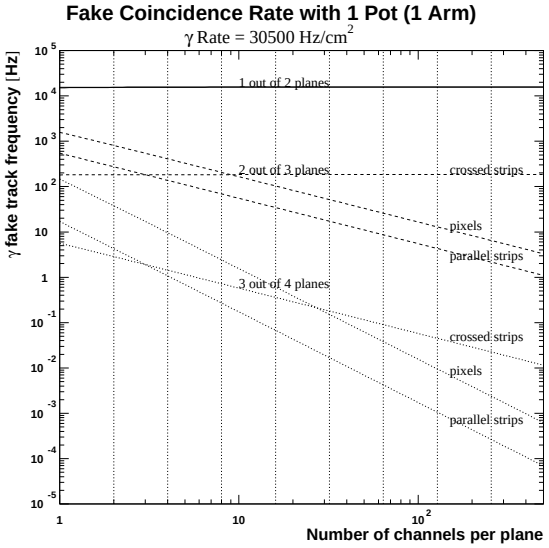

Figure 6.3: Frequency of fake tracks from photons for the scenario with $\mathcal{L} = 2.4 \times 10^{29}\,cm^{-2}s^{-1}$ as a function of the detector segmentation and the number of detectors per Roman Pot. The detectors considered in this example cover an area of 33.792 × 33.792 mm² (corresponding to 512 strips of 66 μm in the precision trackers)

For a given number of segments the best fake track suppression is achieved using strip detectors with parallel strip orientation. Pixel detectors would have the additional disadvantage that the coincidence between different planes would involve 8 neighbouring segments instead of 2 which would complicate the front-end electronics.

For the solution with 32 strips, the fake track rate in one Roman Pot would be 0.05 Hz and 11.5 Hz at the two luminosities considered. Conservatively, the peak fluxes were used for these evaluations.

A further reduction of the fake track rate – far below 1 Hz – is obtained by requiring a coincidence between the two Roman Pots in a station.

6.4.3 Other Shower Particles

For evaluating the background levels from shower particles other than photons there are currently two approaches:

- The contribution from beam-gas scattering can be estimated from the expected rest-gas densities and shower production simulations for proton-atom scattering.

- Simulation results for the total particle fluxes as used in Section 6.4.2. The data available to us do not include any information about particle angles or energies or their individual production mechanisms.

Expectations for the residual gas densities in the LHC beam pipe have recently been published for the standard LHC current [6]. The results of a recalculation for the TOTEM running scheme [7] with k =156 and $N = 1.15 \times 10^{11}$ are given in Table 6.1. For the other scheme with $k = 43$ and $N = 0.29 \times 10^{11}$ the densities have not been simulated but are expected to be lower by roughly the ratio of beam currents $\frac{0.29\times43}{1.15\times156} = 0.07 \approx 0.1$.

Gas	ρ [10^6 molecules / cm^3]	σ [mb]
H_2	0.311	94
CH_4	0.063	568
CO	0.007	840
CO_2	0.018	1300

Table 6.1: Residual gas densities [7] for $k = 156$ bunches with 1.15×10^{11} protons, and the proton-gas scattering cross-sections [8]

The beam-gas interaction rate in the whole ring is

$$\begin{aligned} f_{bg} &= k\,N\,c \sum_{\text{gas}\,i} \rho_i\,\sigma_i \\ &= 156 \times 1.15 \times 10^{11} \times 2.8 \times 10^{-9}\text{s}^{-1} = 51\,\text{kHz} \end{aligned} \tag{6.21}$$

or 1.9 Hz/m ring length.

Elastic beam-gas collisions produce hard protons mainly at small scattering angles and thus contribute to the beam halo already discussed. Inelastic collisions on the other hand produce showers of softer particles. The binding energy of the gas molecules being negligible, the fundamental process characterising the shower production is the collision of a proton with a constituent atom of the gas. To study a representative process, a simulation of 7 TeV protons hitting oxygen atoms at rest was performed [1].

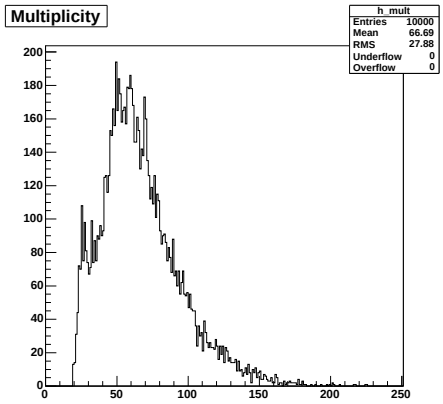

Figure 6.4: Multiplicity distribution for particles produced in proton-oxygen collisions

The multiplicity distribution for the collision products (Fig. 6.4) gives an average of 67 particles created per event, which suggests suppressing such events with a multiplicity cut. Furthermore, given the wide pseudorapidity distribution (Fig. 6.5), angular cuts can be used to eliminate background events not caught by the multiplicity cut. The efficiency of these cuts was quantified in a simple study where the simulated proton-oxygen events were uniformly distributed along the LHC ring segment between the CMS interaction point and the Roman Pots at 220 m. For each shower particle the production angle decided

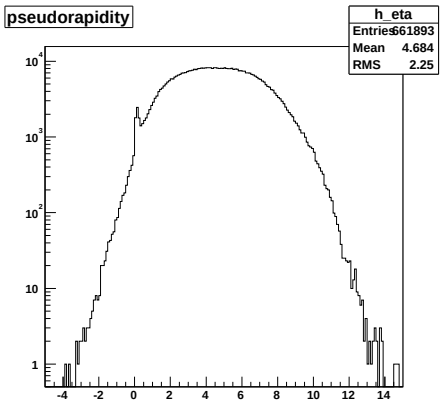

Figure 6.5: Pseudorapidity distribution for particles produced in proton-oxygen collisions

Particles	Flux [Hz/cm^2] at $\mathcal{L}$[Hz/cm^2] =		
	10^{33}	1.6×10^{28}	2.4×10^{29}
Photons	8.1×10^6	113÷404	$(2.1\div6.1)\times10^3$
Electrons	1.2×10^6	17÷60	$(0.31\div0.90)\times10^3$
Charged			
Hadrons	58×10^3	0.81÷2.9	14.8÷43.7
Neutrons	37×10^3	0.52÷1.8	9.4÷27.9

Table 6.2: Particle fluxes at the Roman Pots at 220 m at $\mathcal{L} = 10^{33}\text{cm}^{-2}\text{s}^{-1}$ (simulated [2]) and scaled to $\mathcal{L} = 1.6\times10^{28}\,\text{cm}^{-2}\text{s}^{-1}$ and $\mathcal{L} = 2.4\times10^{29}\,\text{cm}^{-2}\text{s}^{-1}$. The two limits given for the scaled values correspond to $p_0 = 0.001$ and 0.01 respectively (defined in Section 6.4.2)

whether or not it was inside the Roman Pot detector acceptance. Magnetic field effects were neglected. This simplification leads to an overestimate of the background acceptance since off-momentum particles would be swept out by the magnetic fields. The following cuts were applied:

- Multiplicity at most 3 in each detector.
- Collinear coincidence of 2 out of 3 planes as shown in Fig. 6.1.
- Collinear coincidence of 2 Roman Pots per arm.
- Up to 3 surviving tracks.

These conditions are met by 54.6 % of the proton-gas collisions occurring between the interaction point and the Roman Pot station. This corresponds to a rate of $1.90\,\text{Hz/m} \times 220\,\text{m} \times 0.546 = 229\,\text{Hz}$ per arm of the experiment. Requiring a coincidence with the other arm, reduces the fake-track rate from beam-gas scattering to 0.030 Hz.

To include also collisions of halo particles with machine elements, another approach was taken. Count rates from shower particles can be estimated from the total fluxes listed in Table 6.2.

These values originate from the same simulation that also served for obtaining the photon background. The scaling from $\mathcal{L} = 10^{33}\text{cm}^{-2}\text{s}^{-1}$ to TOTEM luminosities was done as explained in Section 6.4.2.

Even without any knowledge about the individual production mechanisms, energies or angles of the particles in Table 6.2, the following conclusions can be drawn:

- The contribution from neutrons is small compared with the charged particle rates.
- To obtain a very conservative upper limit for the combined effect from charged hadrons and electrons, we disregard multiplicity and angular constraints and calculate only the impact rates.

For $\mathcal{L} = 1.6 \times 10^{28}\,\mathrm{cm}^{-2}\mathrm{s}^{-1}$, the rate for a detector pair with a total area of $2 \times 3 \times 3\,\mathrm{cm}^2$ is $(0.33 \div 1.17)\,\mathrm{kHz}$. Assuming a similar efficiency of multiplicity and angular cuts as found from the beam-gas calculation (see above), we can expect a reduction factor of about 0.5. Hence the single arm rate will be about $(0.16 \div 0.59)\,\mathrm{kHz}$. The coincidence with the second arm reduces it to $(0.05 \div 0.70)\,\mathrm{Hz}$. For $\mathcal{L} = 2.4 \times 10^{29}\mathrm{cm}^{-2}\mathrm{s}^{-1}$ the rate per detector pair is $(6.0 \div 17.5)\,\mathrm{kHz}$, the single arm rate is $(3.0 \div 8.3)\,\mathrm{kHz}$, and the double arm rate is $(5 \div 39)\,\mathrm{Hz}$.

6.4.4 Summary of Background Rates

The single-arm and two-arm background rates shown in Tables 6.3 and 6.4 can be used to estimate the backgrounds relevant for the physics processes of interest. The results are summarised in Table 6.5.

	Background Rate in			
	one RP	single arm	double arm	double arm with collinearity
Beam halo	11 kHz	11 kHz	245 Hz	19 Hz
Photons	≤ 0.05 Hz	< 1 mHz	< 1 mHz	< 1 mHz
Other shower particles	< 590 Hz	< 590 Hz	< 0.7 Hz	< 0.05 Hz
[beam-gas component]	[≈ 25 Hz]	[≈ 25 Hz]	[≈ 0.005 Hz]	[<1 mHz]
Total	(11÷12) kHz	(11÷12) kHz	(245÷288) Hz	(19÷22) Hz

Table 6.3: Background Rates for $\mathcal{L} = 1.6 \times 10^{28}\,\mathrm{cm}^{-2}\mathrm{s}^{-1}$.

	Background Rate in			
	one RP	single arm	double arm	double arm with collinearity
Beam halo	59 kHz	59 kHz	2.0 kHz	154 Hz
Photons	≤ 11.5 Hz	< 1 mHz	< 1 mHz	< 1 mHz
Other shower particles	< 8.3 kHz	< 8.3 kHz	< 39 Hz	< 3.0 Hz
[beam-gas component]	[235 Hz]	[229 Hz]	[0.03 Hz]	[0.002 Hz]
Total	(60÷68) kHz	(60÷68) kHz	(2.0÷2.6) kHz	(154÷206) Hz

Table 6.4: Background Rates for $\mathcal{L} = 2.4 \times 10^{29}\,\mathrm{cm}^{-2}\mathrm{s}^{-1}$.

Background for elastic events:
Elastic events can only be faked by double-arm background. To push the background below the elastic signal rate the collinearity cut is mandatory.

Background for central diffractive events:
At leading order, three combinations of processes can simulate a central diffractive event:

- An elastic event coinciding with a Non-Single-Diffractive (NSD) event: With a cross-section of 65 mb for NSD events, the fake trigger rate is

$$\begin{aligned} f(1.6 \times 10^{28}\,\mathrm{cm}^{-2}\mathrm{s}^{-1}) &= 1.0\,\mathrm{Hz} \\ f(2.4 \times 10^{29}\,\mathrm{cm}^{-2}\mathrm{s}^{-1}) &= 64.0\,\mathrm{Hz}\,. \end{aligned}$$

  Later trigger stages or the offline analysis will aim at recognising this background using the collinearity of the two protons and the energy deposited by the NSD event.

- A double-arm background event coinciding with an NSD event:

$$\begin{aligned} f(1.6 \times 10^{28}\,\mathrm{cm}^{-2}\mathrm{s}^{-1}) &= 0.6\,\mathrm{Hz} \\ f(2.4 \times 10^{29}\,\mathrm{cm}^{-2}\mathrm{s}^{-1}) &= 23.1\,\mathrm{Hz}\,. \end{aligned}$$

- Two opposite single-diffractive events coinciding:

$$f(1.6 \times 10^{28}\,\mathrm{cm^{-2}s^{-1}}) = 0.05\,\mathrm{Hz}$$
$$f(2.4 \times 10^{29}\,\mathrm{cm^{-2}s^{-1}}) = 3.3\,\mathrm{Hz}\,.$$

These numbers show that it will be difficult to isolate central diffraction events. For the low-luminosity scenario the sum of the above background contributions is still smaller than the physics signal rate whereas for the higher luminosity the background dominates.

Background for single-diffractive (SD) events:
SD events can be faked by a one-arm background event coinciding with a beam-gas scattering event in the central detector region. With the beam-gas production rate of 1.9 Hz / m at $\mathcal{L} = 2.4 \times 10^{29}\,\mathrm{cm^{-2}s^{-1}}$ per unit ring length (Section 6.4.3), the frequency of beam-gas events in the 18 m long section between the two T1 trackers is 34.2 Hz. Depending on the inelastic trigger scheme (see Section 8.3), at most 58 % of these events are accepted, which corresponds to a frequency of 20 Hz. In the 5 m long sections between T1 and T2 on both sides of the IP, the beam-gas event frequency is 2×9.5 Hz out of which at most 2.4 % or 0.5 Hz are accepted. For the scenario with $\mathcal{L} = 1.6 \times 10^{28}\,\mathrm{cm^{-2}s^{-1}}$ the beam-gas collision rates are about 10 times lower.

The frequency of coincidences between one-arm background and accepted beam-gas events is

$$f(1.6 \times 10^{28}\,\mathrm{cm^{-2}s^{-1}}) \approx 0.1\,\mathrm{Hz}$$
$$f(2.4 \times 10^{29}\,\mathrm{cm^{-2}s^{-1}}) = 1.6\,\mathrm{Hz}\,.$$

It is far lower than the signal rate.

	σ [mb]	Event Rate for $\mathcal{L} = 1.6 \times 10^{28}\,\mathrm{cm^{-2}s^{-1}}$		Event Rate for $\mathcal{L} = 2.4 \times 10^{29}\,\mathrm{cm^{-2}s^{-1}}$	
		Signal	Background	Signal	Background
Elastic scattering	30	480 Hz	(245÷288) Hz	7.2 kHz	(2.0÷2.6) kHz
[with collinearity cut]			[(19÷22) Hz]		[(154÷206) Hz]
Single diffraction	20	320 Hz	0.1 Hz	4.8 kHz	1.6 Hz
Central diffraction	0.5	8 Hz	1.7 Hz	0.12 kHz	0.09 kHz

Table 6.5: Physics event rates and estimated backgrounds for the two luminosities forseen for TOTEM. The background rates given correspond to a configuration with 3 trigger detector planes per Roman Pot. The maximum DAQ sampling rate is 100 kHz

6.4.5 Background Monitoring during LHC Operation

All backgrounds not related to proton-proton scattering in the interaction point can be monitored whenever there are no collisions between the two beams. To accomplish this monitoring in practice there are two possibilities:

- Have dedicated run periods where the beams are not brought to collision.
- Exploit the fact that not all bunch positions in the beam are occupied (e.g. 43 out of 44). When an empty position meets a filled position, the detectors will only see the background.

References

[1] A. Morsch: private communication.

[2] N.V. Mokhov et al.: Accelerator Related Backgrounds in the LHC Forward Detectors, Fermilab-Conf-03/086, May 2003.

[3] R. Assmann et al.: Status of the LHC Collimation System, LEMIC talk, 8. April 2003, CERN.

[4] R. Assmann: private communication.

[5] LHC home page, http://lhc.web.cern.ch

[6] A. Rossi and N. Hilleret: Residual Gas Density Estimations in the LHC Experimental Interaction Regions, LHC Project Report 674, September 2003.

[7] A. Rossi: private communication.

[8] K. Eggert et al.: Luminosity Considerations for the LHC, LHC Note 263, 1994.

7 Electronics

7.1 Overall Electronics Requirements

7.1.1 Introduction

The physics requirements of TOTEM impose on the detector-electronics system to provide the trigger primitive and the accurate coordinates of triggered leading proton tracks. This is an unusual feature for a precise tracking system based on silicon strip sensors, and a part of what is presented in the TDR is based on extra R&D work done in the MIC group since no available study of silicon strip based trigger exits from previous work done for LHC experiments. Another unusual characteristic of TOTEM detector-electronic system is the geographical distribution of the Roman Pots (RP's) situated in the two arms 220 meters away from the CMS interaction point. Silicon strip planes and front-electronics located in RP's generate trigger signals and tracking data stream that should come back to the IP to be assembled and interconnected to CMS. This widely spread detector layout imposes a severe constraint in data communication between RP's and CMS. In particular, the quality of the timing precision is vital to ensure a reliable trigger system operation and synchronization, and to keep a minimum latency in the data and trigger signal transmission.

The full TOTEM detector consists of the Roman Pots housing silicon strips for tracking and triggering purposes, the T1 detector with Cathode Strip Chambers, and the T2 detector, which is still at the definition stage.

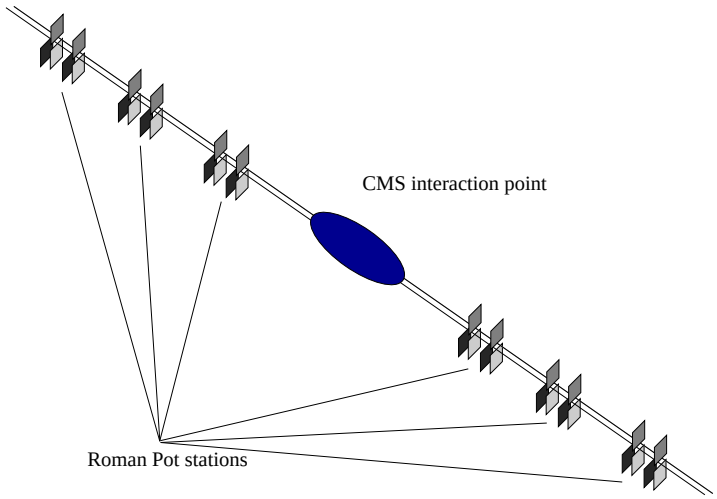

Figure 7.1: General Roman Pot Electronics System Oveview: there will be at least 6 Roman Pot Stations, three on each side of the CMS interaction point. Each of the Roman Pot station comprises two sets of three Roman Pots. Initially two out of three stations will be equipped

Three locations on each side of the interaction point for CMS have been foreseen for the Roman Pots (see Fig. 7.1). The distance between these two Roman Pot units will be a few meters. Each Roman

Pot unit consists of three Roman Pots. These Roman Pots provide trigger information and tracking information.

The T1 and T2 detectors are located in the very forward region of CMS, a few meters away from the interaction point.

In addition to the detector and associated readout electronics, and electronics for timing generation, electronics for fast coincidence processing and trigger generation, there are the control room and services electronics.

7.1.2 Timing Precision and Requirements

Events in CMS are synchronized with the 40.08 MHz bunch crossing clock of the LHC machine, and this clock is the baseline for the timing in CMS. Since the TOTEM experiment is working in close collaboration with the CMS experiment, and will for certain modes of operation provide part of the triggering information for CMS, the tracking data stream will be synchronized with the bunch structure, and all data gathered by TOTEM will have to be binned in 25 ns time bins corresponding to this 40.08 MHz clock. Since this problem is common to all LHC experiments a special system was developed in the framework of RD-12: The Timing, Trigger and Control (TTC) system, and it should normally also be adequate for TOTEM. The system is interfaced to the LHC machine signals, the global trigger processor, the front-end electronics controllers, the data acquisition, and status, calibration and test systems, and is based on the use of a few relatively high power laser sources which distribute the signals via a hierarchy of passive optical tree couplers to several thousand destinations each.

7.1.3 Trigger issues

A special chapter in this TDR is devoted to trigger generation. The general idea is that a trigger signal has to be constructed from the silicon strip planes in the Roman Pots, which will generate a signal for each minimum ionizing particle (MIP), i.e. primary scattered protons, passing through the active area of the Roman Pot. The efficiency to generate this trigger signal is a crucial parameter for the quality of the TOTEM Experiment and a special design effort is made to maintain the non-efficiency uniformity lower than 0.1%.

The current plan is to use silicon detectors to generate the trigger signal. The main advantage of silicon strips detector is its compactness and excellent spatial resolution. The silicon detectors foreseen (see Chapter 5) provide almost no dead volume at the edge. However, the main disadvantage of silicon strips is their potential susceptibility to beam coupling, interference generated by the time bunch structure of the beam. The current belief is that this effect can properly be shielded by the Roman Pot itself, and discussions with RF specialists are currently ongoing to improve our understanding of RF beam coupling. Tests are planned in 2004 at the SPS using a prototype Roman Pot and silicon detectors to prove that this interference is not an issue for the TOTEM experiment. However, if contrary to the expectations beam coupling really turns out to be a problem, scintillating fiber detectors will be our back up trigger detector technology, a technology under study by the ATLAS Very Forward team.

The non-negligible possibility of dead channels in silicon strip detectors precludes the efficiency uniformity required for the trigger if only one detector plane is used. Therefore several detector planes are foreseen to provide such efficiency uniformity, where then the signals generated by each plane will have to be combined and put in coincidence with the signals from the other planes to provide a reliable trigger signal at the Roman Pot level.

Apart from this requirement to combine signals from the same Roman Pot, it will be necessary to combine signals from different pots, even from pots on both sides of the CMS interaction point. This means that in any case some trigger box needs to be placed in the central counting room.

One very stringent requirement for the trigger signals is that they have to arrive in time in the counting room to provide a trigger signal to the CMS detectors and to the TOTEM detectors within the maximum level-1 trigger latency. This requirement is particularly stringent for the Roman Pots which are far remote from the CMS interaction point, up to a maximum of 220 m from the CMS control room. The present estimation of the cable length is 260 m, but further optimization is under investigation. Given that current state of the art cables will introduce a delay of about 5 ns/m length, we introduce already more than a microsecond of delay in the cables. In addition the particles will have travelled the distance to

the last Roman Pot from the interaction point, and this roughly at light speed, so we obtain for the time already consumed for the CMS trigger:

$$5\,\frac{\text{ns}}{\text{m}} \cdot (260\,\text{m}) + \frac{220\,\text{m}}{3 \cdot 10^8\,\frac{\text{m}}{\text{s}}} = 1.3\,\mu\text{s} + 0.733\,\mu\text{s} = 2.033\,\mu\text{s} = 81\,\text{bx}\ , \tag{7.1}$$

where 81 bx means 81 bunchcrossings. Adding a few bunchcrossings to account for the delay of the electronics, one arrives at 85 bunchcrossings. The inputs for the final coincidence for level 1 trigger formation should be at 91 bunchcrossings, so we are still within the limit for providing trigger inputs to CMS.

Trigger signals also need to reach the Roman Pot in time again. The limit defined by the pipeline depth of the trigger chip is $128 \times 25\,\text{ns}$ or $3.2\mu\text{s}$. Just counting the trigger delay going back and forth represents:

$$2 \cdot 5\,\frac{\text{ns}}{\text{m}} \cdot (260\,\text{m}) = 2.6\,\mu s = 104\,\text{bx}\ , \tag{7.2}$$

so we only would have 600 ns left. From these 600 ns, 150 ns will be used by the TTC system, we are left with 450 ns for the trigger electronics to take a decision.

A question is whether the Roman Pots at 220 m could be triggered by a general CMS trigger. This trigger is at the latest available at 103 bunch crossings after the event at the CMS interaction point and would need to reach the Roman Pot in time again, where however the particles from the interaction arrived later:

$$103 \cdot 25\,\text{ns} + 1.3\,\mu\text{s} - 0.733\,\mu\text{s} + 6 \cdot 25\,\text{ns} = 3.292\,\mu\text{s} = 132\,\text{bx}\ . \tag{7.3}$$

The six bunchcrossings correspond to the TTC receiver delay. 132 bunch crossings is well within reach for the APV chip which has a 192 long pipeline buffer. The trigger chip can provide digital tracking data but in its actual design only has a buffer depth of 128: this will force us to extend the VFAT buffer length to 192 as in the APV to allow CMS triggers to reach the Roman Pots in time. This extension can be included in a redesign planned for the end of this year.

Figure 7.2 gives an overview of the timing.

7.1.4 Readout Data rates

The trigger rate in TOTEM will be maximally 60 kHz (see section 6.4.4), which is less than the first level trigger rate in CMS of 100 kHz [1]. Since the same readout chain is planned for the TOTEM experiment as for CMS, the bandwidth of the readout should be sufficient to handle the readout rates in the Roman Pots.

7.2 System Overview

7.2.1 Overall layout and control system

The overall layout of TOTEM is deeply related to the geometry and implementation of the LHC machine warm pipe region and CMS. A schematic overview of the TOTEM electronics is described in Fig. 7.3. The Totem detector consists of the Roman Pots (RP1-4) which are up to 220 m removed from the control room and the central TOTEM trigger box. Two detectors will be located in the forward region of the CMS experiment itself which is at 90 meters cable length away from the counting room. Triggering will need signals from the Roman Pots, and after trigger generation trigger signals need to be sent back to all detectors, with the proper delay added. After level 1 trigger, data is transferred to the control room. The timing and control signals will be sent to each detector from the control room.

The electronics for T1 is briefly discussed in the T1 chapter itself. Since the T2 detector is still very much in the definition stage, it will not be discussed further here.

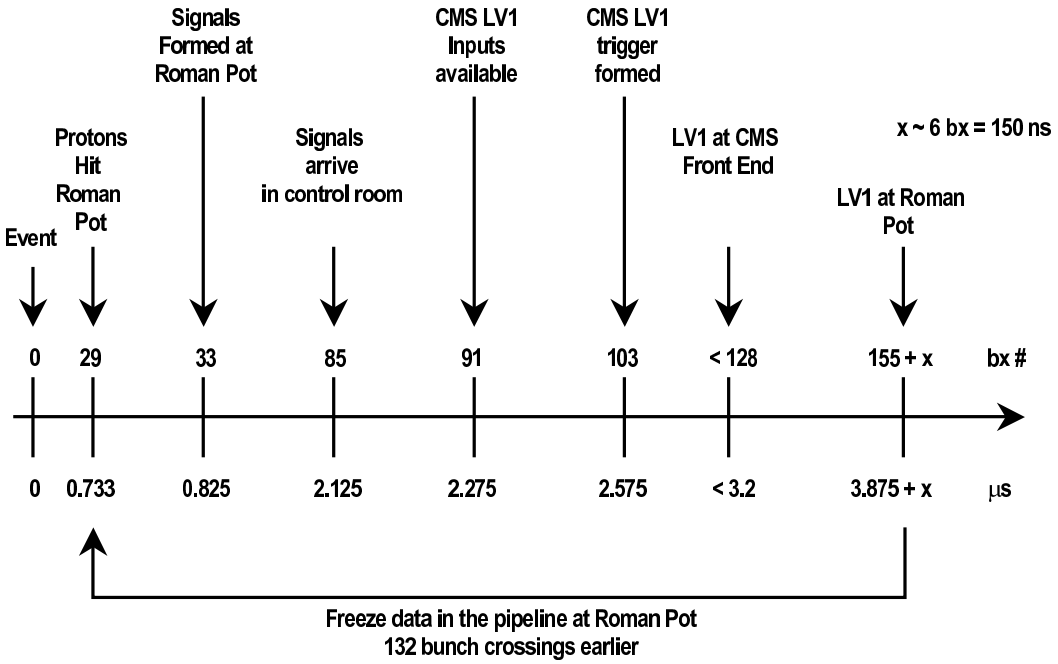

Figure 7.2: Overview of the delays in trigger formation

7.2.2 Roman Pot electronics

In the following the electronics for the Roman Pots is described in detail. First an overview of the system will be given, and then further details will follow.

Fig. 7.4 gives an overview of the Roman Pot electronic system: it consists of at least 6 Roman Pot Stations – three on each side of the CMS interaction point. Each Roman Pot Station consists of two Roman Pot units spaced at a distance of about 4 meters. Each unit consists of three Roman Pots, two vertical, one horizontal. Three Roman Pots are mounted at each unit (see Fig. 7.1). These three Roman Pots comprise several planes each and move towards the beam from different angles. The core of the electronics of each Roman Pot is the Roman Pot Mother Board, through which all signals from and to the Roman Pot pass. It contains some trigger formation circuitry, the readout drivers, it receives the trigger and clock signals, and also acts as an interface for the controls and interlocks.

Roman Pot Electronics System Overview and Strategic Choices

Since it was decided to send trigger signals to the counting room without carrying out coincidences locally, it is not yet clear whether a Roman Pot Trigger and Control station will be necessary in such form, or whether the Roman Pot mother Boards could be equipped in an area and cost effective way to perform the desired functions. In case the Roman Pot Mother Board receives those functions for the Roman Pot planes, the Roman Pot Timing, Trigger and Control station would be simplified considerably and probably be reduced to the functions essential to the control of the Roman Pot itself (position, temperature, vacuum, etc.). It might even be that since the CMS tracker control system is very modular, that somehow a motherboard can be configured to carry out the control functions for the pot itself, but this is still under study.

The strategy is to remain as close as possible to the CMS tracker system design [2], depicted in Fig. 7.5. The CMS tracker system contains an analog readout part and a digital control part, but does not provide a trigger itself. Therefore for TOTEM a trigger part needs to be added (see Fig. 7.6), which is planned

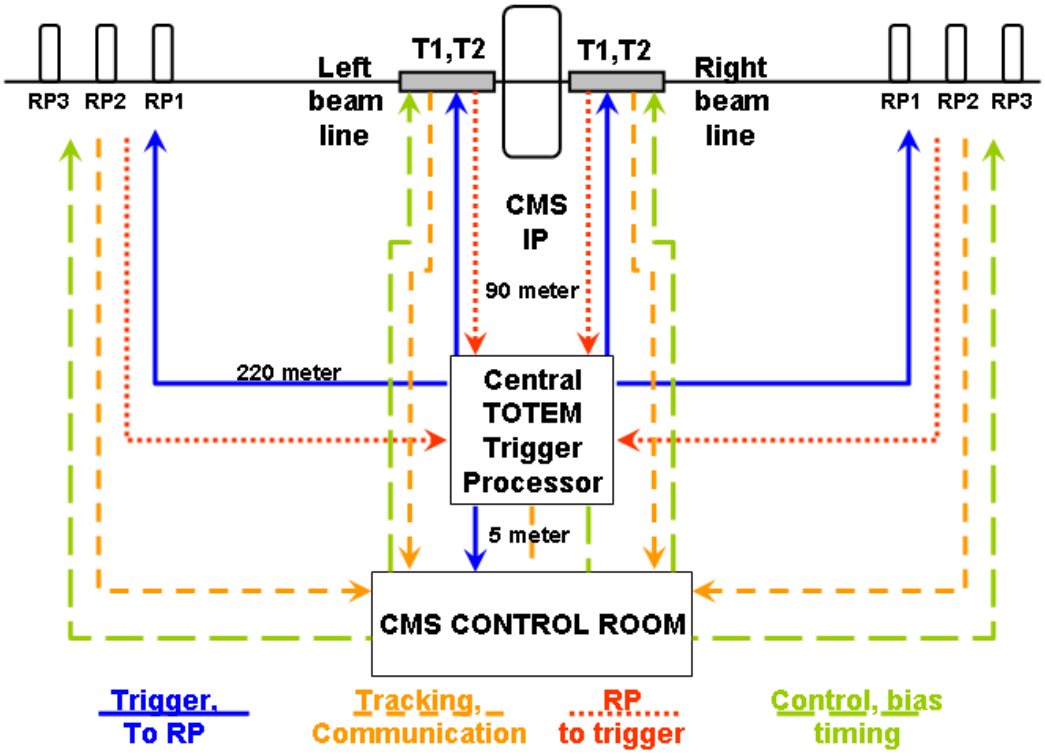

Figure 7.3: Schematic overview of the TOTEM electronics

to be implemented using the VFAT chip in the Roman Pot, from which the data will be transmitted by means of a digital optical link to the central TOTEM trigger processor. Note that the optical components for this digital link are the same as for the analog link. Patch panels near the detector are needed to group the optical fibers into bundles, since the long-distance optical communication makes use of cables which contain 96 optical fibers grouped in 8 optical ribbons of 12 fibers each.

General Mounting and Alignment Strategy and Implications

The packing of the planes inside the Roman Pots will be quite dense, and therefore an alignment procedure was devised which is based on alignment marks located on the silicon detector and on the frame holding the board on which the silicon detector is mounted. The procedure is described in detail in Chapter 4.

The boards will be aligned to the frame using as a reference the detectors mounted on them. Since the glueing of the detector on this board is subject to some tens of microns of imprecision, which probably holds for the connector as well, the position of the connector on the board will vary with respect to the frame. A fully fixed connecting scheme will therefore in all likelihood be too much of a mechanical constraint. The current baseline solution is to use a flex circuit (see Fig. 7.7). In view of the possible reliability issues, the flex and its connections are under extensive study. The most reliable way to connect these flex connections is to use zero insertion force connectors. These connectors will have to provide of the order of 50 electrical connections, which will bring the pin-to-pin pitch below 1 mm. Since typically such pitches are incompatible with high voltage, we might be forced to use separate connectors for a few high voltage lines.

One other possibility being considered is to house the optohybrids for the readout into the Roman Pot.

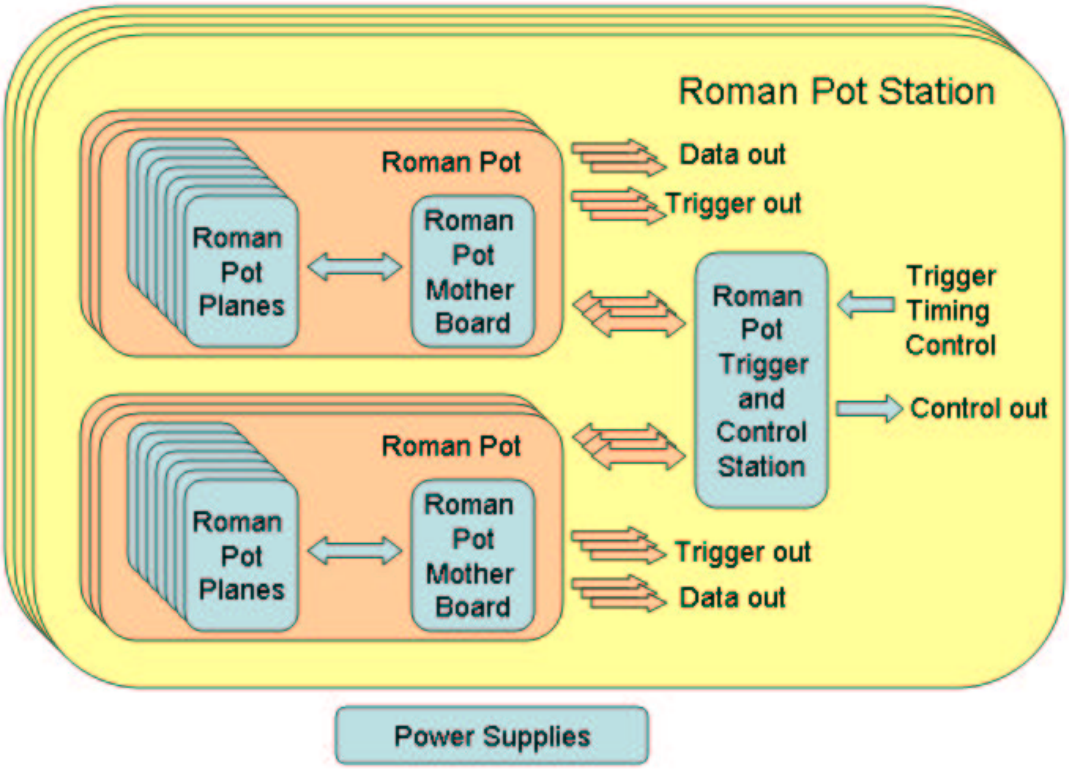

Figure 7.4: General Roman Pot Station Electronics Overview

This is not impossible, since the power of the hybrid (1 W) dominates the overall power consumption including those of the optohybrids. The optohybrids come in fact as mezzanine cards, which are to be plugged into a (NAIS) connector on the board from which they transmit the electrical signals in optical form. This solution would reduce the number of connections to be implemented in the feed through, but will require optical feedthroughs.

The third possibility considered is to have a feedthrough per detector plane. In that case the board on which the detector is mounted could serve as feedthrough. While from a connectivity point of view this would be an attractive solution, it does require an air tight mounting between the frames of subsequent planes, at least for the top part. Whether this in the end is practical remains to be seen, and therefore currently the first solution with one feedthrough card and flex connections from the individual detector planes board to this feedthrough card is retained as the baseline solution.

Trigger and Tracking Communality

Given that both trigger and tracking detectors consist of silicon strips, and that space is extremely constrained in the Roman Pots, the most logical solution a priori would be to use the same planes for triggering as for tracking as that would make most efficient use of the space available. However, the APV, which is the analog readout chip for the CMS tracker, and which is the baseline readout chip also for the Roman Pots, does not have self-triggering capability. Therefore another chip was developed in the Microelectronics Group at CERN, the VFAT chip, which provides digital trigger outputs but also tracking data in digital form (a yes/no answer is obtained about whether a strip was hit or not during a certain clock period). Currently analog readout is still considered to be advantageous for readout of heavily irradiated strips, and therefore the APV has been retained as baseline for TOTEM as it provides

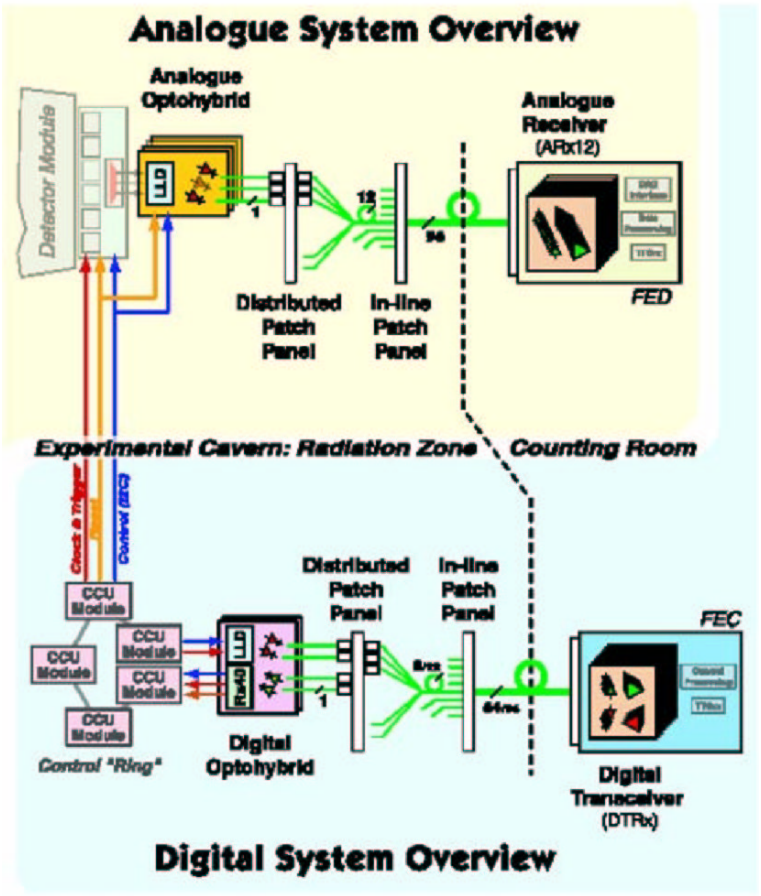

Figure 7.5: The CMS tracker system [2]. For TOTEM the trigger part needs to be added

analog information. However, it is desirable that the tracking data from the trigger planes provided in digital form by the VFAT be made available as that increases the number of tracking planes and makes more efficient use of the space in the Roman Pots.

Therefore, in summary, three types of detector data would come from the silicon strip detectors in the Roman Pots:

* Analog tracking data from the APV tracking planes.

* Digital tracking data from the VFAT trigger (and tracking) planes

* Digital trigger data from the VFAT trigger planes

To simplify the system as seen from the outside, the current plan is to adjust the digital level and signal outputs of the VFAT in such a way that the standard analog APV readout chain can accept the digital tracking data from the VFAT planes. This would allow to have a more uniform readout system, making the remaining system, from the connectivity in the Roman Pot to the outside up to the data acquisition, fully transparent for the two different types of tracking planes. It is also planned to maintain this transparency for the control signals.

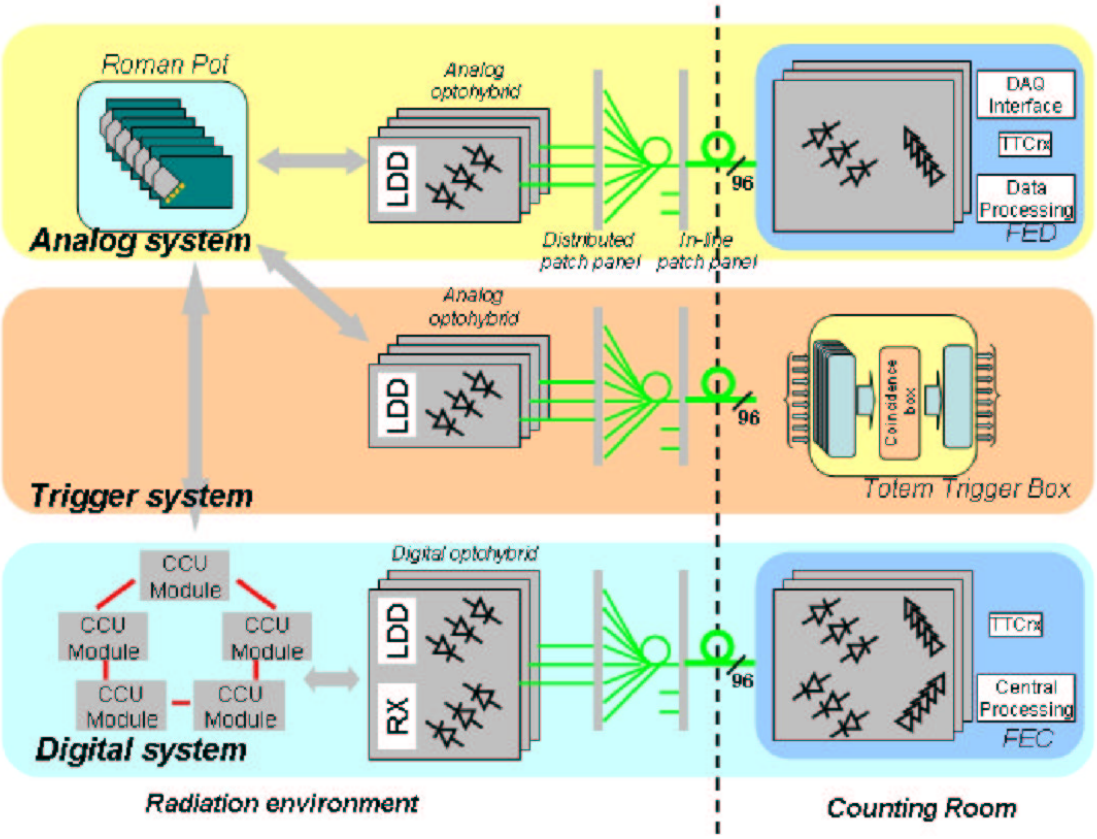

Figure 7.6: The TOTEM Roman Pot Electronics System. A trigger slice has been added based on the same optical components and a digital serial link

Radiation Tolerance

The radiation levels near the beam in the Roman Pots will be comparable to the radiation levels in the CMS tracker. The front end chips, APV and VFAT, will be 3 to 4 cm away from the beam. They were both designed for radiation tolerance using special design techniques and have been manufactured in 0.25 micron CMOS technology, and should withstand without problems the radiation levels predicted at that location (2 years at a luminosity of $10^{32}\,\mathrm{cm}^{-2}\mathrm{s}^{-1}$ would give about $10^{13}\,\mathrm{n/cm}^2$ equivalent at that location, and several hundred kRad (see Section 4.10). The rest of the electronics chain is further removed from the beam and will be subject to radiation levels lower than what is required for the CMS electronics in the tracker. The rest of the electronics will be placed in the counting room and will not be subject to radiation.

7.3 Trigger

The trigger specification was already discussed in the overview of the electronics. It was mentioned there that the trigger processing in the counting room should not take more than 450 ns. The delay was assumed to be 5 ns/m. Should there not be sufficient margin, other types of optical fibers could be used which are hollow (air-core), which should offer delays corresponding to the speed of light.

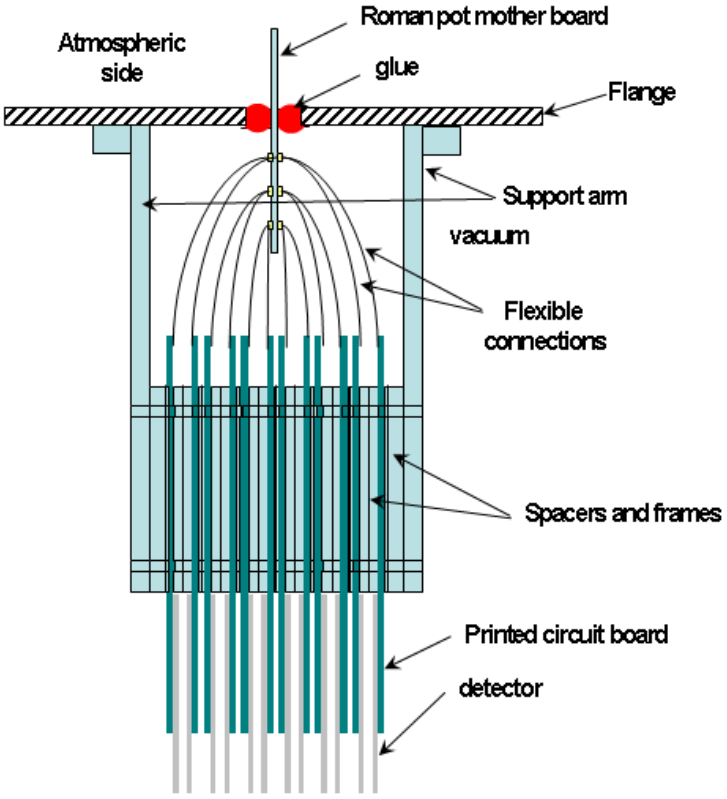

Figure 7.7: Current baseline solution for the feedthrough between the secondary vacuum inside the Roman Pot and the outside. The flexible connections would use dedicated connectors

7.3.1 Trigger Formation

As explained before, it will be necessary to make coincidences between different planes of the same Roman Pot in such a way to obtain an efficiency uniformity compatible with the physics goals of the TOTEM experiment. In addition, coincidences between trigger signals of different pots will have to be carried out as well, including these from opposite sides of the CMS interaction point. Therefore, a central trigger box in the counting room will be necessary in any case.

The VFAT chip [3] is described in detail later. We recall here that it provides 10 trigger outputs, which combine the comparator outputs of 24 strips with some overlap on each side (see Fig. 7.14). Two of these outputs are combining the edge channels on each side of the VFAT chip so that these can be combined with the edge channels of neighboring channels to obtain a uniform number of channels per trigger output for a detector to which more than one VFAT chip can be connected. In the case of TOTEM there will be four VFAT chips connected to one detector to form one trigger plane. Depending whether the trigger will take these edge outputs or not (the detector channels represented by these edge trigger outputs are in any case represented by the other outputs of the VFAT) there would be thirty two ($32 = 4 \times 8$) trigger outputs per trigger plane or forty ($= 32 + 4 \times 2$) in case the edge trigger outputs are also included.

Since a digital optical link (GOL [4]) exists which is capable of 1.6 Gbit/sec (or 32 bit words at 40 MHz), one or two digital optical links per trigger plane would be sufficient to transfer the trigger information to the counting room. Such a solution would make all trigger signals centrally available, with the significant advantage that the trigger algorithm could be modified relatively easily, that more complex trigger algorithms could be used, and that the trigger box could be replaced by a more advanced system if needed. As the number of additional optical links would not be excessive it was decided to opt for such a system

and to profit from its advantages.

The GOL driver chip is designed in 0.25 micron CMOS using special layout for radiation tolerance, both in terms of total dose and single event upset, and is therefore not expected to create reliability issues related to radiation. Note that it was specifically designed not only to withstand radiation, but also to be compatible with standard receivers - in fact the receiver was never designed at CERN.

One issue with a serial link is that it requires the transmission of some idle data to synchronize the receiving end with the data flow. The LHC bunch structure actually provides some time slots during which no particles are being brought into collisions. If a control pulse is sent to the GOL to tell it to ignore any input and to transmit idle data, these idle periods could serve for this purpose.

7.3.2 The trigger box in the counting room

Some advantages of carrying out all trigger processing in the central counting room were already mentioned. Another very significant advantage is that standard of-the-shelf components can be used.

The number of optical links carrying trigger signals will depend on the final decision on the number of trigger planes per Roman Pot and on the final number of Roman Pots. If one assumes 5 trigger planes per pot and 6 pots per station and a maximum of 4 stations on either side of the CMS interaction point, and one fiber per plane, there will be about 120 fibers for triggering, corresponding to about 4000 trigger bits, which will have to be treated by some trigger algorithm.

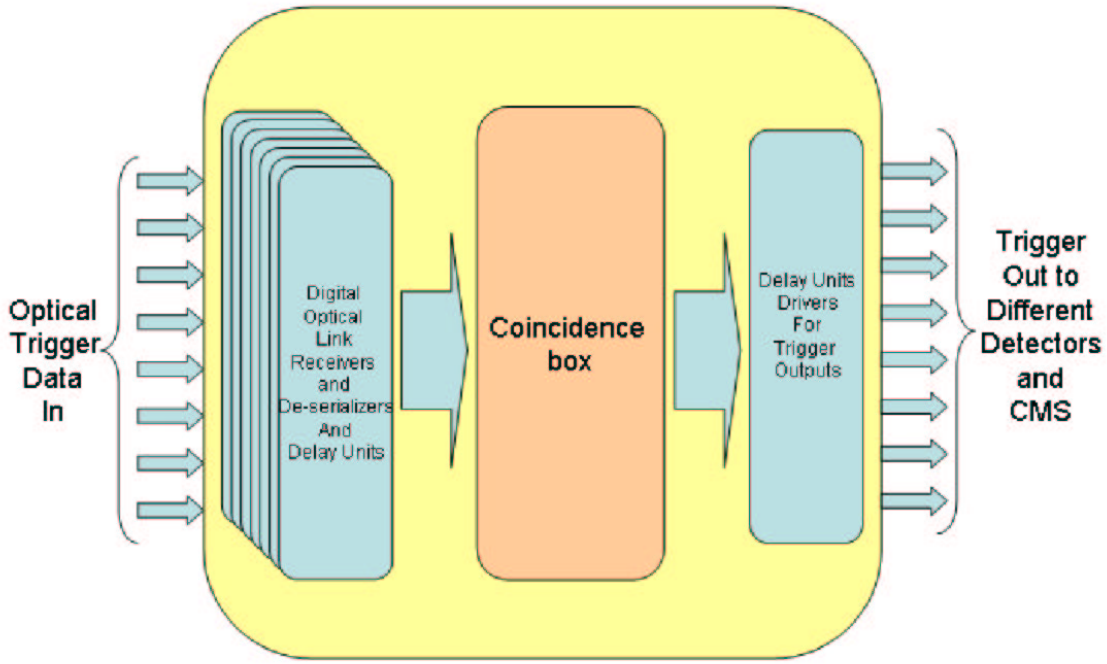

Figure 7.8: The central TOTEM Trigger Box

Since these signals will arrive at the trigger box (see Fig. 7.8) from different locations with different delays, these channels will have to be synchronized, not only with regard to phase versus the LHC machine clock, but also with regard to differences in delay over many LHC clock cycles.

It has to be noted that the TOTEM trigger will include trigger signals also from the other detectors

within TOTEM. These will be added as inputs to the TOTEM trigger box in the same way as the ones from the Roman Pots. Since these detectors are closer than the Roman Pots, they are not subject to the same delays, and will therefore not impose the same constraints on the system.

As the TOTEM detectors are located in very different positions and are subject to different delays, an additional capability is needed in the trigger box for setting the proper delay.

Several possibilities exist for implementing this coincidence processor. It could be made of some field programmable devices (a la Xilinx, or Altera), but it might be possible that some of the coincidences could be done in a much more time efficient way using some dedicated hardware. Since the required volumes of such hardware would be very small, it could even be envisaged to submit a dedicated chip to a multiproject wafer and obtain the full production from such a single run. Whether this will be done or not will depend on further developments with respect to the trigger formation. In any case the production cost for a dedicated chip if needed will not be prohibitive.

7.4 Timing distribution and Trigger Reception

7.4.1 The Trigger, Timing and Control System (TTC) for LHC and CMS

The TTC system [6] for the baseline design employs the multifunction optoelectronic distribution system being developed within the framework of the DRDC projects RD-12 and RD-27. The system is interfaced to the LHC machine signals, the global trigger processor, the front-end electronics controllers, the data acquisition, and status, calibration and test systems. The RD-12/RD-27 system is based on the use of a relatively high power laser sources which distribute the signals via a hierarchy of passive optical tree couplers to several thousand destinations each.. Each laser operates at 1310 nm, at which the chromatic dispersion of optical fiber is negligible, and the single source-architecture allows it to be well protected an easily upgraded as technology improves. The optical couplers have small size, low mass and effectively unlimited bandwidth, require no power and are highly reliable. The TTC system compensates for time-of-flight, electronic and signal propagation delays, and delivers properly synchronized bunch crossing and event numbers to the controllers together with each trigger decision. In CMS two independent time-division-multiplexed data channels are transmitted, one of which has very low latency and is dedicated to the broadcasting of the Level-1 trigger accept signal, while the other transmits broadcast and individually-addressed commands and data. The bunch crossing timing reference can be recovered from the encoded data stream with a jitter comparable with the spread in event origin time due to the LHC bunch lengths and expected longitudinal phase modulation of the circulating beams.

7.4.2 The TTC system for the Roman Pots

At the time the TTC system was planned base stations for TTC were planned for ATLAS, CMS, ALICE and LHCB, but no request was made for TOTEM. This means that TOTEM will most likely receive the TTC signals from the TTC base station from CMS. This means that special precautions will have to be taken to synchronize the electronics of the Roman Pots. Two cases have to be distinguished:

* Synchronization signals for the optical links. As mentioned before, serial links require timeslots where idle signals are transmitted, and it is foreseen to use the timeslots in the LHC beam structure where no particles are being brought into coincidence. Since the LHC beam structure is well-defined and repetitive, it can be foreseen to adjust these signals appropriately taking into account the travel time of the particles from the interaction point to the Roman Pot, and the travel time of the synchronization signal itself.

* Trigger signals. Since trigger signals by nature cannot be predicted, one can only add additional delay to these signals. As mentioned before it is foreseen to provide the delay required in the central trigger box in the counting room.

7.5 Readout Architecture and Datapath

7.5.1 General strategy

It was already explained that it is planned to make the digital tracking data available from the trigger planes, and the analog tracking data provided by the analog tracking planes, equipped by the APV, through the same analog readout chain. This will require adaptation on the trigger plane boards of the signals output by the VFAT trigger chip, as well as of the control signals required by this chip.

The advantage is that the rest of the readout system is fully transparent with respect to whether it receives tracking signals from a trigger plane or from a regular APV plane.

7.5.2 Data Transmission to Roman Pot Mother Board

In the current baseline solution it is planned to have a Roman Pot Mother Board which is connected to the feedthrough board which provides the feedthrough of the signals from inside the Roman Pot to the outside. In fact, some solution is being considered where the Mother Board immediately serves as feedthrough card, but that will require some adapter piece which provides an envelope to the card to which the card can be glued. This adapter piece can then in turn be bolted to the top flange of the Roman Pot. This approach would avoid to have the full (heavy) flange hanging from the Roman Pot Mother Board.

7.5.3 Data Transmission to Control Room

The Roman Pot Mother Board will comprise the optohybrids responsible for transmitting the tracking data to the counting room. The CMS collaboration has in fact developed a modular system where the optohybrids are implemented in the form of mezzanine cards which can be plugged onto the board from which the data is to be transmitted. Currently close collaboration with CMS is ongoing to ensure that the Mother Board is fully compatible with the CMS system.

7.6 Control and Interlock

The electronics system will need to comprise several control functions, including:

* position control of the Roman Pot
* pressure (vacuum) control of the Roman Pot and the compensation chamber
* temperature control of the modules
* various supply voltage and current controls.

The CMS tracker system comprises a full control system for the standard CMS electronics. It uses a token-ring architecture with a master control node (the Front-End Controller or FEC) located in the counting room and which interfaces by means of a digital serial optical link with the Communication and Control Units (CCU's), located on the larger mechanical sub-structures of the CMS tracker. These CCU's are configured in control rings, which receive the control signals from the FEC, transmit it from one CCU to the next within the ring, and then transfer the data back to the FEC. The optical link therefore contains both 40 MHz clock and digital control data. The data is encoded by missing clock pulses in the clock signal.

The CCU's have the possibility to control modules by the I^2C standard, and have the possibility to measure 16 channels of sensor information by means of an analog-to-digital converter.

Currently it is not yet fully clear who is responsible for the control system of the Roman Pots, this could be the responsibility of the machine, or of the experiment. This is currently being discussed in more detail with the machine division. Since the control system for CMS is very modular it could be envisaged to incorporate the control of the pot into the control of the readout system. One could, for instance, envisage a control ring based on one or two CCU's per Roman Pot motherboard, which would

not only take care of the control directly related to the readout, but also of the Roman Pot position, vacuum, etc. A control ring per Roman Pot Station could then be made. All this would be possible if the systems used to control the motors moving the Roman Pots can be made compatible with the I^2C standard.

Independent of who will be responsible for this control system, it will be necessary to send and to receive interlock and interrupt signals from the experiment to the machine and vice versa. If the CMS control system is used, it is likely that this will be taken care of from the counting room.

7.7 Front End Chip Descriptions

7.7.1 APV

The APV25-S1 [5] is an analogue pipeline ASIC intended for read-out of silicon strip detectors in the CMS tracker. The architecture of the CMS tracker read-out system is based on analogue processing of data in the detector prior to transmission in analogue form to the DAQ. The chip contains 128 channels of preamplifier and shaper driving a 192 column analogue memory into which samples are written at the LHC 40 MHz frequency. This memory always contains a record of the most recent beam crossing that the chip has sensed. A data access mechanism allows the marking and queueing of requested memory locations for output. Requested samples from the memory can then be processed with a FIR filter. This is a switched capacitor network which deconvolves the shaping function of the preamplifier and shaper stages to give a pulse shape confined to one 25 ns period. After the filtering the data is held in a further buffer until it can be read out through an analogue multiplexer.

The chip also includes a programmable bias generator, an internal test pulse generation system, and a slow control communication interface.

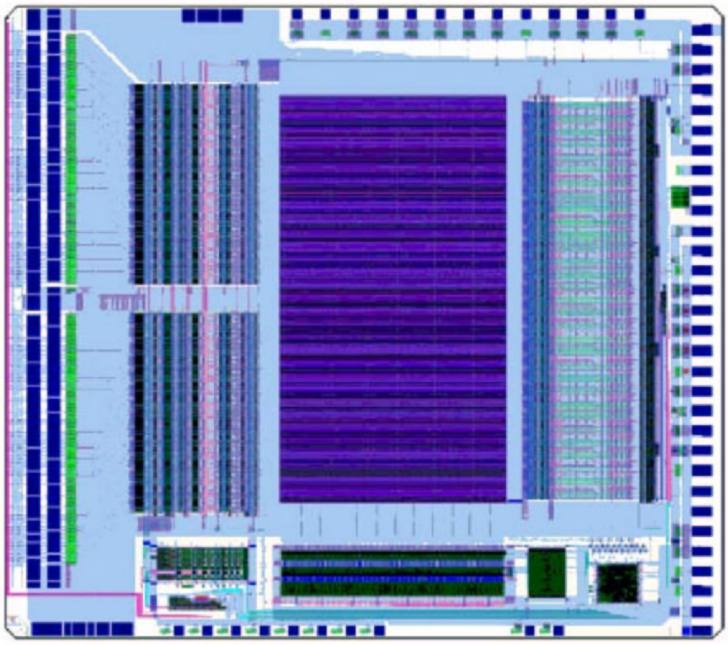

Figure 7.9: The APV25-S1 chip [5]. The pads on the left comprise the input pads to be connected to the detector and the power supplies and ground for the analog front end. The pads on the right provide the remainder of the power supplies and the I/O to the external world. Pads on top and bottom are for testing purposes only

The size of the chip is 8055 by 7100 μm (see Fig. 7.9). It is fabricated in 0.25 μm CMOS technology

using 3 metal layers. The 128 analogue inputs are grouped into 2 sections. The sections are arranged in two staggered rows with even numbered pads on the outside and odd numbered pads on the inside. The pads are 136×58 microns on a $44\,\mu$m pitch.

The remaining 31 IO and power supply pads of $95\,\mu\text{m} \times 95\,\mu\text{m}$ are located along the back edge of the chip at a 225μm pitch. There are no pads on the side to allow side by side mounting.

The clock and trigger inputs are of the LVDS type, while the remaining digital inputs require switching at full CMOS swing.

7.7.2 VFAT-128

In view of the fact that the APV does not have self-trigger functionality, the initiative was taken in the microelectronics group at CERN to develop a trigger front-end chip. This chip, called VFAT-128, is based on the ATLAS tracker front end (SCT [3]). It converts the analog information immediately to the digital domain, giving a yes/no answer as to whether a particle hit was present on the detector channel or not. The VFAT-128 chip block diagram is shown in Fig. 7.10.

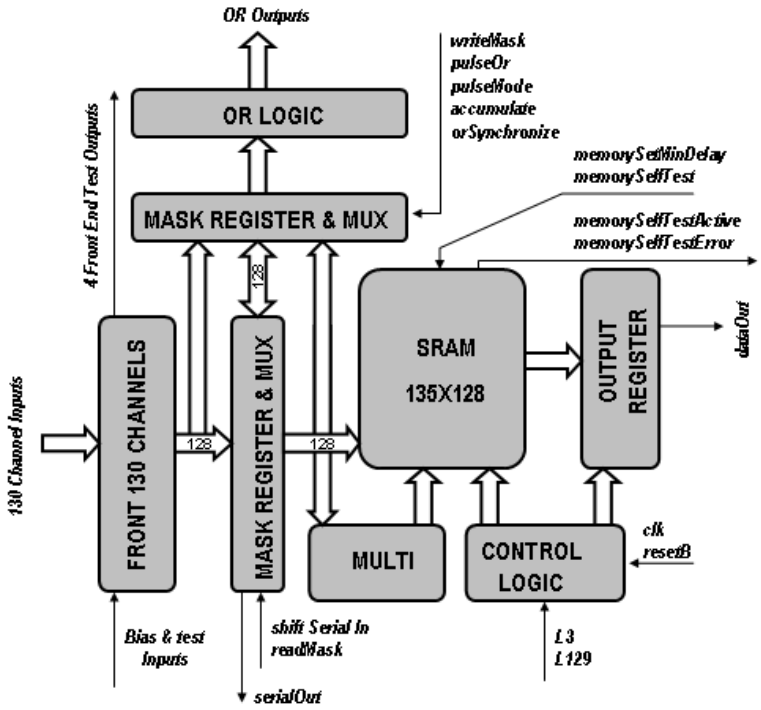

Figure 7.10: The VFAT-128 block diagram [3]

The data coming form 130 detector inputs is amplified, shaped and compared to the threshold in the front-end; a single 0/1 bit information for each channel is generated here. The data (so far asynchronous) is latched in the **Front Register** and then stored in the **SRAM** for 128 clock cycles. Additionally, the number of hits in the current time slice is counted by the multiplicity logic (block **Multi**) and also stored in the memory. When requested (L3 or L129 signal) the data from the memory is sent out (see **Control Logic** and **Readout Data Format** sections for details).

The **OR LOGIC** block generates ten OR output signals either directly from the **Front-End** outputs, or using the synchronized output of the **Front Register** (See **OR Logic** section for details).

The building blocks of the chip will be described in more detail later.

Fig. 7.11 shows the schematic diagram of one channel of the VFAT chip. The **front-end** channel comprises three basic blocks: fast transimpedance preamplifier with 14ns peaking time, shaper providing additional amplification and integration of the signal and differential discriminator stage. The preamplifier stage is designed as a fast transimpedance amplifier employing an active feedback circuit. The choice of the architecture was driven by the possibility to obtain much higher bandwidth of the preamplifier stage than in the case of simple resistive feedback using low-resistivity polysilicon available in the process used.

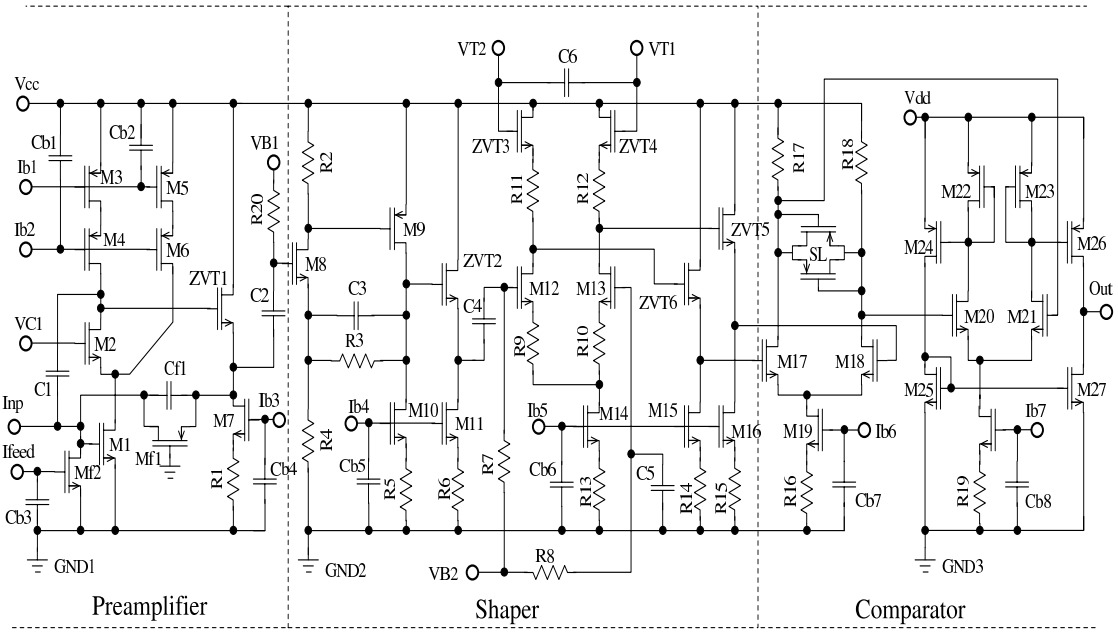

Figure 7.11: Schematic diagram of one channel of the VFAT chip

Fig. 7.12 shows the expected noise performance of the front end, which is very similar to that of the ATLAS tracker chip. The detector capacitance will depend on the type of detector. For regular strips in our geometry the detector capacitance will not exceed 10 pF, so the noise should be less than 700 electrons (compared to a most probable signal of 24000 electrons for a 300 μm thick detector).

The **front register** is a 128-bit register which feeds the 128 bits of the memory. When both shift and readMask signals are inactive it just latches the data coming from the Front-End. When shift is active the Font-Register is loaded serially with serialIn as input data, sending serialOut out. The Front Register is used to load and read Mask Register. It can also be used to readout the Front-End data. Check the **Mask Register and MUX** section for detailed description of the control signals.

The **multiplicity logic** is a combinatorial logic which counts the number of hits in the 128-bit synchronized input data and sends the 7-bit number to the memory. NOTE: the output value is the same for 127 and 128 hits - in both cases 127 is sent out.

The **memory** is a dual ported static RAM, which was built using Kostas Kloukinas' memory blocks as a basis. The main modifications are:

* readout amplifiers were added,

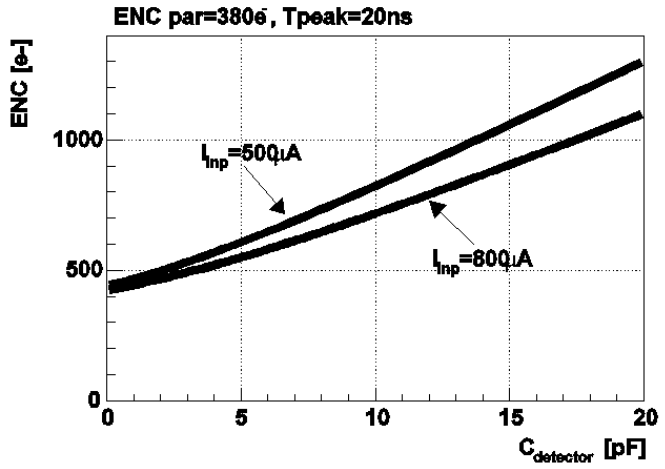

Figure 7.12: Expected noise performance of the VFAT front end

* a new control logic was designed, which is now a fully asynchronous state machine, which is triggered by the rising edge of the clock, and performing read and write in the same clock cycle.

The memory has built-in self-test, which can be triggered by asserting the *memorySelfTest* signal. During self-test execution the *memorySelfTestActive* flag is set to high. If an error is encountered, the *memorySelfTestFlag* is set high, and remains high until the reset is sent to the chip.

The **output register** is a shift register which is loaded in parallel. For each L3 trigger 3 data samples (time slices) are loaded from the memory into the register and serially shifted out. Load **Readout Data Format** section for more information about output data format.

The **Control Logic** drives the memory adresses and read/write signals, as well as the Output Register signals. There are two trigger signals processed by the Control Logic: L3 - when asserted, the three data samples are copied from the memory into the output register and shifted out; during the readout incoming data is still written into the memory; L129 - when asserted, writing into memory is stopped and the whole memory contents is dumped to the data output (via Output Register). 129 data samples are sent out (the 129^{th} is the copy of the first one). NOTE: no trigger is accepted during the data readout.

The Mask Register is a 128-bit register used to mask data signals coming to the OR Logic. It is loaded from the Front Register and can be read back via Front Register. The masked input data can be selected using orSynchronize input signal. When the orSynchronize is set to 0, the data comes directly from the Front-End, otherwise the data latched by the Front Register is used. The Mask Register can be switched into the accumulation mode using the accumulate input signal. In this mode the data coming from the Front-End is sampled each clock cycle and accumulated - the register hits stay in the Mask Register until it is rewritten. The functionality of the Mask Register and Front Register is described in Table 7.1.

The **OR Logic** generates ten OR signals (*OR_PREV,OR0, ... ,OR7,OR_NEXT*) from either the masked **Front-End** data or the masked synchronized **Front-Register** data (the selection is done using the *orSynchronize* signal. The method of creating the OR signals is explained in Fig. 7.13. The *OR_PREV* is the logic OR of the first four data bits. Then, each 24-input-OR gate takes 16 data bits + 4 additional bits from left and right - so each two consecutive OR gates have 8 inputs in common. Finally, *OR_NEXT* is generated from the last four data bits.

All the logic is fully asynchronous, so the OR outputs can be analysed without clock running if the **Mask Register** is loaded before and *orSynchronise* signal is set low. On the other hand the OR outputs can be kept quiet by setting the mask to one for all the channels, while the data still will be available via the **Front-Register** or memory and the **Output Register**.

The chip can be set in the **Pulse Mode** using the *Pulse Mode* input. The pulse mode is intended to

accumulate	shift	readMask	writeMask	Mask Register	Front Register
0	0	0	0	Note modified	Latches data from the Front-End.
0	0	0	1	Loaded from the Front Register.	Latches data from the Front-End.
0	0	1	0	Not modified.	Loaded from the Mask Register.
0	1	0	0	Not modified.	Shifted. (reading *serialIn*, sending *serialOut*)
1	0	0	0	Latches data from the Front-End and accumulates hits.	Latches data from the Front-End.
1	1	0	0	As above.	Shifted.
1	0	1	0	As above.	Loaded from the Mask Register.
All other combinations				Not modified.	Not modified.

Table 7.1: Mask Register and Front Register functionality

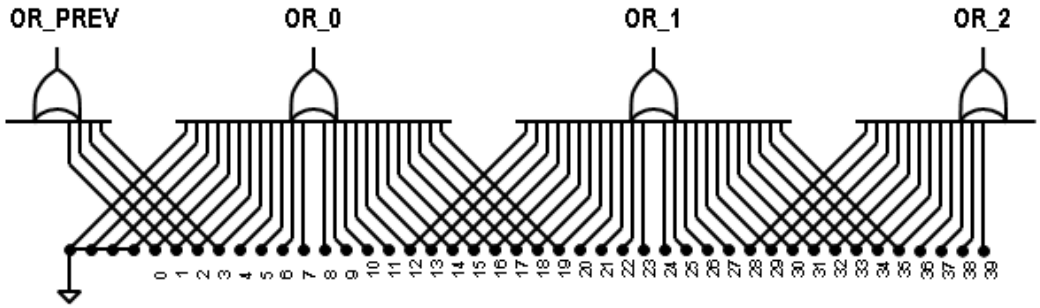

Figure 7.13: OR logic to combine the comparator outputs on the VFAT chip to generate the trigger signals

be used for testing the 'OR' functionality. When the pulse mode is active and the *pulseOr* is inactive, the **OR logic** is beeing fed with zeros. Switching the *pulseOr* to one will send the pattern currently stored in the M**ask Register** to the **OR logic**. This way the OR logic can be thoroughfully tested using any pattern/timing combination (as the *pulseOR* is applied asynchronously).

The readout data format is as follows: after receiving the L3 trigger, the chip sends out serially three data frames (for three timeslices). These data frames are defined in Tab. 7.2 The whole frame is 150 bits long. When L129 trigger is sent, the chips sends 129 data frames (this is the full memory dump). The last frame is the copy of the first one. The L3 signal takes priority over the L129: if both are asserted at the same time, L3 will be executed. During data readout no triggers are accepted.

A die picture of the VFAT is presented in Fig. 7.14.

7.7.3 APV and VFAT compatibility

One key strategy to limit the number of different items to be developed for the TOTEM experiment is standardization. Although the VFAT and the APV differ significantly, considerable savings could be made if the boards on which they are mounted would look identical to the remainder of the system. The boards will have to be different for a number of reasons including the different pad layout, but we will try

<HEADER> <ADDRESS> <DATA> <TRAILER>
where:
<HEADER>=0101
<ADDRESS>=7-bit address corresponding to the memory location (MSB first);
this is not the physical location on the chip however,
because the addresses are internally gray-encoded.
<DATA>=<CHANNEL DATA><MULTIPLICITY DATA>
<CHANNEL DATA>=128 bits of front-end data, channel #0 first;
<MULTIPLICITY DATA>=7-bit integer showing the number of hits (“1”) in the
CHANNEL DATA; for 128 hits it shows 127. MSB first.
<TRAILER>=1000

Table 7.2: Schematic overview of one data frame sent by the VFAT chip

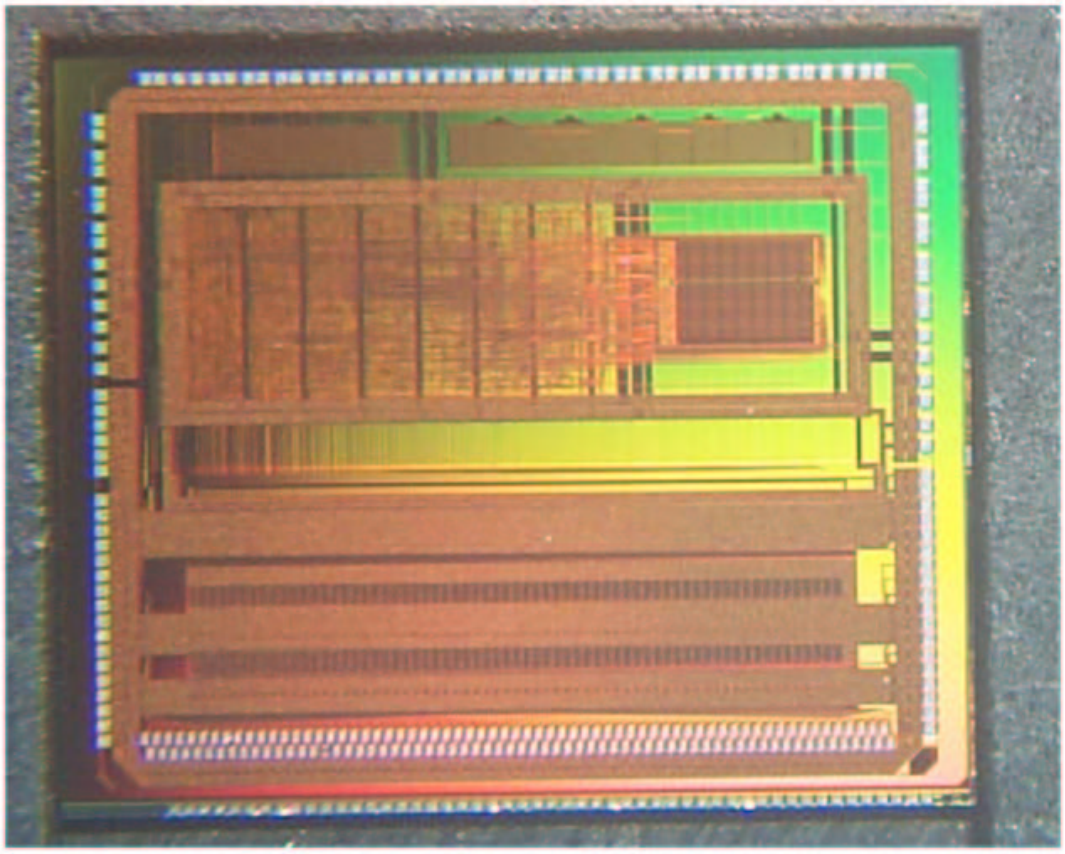

Figure 7.14: Die picture of the VFAT [3]. The input pads to be connected to the detector are located on the bottom. An important difference between the VFAT and the APV is that the VFAT in its current version has pads on the sides of the chip requiring additional spacing between front end chips for bonding

to make the readout channel of the trigger planes compatible with the APV readout. Challenges in this area exist, namely in the fine details which require to make the headers sent by both APV and VFAT and their control signals compatible. This is currently under study, from the differences in header and frame length it seems that it is likely that some redesign of the trigger chip will be desirable to make it compatible with the APV.

7.8 Roman Pot Detector Plane Board Descriptions

7.8.1 General Strategy

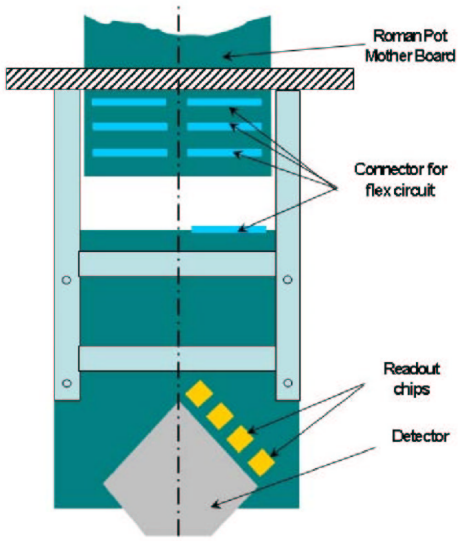

Figure 7.15: Front view of a detector board mounted in the Roman Pot. To allow close face-to-face mounting of the detector boards within the Roman Pot, electronics will only be mounted on the right side of the symmetry axis (dotted line) of the board. The connection to the feedthrough board will be done by means of a flex circuit

As described in Chapter 5 the sensitive area of the silicon detectors has an hexagonal shape. It was decided to carry out the pitch adaptation from the strips to the readout chip inputs directly on the detector silicon; this eliminates the need for a separate pitch adapter, which is costly, would take too much space in our environment, and could also present some reliability risk.

To minimize the pitch between subsequent detector planes in the Roman Pot, it was decided to try to fit all the electronics on one side of the board, to the right in a top view (see Fig. 7.15), so that when two planes are mounted face-to-face, the space to fit components is only necessary once. In addition, this should normally reduce the interference between these two planes. The connection from these planes to the feedthrough card (see section on detector segmentation), will be carried out by means of a flex circuit.

As mentioned before, the baseline option is to bring the electrical signals via the feedthrough to the outside of the Roman Pot, where the signals are converted to optical signals for transfer to the control room. Maybe at a later stage an optical feedthrough might be considered in combination with a mounting of the optohybrid within the Roman Pot.

One question raised was whether the detector could be unmounted from the board should it be defective, so that it is possible to recover the board for a new detector. This will be investigated. It will in any case be possible only a few times for the same board, as this would require the wirebonds between detector and electronics to be redone. Normally, bond pads will only withstand a few bonding iterations.

7.8.2 APV board

Given the very limited physical space in the Roman Pot, it would be desirable to embed the full CMS hybrid containing the APVs into the board which goes in the Roman Pot: this would mean that the components normally intended for the hybrid would be mounted directly on this board. Otherwise the spacing between planes will have to be increased to accommodate the hybrid on top of the board.

However, it might be that in a first phase this cannot be done due to time constraints. In that case an APV provisional board will be designed which will receive the hybrid in fully mounted form: it will have to comprise also the pitch adaptation between the detector and the hybrid which will not be geometrically matched in that case.

The board needs to read out a 512-strips detector which, and will therefore contain four APV's and incorporate the full CMS hybrid. The connector and flex carrying the signals will be the same as for the trigger board, the lines devoted to trigger signals for the VFAT board will be grounded.

7.8.3 VFAT trigger board

The VFAT trigger board will be made compatible with the APV board, so that both can receive the same detector, and can interface to the same readout system. The board will contain 4 VFAT chips which each have 10 trigger outputs (see the description of the chip). However, if data is transferred to the counting room, it might be sufficient to only transfer 8 of those. This means that for every bunch crossing, a VFAT trigger board will produce 32 to 40 trigger data bits. These will need to be sent to the central trigger box by means of optical serial links. The digital optical link based on the GOL can transfer 32 bits in a 25 ns period. Given the redundancy of two of the trigger outputs on the VFAT it seems sensible to have that data sent over one serial link per card.

7.9 Roman Pot Mother Board and Timing and Control Station Description

7.9.1 List of functions

In principle the Roman Pot Mother Board (Fig. 7.16) should be the board which gathers all signals from and to one Roman Pot. It interfaces with the different planes in the pot, both the trigger and the APV planes, and receives and sends the optical signals from and to the control room. It also receives the electrical power and the high voltage biases for the detectors in the Roman Pot. It might be that the Roman Pot Mother Board will have to be split in several boards. The optical components will be mounted on this card as mezzanine cards, which should keep the system very modular. If a control ring is to be envisaged which covers more than one Roman Pot, some connection between Roman Pot Mother boards has to be foreseen.

As mentioned in the section on control, the respective responsibilities of the TOTEM experiment and the machine for the control of the Roman Pots are still under discussion. In case the experiment will be responsible, the CCU control system could be expanded to include also the control for the Roman Pot itself, which would provide an elegant solution. This assumes that motors moving the pot can be found which are compatible with I2C control which is the protocol standard for the CCU system. The power for these motors would normally not be provided to the mother board, but to the motor system, which in this scenario would be controlled via the CCU. If the Mother Board also takes care of this control, it essentially incorporates the TTC Station function. If the control is separate, it might be that still some functions (trigger and timing) are taken care of by the Roman Pot Mother Board. Currently TOTEM is in close contact with the CMS people to define the different options.

7.9.2 Cables, Crates and Counting Room Electronics

In the counting room there will be the Central TOTEM Trigger Processor, readout electronics for the tracking data (FED): the control electronics for the Roman Pot detectors (FEC), and the connections between the control room and the Roman Pots will be carried out by means of optical fibers. These fibers will first be grouped on patch panels near the Roman Pot and in the Counting Room, while the long distance (up to 220 m) will be covered by the optical ribbon cable which comprises 96 optical fibers.

Apart from the optical data communication, it will be necessary to provide power supplies and some other electrical connections. For the Roman Pot stations at 220 m distance, there is some cavern foreseen at about 30 m away where some of these services can be installed in racks. These services are to be wired to the Roman Pots by means of the CMS standard multi service electrical cable.

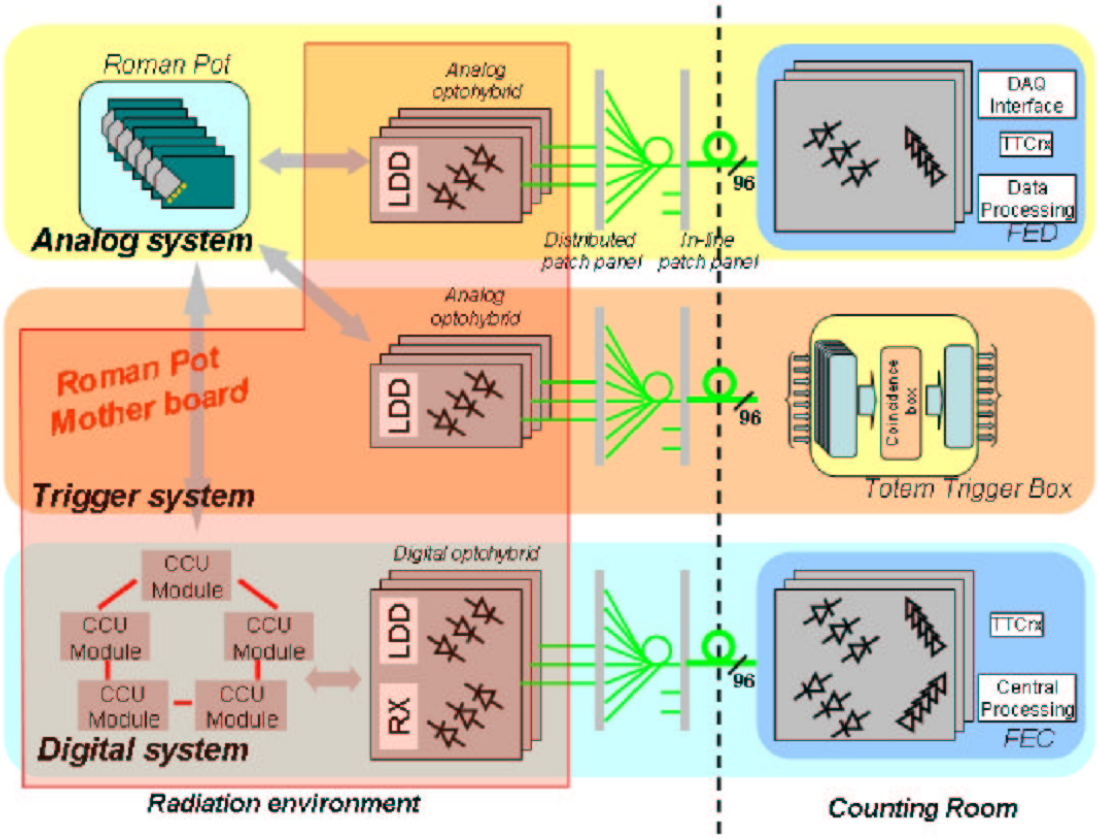

Figure 7.16: Overview of the Roman Pot electronics system and the part which should be part of by the Roman Pot Mother Board

References

[1] The CMS Technical Proposal. CERN/LHCC 94-38, LHCC/P1 (1994).

[2] J. Troska et al. "Optical Readout and Control Systems for the CMS Tracker", submitted to IEEE.

[3] R. Szczygiel and J. Kaplon "The VFAT-128 Test Chip User Guide", CERN (2003).

[4] P. Moreira et al.:"A Radiation Tolerant Gigabit Serializer for LHC Data Transmission". LHC Electronics Board Workshop (2001). http://proj-gol.web.cern.ch/proj-gol.

[5] L. Jones. "APV25-S1 User Guide Version 2.2". http://www.ins.clrc.ac.uk/INS/Electronic_Systems/Microelectronics_Design/Projects/High_Energy_Physics/CMS/APV25-S1/index.html.

[6] http://ttc.web.cern.ch/TTC/intro.html.

8 Inelastic Detectors

8.1 Measurement of the inelastic rate

An important part of the experimental program of TOTEM at the LHC is the measurement of the total cross-section with the luminosity-independent method [1]. This method requires the simultaneous determination of elastic scattering at low momentum transfer and the total inelastic rate. The detector for the measurement of the inelastic rate has to be in an angular range such as to detect particles from most of the events. The fraction which is not seen has to be evaluated properly and accounted for.

The total cross-section and the integrated luminosity $\mathcal{L}$ of the machine are related by the equation

$$N_{el} \; + \; N_{inel} \; = \; \mathcal{L} \; \sigma_{tot}$$

where N_{el} and N_{inel} are the observed rates of elastic and inelastic interactions, respectively. The measurement of the total inelastic rate will be made by measuring with precision the efficiency and geometric acceptance of tracking telescopes positioned in the forward region. This chapter is devoted to the measurement of the total inelastic rate.

8.1.1 Detector requirements

A study of the two large categories of events, minimum bias and diffractive, that make up the inelastic rate will be discussed later in more detail. Properly tuned event generators enable the calculation of the fraction that can be seen for any practical setup. The *forward inelastic detector* must:

- provide a fully inclusive trigger for diffractive events, with an expected loss of the inelastic rate of a few %;
- enable the reconstruction of the vertex of an event, to disentangle beam-beam events from background; and
- achieve a detector position that is left-right symmetric with respect to the IP, to better control the systematic uncertainties.

In our Technical Proposal [2] we have shown that a detector has to cover, with some flexibility in the choice of the angular range, approximately four units of rapidity on each side of the IP. The losses for the actual detector are calculated and discussed below in the section on simulation and trigger.

The inelastic cross-section at the LHC center-of-mass energy is expected to be 85 mb [3]. Considering the large fraction of cross-section seen by the detectors, the rate of inelastic events will be very high, even for the specific TOTEM runs with high-β^* or low luminosity for the simultaneous measurement of the inelastic and elastic scattering.

8.1.2 Design consideration and Detector description

The telescope to trigger and partially reconstruct the inelastic events will be placed in the forward region of CMS (see Fig. 1.1). In order to cover a sufficient range in rapidity, it will be split in two telescopes:

- T1 ($3.1 \; \leq \; |\eta| \; \leq \; 4.7$) will be installed in the End Cap of CMS in a detector-free region between the vacuum chamber and the iron of the magnet on each side. The region reserved for TOTEM is between 7.5 m and 10.5 m from the IP.

- T2 ($5.3 \leq |\eta| \leq 6.7$) will be installed in the forward shielding of CMS between the vacuum chamber and the inner shielding of the HF calorimeter, in front of the newly proposed CMS CASTOR calorimeter, at a distance of 13.5 m from the IP.

Multiwire Proportional Chambers with cathode R/O (Cathode Strip Chamber or CSC) have been chosen as the detectors for T1. This choice has been dictated by the characteristic features of these detectors whose properties are well known [4] and by their ruggedness. The TOTEM CSCs will be very similar to the analogous detectors being built for both ATLAS [5] and CMS [6], using the same technology and tailoring the relevant parameters to the TOTEM requirements. The TOTEM detectors will be described in detail in one of the following sections.

This technology is, in fact, well suited for the requirements for T1, in which each detector plane is made up of 6 overlapping detectors to obtain a full azimuthal coverage. The solution proposed also makes it possible to obtain an overlap of the sensitive region between the two halves of the telescope. The telescope is composed of 5 planes of detectors distributed over a distance of 2.5 m to properly track the traversing particles to the interaction point and reconstruct the vertex of the interaction. The precision should be sufficient to show that the vertex is reconstructed safely inside the vacuum pipe. To allow a fast pattern recognition in events with large particle multiplicity and to reject background, each detector plane will be slightly rotated with respect to the others. Tracks from beam-beam events display a projective topology. Hence the stereo angle layout is a very powerful tool to solve ambiguities in high multiplicity events.

The amount of material in the detector has to be kept to a minimum so as not to degrade the performance of the HF calorimeter which covers the same angular range and sits behind T1. In the present design of the detector, the amount of material in front of HF amounts to $\simeq 10.8\%$ radiation lengths and to $\simeq 3.4\%$ interaction lengths in most of the acceptance region, and up to $\simeq 30\%$ radiation lengths and to $\simeq 10\%$ interaction lengths in the small, localized regions corresponding to the chamber frames.

The following table details the materials present in the detectors.

	1 detector	5 detectors	Material	Rad. Length	Int. length
	(mm)	(mm)	(g/cm^2)	(%)	(%)
copper electrodes	0.07	0.3	0.3	2.4	0.2
Honeycomb (Nomex)	30	150	0.48	1.20	0.6
G10 (FR4 skins)	2.8	14	2.38	7.21	2.6
total (no frames)			3.2	10.8	3.4

Table 8.1: Materials in the TOTEM CSC's

A solution for an easy installation in CMS which fulfills all the requirements and can be accomplished in the short time available has been found (see Section 8.5.5) and discussed in detail with CMS.

The choice of the detector technology is more delicate in the case of T2: the requirements on spatial resolution are more stringent for $|\eta|$ between 5.3 and 6.7 . The final design of the vacuum chamber in the forward region between 10.7 m and 18 m has only recently been defined and agreed upon to be consistent with the desire of CMS to fit a new calorimeter in the region previously allocated to the T2 telescope.

The vacuum chamber that traverses T2 is cylindrical in shape. This makes the detector region very sensitive to interactions in the vacuum chamber wall. The choice has to favour detector technologies that allow building a telescope with the same $\frac{\Delta\theta}{\theta}$ as T1, but with a length (lever arm) of only 40 cm, in order to minimize the probability of detecting secondary particles generated by interactions in the beam-pipe. T2 will detect mainly the diffractive component of the inelastic cross-section and must be able to cope with the special topologies of this category of events.

Two possible technologies are under study and will be briefly described in Section 8.7. These are:

- Gas Electron Multiplier (GEM) with pad and strip R/O [11]; and

- silicon microstrips for tracking, using the same detectors as designed by CMS for the Tracker Outer Barrel.

The first technology considered is the recent GEM technology. This technology gives the freedom to design detectors with any geometry and to not be dependent on the geometry imposed by wires or strips. Possible T1 compatibility for the electronics is another interesting possibility in terms of system integration and operation. The detector has good characteristics in terms of radiation hardness and rate capability which are consistent with the TOTEM requirements.

The other solution has its appeal in the fact that the detectors have already been designed and engineered and would need simply to be integrated into a suitable telescope. The T2 telescope for the silicon solution will have some of its planes equipped with the same trigger electronics developed for the detectors in the Roman Pots.

Both solutions have been evaluated and estimates of the cost of each solution will be presented later.

8.1.3 CMS vacuum pipe in IP5

The shape of the CMS vacuum chamber in the forward region has been optimized by CMS and is suitable for both CMS and TOTEM operation. The present design is also considered good for the high luminosities of 10^{34} cm^{-2} s^{-1}. For simplicity, the description of the vacuum chamber considers two regions: the End Cap region from the IP to 10.6 m (end of the CMS End Cap) and the Forward region from 10.6 m to 18 m (end of the experimental cavern UX5).

The Endcap region vacuum chamber (Fig. 8.1) is made of two cones pointing to the IP, joined at the center by a cylindrical section. The inner surface of the cone is very carefully aligned to be at $\eta = 4.9$. The central part (± 2 m around the IP) is a beryllium cylinder with an inner diameter of 58 mm and a wall thickness of 0.8 mm.

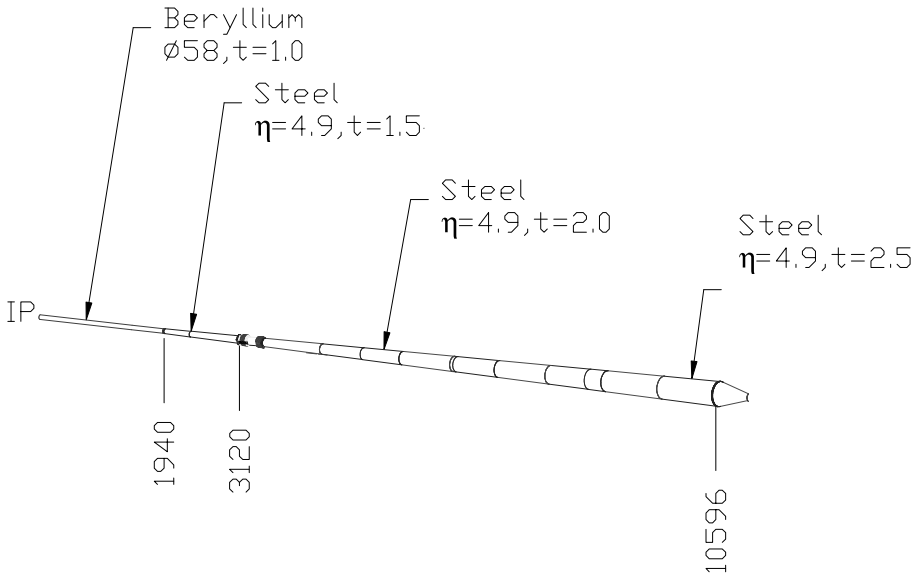

Figure 8.1: The End Cap region vacuum pipe

Simulations of the radiation background have shown that this shape minimizes the background induced in the muon chamber of CMS. At the same time the beryllium section has been extended to offer a minimum of material in front of T1. The central and the conical sections are connected by an expansion bellow, dimensioned to absorb the thermal dilatation of the long pipe during the bake-out. The End Cap vacuum chamber is supported by the CMS Tracker at 4 m from the IP and by four stainless steel wires

at the end of the conical shape at 10.6 m where the vacuum chamber has reached an inner diameter of 313.8 mm.

At 10.6 m from the IP, the Forward region vacuum chamber begins (Figs. 8.2 and 8.3). A conical section with an angle of 30 degrees reduces the diameter before the HF to 170 mm. Another cone section pointing to the IP and corresponding to $\eta = 5.53$ runs inside the HF.

The region to accommodate the T2 telescope begins at $z = 13,340$ mm where the diameter of the vacuum pipe drops with a step to an inner diameter of 55 mm. The transition in the diameter of the vacuum chamber is performed according to the LHC RF requirements with a perforated conical copper RF shield (0.2 mm thick). The thin stainless steel window (0.1 mm thick) is roughly perpendicular to the particle trajectories from the IP. Due to the sudden change in vacuum chamber cross-section, ion pumps must be installed at this position to provide the required pumping speed at the IP. T2 is installed at 13,560 mm immediately behind these pumps, which have been designed to stay outside of $\eta = 5.53$ where the acceptance for T2 should begin.

The vacuum chamber is cylindrical with an inner diameter of 55 mm up to 16 m where a bellows is needed to compensate for the imbalance of the hydrostatic pressure on the long conical shape and to compensate for the thermal dilatation of the vacuum chamber during the bake-out operation. After the bellow and up to the *fixed nose* at 18 m, the vacuum chamber diameter increases to 400 mm. The inner diameter of 55 mm for the vacuum chamber in the T2 and CASTOR region is the minimum acceptable to the Vacuum Group after evaluating the vacuum stability, beam-gas induced background and a beam aperture compatible with the beam size. Vacuum simulations have shown [12] that 55 mm is a safe value.

The forward vacuum chamber between the two bellows is supported by the wires at 10.6 m. Finite element calculations show that the maximum sag is less then 4 mm with stresses well below the limit. During the shutdown of the machine and the opening of the CMS Endcap, T2 and HF are removed and a temporary tube, cantilevered from the fix nose, supports the vacuum chamber at the flange at 10,600 mm.

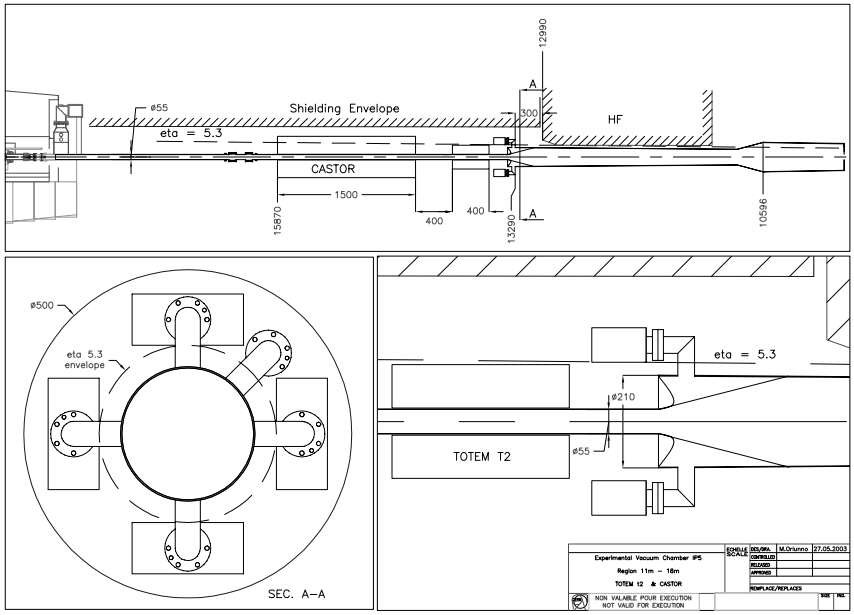

Figure 8.2: The forward region vacuum pipe: a section of the T2 region (upper), a section of the vacuum pump in front of T2 (lower left) and a zoomed section of T2 (lower right)

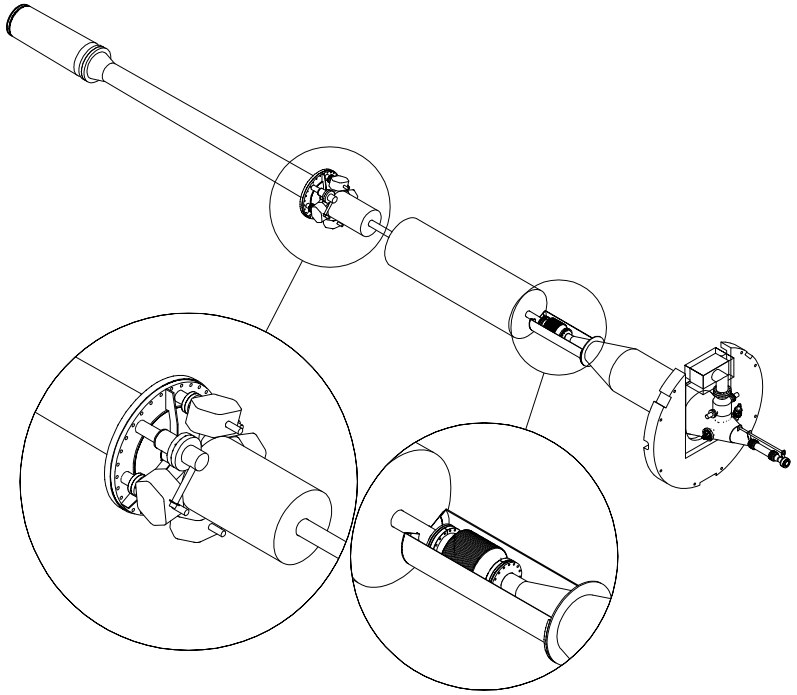

Figure 8.3: The forward region vacuum pipe: a 3D view. The inserts show the details of the pump in front of T2 and of the bellow behind the CMS CASTOR detector

Particle	T1	T2
neutrons	$10^6 \div 10^7$	$10^7 \div 10^8$
charged hadrons and μ	$10^6 \div 10^7$	$10^5 \div 10^6$
photons	$10^6 \div 10^7$	$10^7 \div 10^8$
CMS Doses in Gray for 10 years of LHCC		
	10^3	10^5

Table 8.2: Particle fluxes (in cm^{-2} s^{-1}) and doses in the region of T1 and T2 for a peak luminosity of 10^{34} cm^{-2} s^{-1} (from CMS)

8.1.4 Radiation environment

Particle fluxes and radiation doses

These figures, taken from the CMS Muon TDR [6], assume a low luminosity start-up phase and integrate over 10 years to a luminosity of 5×10^5 pb^{-1} with 5×10^7 s of operation per year of LHC.

More recent evaluations [7] have confirmed the figures reproduced in Table 8.2, which is calculated for the peak luminosity of 10^{34} cm^{-2} s^{-1}(see pag. C13 of [6]).

To obtain the dose received in the first years of operation by the TOTEM inelastic telescopes, one can assume that each of the 3 years foreseen at low luminosity with an average $\mathcal{L} \approx 10^{33}$ cm^{-2} s^{-1} contributes 1/10 of the dose for one year at design luminosity.

Assuming that the TOTEM telescopes stay installed during the first three years, these detectors will receive $\approx 4\%$ of the total luminosity foreseen for 10 years of operation.

In the angular range covered by T1 and T2 the radiation dose is evaluated by CMS to be 100 times larger than the one received by similar detectors (for example, the CSC's placed at $\eta \sim 2$), hence T1 (detector and on board electronics) will receive, in a few months of operation at $\mathcal{L} \approx 10^{33}$ cm^{-2} s^{-1}, the dose that the CMS detector can sustain in 10 years.

Therefore, we are confident that our detectors and their associated electronics (for the part that must be installed on or very near to the detectors) will be able to remain installed in CMS as long as the average luminosity over one year does not go above 10^{32} cm^{-2} s^{-1}.

For the rates in the region where T2 will be installed, there is more uncertainty: fluxes in the T2 region are one order of magnitude larger than those in the T1 region and there is more uncertainty on their evaluation. The T2 detector must be able to work up to luminosities of 10^{32} cm^{-2} s^{-1}.

T2 requires a detector technology that can withstand a larger radiation dose. If the dose proves to be larger than the values quoted, this may require the removal of the T2 electronics at the end of each TOTEM run.

8.2 T1 and T2 performance

8.2.1 Event generation and simulation

The main aim of the T1 and T2 telescopes is to count the inelastic events. The event generation has been performed with Pythia 6.158 [13]. In order to study the $p-p$ inelastic interactions, different physics processes, which can be classified in two classes with very different topologies, have been considered:

- the non-single-diffractive events (NSD) where the secondaries have a rapidity range distribution extending over the full phase space; they include the contributions of the non-diffractive minimum bias and of the double diffractive processes.
- the single diffractive events (SD): $p + p \to p + X$, where one proton is scattered quasi-elastically at very small polar angle with energy close to the beam energy. The system X which recoils against the quasi-elastically scattered proton fragments into secondaries having a typical rapidity distribution concentrated in the opposite hemisphere.

The cross-sections used for the different processes are:

$$\sigma_{NSD} = \sigma_{mb} + \sigma_{DD} \sim (58 + 7)\,\text{mb} = 65\,\text{mb} \qquad \sigma_{SD} \sim 14\,\text{mb}$$

which are in agreement with recent extrapolations and evaluations [14, 15, 16].

The detector simulation has been performed by means of the CMS framework for simulation (OSCAR [17] version 2.4.0) which is based on the Geant4 [18] simulation toolkit.

The simulation setup included the two TOTEM telescopes and the beam-pipe. To study the physics performance, the standard CMS physics cuts have been used in the simulation, but with no particular tuning of the cuts for the beam-pipe material in the very forward regions. These cuts are responsible for a low interaction rate of the primary particles in the very forward beam-pipe. However, in order to estimate the background generated by the interactions in the beam-pipe, a limited amounts of events have been simulated with lower physics cuts for the very forward beam-pipe, and the results are summarized at the end of this section and in Section 8.2.4.

The T1 telescope description is very accurate for both the support and the sensitive regions; the T2 telescope is described instead as 5 silicon circular planes with $r_{min} = 30$ mm and $r_{max} = 150$ mm, installed at 13570 mm$< |z| <$ 13970 mm.

The simulation is done as for the TOTEM dedicated runs with the CMS magnet turned off. In Section 8.3.3, we make some considerations of the degradation on the performance in the case when the magnetic field is on.

The beam-gas interactions which take place when a beam proton collides with a residual molecule in the beam-pipe vacuum can generate events of very similar topology to SD and become one of the main background sources. In order to study such processes, events have been generated, requiring Pythia to simulate the interaction of a 7 TeV proton with a proton at rest randomly placed in the beam-pipe. The parameters for the description of the residual gas chemical composition and correspondent cross-sections are the same as described in detail in Section 6.4.

Another significant source of background for the inelastic telescopes is the interaction of the scattered particles with the beam-pipe. The number of charged particles generated from secondary interactions

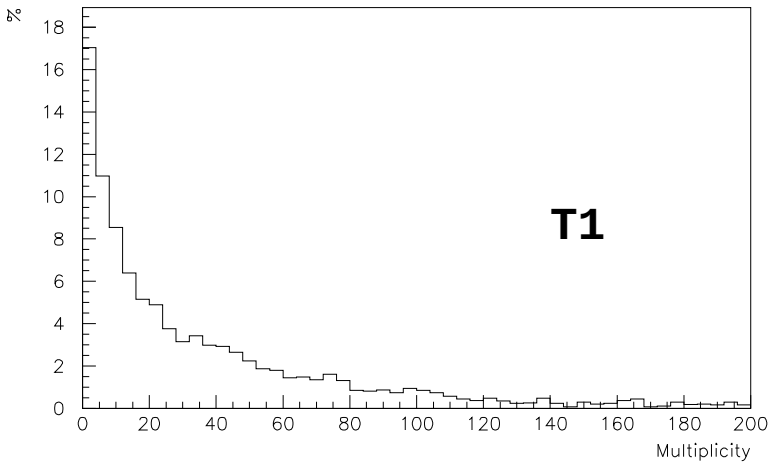

Figure 8.4: The T1 multiplicity for one arm in minimum bias events (beam-pipe included)

in the beam-pipe material is not negligible. The mean number of hits per event in one arm of the T1 telescope grows from 15 to 40 if the beam-pipe is included in the simulation; the charged particle multiplicity per event is shown in Fig. 8.4. For the T2 telescope the effect of the beam-pipe material is more evident, and the mean number of hits per event grows from ∼7 to ∼80.

8.2.2 Event identification

In order to measure the inelastic rate, the T1 telescope has to discriminate between beam-beam events and background. The strategy for the event identification is the following.

Track reconstruction is done on the triggered events (see Section 8.3) and a primary vertex fit is attempted when more than one track has been found. Since a full event reconstruction is not needed, a minimum of two tracks will be used in the fit. The track isolation, $\eta - \phi$ distribution, number of hits and χ^2 will be used as criteria for track selection.

The event identification chain is divided into three steps:

- pattern recognition: space regions (roads) with a high probability of having a track are identified;
- track reconstruction: tracks are reconstructed in the selected roads;
- vertex reconstruction: the reconstructed tracks are fitted to a primary vertex.

Pattern recognition

The inelastic event identification needs the reconstruction of tracks coming from the primary vertex, which are characterized by hits with the same rapidity and azimuthal coordinate when the magnetic field is not present. When hits from different detectors are projected on a θ-ϕ plane and then superimposed, the result is a clustering of hits in the regions where a primary track passes. These regions in the θ-ϕ plane correspond to different regions in the different detector planes (rotated by 3 degrees to each other) and are considered as roads where the tracks can be looked for. This method is not only a way to limit the track finding to a few space regions, but it is also a method to discriminate real hits from ghosts.

In fact, when the event multiplicity per detector is high, the pairing of the measured coordinates can generate fake hits. The slight rotation between adjacent planes ensures that the good pairing is always in the same $\theta - \phi$ region, while the fake ones are distributed over different roads.

This method has been tested on minimum bias events, requiring a hit per plane in a pseudo-cone of amplitude $\Delta\theta = 6 \cdot 10^{-4}$ rad and $\Delta\phi = 6 \cdot 10^{-3}$ rad. The test has shown a very high efficiency for distinguishing the good primary tracks from wrong roads (∼3% are misidentified).

Track reconstruction

The track reconstruction is performed only for the roads identified by the pattern recognition, fitting with straight lines the hits coming from at least three planes and choosing the combination with the lowest χ^2. The residuals for the direction coefficient of the fitted tracks show an RMS of $\sigma_{RMS} = 5.6 \cdot 10^{-3}$ (see Fig. 8.5).

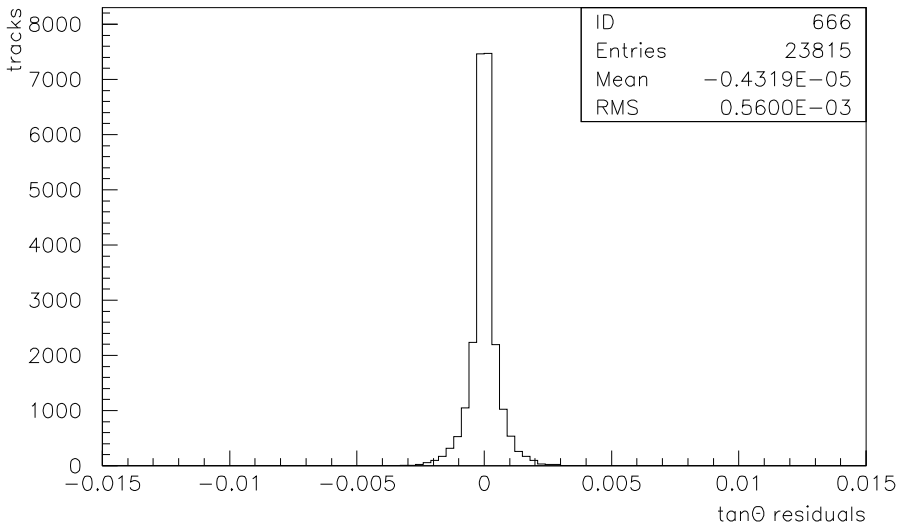

Figure 8.5: Residuals of the direction coefficient of the fitted tracks

The analysis of the track fitting results at different values of η shows that, to have an angular resolution of $d\theta/\theta \sim 1.5\%$, the uncertainty on the transverse coordinates of the hit is required to be 600 μm for T1 and 100 μm for T2.

The track multiplicities for NSD events in the T1 and T2 range are shown in Fig. 8.6.

The conditions used in the test for the road construction are quite tight and result in a very low number of possible combinations per road (usually only one). A different strategy might be to loosen the cuts on the roads and to accept more combinations in the track fitting.

Vertex reconstruction

The reconstructed tracks are submitted to an isolation criteria, before performing the vertex fit, in order to avoid complications due to the presence of jets. Applying these criteria results in a 92% efficiency.

The vertex finding follows different procedures for xy and z coordinates:

a) vertex in xy: the vertex position in the xy plane is determined from the distribution of the track coordinates in the plane $z = 0$. The procedure is acceptable since the tracks have a very low angular coefficient. Fig. 8.7 shows that the resolution in the radial coordinate R is 2.9 mm.

b) vertex in z: the z vertex position is estimated by determining the distance of minimum approach to the nominal z axis for each track and then calculating the mean value: $z_{vertex} = \langle z_{track} \rangle$. This

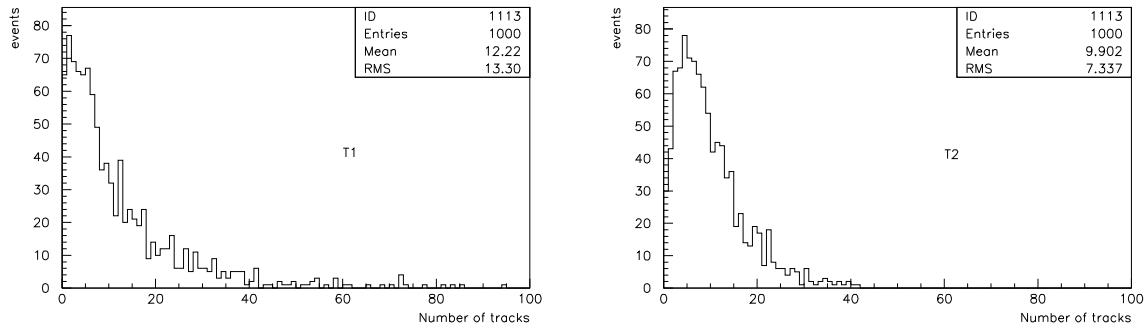

Figure 8.6: The T1 (left) and T2 (right) track multiplicities for 1000 NSD events

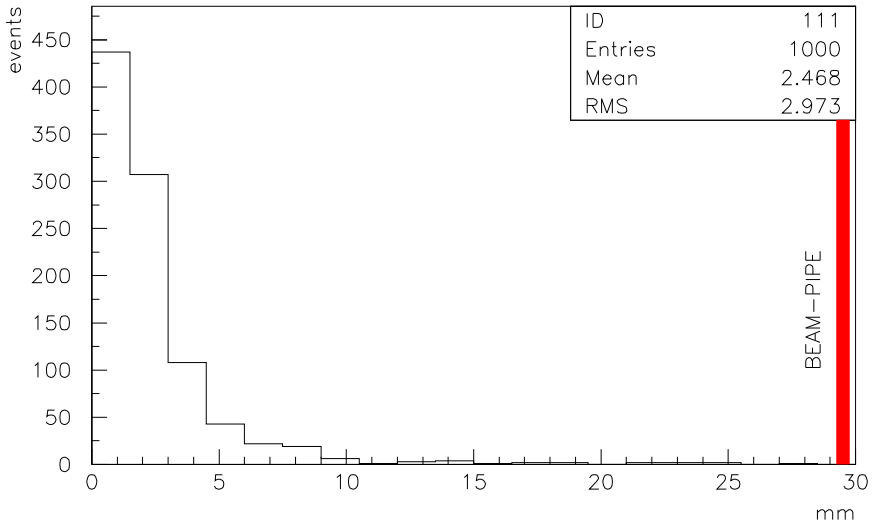

Figure 8.7: The reconstructed R-vertex position R

simple method allows the estimation of the primary vertex z coordinate and the resolution achieved on minimum bias events is $\sigma(z_{vertex}) = 4.5$ cm (see Fig. 8.8).

The final vertexing algorithm will consist of a fitting routine which will determine the point which best describes the vertex for all the considered tracks (3D vertex point).

8.2.3 Representative physics processes

The inelastic processes which are significant for the TOTEM physics can be classified into non-single-diffractive (NSD) and single diffractive (SD), as already mentioned in Section 8.2.1. The p_T and η distributions of the particles at the generation level (Figs. 8.9 and 8.10) show that the tracks have a very small p_T.

The most probable number of charged particles generated per hemisphere in the T1 rapidity range is

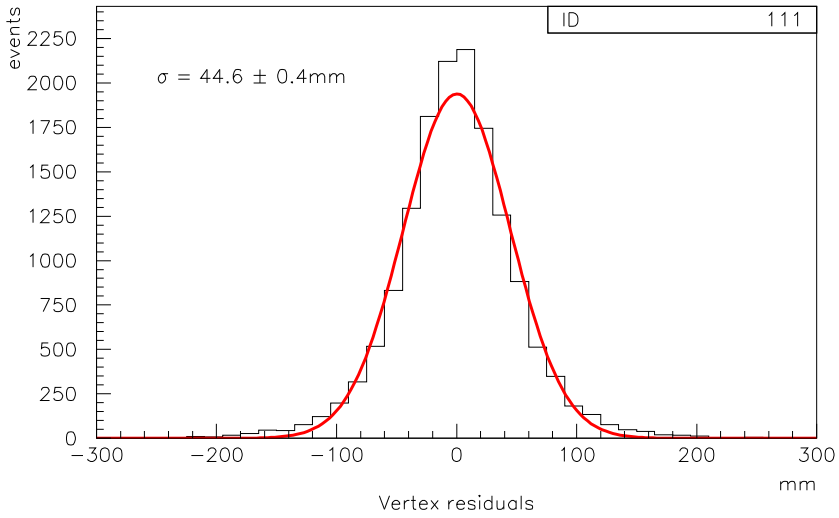

Figure 8.8: Residuals of the z-vertex position reconstruction

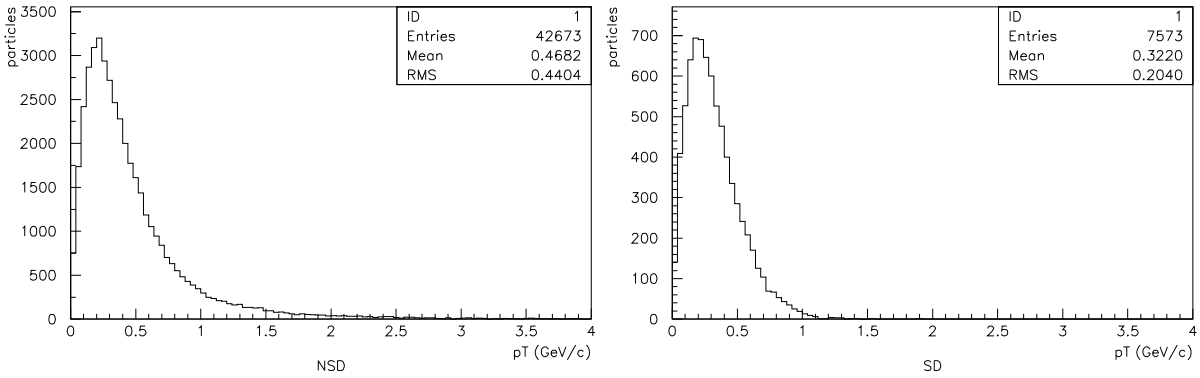

Figure 8.9: The p_T distributions for NSD (left) and SD (right) events, as generated by Pythia for 1000 events

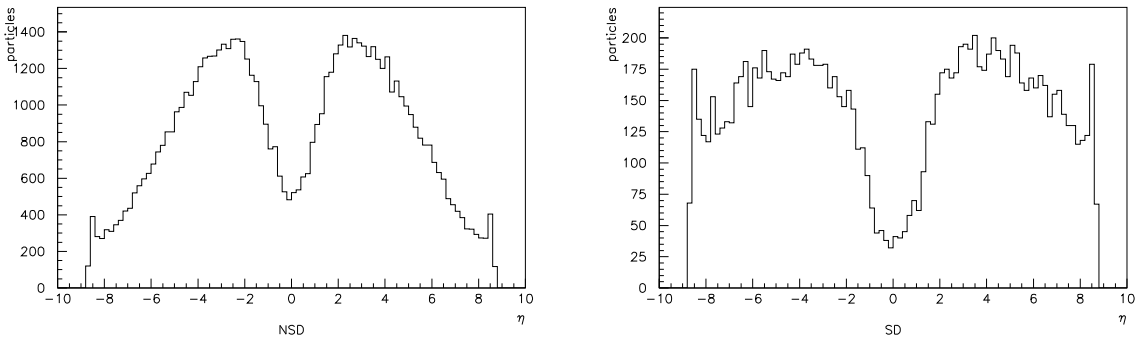

Figure 8.10: The η distributions for NSD (left) and SD (right) events, as generated by Pythia for 1000 events (a 500 MeV cut on $|p|$ has been applied)

$n_{T1}^{NSD} = 12$ for the NSD and $n_{T1}^{SD} = 2$ for the SD events, while in the T2 rapidity range the numbers are, respectively, $n_{T2}^{NSD} = 7$ and $n_{T2}^{SD} = 2$. This small multiplicity for single diffraction accounts for most of the SD losses (see Section 8.3).

Non single diffractive and single diffractive events

The triggered events (see Section 8.3) can be identified by means of the vertex reconstruction. This tool is particularly useful when a single arm trigger is considered. The requirement of a primary vertex also provides rejection of the beam-gas background: the percentage mis-identified as beam-beam events depends strongly on the z coordinate of the interaction between the incoming proton and the gas molecule. To estimate the different rates of mis-identified events, a proton coming from the left side has been simulated to interact with a proton at rest at different z positions and the right arm of the telescopes have been used to detect the particles. Three different positions have been chosen on the left side of the beam-pipe (w.r.t. the IP): -1 m, -5 m and -15 m.

Reconstructing the primary vertex and requiring that it be within 50 cm of the nominal IP rejects a huge fraction of the beam-gas events. Only 3.5% of the events generated at $z = -1$ m are mis-identified, while the percentage is well below 1% for those generated at $z = -5$ m and $z = -15$ m.

The beam-gas interactions generated in the right side have been smeared for two regions: from $z = 0$ to $z = 10$ m and from $z = 10$ m to $z = 15$ m. The result is that in the second case the rate of mis-identified events is negligible, while for the first case the rate is 2.9% over the full acceptance of T1 and T2. The pattern recognition tuned to reconstruct the primary tracks is a powerful tool to reject beam-gas events, whose main contribution is given by the interactions which take place in the 30-40 cm of beam-pipe near the IP. Moreover, tagging a proton in the Roman Pots is a useful tool to discriminate single diffractive from beam-gas events (see Section 8.3).

Geometric acceptance

The geometric acceptance has been estimated by performing a scan which has covered 6 rapidity units ($2 < |\eta| < 8$) and the full ϕ range. In this simulation, the two telescopes have full acceptance in the regions $3.2 < |\eta| < 4.7$ and $5.3 < |\eta| < 6.7$. With a reduced acceptance, the covered regions extend to $3 < |\eta| < 4.9$ and $5.2 < |\eta| < 6.8$. The results are shown in Fig. 8.11. The different shapes of the two telescopes (conical T1 and cylindrical T2) result in different slopes in the acceptance.

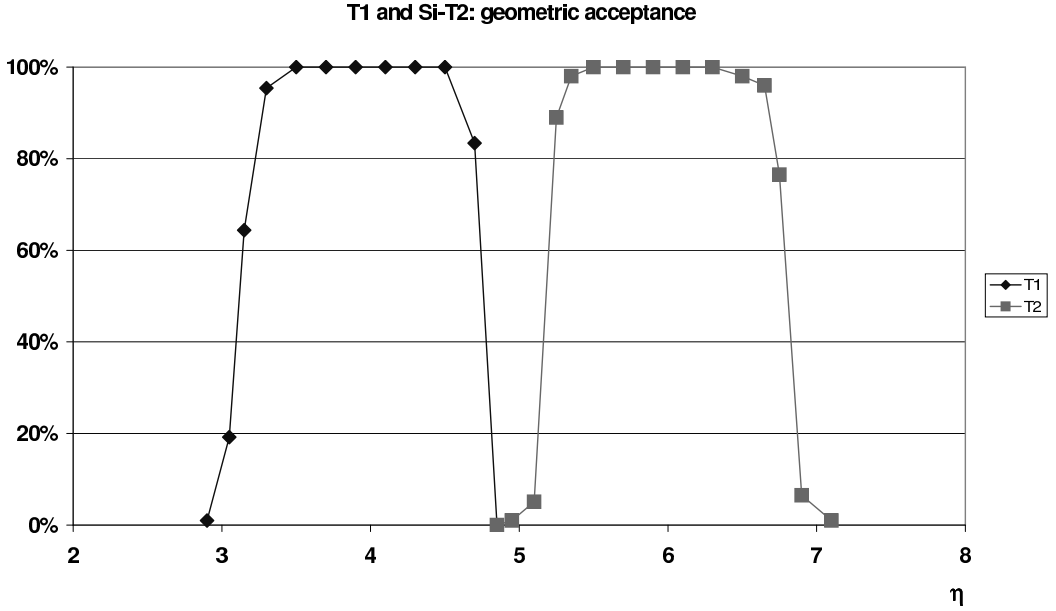

Figure 8.11: The T1 and T2 geometric acceptances

8.2.4 Hit rate

The detailed simulation of the detectors allows the calculation of the detector rates, which are an important parameter to determine the requirement of the front-end electronics and, finally, the data flow.

The average hit rate per strip and per wire has been simulated, using minimum bias events and assuming that each charged particle generates a signal on one wire and on three adjacent strips. This choice conforms with the measurements performed during the last test beam.

The calculated average hit rate for the first T1 plane and for a luminosity of 10^{28} cm^{-2} s^{-1} is shown in Figs. 8.12(left) and 8.12(right).

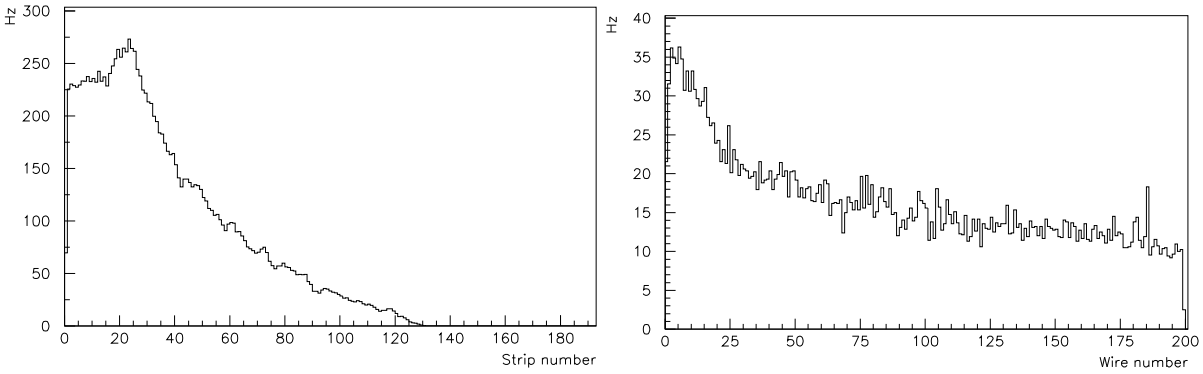

Figure 8.12: The 5mm strip (left) and wire (right) occupancy for 10^{28} $cm^{-2}s^{-1}$

8.3 Trigger

8.3.1 Single and double arm trigger considerations

Given the event categories to be identified, TOTEM needs to consider two trigger topologies: single arm and double arm. In the first case, each arm of the telescopes can trigger the event, while in the second, the event is triggered only if both arms have observed at least some particles. A particle is considered observed if it has traversed at least two planes of the same telescope. This choice tries to reproduce the hardware trigger which will select the event if there are two hits on two different planes of the telescope.

The double arm trigger is, as expected, rather clean and allows the reconstruction of the collision vertex without any particular complication, because charged tracks at relatively large angles are observed in both hemispheres.

The single arm trigger detects a large fraction of the SD events. It may be affected by a large background and the intrinsic inefficiencies, due partly to the η coverage, make the reconstruction of the collision vertex more difficult.

The double arm trigger can be used to select a large number of the events generated by central interactions, while the single arm can be used to recover the lost central events and the single diffractive events.

A large data set of NSD and SD events has been analyzed in order to estimate the event loss for the single and double arm triggers. In Table 8.3, the double arm trigger loss rates are shown for NSD and minimum bias events, while Table 8.4 shows the loss rates for the single arm trigger.

Double arm	*MB*			DD			$NSD = MB + DD$		
Type	T1+T2	T1	T2	T1+T2	T1	T2	T1+T2	T1	T2
2(L*R)	0.5	3.7	5.5	39.5	59.4	48.2	4.7	9.7	10.1
3(L*R)	0.5	3.8	5.9	40.4	61.4	49.5	4.8	10.0	10.6
4(L*R)	0.6	4.2	6.8	41.4	61.8	52.3	4.9	10.4	11.7
2L*2R	1.7	7.9	13.7	50.9	65.5	58.3	7.0	14.1	18.5

*Table 8.3: Percentage of lost events using the double arm trigger for minimum bias and double diffractive events. The NSD is the global loss with the MB and DD losses weighted with the correct cross-sections. n(L*R) means at least n particles seen with at least one particle per arm. 2L*2R means at least two particles per arm*

Single arm	MB			DD			$NSD = MB + DD$		
Type	T1+T2	T1	T2	T1+T2	T1	T2	T1+T2	T1	T2
1(L+R)	< 0.01	0.2	0.2	4.6	15.0	7.6	0.5	1.8	1.0
2(L+R)	< 0.01	0.4	0.8	8.4	21.7	15.6	0.9	2.7	2.4
3(L+R)	0.06	0.9	1.7	11.6	29.7	23.0	1.3	4.0	4.0
4(L+R)	0.1	1.7	3.2	15.0	37.0	31.0	1.7	5.5	6.2

Table 8.4: Percentage of lost events using the single arm trigger in NSD for minimum bias and double diffractive events. The NSD is the global loss with the MB and DD losses weighted with the correct cross-sections. n(L+R) means at least n observed particles in one arm

The loss rates for single diffractive events are shown in Table 8.5. The double and single arm trigger losses are also compared in Fig. 8.13.

The generated beam-gas (BG) events have also been analyzed. In order to estimate the contribution of the BG events to the trigger, the interaction between a 7 TeV incoming proton and a proton at rest has been simulated in different parts of the beam pipe. The simulation has been made assuming a proton coming from the left and using the right arms of T1 and T2 to detect the particles. In order to check the contribution to the trigger of protons which interacted on the left side, three different z-positions have been chosen to generate the interaction vertex: -1 m, -5 m and -15 m (see the results in Table 8.6).

Single arm -*SD*

Type	T1+T2	T1	T2
1(L+R)	17.9	29.7	22.1
2(L+R)	22.6	35.9	32.7
3(L+R)	26.1	42.0	42.5
4(L+R)	29.6	48.4	51.2

Table 8.5: Percentage of SD events lost by the single arm trigger. n(L+R) means at least n observed particles in one arm

The contribution of the beam-gas events with a vertex in the right arm has been simulated by smearing the vertex position through two regions: the so-called T1 region (from $z = 0$ to $z = 10$ m) and the T2 region (from $z = 10\,\text{m}$ to $z = 15\,\text{m}$). The number of single arm triggered events is shown in Table 8.7. As expected, the double arm trigger rejects all of the events.

Single arm	1 m			5 m			15 m		
Type	T1+T2	T1	T2	T1+T2	T1	T2	T1+T2	T1	T2
1(L+R)	68.1	63.2	55.2	73.7	69.8	65.0	77.4	75.8	75.3
2(L+R)	61.9	59.0	59.1	70.4	66.6	58.8	71.9	70.2	59.6
3(L+R)	55.0	55.1	53.2	67.9	64.4	52.6	70.1	68.2	53.7
4(L+R)	53.3	52.8	50.4	66.8	62.5	47.2	68.2	66.9	48.9

Table 8.6: Percentage of BG events triggered by the single arm trigger. The events detected in the right arm of TOTEM and generated in the left arm of the beam-pipe by a 7 TeV proton coming from the left. The interaction has been simulated at three different z-coordinates: -1 m, -5 m, -15 m

Single arm -*beam-gas T1*

Type	T1+T2	T1	T2
1(L+R)	57.5	13.3	56.6
2(L+R)	53.1	8.7	51.5
3(L+R)	46.7	6.3	45.1
4(L+R)	43.5	5.2	41.6

Single arm -*beam-gas T2*

Type	T1+T2	T1	T2
1(L+R)	2.4	0.0	2.4
2(L+R)	0.7	0.0	0.7
3(L+R)	0.2	0.0	0.2
4(L+R)	0.07	0.0	0.7

Table 8.7: Percentage of BG events generated in the T1 (left) and T2 (right) regions that satisfy the single arm trigger condition. n(L+R) means at least n observed particles in one arm

The single diffractive trigger becomes more background free if the Roman Pots are included in the trigger system, since they allow the detection of the forward proton. In fact, preliminary results show that 90% of the forward protons can be tagged in the Roman Pots, assuming:

- β^*=1540 m;
- $\sigma_x^{*beam} = \sigma_y^{*beam} = 0.45$ mm at the interaction point; and
- full detector acceptance if $\log_{10}(-t) < -0.5$ and the proton coordinates at the Roman Pot position $x_P > 10 \cdot \sigma^{beam} + 0.5$ mm and $|y_P| > 10 \cdot \sigma^{beam} + 0.5$ mm (see Section 11.6)

The condition of a track in the Roman Pot can be used, in addition to the inelastic telescope, to improve the single diffractive event selection.

8.3.2 Technical description

The trigger signal generated by each arm of each telescope is collected by the electronics in the counting room. A simple logic allows the choice of the condition (single arm, double arm, only T1, only T2, both

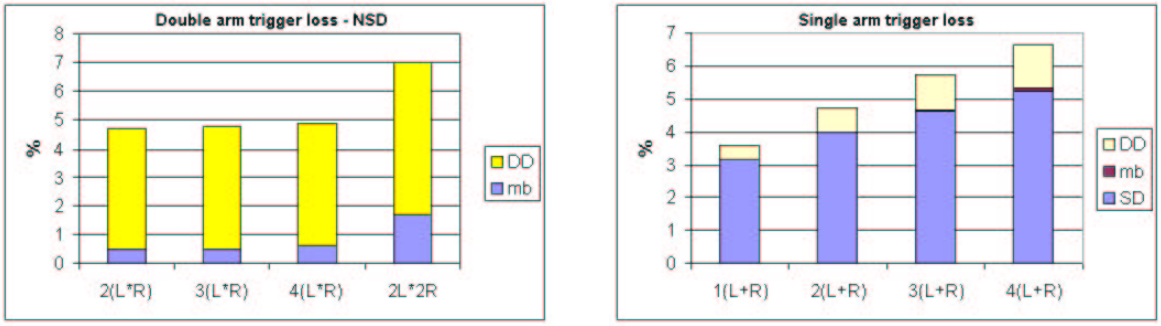

Figure 8.13: Double (left) and single (right) arm trigger losses

telescopes) which generates the level-1 trigger.

The trigger latency is sufficient to transfer the Roman Pot trigger signal to the counting room. This is exploited to combine telescope and RP trigger signals to have a more efficient level-1 selection.

The rate of the inelastic trigger is estimated to be below 1 kHz for a luminosity of 10^{28} cm^{-2} s^{-1}. In order to reduce the data flux, if requested by the readout system, one could decide to save only some of the triggered events and to record at least the trigger pattern of the prescaled events.

8.3.3 Inelastic performances with magnetic field

The T1 detector is partially in the CMS magnetic field which may be on for some of the TOTEM runs. This section presents, using the available field maps, the study performed in order to understand how the magnetic field affects the event identification. The simulation with the magnetic field is affected by the uncertainty on the field maps in the forward region of CMS. It has been found that tracks generated by electrons with energy $E_e > 15$ GeV and pions with energy $E_\pi > 20$ GeV are identified as in the case with no field if their rapidity is in the T1 range. For particles in the T2 range, the corresponding threshold energy is 10 GeV for both electrons and pions.

A sample of minimum bias events has been used as reference; the trigger losses are reported in Table 8.8.

Double arm -*MB B field on*

Type	T1+T2	T1	T2
2(L*R)	2.8	32.0	6.9
3(L*R)	3.2	35.0	7.7
4(L*R)	3.9	40.2	9.4
2L*2R	9.0	51.8	18.4

Single arm -*MB B field on*

Type	T1+T2	T1	T2
1(L+R)	0.09	6.4	0.24
2(L+R)	0.35	14.8	1.2
3(L+R)	1.1	24.2	2.8
4(L+R)	2.2	33.4	5.3

*Table 8.8: Percentage of minimum bias events with magnetic field lost using (left) the double and (right) the single arm trigger. n(L*R) means at least n particles per arm. n(L+R) means at least n observed particles in one arm*

8.4 T1 Telescope

8.4.1 Cathode Strip Chambers

General description and requirements

In order to reconstruct the event that has generated a trigger, 5 planes of Cathode Strip Chambers (CSC) [6] will be installed in each of the two T1 telescopes in the End Cap of the CMS magnet.

The T1 telescope is positioned in between two conical surfaces centered on the beams, so to cover the rapidity acceptance range $3.2 \leq \eta \leq 4.7$.

T1 will be built in two halves since installation in CMS will occur when the vacuum chamber is in place. In the following we will call them **T1 half telescopes**.

The Cathode Strip Chamber is a multiwire proportional chamber whose cathode planes are segmented into parallel strips. The avalanche developed on a wire induces on the cathode strips a charge of well known shape [19]. Recording the charge and finding the centroid of this charge distribution allows a precise determination of the position where the avalanche has developed. Information from the cathode and anode planes gives three (with the information from 2 cathode planes) measurements of the coordinates of the traversing particle in the detector plane.

The advantages and capabilities of CSCs have been studied in detail in RD5 and CSCs of very large dimensions are at present being built for ATLAS [5] and CMS [6]. We will limit our description to the features particular to our experiment. The advantages that have suggested the choice of this detector technology for TOTEM are:

- the proven detector technology;
- the simultaneous measurement with one detector of three independent coordinates of a track point in a plane;
- the capability of attaining the necessary precision even in the absence of a very accurate calibration;
- the use of a safe gas mixture ($Ar/CO_2/CF_4$).

At the effective luminosity of 10^{28} cm^{-2} s^{-1}, the inelastic interaction rate will be ≈ 1000 Hz and the expected number of interactions per bunch crossing, at a reduced number of bunches, will be $2.5 * 10^{-3}$. Since the average number of charged particles per event in T1 is expected to be ≈ 40, we do not foresee any problems in the operation of the chambers at this level of particle fluxes.

To cover the circular region of each plane, the detector has been divided into sextants, each CSC covering roughly a region of 60° in ϕ. The detector measuring plane being a normal section of a cone, each plane is composed of detectors of different dimensions. Moreover, in each plane two of the six detectors will be slightly smaller to fit the special support structure.

Table 8.9 summarizes the main chamber parameters.

Detailed chamber design

a. Introduction

Each T1 plane is composed of six CSC detectors of trapezoidal shape, each covering $\simeq 60°$ in ϕ, overlapped on the sides. To obtain the largest acceptance and remain compatible with the support frame in the envelope of the circular cross section of T1, two of the detectors are smaller than the other four.

One half telescope plane is made of 2 large-size and 1 small-size chambers, doweled and secured to each other and to the global skeleton frame. Since the chamber sizes are different in the different 5 planes, the T1 CSC detectors will be of 10 different geometric sizes. The outline is shown in Fig. 8.14 for the largest CSC (plane 5).

The small CSC is mounted between the two large CSCs. The detectors are overlapping to avoid loss of efficiency; with a careful design and an appropriate installation sequence, it will be possible to slightly stagger and overlap the chambers on the same plane of the two half telescopes (see Fig. 8.15).

There is a rotation of 3 ° around z between consecutive planes (see Fig. 8.16) to improve the pattern recognition for track reconstruction.

This small rotation is useful for pattern recognition and helps in reducing the local concentration of material in front of the HF Calorimeter.

Figure 8.24 outlines a CSC half plane sub-assembly, where one can see that the adjacent CSCs overlap each other as well as the skeleton frame (see description below).

b. Panel, cathode strips, gap bar and gas seal

The installation of the detectors inside CMS requires that the external and non-sensitive structure of the detector be of the smallest dimensions and as light as possible. These requirements, also common to

Basic parameters

full gas gap, (mm)	10
wire spacing, (mm)	3
wire diameter, (μm)	30
strip pitch, (mm)	5
strip width, (mm)	4.5
chamber thickness, (mm)	43

Detector segmentation

	CSC1	CSC2	CSC3	CSC4	CSC5
full width (large base) (mm)	833	892	963	1037	1084
full width (small base) (mm)	200	209	220	232	240
full height (mm)	574	616	668	722	756
wires per anode plane	178	192	209	227	239
strips per cathode plane	149	161	175	190	199
strip channels per detector	298	322	350	380	398
total anode channels (both sides)		12,540			
total cathode channels (both sides)		20,900			
Weight					
chamber weight, (kg)	4.3	5.0	5.3	5.8	6.2

Table 8.9: Table of the CSC detector parameters

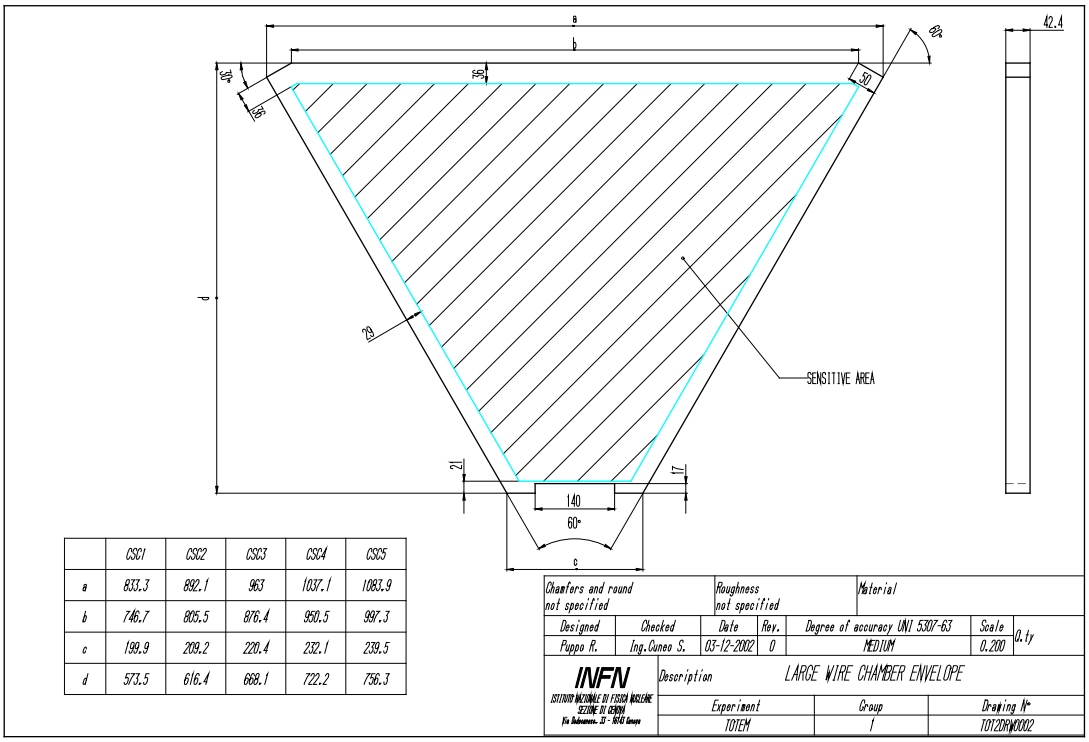

Figure 8.14: CSC outline

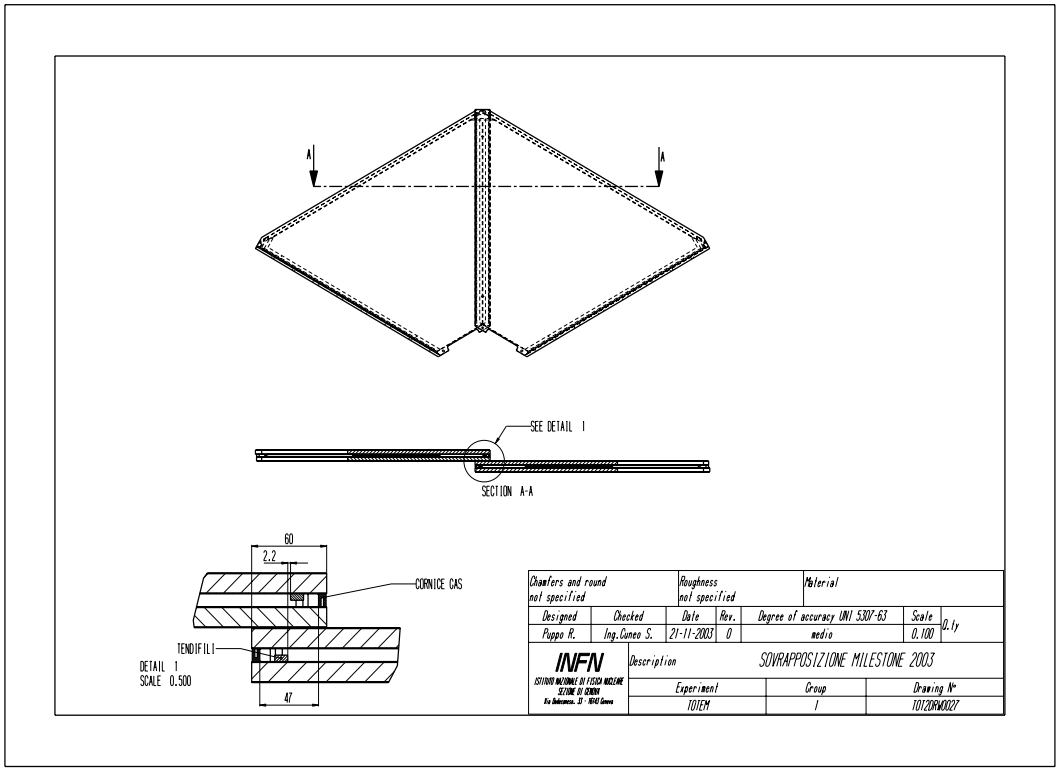

Figure 8.15: The chamber overlap (same plane of the two half-telescopes)

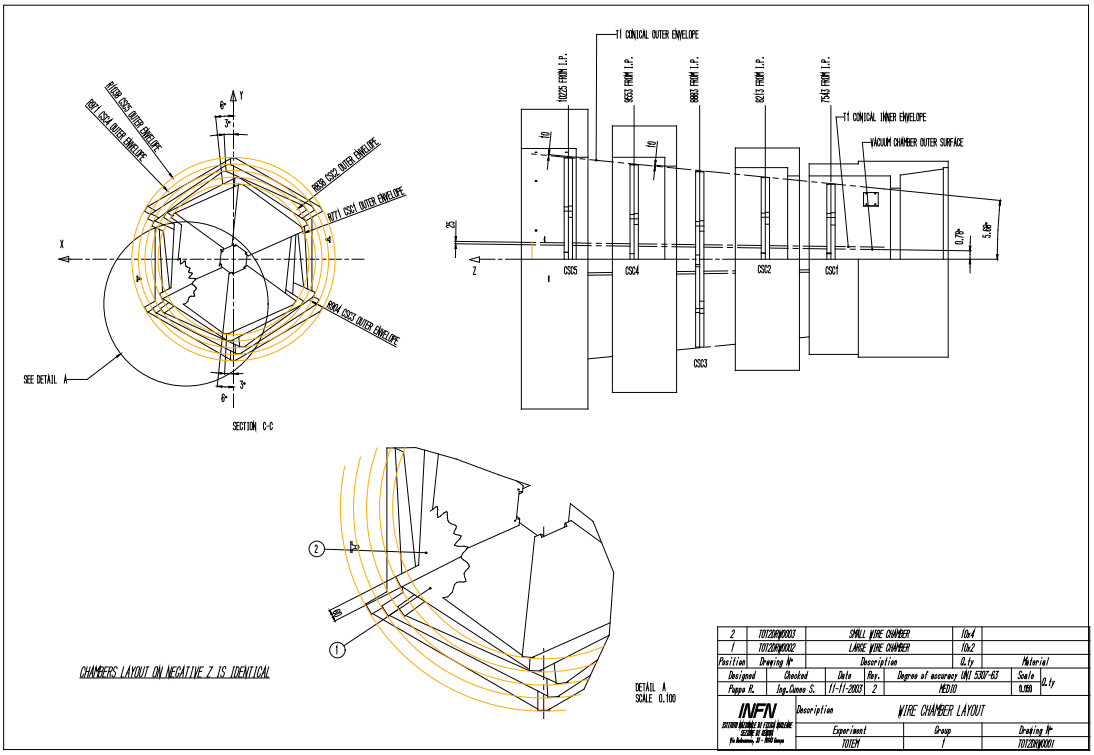

Figure 8.16: T1 detector layout

ATLAS and CMS, have led to detectors built using special rigid panels; the same technology, adapted and optimized to the new situation, will be used by TOTEM.

Two stiff and light honeycomb panels (*Nomex* [22]) support the flat surfaces of the cathode planes. The honeycomb structure, 15 mm thick, is contained between two skins of FR4 (fiberglass and epoxy laminate) whose thickness has been carefully calculated for the TOTEM detectors. A study [23] has been performed to optimize the laminate thickness and the core dimensions in the honeycomb and subsequent tests have shown that skins of 0.7 mm are sufficient for the dimensions and overall weight to be sustained.

The detector is composed of one wire plane sandwiched between two facing and properly segmented cathode planes. The two skins in a panel are obtained from FR4 epoxy laminate covered by a 17 μm copper layer etched to form the cathode strips. The etching is done by standard printed board technology. The strips are parallel and have 4.5 mm width and 5.0 mm pitch. Their capacitance ranges from ~ 5 pF to ~ 25 pF. They form an angle of 30° with respect to the chamber symmetry axis and the strips of the two cathodes lie at an angle of 60° with respect to each other. The number of strips per plane varies between ~ 150 and ~ 200.

While the printed board technology is standard, the sizes involved are at the limit of present fabrication possibility. Different fabrication methods to etch the cathode skin on the honeycomb panel have been studied; the best results are obtained by producing a large rectangular printed board, 0.7 mm thick, which is then glued onto the honeycomb panel. The panel is then cut to the desired shape as the final operation before detector assembly. In a way similar to the CMS design, one panel provides the support for the wires, the second determines the distance between the two and completes the gas gap.

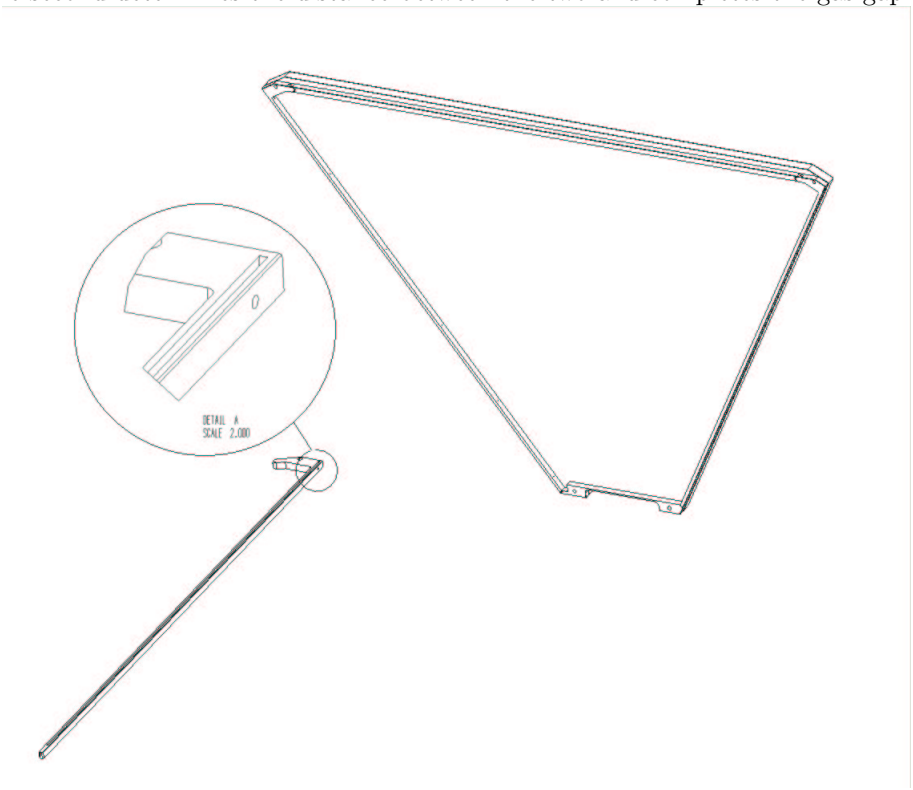

Figure 8.17: A fiberglass frame is glued onto a panel to provide precise spacing of the cathodes, gas distribution and gas volume enclosure. The details on the left show the gas distribution bar: gas arrives via the pipe fitted into the large circular hole and is distributed uniformly to the gap via small holes milled on the side of the frame

The spacer frame (see Fig.8.17) also defines the volume for the gas mixture which will be flushed at an over pressure of $0.5 \div 1.0$ mbar. Gas input and output are from the two sides of the frame: the gas enters from the pipe at the corner of the detector and flows in a channel that runs lengthwise in the side

frame. Between the channel and the detector volume a series of small holes milled in the separating walls guarantees the appropriate distribution of the gas. The hole diameter varies from 0.7 mm to 1.5 mm in order to equalize the gas flow over the detector volume. Gas tightness of the detector is obtained by gluing together the two panels with epoxy.

c. Anode wires: fixture bars, winding, soldering and gluing

Two FR4 fiberglass bars of very precise thickness, with soldering pads etched on them, are glued onto one of the panels. 30 μm diameter goldplated tungsten wires [24] will be soldered parallel to the bases with a 3 mm pitch.

The wires are stretched to a tension of 1.3 N. This tension is larger than the one required to guarantee the wire plane stability in the presence of the strong applied electric field. For safety, the wires are glued onto the fixture bar after soldering.

d. Cathode strips layout

The cathode strips are obtained by etching the copper layer of the panel as in a simple single sided printed board. Strips of equal width have a pitch of 5 mm and run parallel to one of the sides of the detector. The printed board for the two sides are identical, giving an assembled detector with cathode strips with an angle respectively of $\pm 60°$ with respect to the anode wires orientation. Figure 8.18 shows a detail of the cathode printed circuit drawing. On the top the lines that connect the cathode strips to the readout connectors are visible.

Visible on the top-right corner of the picture are: the high voltage distribution connection and superimposed in the same picture the anode wires soldering pads obtained on the special spacer bar. The soldering pads for the SMD decoupling resistors (400 kΩ) placed on the cathode plane between the anode wires bar and the gas frame can also be seen.

The board layout is optimized to minimize the frame width.

e. Tests on prototypes

To verify our design options, various mechanical measurements have been performed. Full size prototypes have been built and have provided information on:

1. panel flatness:
   The gap width increase at the center, under $\times$ 3 gas pressure, was ≤ 0.1 mm;
2. wire tension uniformity:
   The measurement has been performed with an instrument [25] that allows a fast and semi-automatic measurement without electrical contact. The distribution of the values measured shows a good uniformity with an average value of 1.1 N; and
3. gas flow uniformity:
   This was checked with a transparent model by flowing smoke through the chamber and visually inspecting its uniform diffusion over the entire volume.

Front end readout and trigger electronics

The design of the readout electronics for the TOTEM CSC is based on the experience and the development work done by the ATLAS, ALICE and CMS colleagues. Whenever possible, given the somewhat different requirements of TOTEM CSC's, the usage of the ASIC's and the boards developed by the other Collaborations is foreseen.

a. General description

The TOTEM telescopes need to trigger and read out the information which is collected by detectors which are distributed over a distance of 2.5 m, hence the trigger R/O chain of the CMS muon CSC can be employed only with some modifications. One of the main modifications is due to the necessity of having an efficient trigger whenever a track goes through the telescope and this requires the redesign of the section that decides locally the fast storage of the information waiting for a LV1 trigger decision.

The main idea is to use the anode wires information to generate locally a *strobe* signal, called LV0. This signal will allow the detectors to store the cathode strip analog information waiting for a LV1A.

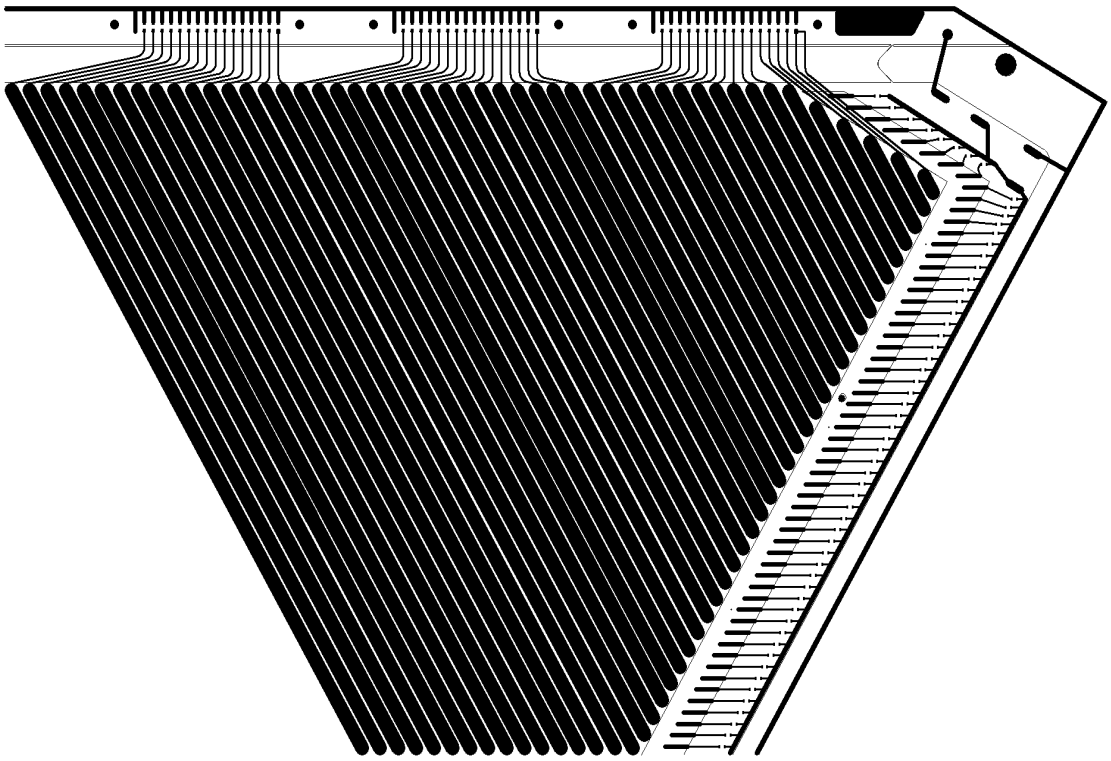

Figure 8.18: Cathode printed circuit drawing (detail at the CSC corner). On the right one notices the HV distribution lines and the wire soldering pads on the fixture bar. The gas distribution bar is shown superimposed with a dotted line

The information of the LV0 from the different detectors and planes of the telescopes will be analyzed in the ancillary crate and fed back to the entire telescope on one side. The information from the two sides to form a double or single arm trigger will be analyzed in the counting room where both signal will be available for a LV1 decision. The composition of the triggers with the other TOTEM detectors and with CMS is described in Chapter 9 of this document.

The system will be synchronized with the 40 MHz LHC clock. All stored data will keep track of the bunch-ID, and then each event will be tagged with a LV1-ID. There will be the need of at least one synchronization signal to align all the counters used to build up the IDs.

The readout modules may be the same as that in CMS, only the on-board software will be rewritten.

b. Anode front end

The anode wires signals are sent to the AFEB anode front end boards developed by CMS. These cards contain essentially the AD16 [26], a 16 channel ASIC preamplifier discriminator with one adjustable threshold and with LVDS outputs. All the shaped anode signals from the detector on the half-plane will be routed to a dedicated Anode Processing Card (APC) conceptually similar to the CMS ALCT, but with slightly different functionalities. On the telescope plane with the largest number of anode channels there are 717 wires from 45 AFEB cards.

The Anode Processing Card (APC) will be located on the detector and its main functionalities will be the following:

- power the AFEB boards and set the threshold voltage for their discriminators;

- receive the anode signals from all the AFEB boards from the half-plane (3 detectors);
- generate a fast-or signal for each detector;
- fanout the fast-or signal to the cathode processing cards (CPC) of the involved detector; the anode signal is by definition in time with the induced signal on the cathodes and will give the possibility to store one single sample having eliminated the jitter in time between the passage of the particle and the generation of the signal in the detector due to the slow drift velocity.
- fanout a copy of all fast-ors to the off-detector logic for triggering and bunch identification purposes;
- store all anode data locally in a FIFO, if an LV0 arrives from the telescope logic in the ancillary crate within $300 \div 400$ ns;
- later in case of a LV1A, tag the event and store it in a readout FIFO; or, in the absence of a LV1 for more than the maximum allowed latency, discard the data from the input FIFO.

The APC output data stream will be compatible with existing CMS readout modules, which will be used for data acquisition.

c. Cathode front end

Cathode signals will be processed by a dedicated unit: the Cathodes Processing Card (CPC). Modularity of the CPC is at present of 96 channels.

The BUCKEYE [27] from the CFEB of CMS is the choice amplifier. As in the CFEB the Buckeye will be followed by the SCA[28] analog pipeline and its associated analog to digital converter.

The Buckeye analog output signal is sampled in the SCA input stage using the anode fast-or (coming from the APC), with the correct timing adjusted by means of a delay line, in order to sample only the peak of each cathode signal. This is possible locally in the APC since the shaping time of the AD16 is 30 ns and the one of the Buckeye 100ns.

With a LV0 within $300 - 400$ ns, the information is tagged for R/O in the SCA main capacitor array, otherwise it is discarded.

A bunch-ID is generated and saved in a FIFO, in parallel with the analog data.

For each event, a few samples are stored in the SCA, not only the peak value, in order to be able to evaluate the baseline and a possible pile-up at readout time. In case of a LV1A the analog data are taken out of the SCA, digitized and stored in a 'event fifo' in the VME crate in the ancillary rack, together with the corresponding bunch-ID and a LV1A-ID. If the LV1 does not arrive within the latency, both the bunch-ID and the analog data are discarded.

The event FIFO is then read by the DAQ. The CPC output data stream will be compatible with existing CMS readout modules, which will be used for data acquisition and configuration.

d. Off-detector logic

The off-detector logic will be housed in a VME crate (one or more), located in the cavern at a distance $\leq 10\ m$ from the detector. this is the location where the fast-or's from all anodes (generated in the APCs) are analyzed together. A trigger logic requiring signals in corresponding detectors in at least two different planes generates a LV0 signal and identifies the bunch with the time of the second or third detector signal in the coincidence.

The LV0 is then sent back to all APCs and CPCs. The LV0 will arrive back at the APCs and CPCs within $300 \div 400$ ns from the event, and the information will be stored in a FIFO (for both anodes and cathodes).

8.4.2 System features

a. High voltage system

Each CSC detector will receive its HV individually from a high voltage floating channel, computer-controlled and capable of delivering a current of 100 mA at the maximum of 4 kV. The power supply

controller will be mounted in the ancillary rack. The maximum distance for the connection between the detector and the HV control is approximately $9 \div 11$ m.

The HV system design allows the possibility of setting the gain of each detector separately and turning off a single chamber under computer control in case of any high voltage problem or excessive noise.

At nominal running conditions, the total charge in an avalanche is about 1 pC. At the expected average background rates of up to $20 \div 40$ kHz/strip , this translates into roughly 5 mA/plane. Adding safety factors to cover uncertainties (background calculations, local splashes in backgrounds) and leaving open the option of operating the chambers at a higher gas gain, we arrive at a requirement that the HV system be capable of supplying at least a current of 100 mA/plane . This requirement is easily met by commercial systems.

The HV distribution to the 15 CSCs in a half telescope will be installed in the ancillary rack located on top of the HF detector. The HV interlock will be activated by the gas system.

b. Low voltage system

Each CSC of T1 will have FE electronics mounted on the detector itself; a card for fan-out and LV control is foreseen for each plane. These cards are powered by two separate and floating power supplies, located in the ancillary rack, on top of the HF detector. Two lines $9 \div 11$ m long, one for analog and one for digital FE electronics parts, serve each LV board. This will reduce the possibility of the digital noise corrupting the analog signals.

Each line on a LV board may be remotely switched on-off. Voltage and current are monitored. This is performed on an intermediate LV controller board which sends digitized LVDS information via cable to the slow control system. The controller of the power supplies and the LV board controllers are in the control room (UC5). The LV interlock will be activated by electronic temperature sensors and by the cooling water system (see below).

c. Cooling

A detailed heat balance of the detector has not been done. We roughly estimate a power dissipation of $\sim$ 200 W /plane, i.e. $\sim$ 1 kW /half T1. Provisions are made to arrange the electronics to allow easy heat extraction. A cooling pipe is integrated into the metallic skeleton frame on which the front end electronics will be fixed. The cards will be cooled mainly by heat conduction through the metallic plates of the support by the coolant circulation inside the pipe. Monophase liquid coolant is the baseline choice. To be precautionary, the cooling due to natural air draft is not considered in the cooling system design.

d. Cables

Each T1 half telescope will have its own partially flexible cable bundle of $9 \div 11$ m length; it will contain low voltage, ground, high voltage and digital signal cables, flexible gas and cooling pipes. The cable meets electric isolation, fire (zero Halogen) and radiation resistance requirements.

In electronic systems of such a scale and complexity as for the CMS Endcap Muon detector, careful attention must be paid to the implementation of grounding, shielding and power distribution. Any deviation from the following implementation principles can lead to significant problems with EMI pickup and signal integrity and should be avoided.

All cables (including power) are shielded with braid (preferred) or foil with drain wire. The shields are connected to the return lines, only at the source.

The high voltage cables have a partial discharge screen.

Digital signal are exchanged between detector and ancillary racks, with LVDS standard technology on a low skew cable, for better signal integrity and for reducing power consumption and EMI emission.

CMS requires that cables, tubes and any other kind of service connected to the detector come out upwards through 4 square windows positioned at $z = \pm 10750$ mm and $\pm 45^\circ$ with respect to the vertical Y axis. The cross-section of each is approximately 300 cm^2.

In T1 the services bundle cross section increases from the inner to the outer end of T1 and the required cables can be arranged in the detector dead space between the CSC outer edge and T1 conical outer envelope.

e. Gas system

The gas system was discussed and detailed specifications agreed upon with the CMS Collaboration; refer to [20].

The basic function is to mix the three gas components in appropriate proportions and to distribute the clean gas mixture to the CSC detectors installed in the two separate T1 half-telescopes at a pressure of ~ 1 mbar above atmospheric pressure.

The three CSCs of a T1 half-telescope plane will be gas-piped in series.

The operating gas is a non-flammable mixture of $Ar/CO_2/CF_4$ (40%/50%/10%).

The functional modules of the TOTEM gas system will be located in the SGX gas building, in the US cavern and in the UX cavern (see Fig. 8.19).

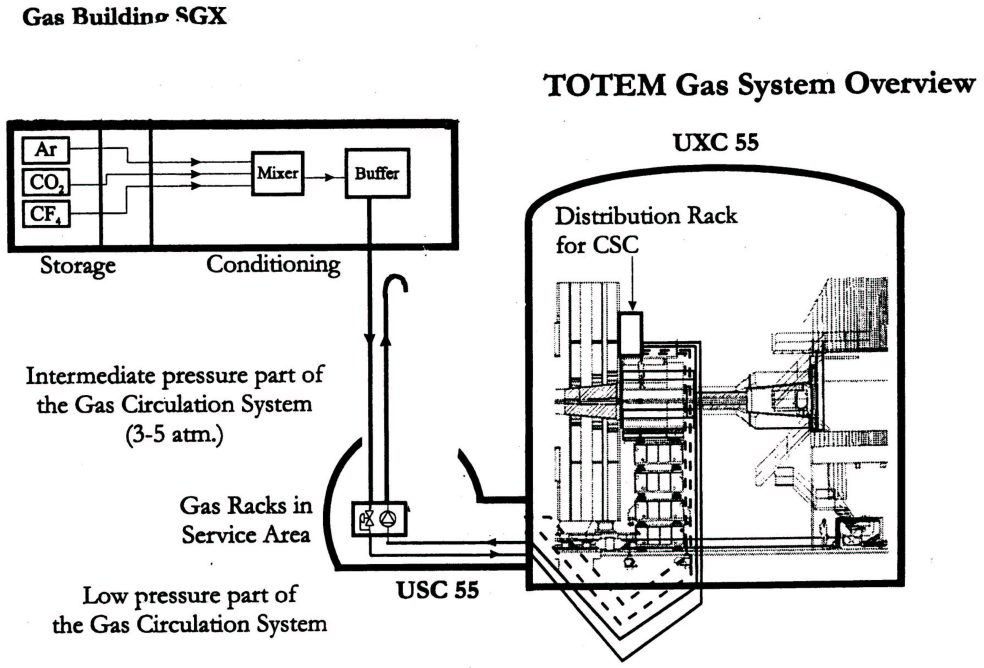

Figure 8.19: Schematic drawing of the CSC gas system. Only one endcap is shown; the gas piping for the two endcaps is split in the US area

Some basic parameters are listed in Table 8.10.

Gas volume	400 l
Concentration ratio Ar-CO2-CF4 (%)	40-50-10
Chamber relative pressure	0.5 - 1 mbar
Leak rate of the whole system	Undetectable
Maximum flow rate	200 l/h
Gas flow rate at operating conditions	70 l/h

Table 8.10: Basic parameters of the TOTEM-CSC gas system

The total detector volume for one T1 half-telescope is approximately 200 liters. During normal running, CSC gas should be circulated with a flow such as to allow the exchange of one gas volume in the detector once every 6 hours.

The expected total gas flow at operating conditions is about 60 to 70 l/h, which is $30 \div 40\%$ of the maximum flow, allowing variations by nearly a factor three up or down; $6 \div 8$ full volume changes with fresh gas at maximum flow will be needed to obtain operating conditions, leading to a start-up time of 1/2 day.

The SGX Building hosts the gas input for the mixer, and the buffer. In the mixer, the flows of component gases are metered by mass flow controllers. Flows are monitored by a process control computer, which continually calculates the mixture percentages supplied to the system. The gases are mixed in the buffer and piped to the US cavern through a stainless steel pipe of 12 mm diameter.

The US Cavern hosts the primary chamber pressure regulation, the flow regulation and the gas analysis instruments.

In the UX Cavern, the distribution of gas for T1 on the same side of the cavern will be done from the same rack. Therefore two experiment racks (one on each cavern side) are installed on the top of the HF. The patch panel can be easily disconnected in case of TOTEM removal.

A gas distribution set is also installed in the experiment rack. Due to the high residual magnetic field (up to 0.1 Tesla) at the rack location, pneumatic or manual valves have to be foreseen.

The volumes and foreseen gas flow rates for the CSCs are specified in detail in the technical note [20].

Gas purity: although CSC detectors are very robust and insensitive to air, a purifier system might be necessary to limit and stabilize oxygen and water contamination in the gas (in case of usage of lower purity grade Ar or CO_2).

8.5 The support structure

The T1 detector will be installed in a very delicate position inside the CMS detector, close to the vacuum chamber in both End Caps in front of the HF calorimeter.

With its conic shape, T1 fills the gap between the vacuum chamber and the iron of the End Cap and it can be looked at as the keystone of the CMS forward detectors. It is obviously the last device to be installed and ,consequently, the first to be removed in case of access to the inner part of CMS.

For this reason, the support structure and the installation process has to be studied carefully, has to allow installation in a very short time of less than 48 hours and has to comply with all the requirements imposed by the CMS Collaboration.

Installation will be possible after the End Cap has been closed and the vacuum chamber is in place and has been aligned. In turn, this requires that T1 be built in two halves. The support design foresees a rigid support frame with rails fixed to the CMS End CAP. The detectors are assembled on a light frame that slides into position by means of rails.

T1 envelope definition

The TOTEM T1 detector telescopes are installed in the CMS magnet End Cap, in the empty cone between the End Cap and the vacuum chamber.

The telescopes are positioned symmetrically with respect to the IP along the beam axis between $z = 7,500$ mm and $z = 10,500$ mm.

When in position, T1 must not interfere with the beam of the CMS Muon alignment system, see drawings CMS 5185-113 and CMS 5185-114, which define cylindric regions of 40 mm radius.

The T1 inner envelope is positioned relative to the vacuum chamber (a cone pointing to the IP with a half angle of 13.61 mrad or $\eta = 4.9$). Considering all the requirements listed in Table 8.11, the detector volume will be limited at large η by a cone whose distance will be of 25.5 mm from the $\eta = 4.9$ cone.

In a similar way, the T1 outer envelope is defined by the inner shape of the CMS End Cap spacer rings, as they are defined in drawing CMS 5185-125. Also in this case, CMS requires that the T1 outer envelope be 10 mm away from the envelope of a neighbouring detector (the End Cap yoke). The surface is again a cone with the beam as axis and with half angle of 99.12 mrad ($\eta = 3.0$).

Considering that the End Cap may move (even if slightly) under the magnetic forces, it is required that T1 be supported only on one point as close as possible to the support of the vacuum chamber i.e. to the external CMS yoke ring. This should avoid any motion relative to the vacuum chamber, which is supported at $z = 10,570$ mm by means of 4 wires (2 horizontal and 2 vertical) of 2 mm diameter; the

Vacuum chamber thickness	2.5 mm
Vacuum chamber mechanical and survey tolerances	2.5 mm
Vacuum chamber gravity sag	4 mm
Free region between envelopes	10 mm
TOTAL offset from vacuum chamber	19 mm
T1 support max. gravity sag	1.5 mm
T1 detectors mechanical tolerances	5 mm
Detector distance from the $\eta = 4.9$ cone	25.5 mm

Table 8.11: Clearance Parameters for T1

horizontal wires will be temporarily removed during T1 installation.

T1 installation and removal should be easy, and should not require the access of people inside the gap; installation and removal should be done in less than 48 hours.

All ancillary components of T1 should be removable.

8.5.1 The support

The telescope is 3 m long and the support must provide sufficient rigidity to hold the weight of the detectors (including cables electronics and other services) with minimal deformations, of the order of 1 mm, to minimize the distance required between the vacuum chamber and the efficient region of the detectors.

A rigid support frame is fastened on one of its end to the external disk of the CMS End Cap. Two supports on each side will work as a cantilever beam and are made in the shape of a truss, with an appropriate interface plate at one end to fix them to the external CMS End Cap ring. Each assembly is secured to the CMS End Cap by means of 4 M16 screws using the threaded holes already present on it, holes foreseen for the fixture of a barite shielding which will not be installed until later. The CMS Collaboration confirmed that they are available for this task.

Dowels to prevent any motion of the structure are advisable and will be discussed with CMS during the next design steps, after an analysis of previous CMS experience.

To improve the behaviour under torsion of the support and to limit the deformations caused by the torque due to the detector weight, the extremities closest to the Interaction Point are joined by rods. The rods at the far end are screwed to the main structure and must be fitted at installation after clearing the vacuum chamber wire support at position ($z = 10,570$ mm). A stainless steel welded frame (Fig. 8.20) provides the stability and guarantees the precise positioning requirements for the detectors.

To increase the acceptance at small η, the rails to slide and to support T1 in position are integrated into the structure, as shown in the detail of Fig. 8.20. This solution couples the stiffness of the structure with a smaller overall cross section to be dedicated to the support. Since the profile is not a standard one, it will be obtained by welding together a $80 \times 80 \times 3$ mm square pipe and $80 \times 40 \times 2$ mm"C".

The total weight of the support frame and the rails is estimated to be ≈ 270 kg, i.e. the two trusses and rails for one full telescope. Finite element structural simulations show (see Fig. 8.21) that the largest radial displacement towards the beam axis remains within the required 1.5 mm. The CSC plane deformation has been included in the evaluation.

Magnetic field forces on the support

The materials for the construction of the support are all non-magnetic, however calculations have been performed to check that the forces acting on the support due to the non-zero magnetic permeability of the materials are indeed small.

Using the available CMS field maps[21] and making the hypothesis that all the material of the support be concentrated in the position of highest field and gradient in the support region, one obtains $F_r = 190$ N and $F_z = 162$ N for the value of the magnetic force acting on the support.

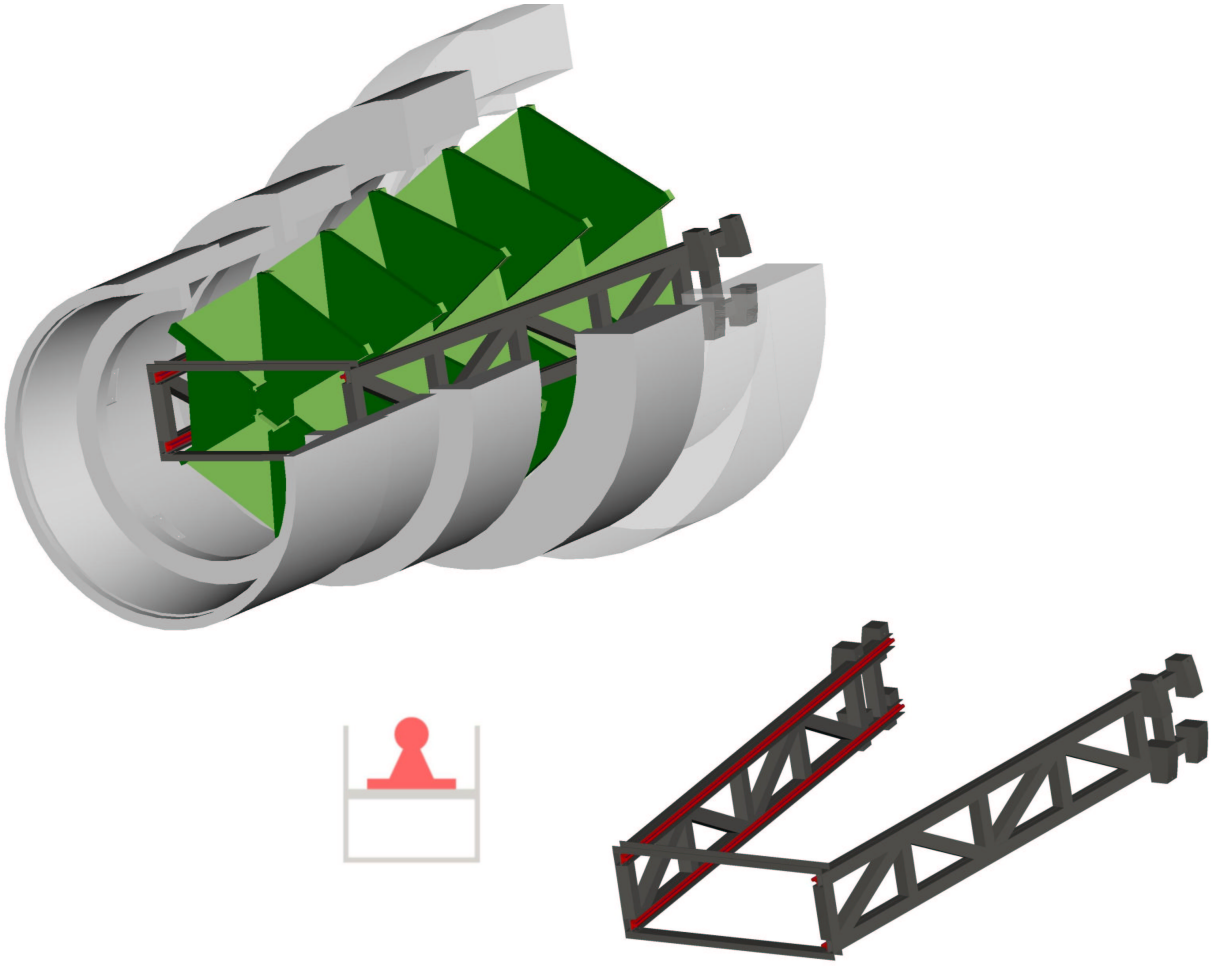

Figure 8.20: T1 in the CMS End Cap cone; only the iron End Cap rings are shown. The details show: the truss and rail assembly (right) and the rail integration inside the stainless steel profile (left).

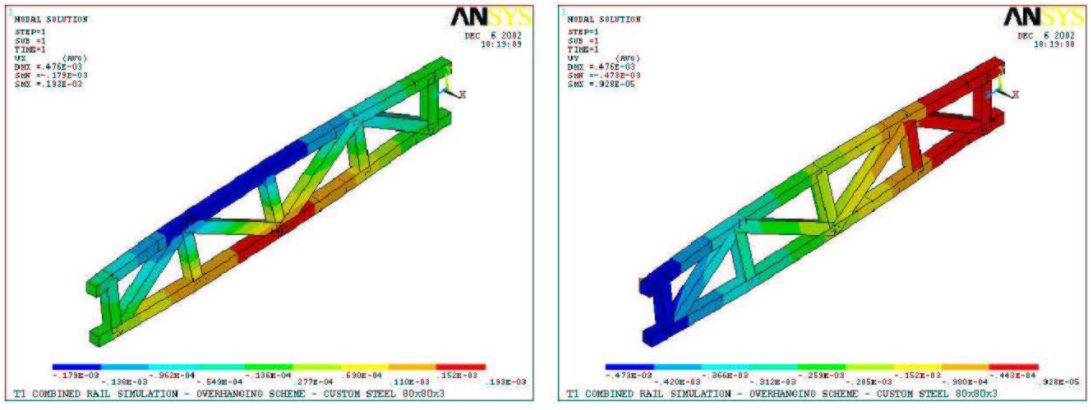

Figure 8.21: Horizontal (UX) and vertical (UY) deformation of the truss under load (displacements in m).

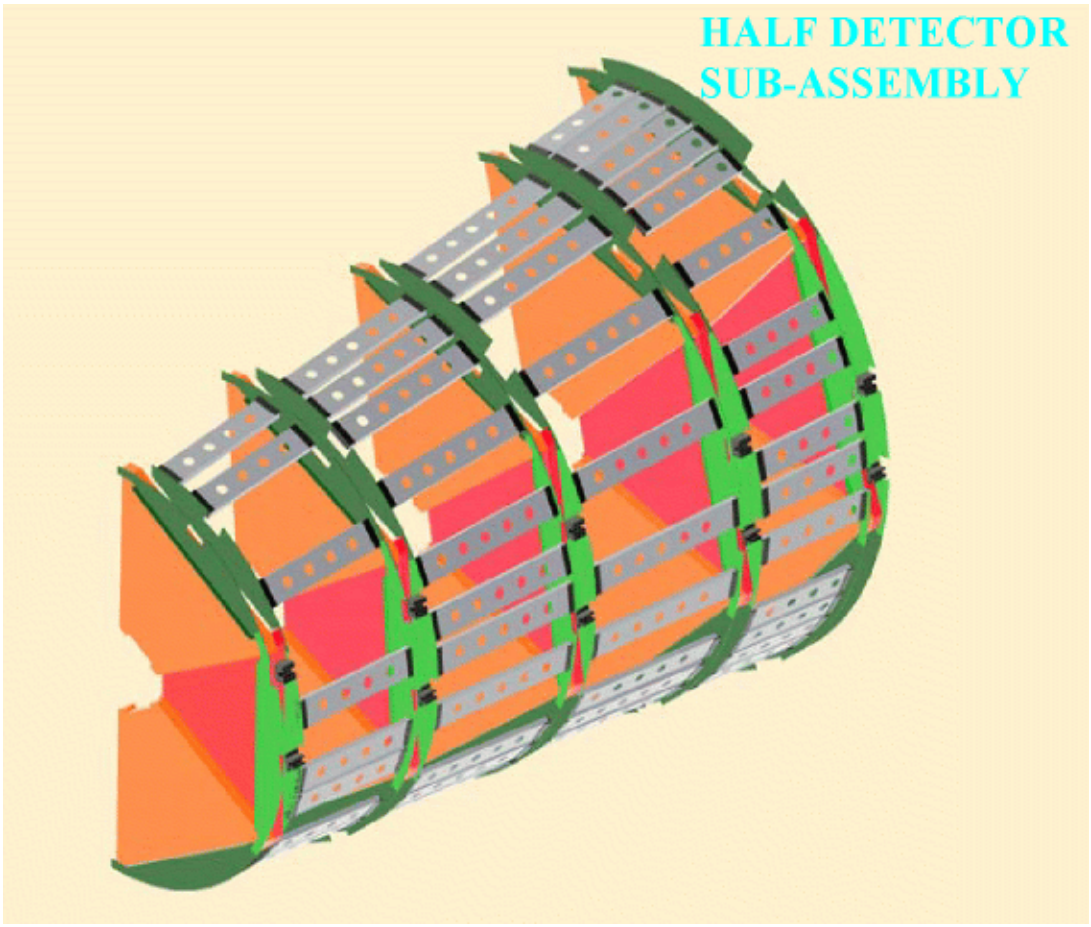

Figure 8.22: Details of the skeleton structure for the detectors of a half telescope. The numerous slats have no structural importance but provide support and cooling for the electronics.

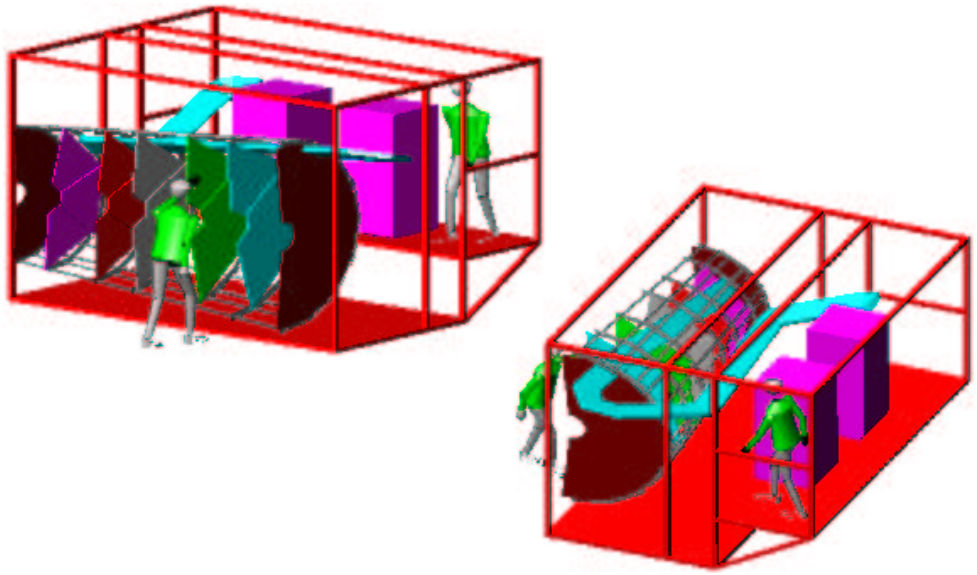

Figure 8.23: External skid, with extension rails, for detector handling outside CMS gap.

PLANE	CSC's (kg)	Services (kg)	Electronics (kg)	Weight (kg)
1	26	8	5	39
2	30	24	9	63
3	32	42	13	87
4	35	64	19	118
5	37	70	19	126
TOTAL	160	208	65	433

Table 8.12: Weight estimate for T1

Another more precise estimation has been performed[1] with a 2-D FEA model for the field in the end cap gap and gives a value of $F_z = 100$ N.

These rough but precautionary estimates show that, even for the less favorable field conditions, the deformation of the truss due to the magnetic field would be negligible.

Table 8.12 summarizes a preliminary weight estimate of the full detector elements (the 2 halves). The calculation includes electronics and services, but not the support structure.

The truss layout design has an opening for the Muon System alignment laser beams to pass freely through it. The laser beams layout requires that the right side truss be different from the left side truss; however the design is such that can be used on both sides.

The cross section of the rail support frame determines the space available to the T1 detectors, which are kept together and fitted to the rails by a skeleton frame.

The telescopes will be assembled and tested in the laboratory on their support frame and coupled to rails similar to the one fixed inside the CMS End Cap. The same platform houses the two ancillary racks for trigger and Read Out electronics and all the services which need to be as close as possible to the detectors. The structures will be used to transport the telescopes to their installation position. As part of the T1 installation procedure, the platform will be fastened on the HF and the rails aligned to the support frame already installed on the CMS End Cap. At T1 removal, the telescopes will be transferred again onto their transport supports.

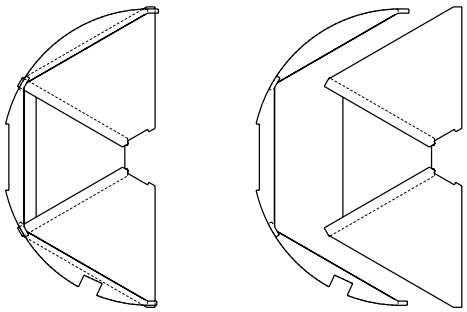

Figure 8.24: View of a CSC half plane and details of the aluminum support to fix it to the rail.

8.5.2 Skeleton frame: the half plane assembly

In each half plane (Fig. 8.24), the 2 large-size chambers and 1 small-size chamber are positioned with dowels and secured to each other and to the global skeleton frame. The small CSC sits between the 2 larger ones. Detectors are overlapped to avoid loss of efficiency at the edge; overlap is foreseen also between chambers on the same plane in the two telescope halves, thus creating a constraint to T1 insertion

[1] P. Fabbricatore and S. Farinon, INFN Genoa.

and extraction sequences. In addition, there is a rotation of 3° around Z of each plane relative to the previous one.

An aluminum skeleton frame is foreseen in each half of T1 to house the planes, front end electronics and services. Such a structure integrates the sliders.

The assembly is made of aluminum 3 mm-thick sheets cut to shape and bent to give them the appropriate stiffness; components are positioned with dowels, glued and riveted together, so that the required accuracy is ensured and any relative motion is prevented. Though the complete assembly has considerable overall dimensions, it is an assembly of much smaller components with simple geometry, that can be easily manufactured and handled in most workshops.

The skeleton features 5 semi-annular housings (see Fig. 8.22), essentially made of 2 shaped plates kept at the required distance through axial spacers; the CSC planes are installed between the plates, doweled and fastened to them.

The sliders

Commercial rails and sliders with IGLIDUR self-lubricating friction bushings have been selected. The rail diameter could be limited to 20 mm considering that the sliders feature a high load capacity with an acceptable friction coefficient and have a considerably large contact area with the rails. Furthermore, the self-aligning capability of such bushings (up to 0.5° of angular error) makes the rail integration onto their supporting frame less critical.

Given the center-of-gravity offset of the CSC planes with respect to the plane of the rails, sliders should transfer both vertical action and torque. Two rails are necessary and each detector half plane features a couple of sliders. The upper slider reacts both vertically and horizontally; the lower one reacts only horizontally and has a feature for automatic compensation of rail misalignment that allows a vertical run of ±3 mm.

8.5.3 Materials

The structure is made of radiation-hard, non-magnetic materials. All metallic parts are made of aluminum alloy AA 5754, where possible, or of AISI 316 stainless steel, where higher stiffness is required. Both alloys are commonly available on the market and are relatively cheap.

Radiation hard CIBA glue Araldite 420 A/B is foreseen as the structural adhesive to bond the components of the skeleton frame. The slider bushings are made of IGLIDUR X, a low-friction commercial polymer declared to withstand up to 10^5 Gy.

8.5.4 The transport and installation platform

The skeleton frame of T1 alone is not stiff enough and it is left to the rail framework to give the telescope the necessary structural rigidity. When outside CMS, T1 needs an external support equipped with an extension of the rails (see Fig. 8.23). This structure will be used for detector assembly and transport and is the one that will be aligned to the rails inside the End Cap before T1 installation.

8.5.5 The installation in CMS

A preliminary study of the installation sequence is presented in the following. The T1 installation procedure may be divided into four main phases and is schematically illustrated in Fig. 8.25:

a) The two rail frames are lowered into the pit and installed in the CMS End Caps.

   The rail frame is the first element that must be installed and aligned and the last to be removed. The rail for the two sides of the same telescope, fitted with traverses and a counter-weight, will be transported into position with a crane. The motion with the crane does not require special accuracy since a large clearance of around 100 mm is left between the vacuum chamber and frame temporary traverses.

   The rail frame is installed behind the 4 vacuum chamber support wires at z = 10,570 mm: of these only the horizontal ones can be temporarily removed. The rods at the tip of the frame can

be installed only after this has passed beyond the support wires and similarly for the temporary traverses which will be removed after the rods have been fixed to the End Cap.

Once the frame is in its final position, it will be aligned, doweled and then secured tightening the screws. To speed up the procedure, the installation and alignment of the fixed part of the T1 support can be done as soon as the End Cap is in position. The removal of the rail frame requires the same operations, but in reverse order.

Considering alignment, shimming and doweling, 8 hours are necessary for the installation of both sides. The structure is such that the lowering into the pit with can proceed at the maximum speed allowed by the crane.

b) The four T1 platforms (with half of a telescope on each) are lowered into the pit and put on the HF. The HF is positioned in a lowered position, i.e. raised to two of the three tiers of its support, and its top is just below the opening in the End Cap.

   Given the delicate equipment loaded on the platforms, this operation must proceed at low crane speed and will require approximately one hour per platform (i.e. four hours of crane use).

c) The platforms are fixed on top of HF and the rails are aligned to the ones already fixed to the CMS End Cap. Four hours are reserved for this operation, which may proceed in parallel on both sides.

d) The two halves of one Telescope are introduced simultaneously into the CMS cavity then blocked in position. Given the overlap between the detectors and the rotation of the CSC, the two halves must slide together to their final position. The ancillary racks are connected to the services (mains, gas pipes and few trigger and R/O cables) which have been precabled in the fixed system of the HF; a short test is performed to check the installation. The operation is then repeated on the other side. The time reserved for this operation is 16 hours.

HF can now be raised to its final alignment on the beam together with the T1 platforms which will sit on it during data taking. The T1 cable bundles are positioned in two slots left in the PE shim, present between the HF and the End Cap, and the HF is then closed.

An evaluation of the timing of the insertion/extraction operations shows that the four phases can be completed in a time of 32 hours with a sufficient margin with respect to the time allocated to TOTEM by CMS (*installation of both T1 telescopes completed in 48 hours*).

Alignment

The alignment of the telescope inside CMS does not have a large impact on the acceptance, due to its very forward location. The telescope is capable of reconstructing the vertex of the event and to align itself. A photogrammetry picture from both sides will be sufficient to determine the position of the two detectors once they are in CMS.

Besides, the alignment of all the detectors in one half telescope has been checked on the test beam prior to the installation in CMS. The small overlap of the detectors from the two sides will allow the alignment of the two half telescopes.

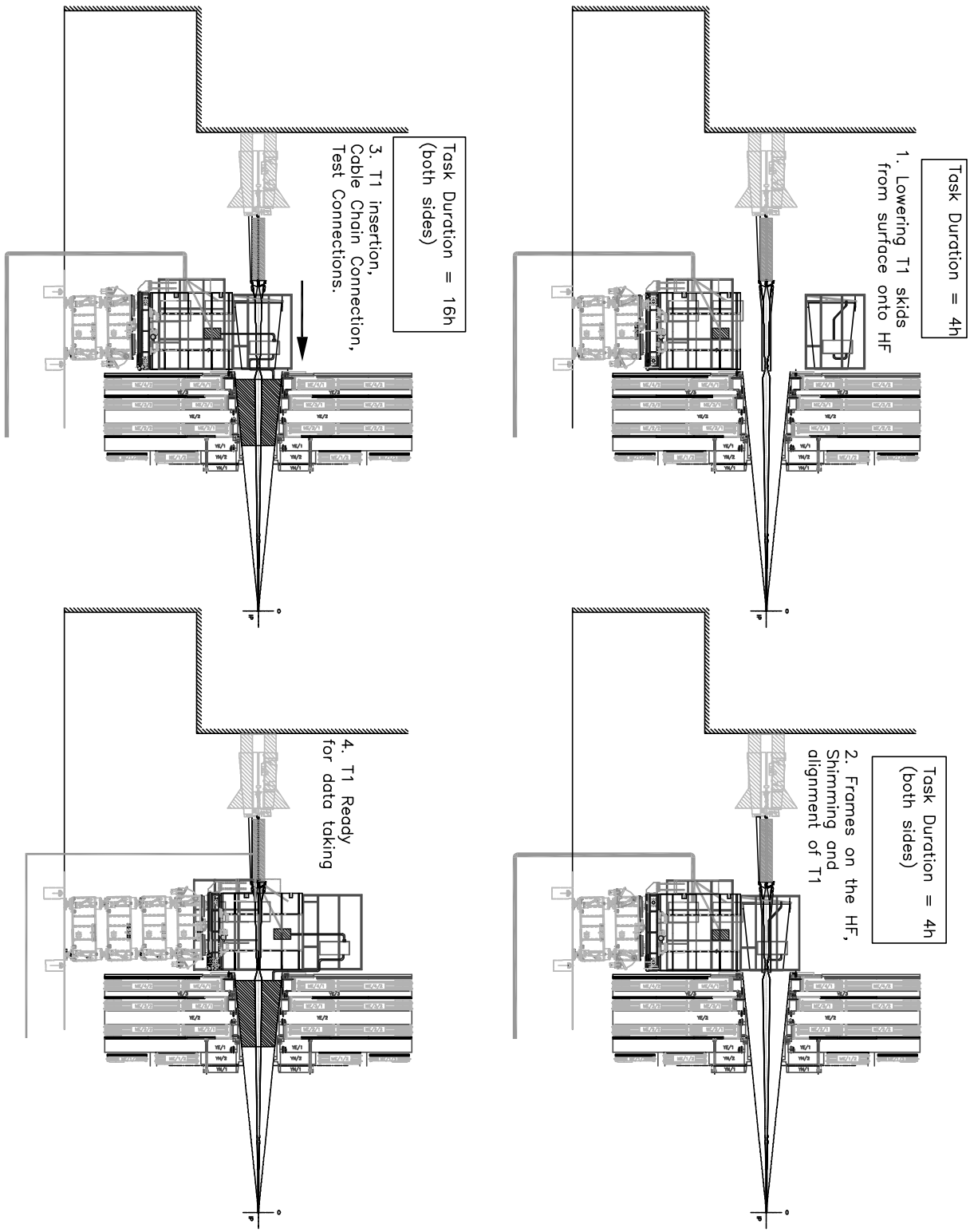

Figure 8.25: The four phases of installation of T1 in the CMS End Cap: (a)The rails are lowered, fixed and aligned in CMS; (b) the platforms with the half-telescopes are lowered in the cavern; (c) the rails are aligned to the fixed part of the support inside CMS; (d) the two halves of the telescope are inserted simultaneously inside CMS and connected to the services.

8.6 Detector performance and test results

The prototypes built in the last years were tested on the CERN X5 muons and hadrons beam line in the summer 2003. Five CSCs planes were installed over a length of $\approx$ 1.5 m, to simulate a complete sextant of T1. Two scintillator counters (9×9 cm^2) provided the signal to trigger on minimum ionization particles. Three of the CSC detectors used in the test had a width of 1 *m* and a height of 80 *cm* and represent the largest size foreseen for T1. All the details of the final detectors had been implemented in the Milestone 03 protoypes. The other two CSC were of smaller dimensions (20×20 cm^2) and were preliminary prototypes built in earlier years.

A photo of the setup is reproduced in Fig. 8.26.

Figure 8.26: The CSC detectors during the tests on the X5 beam

The anodes were equipped with front end electronics from CMS, the *Anode Front End Boards* (AFEB card as described in Section 8.4.1). The signals from the AFEB were then sent to a VME MultiHit TDC[2].

The front end electronics installed on the cathode strips was the GASSIPLEX module [29] developed for ALICE, since the final CPC was not available. The analog information is multiplexed and extracted to a standard 1Mhz 12bit flash analog to digital converter on a VME cards (SIROCO). GASSIPLEX modules are based on the *Gassiplex 1.5* ASIC chip developed for ALICE which includes: a charge sensitive preamplifier with a long integrating time (700 ns), an analog charge measurement stage or *shaper amplifier* and an analog multiplexer (MPX), which allows a read-out speed up to 10 MHz. The synchronization between MPX and SIROCO was obtained with a SEQSI[3] sequencer. 1 MHz clock speed was used in the

[2]Caen V767.

[3]SEQSI, Imperial College, London (UK)

tests.

The gas mixture used for test was Ar/CO_2 (50%-50%) and the detectors were flushed in parallel.

We want to thank here the CMS Muon project for lending us the AFEB and the ALICE HPIMD for lending us the GASSIPLEX system.

8.6.1 Operating point

The induced charge measured on the cathode strips depends on the total charge released in an avalanche, the ion drift velocity, the front-end shaping time and the fraction of charge induced on one cathode plane.

The measurement of the cluster charge is obtained in a standard way:

- subtraction of pedestals: average and $\sigma_{pedestal}$ is evaluated from special runs;
- identification of cluster: selection and tagging the regions with local maxima is obtained by applying a cut equal to $5 \times \sigma_{pedestal}$.
- cluster analysis: each cluster is analyzed to determine cluster width, cluster charge, center of gravity of the charge, maximum pulse height. The number of strips in a cluster is obtained including the strips near to the center of the cluster with a signal above $1 \times \sigma_{pedestal}$. The total charge is evaluated as the sum of the charges of the strips in a cluster.

The charge distribution at the operating voltage is calculated for events with only one cluster in each cathode plane of the detector. The total cathode charge distribution for the prototype operated at 3300 V is shown in Fig. 8.27.

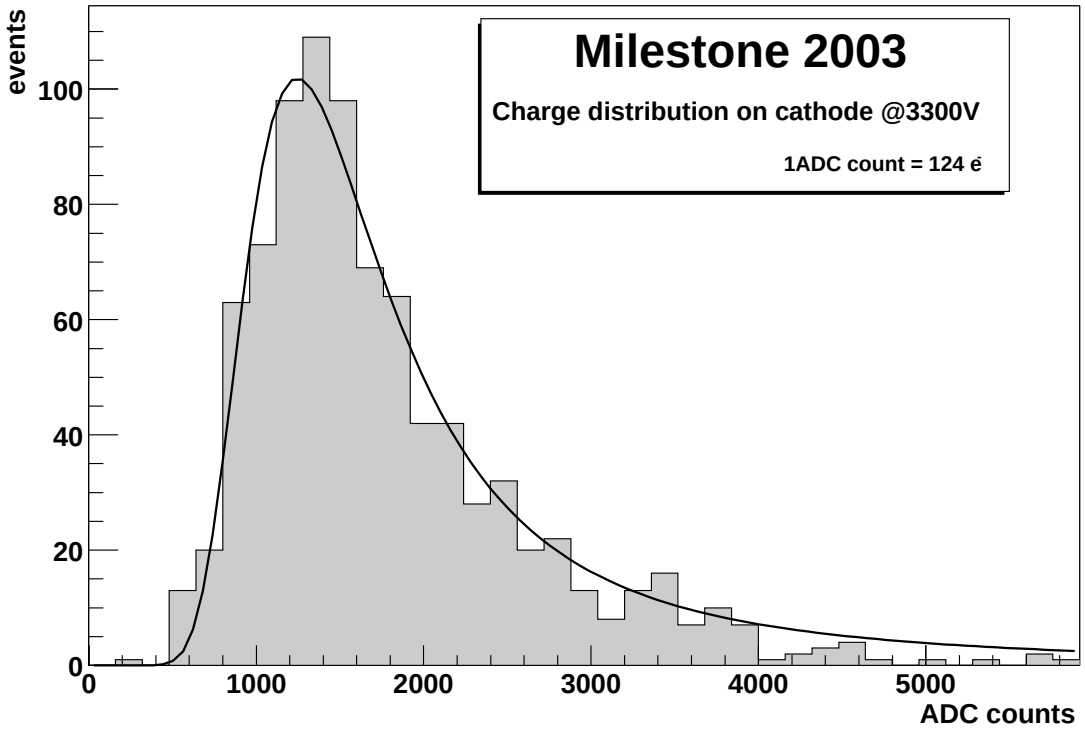

Figure 8.27: Collected charge on the prototype CSC at 3300 V

The gain of the MWPC determines the amount of charge available at the input of the amplifier:

$$\text{Gain} = \frac{N_{el}^{tot\ ch}}{N_{el}^{ion}} = \frac{N_{el}^{measured}}{N_{el}^{ion} \cdot f_{ind} \cdot f_{att} \cdot f_{sh}} \tag{8.1}$$

Front-end	GASSIPLEX	BUCKEYE
N_{ion} (10mm)	180	
f_{att}	0.50	
f_{ind}	0.41	
f_{sh}	1.0	0.19
Equiv. input noise (25pF)	1000 e r.m.s.	1300 e r.m.s.
Shaper peak. time	700 ns	100 ns
Preamp-shaper gain	11.2 mV/fC	0.9 mV/fC

Table 8.13: Parameters of the CSC charge amplification and front-end electronics

where ($N_{el}^{tot\ ch}$) is the number of electrons reaching the anode wire and (N_{el}^{ion}) is the number of electrons generated by primary and secondary ionization in the gas gap.

To calculate ($N_{el}^{tot\ ch}$) from the induced charge measured ($N_{el}^{measured}$) on the cathode plane, we have to consider the following corrections:

- f_{att} : fraction of drift electrons lost due to attachment to gas molecules. It depends on the gas mixture.
- f_{ind} : fraction of the anode charge induced on either cathode planes. It depends on the geometry. The value is the one evaluated by CMS for an identical geometry.
- f_{sh}: this coefficient gives the fraction of the charge seen effectively by the amplifier. It depends on the shaping time and filter constants of the amplifier (ballistic deficit).
- N_{el}^{ion}: the number of ionisation electrons generated in the gas by the traversing particles.

The results presented in this section are obtained using for the various parameters the values from similar tests of the Muon CSC [6, 30] and are summarized in Table 8.13.

Figure 8.28 shows the chamber gain as a function of the high voltage.

The S/N at 3200V is $\approx$ 100 and this can be considered as the operating point for the detector equipped with the GASSIPLEX module. It is interesting to calculate the operating voltage needed if the front-end electronics will be the final one with the Buckeye amplifier.

The capacitance of the longest TOTEM cathode strip is 25 pF : the noise is $\approx$ 1300e for the Buckeye and $\approx$ 1000 e for the GASSIPLEX. The difference in the ballistic deficit contributes another factor of 5 since for the GASSIPLEX no ballistic deficit has to be considered due to the filter at the input. One then concludes that a TOTEM CSC with a Buckeye equipped front-end should operate at 3500V to have a S/N of approximately 100.

Present prototype could be operated up to $3700V$ since for higher voltages, excessive dark currents were observed.

The cathode efficiency is evaluated for each plane as the ratio between the number of events that have at least one reconstructed cluster and a signal in the hodoscope and the number of events that have at least a signal in the trigger hodoscope.

In Fig. 8.29 the cathode efficiency is shown as a function of the voltage.

For the single detector we evaluate the wire efficiency as the ratio between the number of events that have a wire signal and one cluster reconstructed on each cathode plane of the prototype and the number of events that have one cluster reconstructed on the same cathode planes.

Figure 8.30 shows the wire efficiency as a function of the voltage. The different curves are obtained for different thresholds.

8.6.2 Spatial resolution of the cathode planes

The prototype CSC resolution has been evaluated using the four other chambers as a reference telescope, fitting the four measured hits to a unique track and determining the theoretical impact position on the prototype by extrapolation.

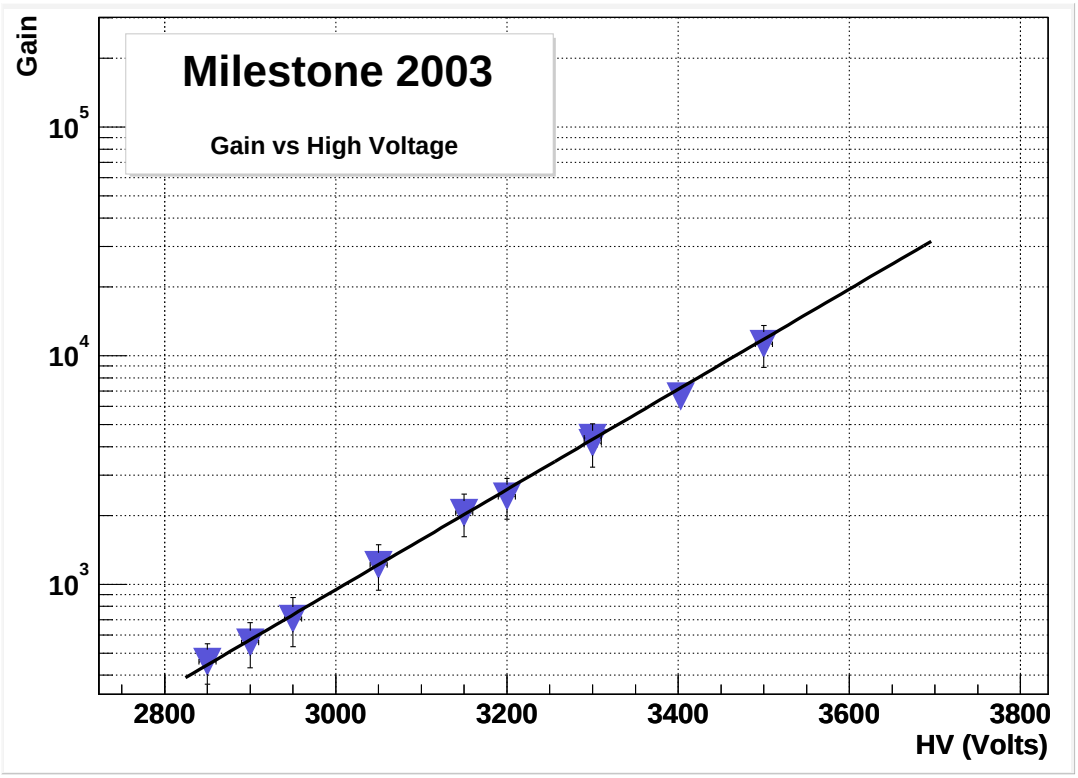

Figure 8.28: Prototype charge gain. The exponential fit gives $(200\ V)^{-1}$ *as slope parameter*

In this analysis we have rejected the events which do not satisfy the following quality cuts:

- only one reconstructed cluster per CSC plane,
- no dead strip found adjacent to the cluster,
- more than 1 but less that 5 strips in the cluster.

Finally, each reconstructed cluster provided a cathode coordinate measurement (U or V) per plane, by means of the center-of-gravity method.

In order to allow a precise track reconstruction by the fit of the cathode coordinates, the alignment of the 5 chambers was first geometrically verified and then refined by means of beam profile gaussian fits done with sufficiently high statistics.

The track parameters were determined performing independent linear fits of the U and V coordinates, by means of a χ^2 minimization method. The extrapolation of the track coordinates at the prototype position has been taken as a reference and has been compared with the measured coordinates. The difference between the measured and extrapolated hit positions (residuals) is shown in Fig. 8.31.

The gaussian fit of the residuals, for both U and V coordinates, result in a resolution of (0.77 ± 0.03) mm.

Due to the fact that the U and V coordinates have a 120 degrees inclination with respect to each other, the solutions transformed into the local X, Y coordinate system (where X is orthogonal to the anodic wires and therefore directly linked to the global θ coordinate) are:

$$\sigma_X = \sqrt{sin^2 30^\circ(\sigma_U^2 + \sigma_V^2)} = 0.5\,\text{mm}$$

$$\sigma_Y = \sqrt{cos^2 30^\circ(\sigma_U^2 + \sigma_V^2)} = 0.9\,\text{mm}.$$

Since the CSCs provide two cathode and one anode coordinate, the same track reconstruction method decribed above was applied using one cathode and the anode coordinate. In this case, the resolution is found to be somewhat larger, $\simeq 1.1$ mm.

This result demonstrates the possibility to take advantage of the additional information from the anodes in order to reconstruct tracks even in the case that one coordinate is missing.

8.6.3 Anode signal timing characteristics

The T1 anode signals will be used to trigger the telescope. A set of measurements on the anode signal timing has been performed during the test period.

The signals from the wires were read by an *Anode Front End Board* and each signal was sent to a channel of a multihit TDC[4]. The timing of each line was previously calibrated with the test-pulse.

The coincidence trigger of the two-scintillator photo-multipliers (PM) was used to define the reference time. The PM signals are also sent to the TDC. The data were taken with a 25 ns bunch structured beam and also the 40 MHz Beam CrossOver (BCO) clock appropriately selected was recorded with the event.

The analysis of the data from the TDC allowed the measurement of the time distribution of the anode signals from a single CSC plane. The data were referred to the timing of the PM and corrected for the length of each line. The measured width of the time distribution is ~ 130 ns at a level of 99% (Fig. 8.32), compatible with the drift velocity of the gas and for a 10 mm gap.

The T1 trigger will be the majority coincidence of the signals from at least two telescope planes. We have simulated offline a *fast-OR* on the anode signals from the same CSC. The arrival time distribution of the n-th signal of the coincidence among the different *fast-OR*'s shows a width of ≈ 60ns at 99% for the second signal (Fig. 8.33).

[4]CAEN V767

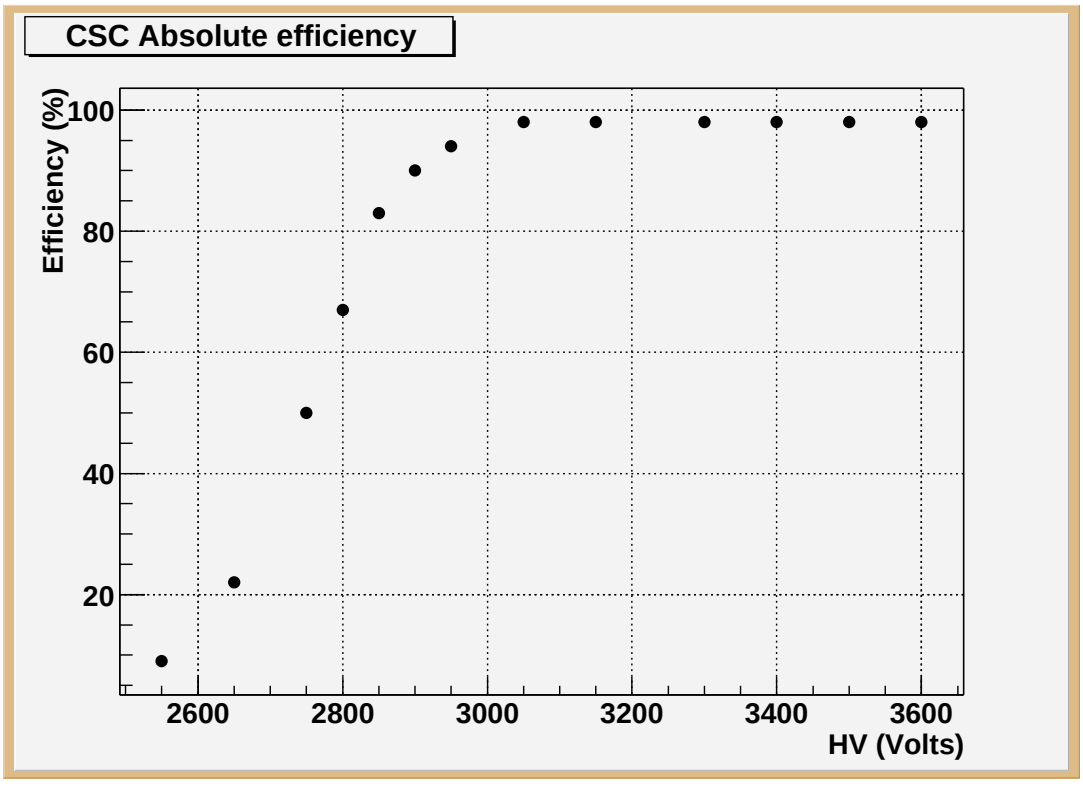

Figure 8.29: Cathode efficiencies requiring at least one reconstructed cluster per event

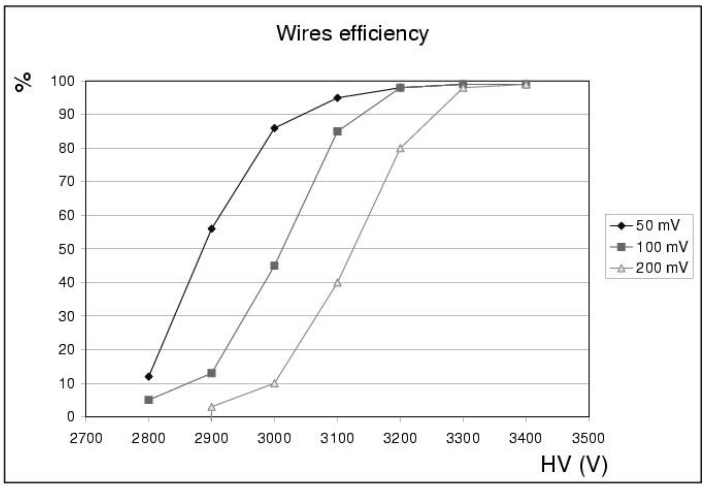

Figure 8.30: Wire efficiency as a function of the voltage and of the anodic readout threshold

This measurement shows that the timing of the anode signals will allow the identification, without error, of the bunch crossing up to a bunch distance of 75 ns, as expected for the low luminosity runs of the LHC.

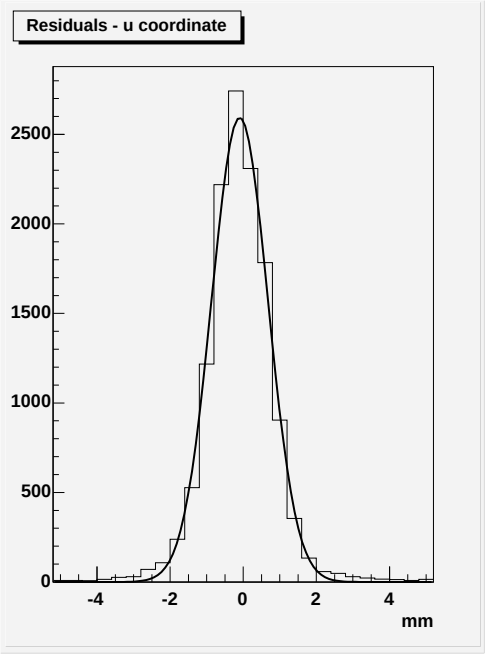

Figure 8.31: Residuals for the cathode U coordinate - tracks reconstructed from U,V coordinates

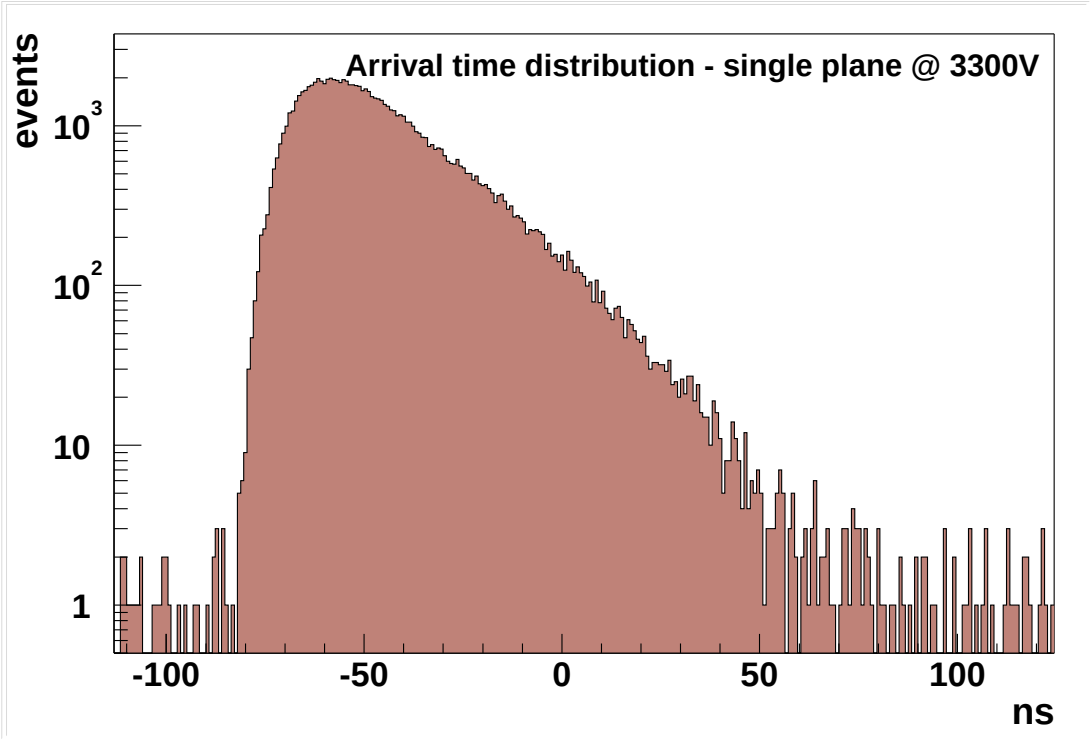

Figure 8.32: Single plane time distribution

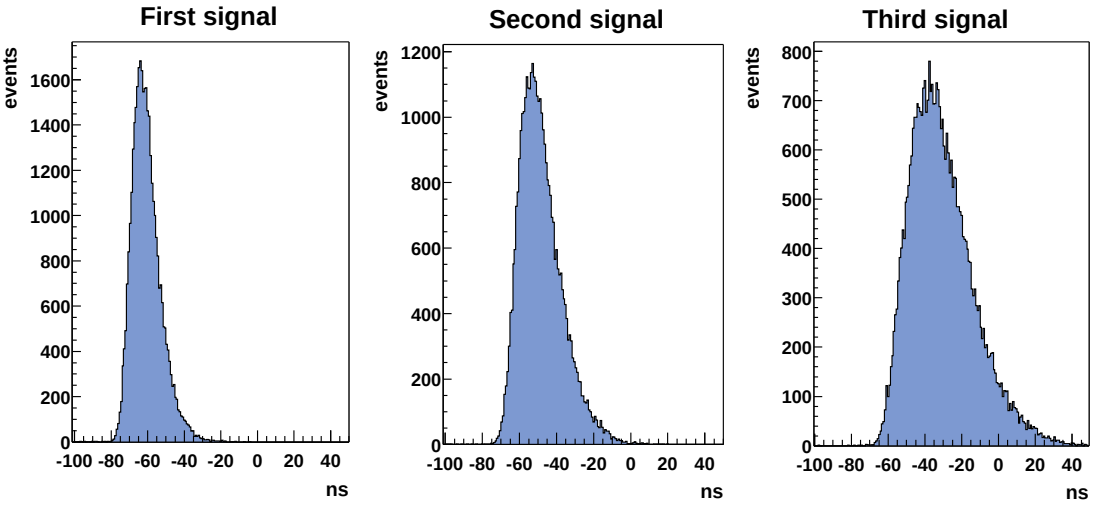

Figure 8.33: Arrival time distribution of n-th signal of the coincidence

8.7 T2 telescope

8.7.1 General description and requirements

The T2 telescope is 400 mm long and placed in the forward region of the CMS experiment centered on the beams at $z = 13,560$ mm from IP5, integrated with the HF calorimeter to cover a rapidity acceptance range $5.3 \leq \eta \leq 6.6$.

The vacuum chamber outer diameter and the forward shielding inner size define and limit the geometric acceptance. The HF fixes the minimum value in pseudorapidity at $\eta < 5.3$, a value reached by its most forward active element, and the aperture of the vacuum chamber, including the mechanical tolerances, sets the maximum at $\eta \approx 6.6$.

Parameters

The T2 detector is integrated inside the plug of the HF calorimeter, very close to the vacuum chamber. The detector sensitive region only needs to start at $\eta \approx 5.3$, since the regions at lower values are fully in the shadow of the HF calorimeter, and this limit is well within the inner diameter of the plug (500 mm) leaving ample space in the external part for the electronics, services and the support structure.

To perform the best measurements in the forward region, TOTEM requires the largest φ acceptance at the largest η (in the region of T2, $\Delta\eta \approx 0.1$ corresponds to a few mm radially). The vacuum chamber has an inner diameter of 55 mm, compatible with the minimum aperture required for vacuum stability [12]. The wall thickness of the beam-pipe is 1 mm; 5 mm are required by CMS for installation clearance, the other 4mm of free space accounts for the uncertainty in the sagitta of the vacuum chamber. Mechanical tolerances on the assembly and the detector dead space should be kept as small as possible: making the conservative hypothesis, independent of detector technique, that this will take 3 mm radially, the inner radius of the sensitive region of T2 becomes 43 mm, corresponding to an $\eta = 6.53$.

T2 has to be built in two halves since the installation into CMS will take place when the vacuum chamber is in place.

Two kinds of detectors can meet the necessary requirements. Solutions with both technologies are considered and will be presented here. Support and services are essentially identical for the two solutions and will be discussed together at the end of the section.

8.7.2 GEM detector for TOTEM T2

Gas Electron Multiplier - GEM

The GEM ([8] and references therein) is a detector which has already been employed in various experiments (HERA-B [9] and COMPASS [10]). It combines good spatial resolution with very high rate capability and a good resistance to radiation.

A thin Cu-clad Kapton foil, 50 μm thick with Cu layers of 5 μm, which has been chemically perforated with a large number of holes of ≈ 70 μm diameter, is inserted between a drift electrode and the readout plane of a gaseous detector. When a potential difference is applied between the two Cu layers of the foil, the field lines are compressed into the holes and charged particles traverse the tiny holes with very little losses and undergo gas multiplication factors of several thousands. Several GEM stages (typically two to three) can be cascaded in a detector to achieve gains of the order of $10^4 \div 10^5$ while operating the foils at moderate voltages. The charge collected on the electrode (depending on the amount of gas traversed) is of the order of $10^5 \div few10^6$ electrons. The lateral spread of the charge cloud is typically ≈ 500 μm, which defines the dimensions of the electrodes when charge sharing is envisaged to improve the position resolution of the detectors which reaches values of $\sigma \approx 70$ μm [10]. At this level of collected charge, the measurement with the recently developed ASIC's does not pose any particular problem.

The detector sensitive area can be tailored into the shapes required by the experiment. This fits nicely with the TOTEM need for a detector to be installed around a vacuum chamber of small diameter.

8.7.3 Description of the triple-GEM for TOTEM

The detector for T2 will be a three-GEM detector that will be able to reach gain values close to 10^5. In its general design, it will resemble very much the three-GEM detectors operating in COMPASS [10]. The shape will be such that it properly covers the annular region around the beam-pipe to obtain the maximum acceptance at the largest possible η. The detector will have to be sensitive up to a radius of 13.5 cm.

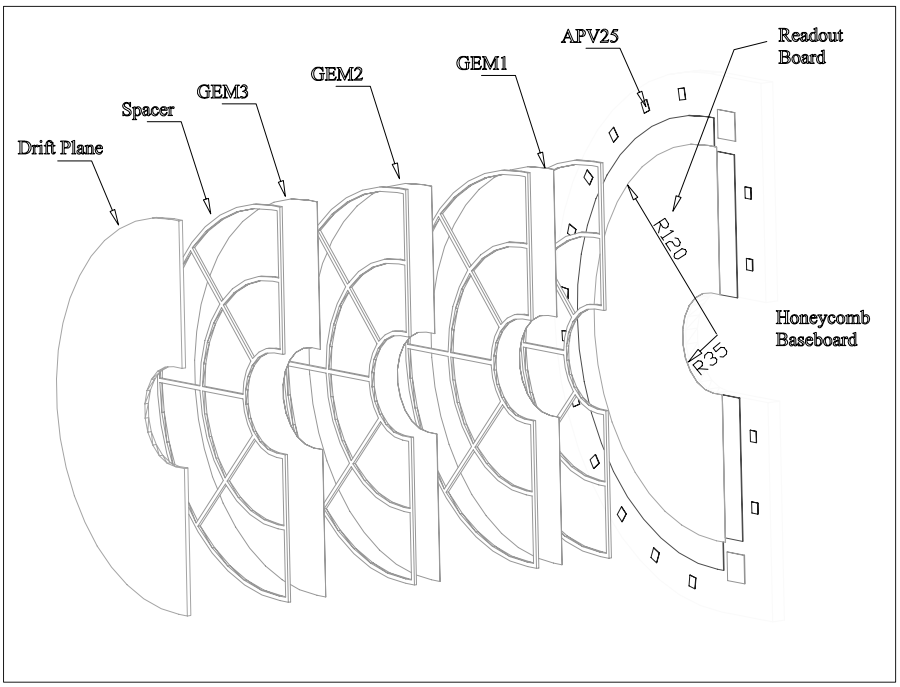

Figure 8.34: Details of the GEM detector for T2

Two identical detectors are needed to complete a measuring plane. The inner diameter is 35 mm to account for the installation tolerances for the vacuum pipe. The sensitive region will start at a larger diameter: a thin solution for a proper fixture for the GEM planes requires 3 mm radially and will be studied in more detail. The tightness of the gas volume in the region will be obtained with the same technique developed for Compass. A drawing of a detector is reproduced in Fig. 8.34.

The configuration of the electrodes on the anode board has to be properly studied since one has to find the optimum compromise between the requirements on the spatial resolution and the number of electronics channels. The necessity to use some detector planes to generate the trigger for the telescope has led us to design two kinds of anode read out boards to equip the detectors of T2 (Fig. 8.35) which will consist of:

- 4 detector planes for a precise position resolution. The read out electrodes are dimensioned in such a way that charge is always shared on at least two of them to obtain the best resolution; and
- 4 detector planes for trigger and pattern recognition. The anode board has pads of larger dimensions appropriate for these tasks.

Position planes

The electrodes on the anode board will be annular strips of 400 μm pitch and will cross radial strips of trapezoidal shape whose maximum width will be 400 μm at the outer edge and 100 μm near the vacuum pipe.

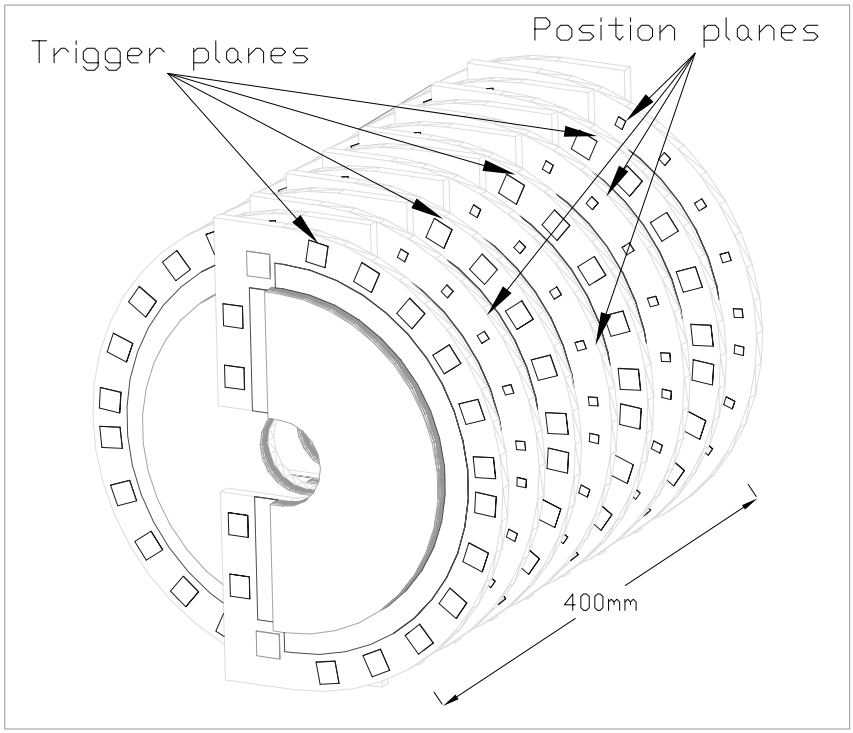

Figure 8.35: The GEM detectors in the TOTEM T2 telescope. 8 planes of 2 detectors are foreseen: 4 will give the track precision with the best resolution and 4 will provide the trigger

This ϑ, φ strip configuration (on the left of Fig. 8.36) has everywhere dimensions such that the ionization will be collected on at least two adjacent strips; this will allow a very precise reconstruction of the position of the ionization charge deposit. Given that the particle tracks to be seen by the detector in the forward region are essentially perpendicular to the detector plane, the spatial resolution will not depend on the angle of the traversing track and will be considered uniform for all the events with a value of $60 \div 70$ μm , as measured by Compass [10].

The 8 measuring planes of the telescopes will be equipped with identical detectors. Thin spacers are necessary to guarantee the parallelism of the three GEM foils in the gas volume and, in order to avoid inefficient regions due to their alignment, they are not symmetric under reflection. The simple flip of the detector at assembly on the support will eliminate problems due to the alignment of the spacers.

The strip's charge will be amplified by APV25 chips mounted on the detector and equipped with suitable protection against the rare but possible discharges encountered in gas detectors. The read-out chain will be very similar to the one already discussed in this document for the TOTEM Roman Pot detectors.

Trigger planes

There will be 4 planes equipped with trigger detectors. For the trigger planes, the detector part will be identical to the other ones, the difference being only in the anode board.

By applying the concept of the *Hexaboard*, developed by Sauli [11] and used in the recent tests made for the TPG Collaboration, tested with the former HARP TPC [31], electrodes in the shape of pads are realized on the anode surface. The small electrodes of the board will be grouped in pads of a variable size that will be traversed by the same flux of particles independent of the position. The anode electrodes are neatly grouped in pads (Fig. 8.36) and connected to the read out electronics with a multilayer printed board.

The grouping of the pads will be such as to obtain detector regions that span a $\Delta\eta$ of 0.1 and a $\Delta\varphi$ of

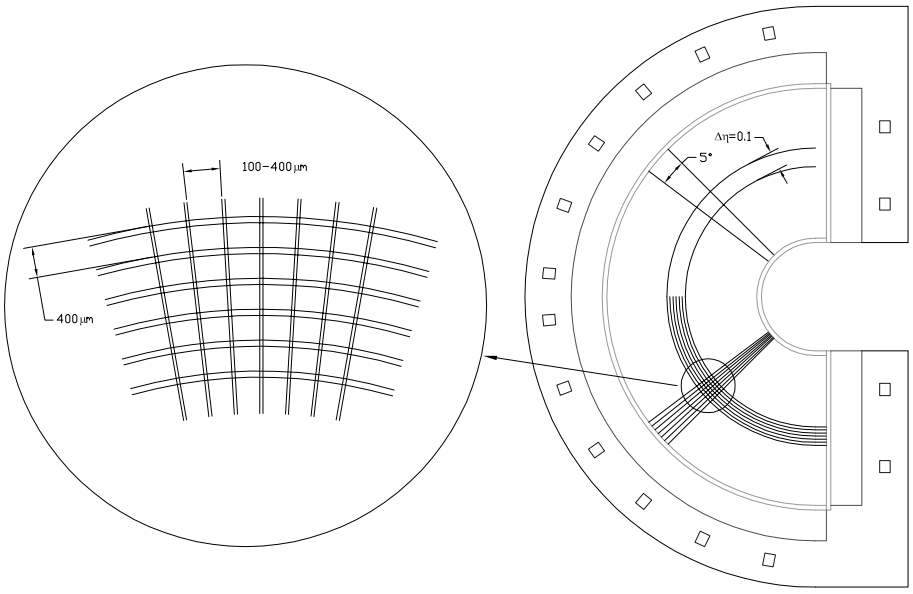

Figure 8.36: The anode boards for the TOTEM GEM. The picture summurizes in the same view the configuration of the two anode boards: with trigger pads (upper) and with strips (lower). The insert shows a view of the strips for the 'position planes'

5^o degrees; in this case, the number of pads per detector will be 540.

Their read out will be easier with a simple amplifier and a discriminator with variable threshold, for example, the AD16 ASIC developed by CMS which is already used in the anode read out of T1 and is capable of giving a trigger signal to the Position detectors within the Level one latency. The trigger electronics will be very similar to the ones which are being developed for T1 and this will simplify the integration of the trigger for the two telescopes.

The information from the hit pad will help in solving ambiguities, thus strengthening the pattern recognition algorithm.

Table 8.14 contains all the parameters of the GEM detectors for the TOTEM T2.

The gas mixture needed for the GEM is (Ar, CO_2), the same as the one foreseen for the CSC and is already available on the HF platform: no new gas system has to be added.

8.7.4 Planar silicon detectors for TOTEM T2

The alternative possibility to build T2 using silicon detectors is described in this section. This solution has also been studied in detail.

Silicon microstrip detectors have the required characteristics in terms of rate capability and spatial resolution required for T2, as described in the previous sections. Using already designed and engineered detectors provides a solution that in principle could be rapidly and easily built by TOTEM without the need of any development effort.

Silicon Detector description

The CMS tracker group has developed planar silicon microstrip detectors for the outer barrel that are capable of operating at high rates in a high-radiation environment, have a good spatial resolution and are built in different sizes.

Number of planes for telescope	8
Number of detetctors per plane	2
Drift space	3 mm
Gap between the GEM	2 mm
Transfer space	3 mm
Total gas gap	10 mm
Thickness of the detector	25 mm
sensitive area inner radius	38 mm
sensitive area outer radius	135 mm
Radial strips number (φ view) per detector	1024
Annular strips number (ϑ view) per detector	512
pad number per trigger detector	$\approx$ 540

Table 8.14: Triple-GEM for T2

The silicon sensors are single side p+ strips on n-type substrate, 600 μm thick, with a pitch of 100 μm . They are radiation hard and can stand up to 10^{14} n(equivalent)/cm^2. The silicon sensors must be kept at -10^oC to avoid thermal runaway due to increase of the leakage current at the inset of radiation damage ; a low temperature is also beneficial for the reverse annealing after irradiation.

The detector with dimensions that fit the space inside the forward plug is the OB2 for the CMS tracker Outer Barrel [32].

The support frame of the detector is made of carbon fibers with high thermal conductivity, on which the readout electronics and sensors are glued and connected trough a pitch adapter. The electronics readout will also be the same as the CMS one based on the APV25 analogue chip and is the same used by the TOTEM for the elastic detectors (see section on Electronics for the forward detectors).

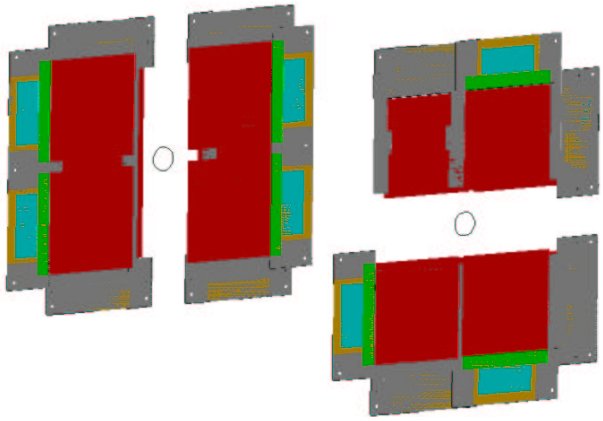

Figure 8.37: Eight silicon detectors will be mounted back to back to cover one plane of the T2 telescope

T2 will be made up of 5 planes of silicon detector in each T2 telescope. Eight silicon detectors are overlapped to form a tracking or trigger plane. Two single side detectors are mounted back to back at 90^o degrees to obtain a module which provides a two coordinate measurement in the plane. Figure 8.37 shows the arrangement of the 8 silicon detectors in one plane.

The structure to hold them in position is a lightweight disk offering good stability and stiffness. A complete view of the T2 telescope is reproduced in Fig. 8.38. Each detector is equipped with 4 APV25 chips, equivalent to one CMS hybrid. The total number of detectors required is 160, considering both sides, for a total of 80K channels. The APV25 readout has been described already in this document.

The R/O board will be installed very close to the detectors on the support structure and from there the optical fibers will exit the rotating shielding and reach a patch panel on the TOTEM ancillary racks mounted on the HF.

8.7.5 T2 Support and integration

The T2 telescope is built in two halves, since its installation will be done when the vacuum chamber is already in place. A cylindrical structure (Fig. 8.38) will enclose the detector planes and fix the relative axial position of the disks.

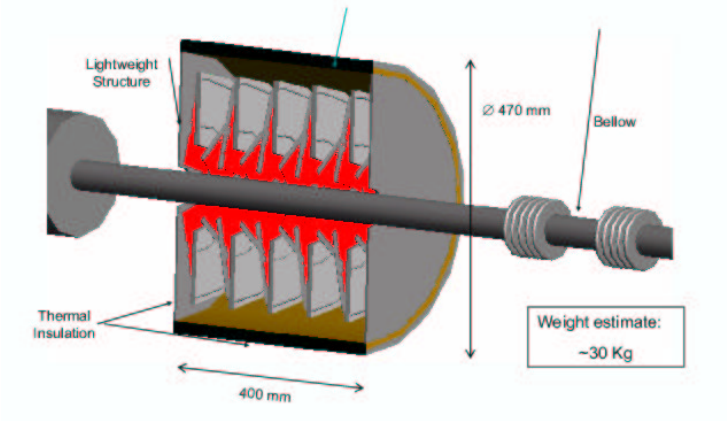

Figure 8.38: One half of the T2 telescope. The support for either detector solution is via the external shell (this figure reproduce the study for one possible Silicon detector arrangement)

The cylindrical structure is made of a light sandwich material with carbon fiber skins. To allow the passage of the electronics cables and services, a bulkhead is foreseen on the front face.

For the silicon option that operates at -10^oC, the support structure will also provide the required thermal insulation, and the entire volume will be flushed with dry nitrogen to eliminate any water vapour which otherwise would condense and freeze. In the design of the support shell near the vacuum chamber, special care has to be given to design of the transition cold/warm. An active thermal shield similar in principle to the one of the CMS tracker will be implemented with thin heaters.

The T2 volume is supported through a cantilever support structure from the extension table of HF. This system is completely independent from the motion of the HF and can position T2 with good accuracy with respect to the vacuum chamber.

Installation and Maintenance

The integration of T2 in the forward region of CMS is compatible with the installation of the CASTOR calorimeter of CMS. The support structure designed can hold both T2 and CASTOR at the same time or only one of them independent of the other. The installation sequence is also completely independent for the two detectors.

The installation procedure is fast and starts with positioning each of the two halves on the cantilevered support structure, with HF in the open position . Once the cables are installed, the two halves are slowly moved to their final position, and in the case of the Silicon solution the thermal tightness is provided. The HF and collar can be successively closed around T2. The clearance between T2 and the collar is larger then the clearance between T2 and the vacuum chamber.

The level of radiation dose in the forward region is already very high during the first year of LHC. The region around T2, as well as the entire inner bore of HF, becomes quickly activated. For this reason and since T2 detectors are in a closed insulated environment, the maintenance can be done only during long shutdowns when the HF and the T2 are in the garage where shielding against radiation is provided.

During this phase, the extension table holding T2 and the shielding collar can be completely taken away from the HF to obtain full access to both systems.

Services

The number of services required by T2 is small, given the size of the detector and the limited number of electronics channels. The T2 halves are installed on the support structure with cables that are routed through the crack between the collar and the plug shielding. They are positioned in the horizontal plane, leaving space in the vertical plane for the cables required by the vacuum pump close to T2. The pump cables have to reach the fixed nose at 18 m and be kept in position with a specific cable tray when T2 is not present.

For T2, racks are foreseen on the same platform on the outside of the collar shielding, where the radiation level is much smaller. At this location, all of the services from the detector are connected to the local crates and distribution manifolds. From the racks to the counting room, they will follow the cable chain between HF and the collar with all the services from HF and T1. The total length from the local racks on the platform to the racks in the counting room is about 100 m. Trigger cables stay in the cable chain until they reach the special trigger passage used by all CMS sub-detectors.

References

[1] The TOTEM Collaboration, Letter of Intent, CERN-LHCC 97-49 LHCC/I 11 (1997)

[2] The TOTEM Collaboration, Technical Proposal, CERN-LHCC 99-7 LHCC/P5 (1999)

[3] C. Augier *et al.*, Phys. Lett. **315 B** (1993) 503

[4] G. Bencze *et al.*, Nucl. Instr. and Meth. **A 357** (1995) 40

[5] The ATLAS Muon Spectrometer, Chapter 6 (1997)

[6] CMS The Muon Project, CERN-LHCC 97-32 (1997)

[7] M. Huhtinen, CMS/TOTEM Forward Physics Meeting, 30 May 2002

[8] F. Sauli, 'GEM: a new concept for electron amplification in gas detectors', NIM A386, (1997) 531.

[9] Y. Bagaturia et al., 'Studies of aging and HV breakdown problems during development and operation of MSGC and GEM detectors for the inner tracking system of HERA-B', NIM A490, (2002) 223.

[10] C. Altunbas et al., 'Construction, test and commissioning of the triple-gem tracking detector for Compass', NIM A490, (2002) 177.

[11] F. Sauli et al., 'Micropattern gaseous detectors', Ann. Rev. Nucl. Part. Sci., 49 (1999) 341.

[12] A. Rossi, 'Residual Gas Density Estimations in the LHC Experimental Interaction regions', CERN-LHC-Project-Report-674 (2003).

[13] T. Sjostrand *et al.*, 'High-energy-physics event generation with PYTHIA 6.1'
Comput. Phys. Commun. **135** (2001) 238

[14] A.B.Kaidalov, 'Soft hadronic interactions at LHC.'
Felix proposal. 20 January 1997

[15] A.D.Martin, 'First workshop on forward physics and luminosity determination at LHC'
hep-ph/0103296 28 March 2001

[16] K.Goulianos, 'The nuts and bolts of diffraction'
hep-ph/0110240 July 2001

[17] P. Arce *et al.*, 'Use of GEANT4 in CMS. The OSCAR project'
Prepared for International Conference on Computing in High-Energy Physics and Nuclear Physics (CHEP 2000), Padova, Italy, 7-11 Feb 2000

[18] S. Agostinelli *et al.*, 'Geant4 simulation toolkit'
NIM **A506** (2003) 250.

[19] E. Gatti *et al.*, Nucl. Instr. and Meth. 163 (1979) 83.

[20] M.Bozzo *et al.*, The TOTEM Gas System , EDMS TOTEM-DI-ER-0001, IN-2002/02

[21] YURI FISIAK (U.C. DAVIES) CMS FIELD MAPS - APRIL 1997

[22] PLYFORM Varallo Pombia, 28040 Novara (Italy)

[23] M.Bozzo *et al.*, Behaviour of Composite Panels for the Totem CSC, INFN-TC (2002)

[24] LUMA METALL AB, S-391 27 Kalmar (Sweden)

[25] Wire Tension Meter WTM-05, developed by S. Czellar of Purdue University for the CMS Muon collaboration

[26] N.Bondar et al. - CMS Muon Endcap CSC Anode Front-End Electronics, For the CMS Endcap Muon Electronics System Review at CERN, September 18, 2000

[27] BUCKEYE chip, developed for the CMS Muon project at Ohio University, Cleveland, Ohio (USA)

[28] A Low-Noise, High Frequency Analog Memory Integrated Circuit', Technology Information Center, UC CASE N. 2001-335-1, UC Davis, CA, (USA)

[29] J.C. Santiard *et al.*, GASPLEX - A Low Noise Analog Signal Processor for Readout of Gaseous Detectors , CERN-ECP 94-17

[30] L. S. Durkin, 'CMS modelling of electron signals for the forward CSC's', CMS TN/95-194 (1995).

[31] U.Gastaldi et al, 'TPG development', in printing, NIM-B. Paper presented at the 9th Pisa meeting on Frontier Detectors for Frontier Physics, La Biodola, Isola d'Elba, May 25-31, 2003.

[32] Technical Specification: Supply of Silicon Micro-Strip Sensors for The CMS Silicon Strip Tracker (SST), Invitation to Tender: IT-2777/EP/CMS

9 Data Acquisition and Trigger

9.1 Introduction

The TOTEM experiment must be able to take data in several different machine status, beam optics, luminosity, trigger and Data Acquisition (DAQ) configurations.

The luminosity has a direct impact on the total data rate. The DAQ infrastructure has to provide enough resources to efficiently exploit the detector capabilities, from reading the event out of the detector electronics, to assembling event fragments originated in different detectors and to storing the data on some medium.

The needs in terms of data rates have been evaluated on the base of the present measurement program and detector design, and of the results of their simulations. On top of this, the DAQ infrastructure has to provide a safety factor on detector occupancy and data volumes, so to accommodate higher noise, or higher trigger rates, or both. In addition, some redundancy will be welcome in case the measurement program would be extended to include higher luminosities or different event topologies.

The very basic requirement on the functionalities of the system is to provide appropriate partitioning of the DAQ resources and of the trigger system to allow TOTEM to run in standalone mode. However, the fact that common runs with CMS are an essential part of the scientific program poses additional constraints and suggests possible technological choices.

Common runs need common triggering. This poses a serious constraint on triggering TOTEM, since the sparse structure of the experiment may be a concern from the point of view of the trigger latency. Integrating the trigger systems of the two experiments is possible as long as the TOTEM input to the a common Level-1 (L1) trigger is provided with a delay acceptable by the CMS Global Trigger processor, and that the the combined Level-1 trigger accept (L1A) can be sent in time to the TOTEM detector front-ends.

Synchronizing the TOTEM and CMS triggers requires that error and overflow conditions are properly reported to the CMS central trigger, in order to throttle down the trigger rate or take appropriate actions. As already detailed in the description of the detectors and of the electronics, this is achieved by using CMS-like front-end systems wherever possible.

The constraints posed on the DAQ infrastructure and software are less binding: TOTEM's data rates are a fraction of the ones of larger experiments like ATLAS [1] and CMS [2]. Event consistency is anyway insured by the event tags, event if TOTEM and CMS will be using completely different DAQ systems and the choice is made to combine the events in off-line. From this point of view, there would be some freedom in choosing the hardware and software architecture, including the possibility of using simpler, and maybe cheaper, DAQ designs with respect to the one of CMS.

One has however to take into account that combining events in off-line is always possible, but it complicates the bookkeeping and the reconstruction. The fact that the front-end electronics is very similar, where not identical, to the CMS design suggests the implementation of a CMS-like DAQ infrastructure. This will keep open the possibility of, whenever needed and possible, combining events early in a single stream during the on-line event-building stage, with the advantage of simplifying the data access pattern during the analysis.

In the following sections we will assume that TOTEM's baseline choice is to implement the DAQ and Trigger interface in CMS-like fashion, which is already described in deep detail in the TriDAS [3, 2] technical design report.

9.2 Triggering

9.2.1 Trigger distribution

The TTC [4, 5] system, developed by the RD-12 group at CERN, provides the distribution of synchronous timing and L1 triggers, and provides control signals to the front-end electronics with appropriate phase relative to the LHC bunches. The TTC system can be configured as a trigger distribution tree, providing the necessary number of branches to each sub-detector.

The four main experimental areas will be provided a TTCmi machine interface, receiving the main LHC timing. Since at the time of fixing the machine timing distribution there was no request for an individual receiver for TOTEM, the experiment will have to rely on the CMS TTCmi crate.

The baseline choice is to equip TOTEM with one TTC partition, to allow the experiment to take data at least in standalone mode.

In standalone running mode, TOTEM-generated L1 triggers are distributed to TOTEM detectors via the TTC system, and are subsequently read out and assembled.

9.2.2 Triggering with CMS

The picture is of course more complicated in the case of common running with CMS.

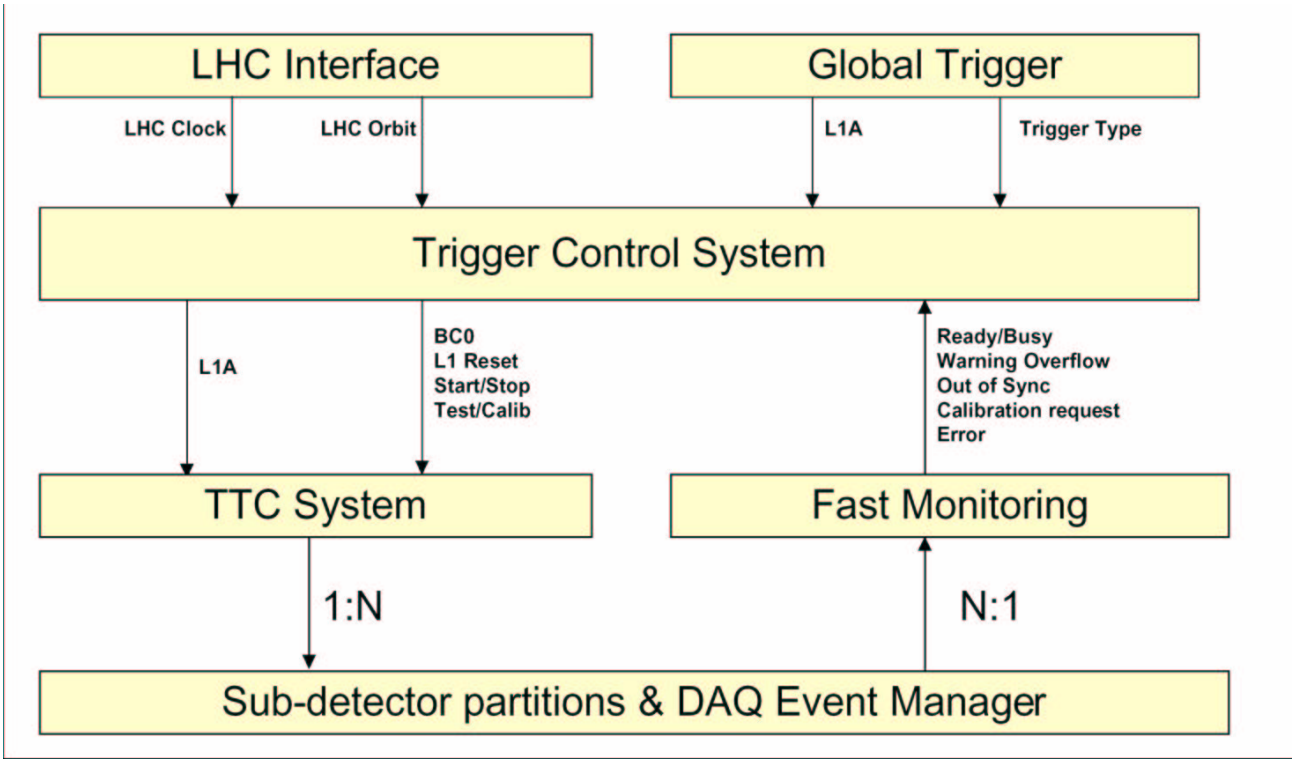

Figure 9.1: The Trigger Control System (TCS) in CMS

In the CMS Trigger system [3], one of the key components is the so-called Trigger Control System (TCS), logically located between the L1 Global Trigger (GT) and the readout and DAQ (Fig. [6]). Its main task is to control the delivery of L1 Accepts (L1A) depending on the status of the electronics and of the DAQ. The TCS is able to gather status information from various sources, to take action on buffer overflow warning or error conditions, and to control the delivery of test and calibration triggers. It uses

the TTC network to distribute information to the various subsystems.

The role of the TCS makes partitioning in a CMS-like environment slightly more complicated than in a pure standalone configuration, since it can be achieved in two possible ways.

- TOTEM participates to the CMS TTC tree and receives global or specific L1A from the CMS GT; the CMS Event Manager will then request to the TOTEM partition the readout of those events.
- TOTEM participates to the CMS TTC tree only during common runs. Standalone running is achieved by shutting off the TTC link between the TOTEM TTC branch and the TCS. In this case, a local DAQ processor in the TOTEM TTC distribution crate will take over the task of managing control data over the TTC network.

At the time of writing of the CMS Trigger TDR, the design of the TCS was providing 32 partitions, out of which 31 allocated to sub-detectors and to the GT. Pending discussion and coordination with CMS, it seems natural to envisage the use of the free partition for common CMS/TOTEM runs.

From the point of view of TOTEM, being able to integrate the CMS Trigger system means that all of the front-ends must comply with the communication protocol imposed by the TCS to keep track of warning and error conditions, and to be able to receive TCS commands.

9.2.3 Trigger latency budget

The matter of L1A latency for the last RP station has already been described in detail in the chapter about the Roman Pot electronics. Table 9.1 summarizes the main numbers.

OPERATION	TIME REQUIRED	TOTEM	CMS
Interaction at CMS		0bx	0bx
Particle TOF to last RP (220 m)	29bx	29bx	
Signal ready at RP	4bx	33bx	
Cables to CMS GT (260 m) (5 ns/m)	52bx	**85bx**	
Latest CMS GT input			**91bx**
CMS GT L1A ready	12bx		103bx
CMS GT back to RP	52bx	155bx	
Trigger chip digital pipeline limit	TOF + 128bx	**157bx**	
Local TTCrx at RP: L1A available at front-ends	6bx	**159bx**	
APV25 chip analog pipeline limit	TOF + 192bx	221bx	

Table 9.1: Trigger latency in the common TOTEM/CMS system in number of bunch crossings (bx)

By paying attention to the first two numbers marked in bold characters, it is easily seen that the latency budget for arriving in time into the main CMS GT coincidence is rather tight.

A second problem could be that the digital pipeline of the VFAT trigger chip, which is just large enough for standalone running, does not have enough time slots (as shown by the second two numbers in bold) in combined CMS/TOTEM running mode. This second problem is considered to be minor: while it would be almost prohibitive in TOTEM's schedule to modify the analog pipeline of the APV25, is is considered to be relatively easy – as mentioned in the chapter on electronics – to extend the digital buffer of the VFAT.

9.2.4 Possible triggering schemes

In what follows we list the possible working scenarios.

- **The TOTEM trigger arrives in time to be included in the CMS GT.** In this case TOTEM acts like a CMS subdetector: events can be flagged as physics triggers, can follow the same data path as the ones of the CMS sub-detectors, and be built together with them.

- **The TOTEM trigger arrives in time to the CMS GT but the CMS L1A is late at the TOTEM front-ends.** TOTEM shortcuts the CMS GT and sends L1A directly to its detectors. CMS, having received the TOTEM trigger, reads out the event on a best-effort basis.

- **The TOTEM trigger does not arrive in time to the CMS GT input.** This is the worst case, in which the two experiments cannot run synchronously.

From the computation of the latency budget, there is confidence that the TOTEM trigger coincidence can be made and provided in time to CMS, allowing the two experiment to make common runs.

9.3 Data Acquisition infrastructure

The role of the DAQ infrastructure is to perform the readout of the detector front-ends after the trigger logic has issued a L1A, and to forward the accepted events to on-line services like control, monitoring and storage.

In a full-fledged DAQ system for a large LHC experiment there is usually one more step between storage and L1A, i.e. some high level trigger selection. We consider in what follows that TOTEM will not have any need for refined Level-2 event selection in standalone running. Any such need arising in common runs with CMS will be satisfied by CMS' own high-level trigger farm.

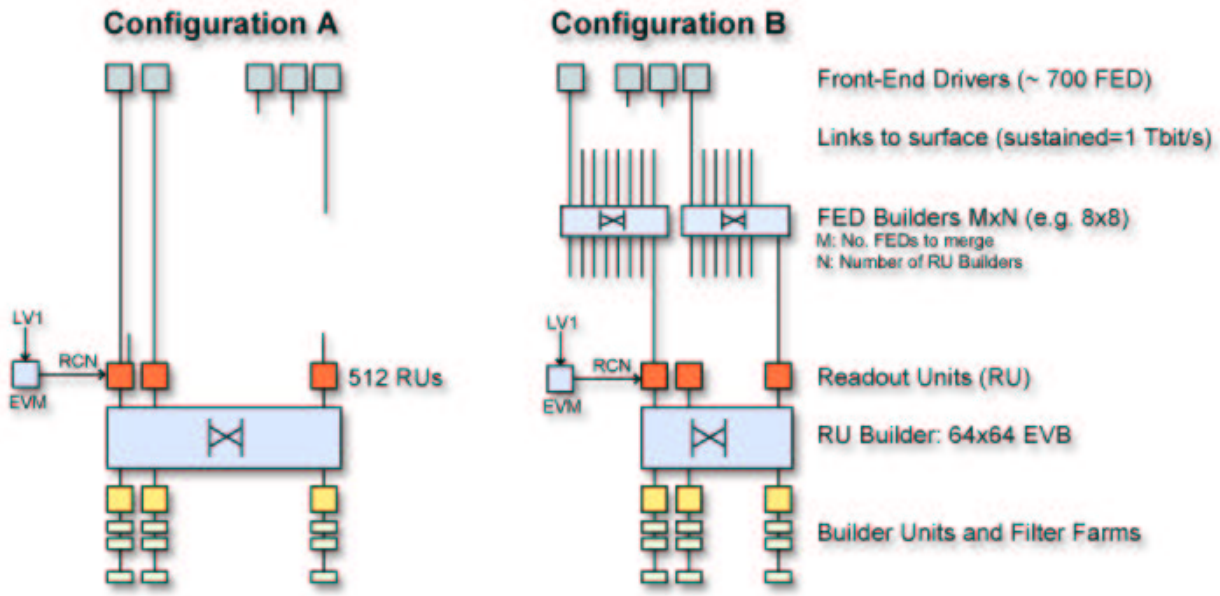

Figure 9.2: Two possible configurations for a DAQ system based on switched network

Figure 9.2 gives an idea of two possible approaches to the implementation of a large DAQ system based on switched network. Several Front-End Drivers (FED) organized in Front-End Readout Links (FRL) form the so-called Readout Column in CMS jargon. All the FRLs have to be connected to some network structure to perform the assembly of their event fragments.

The straightforward approach is to design the flat structure of configuration A, where one single switched network connects all the FLRs to a number of builder machines which is large enough to cope with the rate imposed by the trigger.

A less conventional approach is the one of configuration B, which is based on the idea of multi-stage building. The advantage of such a structure is the possibility of decomposing a large system into smaller and more manageable parts, its better modularity and scalability, and the embedding of more buffering capabilities into the system.

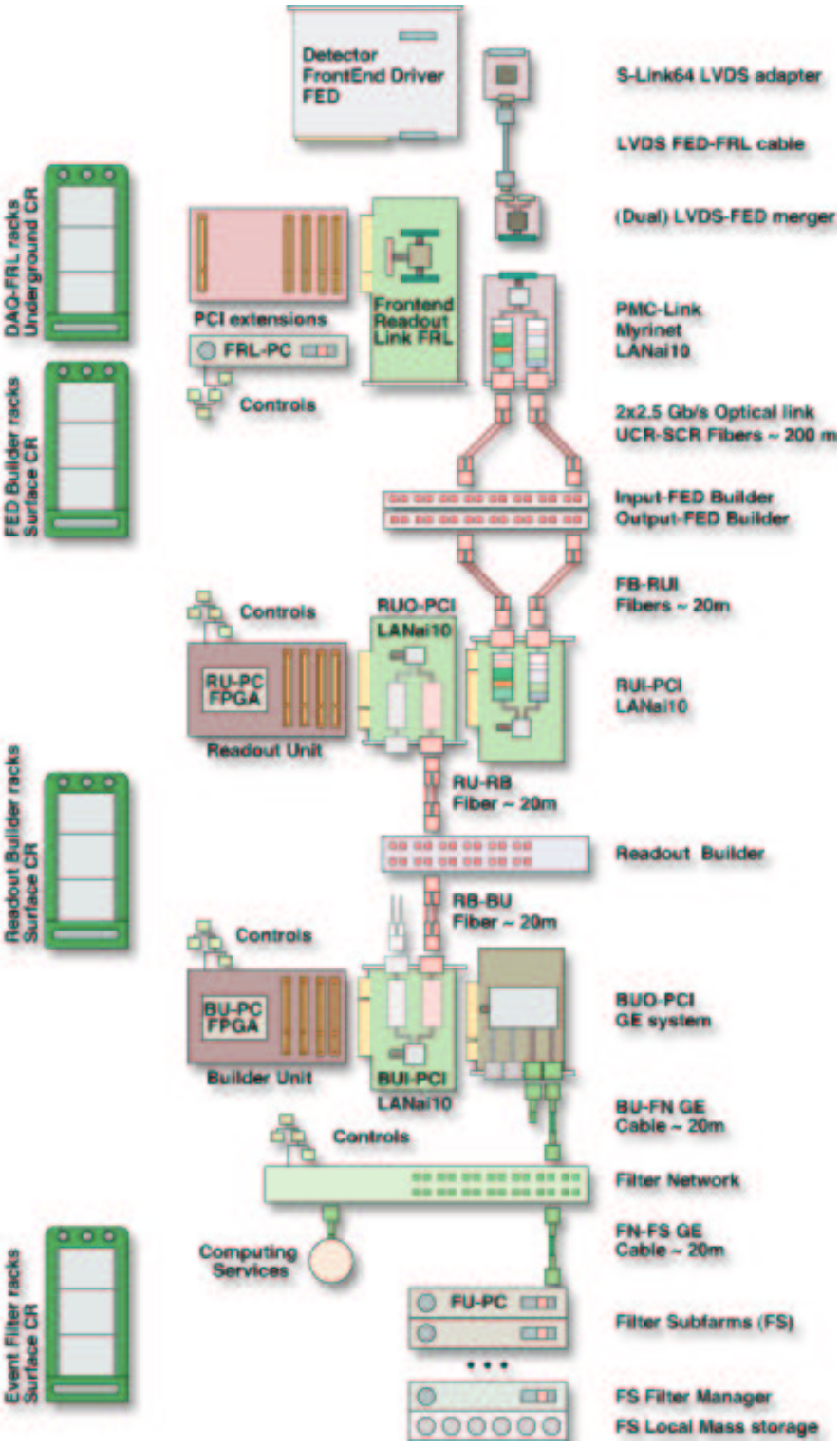

Figure 9.3: CMS DAQ layout, from underground to surface

Figure 9.3 is a sketch of the DAQ layout, showing the main components and giving an idea of the data flow. The first part of the data flow happens in the underground counting room, where detector front-

ends are connected to the FLRs. The role of the FRL is to forward data to the FED-builder network over optical fibers. At this stage the data emerge in the FED-builder racks, located in the surface counting room. The first, intermediate, event-building stage is performed in the FED builder. Event fragments are collected by the Readout Unit computers, assembled, buffered, and then forwarded to the Readout Builder stage, where full events end up in the Builder Unit computers. In the case of CMS, one further step of high-level trigger selection is done in the so-called filter farm before data will eventually come to the storage.

A specific implementation for TOTEM, capable of complying with the basic requirement of standalone running, would stop at the level of the Builder Unit, sending data directly to storage. If TOTEM takes care of keeping hardware and software compatibility with CMS, in common running mode the two DAQ networks could be merged.

9.3.1 Trigger rates and Data volumes

The data volume generated by the TOTEM detectors has been evaluated on the base of the number of channels, geometry, readout electronics and simulation results as described in the relevant chapters of this document.

Luminosity	L1 rates	RP data	T1 data	T2 data
$1.6 \times 10^{28} cm^{-2} s^{-1}$	$\approx 1KHz$	$0.25MB/s$	$26MB/s$	$0.64MB/s$
$2.5 \times 10^{29} cm^{-2} s^{-1}$	$\approx 15KHz$	$7.50MB/s$	$390MB/s$	$9.60MB/s$
$3.6 \times 10^{32} cm^{-2} s^{-1}$	$< 100KHz$	$< 50.00MB/s$	-	$< 64.00MB/s$

Table 9.2: Evaluated trigger and data rates in the TOTEM detectors. The RP L1 rates at $\mathcal{L}_1 = 3.6 \times 10^{32} cm^{-2} s^{-1}$ are hardware limited

Tables 9.2 and 9.3 summarize the number of detector channels, the foreseen trigger rates at different luminosity, and the data rate evaluated on the base of the detector geometry and simulation. A few remarks have to be made.

- Due to the fact that there might be more electromagnetic activity in the detectors, in the supports and in the beam pipe than reproduced in the simulation, the data volumes might be underestimated.
- Detector noise has been assumed to be optimal. If it will be higher than foreseen the data rates will necessarily be higher, or the trigger rates lowered consequently. The same argument applies if, during setting-up, zero-suppression thresholds will be kept at conservative levels.
- T2 data rates may be higher than evaluated on the base of primary tracks, due to the most likely presence of hard photon conversions.

9.3.2 Size of the DAQ system

Detector	Readout channels	Number of FED and FRL
Roman Pots	$\approx 120k$	8
T1	$\approx 33k$	4
T2/GEM or T2/Silicons	$\approx 40k$ or $\approx 80k$	4 or 6 (Depending channels and/or data rates)
TOTAL	$\approx 190K$ to $\approx 230K$	16 to 18

Table 9.3: Number of channels and front-ends in the TOTEM DAQ

Some redundancy has to be implemented in the system, both for the reasons already mentioned about the data rates, and to allow possible extensions and/or modifications to the detector. Such redundancy has been taken into account in the tables by always rounding-up the number of FEDs and FRLs with

respect to the strict minimum, and to assuming that we will not make use of the possibility of merging 2 FEDs into one FRL.

Given the number of front-ends, we believe that at most two FED builders in 8x8 configuration will be needed to accommodate the TOTEM FRLs and to provide the data-to-surface connection. A second-stage building performed by a single RU builder will be largely sufficient to cope with TOTEM's data rates.

In addition, the system will include at least one TTC crate implementing the TOTEM trigger partition, as well as the computing infrastructure to allow on-line monitoring, control and local data storage.

9.4 Cost estimates

Cost estimates are reported in the chapter discussing the overall cost of the experiment. Estimates can be established rather easily by assuming that the cost will scale linearly with the number of front-end links (FRLs) and that the system will be implemented in CMS-like fashion. There might, of course, be a slight underestimation, since re-scaling from ≈ 500 front-ends of the CMS system to the < 20 of TOTEM will not be perfect. The cost estimate includes the TOTEM TTC partition hardware and an on-line computing infrastructure.

References

[1] ATLAS High Level Trigger, Data Acquisition and Controls. CERN-LHCC-2003-022.

[2] The Trigger and Data Acquisition Project, Volume II Data Acquisition and High Level Trigger. CERN-LHCC-2002-026.

[3] CMS : the TriDAS Project Technical Design Report; Volume 1, The Trigger Systems. CERN-LHCC-2000-038.

[4] B.G. Taylor, 'LHC Machine Timing Distribution for the Experiments', Proc. 6th Workshop on Electronics for the LHC Experiments, Cracow, Poland, 11-15 September 2000, pp. 312-317.

[5] J. Varela, 'Timing and Synchronization in the LHC Experiments', Proc. 6th Workshop on Electronics for the LHC Experiments, Cracow, Poland, 11-15 September 2000, pp. 77-87.

[6] J. Varela et al., 'CMS L1 Trigger Control System', CMS NOTE 2003/033.

10 Running Scenarios

The TOTEM physics programme includes the measurement of the total cross-section as well as extensive studies of diffractive process in the very forward region. (See Chapter2 for more details on the physics program.) These various studies require different beam parameters and running conditions. The run scenarios are outlined in Table 10.1. We discuss each in turn.

Running scenario	1 σ_{tot} , low $\|t\|$ elastic scattering, minimum bias	2 diffractive physics large p_T phenomena		3	4 large $\|t\|$ elastic scattering
β^* (m)	1540	1540		200–400	18
Number of bunches	43	156		936	2808
Bunch spacing [ns]	2025	525		75	25
Half crossing angle [μrad]	0	0		100–200	160
Geometric luminosity reduction factor	1	1			0.992
Transverse normalised emittance [μm rad]	1 [0.5]	1	3.75		3.75
Number of particles per bunch	$0.3 \cdot 10^{11}$ [$< 10^{10}$]	$0.6 \cdot 10^{11}$	$1.15 \cdot 10^{11}$		$1.15 \cdot 10^{11}$
Circulating beam current [A]	0.002	0.017	0.032		0.582
RMS beam size at the IP [μm]	454	454	880		95
RMS beam divergence at IP [μrad]	0.29	0.29	0.57		5.28
Horizontal IBS growth time at 7 TeV [hours]	23	13.5	80		80
Peak luminosity [$\mathrm{cm}^{-2}\mathrm{s}^{-1}$]	$1.6 \cdot 10^{28}$ [10^{27}]	$2.4 \cdot 10^{29}$		$7.2 \cdot 10^{30}$	$3.6 \cdot 10^{32}$
Events per bunch crossing (for $\sigma_{tot} = 109\,\mathrm{mb}$)	0.004	0.015		0.08	1.24

Table 10.1: LHC beam parameters for different dedicated TOTEM operation scenarios

In the first three years of LHC operation, TOTEM will mainly run at reduced luminosities and with special insertion optics. Several runs, typically of one day duration, could be spread throughout this time period. While the scenario for commissioning the LHC is not yet fully defined, it seems clear that the LHC will first operate with single beams, then with reduced proton densities in a single bunch, followed by running with a reduced number of bunches. During this initial period both the machine and the experiments will learn how to run so as to maximize the integrated luminosity. The single-beam runs will allow TOTEM to see how close the Roman Pots can approach the beam, and will also permit detailed understanding of the beam induced background arising from processes such as beam-halo and beam-gas interactions. The total cross-section measurement should begin in the initial phase of LHC operation in order to determine the luminosity and calibrate the CMS detectors. However, the low-$|t|$ elastic scattering measurements require clean beam and an excellent vacuum. Further, the accuracy of the total cross section measurement and the need to detect leading protons (elastically or quasi-elastically scattered) close to the beam impose very demanding requirements both on the beam parameters and their

stabilities during a run. While sufficient statistics can be obtained in a single run, several runs will be needed in order to understand and determine the systematic errors on the extrapolation to the optical point ($t = 0$). In the first year we thus suggest several one-day runs with TOTEM running conditions (scenario 1 in Tab. 10.1): 43 bunches, a reduced emittance and a large β^*, resulting in a luminosity of the order of $10^{28}\,\mathrm{cm}^{-2}\mathrm{s}^{-1}$. The 43 bunches filling scheme for the dedicated runs has been approved by the LHC Project and it is, in fact, now foreseen as a baseline for the commissioning of the machine [1]. Once the machine is well understood, we propose to use low current beams with fewer than 10^{10} protons/bunch, further reducing the emittance by scraping the beams (scenario 1). With a lower risk of damage in these runs, we hope to be able to move the silicon detectors sufficiently close to the beam to reach the Coulomb region of the elastic scattering.

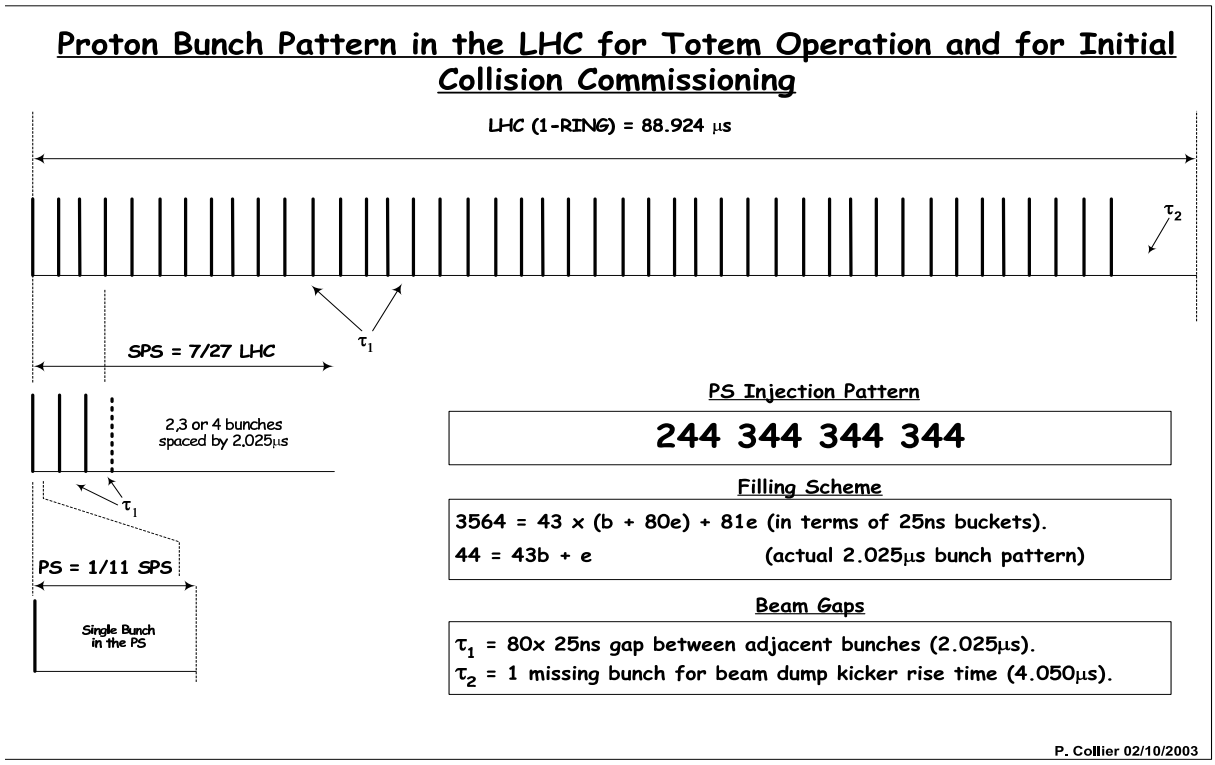

Figure 10.1: Bunch filling scheme for 43 bunches in the LHC

Even at a luminosity of $10^{28}\,\mathrm{cm}^{-2}\mathrm{s}^{-1}$, minimum bias triggers will saturate the DAQ. At this point, triggers involving the combination of diffraction with large transverse momentum phenomena, charm and beauty production, or electroweak phenomena, will provide a much deeper understanding of diffraction and the structure of the Pomeron. These processes, as well as double Pomeron exchange (including hard scales) require runs at higher luminosities, while still maintaining the efficient detection of leading protons. We can meet these requirements by continuing to run large β^* and increasing the number of bunches to 156, the largest number of bunches compatible with zero crossing angle. In this scenario, the first parasitic crossing occurs at 79 m away from the IP (towards the end of the D1 separation dipole) where the beams are sufficiently separated (18.7 mm) to avoid long-range beam–beam effects. Such a filling scheme has recently been studied and will be finally endorsed if machine tests confirm its feasibility [3]. The two filling schemes are sketched in Figs. 10.1 and 10.2.

Still higher luminosities can be achieved by increasing the number of protons per bunch (scenario 2 in Table 10.1). The maximal number depends on the beam size, and hence on the transverse emittance. The particle density in a bunch is limited by tune shift effects. There is a critical interplay between the maximal proton number in a bunch and the achievable emittance. The maximal bunch population given

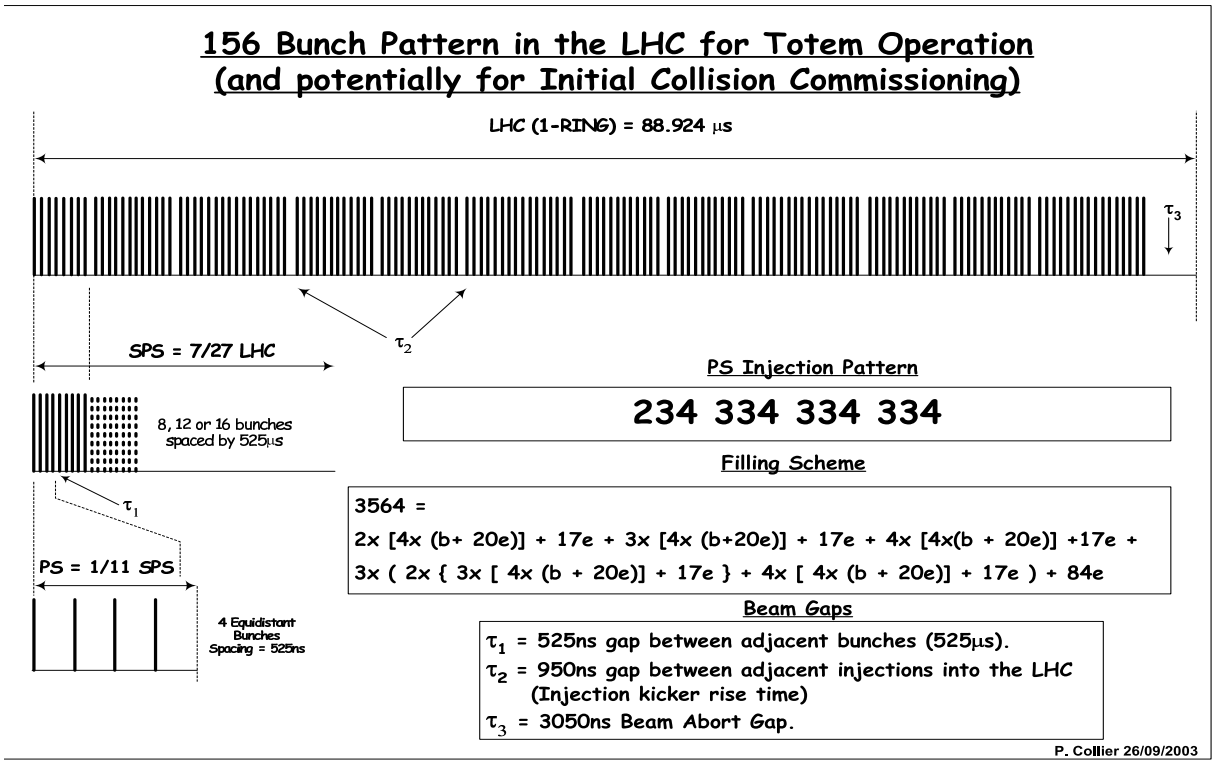

Figure 10.2: Bunch filling scheme for 156 bunches in the LHC

in Table 10.1 is still under discussion. The quoted small emittances can in principle be achieved with the accelerator chain. However, due to recent impedance calculation the beam cleaning collimators have probably to be positioned at a larger distance than previously foreseen. As a consequence, the silicon detectors cannot approach the beams down to 10σ if they are still supposed to profit from the cleaning efficiency. The details of the running scenarios need to be further discussed with the LHC Machine Groups. Operation with a low emittance has the desirable consequences of reducing both the beam size (and hence increasing the luminosity) and the angular spread of the beam. The possibility of achieving a beam emittance of 1 μm $\cdot$ rad, much smaller than the nominal one of 3.75 μm $\cdot$ rad, is presently under discussion. Preliminary results from tests in the SPS during 2003 indicate that the injection oscillations in the SPS are under control and that normalized emittances of $\sim$1 μm $\cdot$ rad can be achieved at 450 GeV for bunch intensities up to $0.7 \cdot 10^{11}$. Such small emittances are also a major challenge for the collimation system in terms of mechanical tolerance and handling of the collimators with only 1 mm full gap opening.

In order to achieve still higher luminosities, the β^* has to be lowered to values around 200-400 m (scenario 3 in Table 10.1). Such an optics is presently under study. During the commissioning phase of the first year, the bunch spacing will be 75 nsec, three times larger than nominal. With a crossing angle of ± 0.2 mrad, this optics could be implemented while still avoiding a large beam overlap at the parasitic crossing at 12 m. Luminosities of a few times $10^{30}\,\mathrm{cm}^{-2}\mathrm{s}^{-1}$ will be achievable.

In all the running scenarios discussed above, the leading proton in diffractive events can be detected with more than 90% efficiency, mainly due to the low $|t|$-acceptance and almost independently of the proton momentum loss (see Section 11.6). This is not the case for a β^* of 18 m (scenario 4 in Table 10.1), where the t-acceptance starts at values above $0.4\,\mathrm{GeV}^2$. A few of these runs will extend the measured elastic scattering spectrum to the order of $10\,\mathrm{GeV}^2$. The overlap between the low and the large t measurements is guaranteed by the runs with intermediate β values.

References

[1] R. Bailey and P. Collier, Standard Filling Schemes for Various LHC Operation Modes. LHC-PROJECT-NOTE-323; 19 Sep 2003.

[2] E. Metral, A. Verdier, LHC-PROJECT-NOTE, to be published.

[3] Minutes of the LHC Technical Committee #2003-16
http://lhcp.web.cern.ch/lhcp/ab_ltc/ltc_2003-16.html

11 Physics Performance

11.1 Low $|t|$ elastic scattering

11.1.1 Experimental method

The displacement of a scattered proton (with momentum loss $\frac{\Delta p}{p}$) at distance s from the IP, $(x(s), y(s))$, is given by its coordinates (x^*, y^*) and scattering angles $\Theta^*_{x,y}$ at the IP, the effective length $L^{eff}_{x,y}$, the magnification $v_{x,y}$ and the dispersion D of the machine:

$$\begin{aligned} y(s) &= v_y(s) \cdot y^* + L^{eff}_y(s) \cdot \Theta^*_y \\ x(s) &= v_x(s) \cdot x^* + L^{eff}_x(s) \cdot \Theta^*_x + \frac{\Delta p}{p} \cdot D(s) \end{aligned} \tag{11.1}$$

From Eqs. 3.1 and 11.1 (for $\frac{\Delta p}{p} = 0$), in principle the measurement of the positions and angles at the detector location allows the determination of the quantities at the IP. In reality, owing to the small angles involved, the direction at the detectors cannot be measured accurately enough. With the special insertion optics (see Chapter 3) which is left-right symmetric, the scattering angle Θ^* can be measured combining the displacements of the left and right arms, using the collinearity of the two scattered protons. From Eq. 11.1

$$\Theta^*_u = \frac{u_R - u_L}{2L^{eff}_u} , \quad u = x(s), y(s) \tag{11.2}$$

Elastic scattering events will be detected with the two Roman Pots stations placed symmetrically on both sides of the IP.

11.1.2 Acceptance

In Fig. 11.1 Monte Carlo calculations of the geometrical acceptance are shown. The events are generated according to the distribution e^{-Bt} ($B = 20$ GeV^{-2}) in the range of $|t|$ from 10^{-4} to 1 GeV^2, uniformly distributed in azimuthal angle (φ), and they are tracked through the accelerator lattice using the program MAD-X [1]. The detector is assumed to be 100% efficient at a distance $10\sigma^{beam} + 0.5$ mm from the beam center.

The two curves correspond to the reduced (1 μm·rad) and nominal normalized emittance (3.75 μm·rad) as discussed in Chapter 3. The cut for large t values is due to the beam screen placed in Q5 at $\sim$ 200 m from the IP.

The precise knowledge of the acceptance at low $|t|$-values is important because it affects the extrapolation to $t = 0$ and hence the precision on the total cross-section. We consider as a safe t-value, where the acceptance can be used with confidence, the value at 50% acceptance $|t_{50}|$=$2.28 \cdot 10^{-3}$ ($5.4 \cdot 10^{-3}$) GeV^2 for reduced (nominal) emittance.

In Fig 11.2 (left) the dependence of t_{50} as a function of the distance to the beam is shown. As a test of the capability of the TOTEM experiment, Fig 11.2 (right) shows the t_{50}-values for different center-of-mass energies for a detector placed at $10\sigma^{beam} + 0.5$ mm (triangles): on each curve the corresponding value in t where the hadronic and Coulomb cross-section are equal is marked (squares). In order to reach the Coulomb region at $\sqrt{s}$=14 TeV the silicon detectors have to be placed at around 10σ, while for energies below 8 TeV the Coulomb region can be accessed for the nominal distance to the beam.

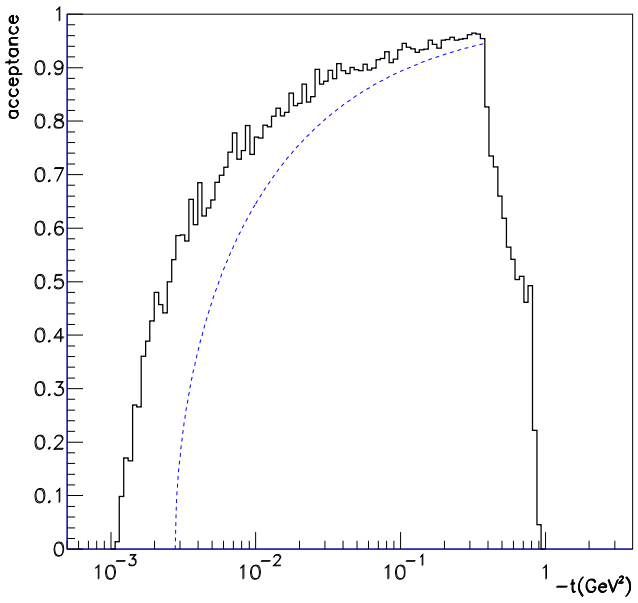

Figure 11.1: Geometrical acceptance of the detectors at 220 m for reduced (solid) and nominal (dashed) emittance

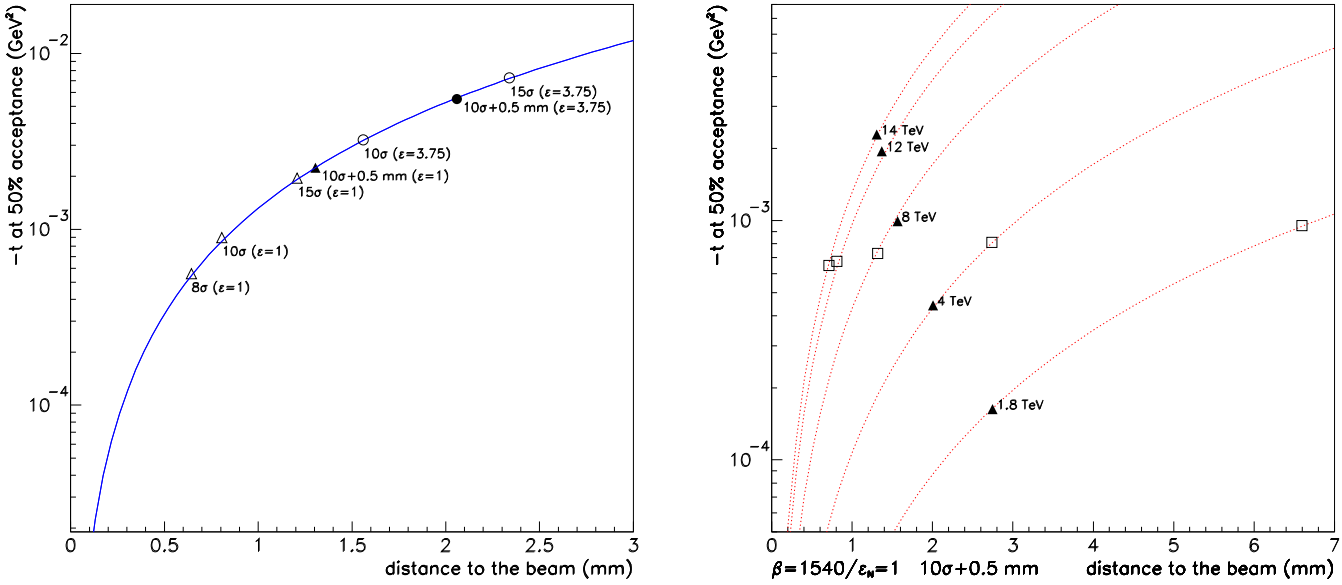

Figure 11.2: $-t$ corresponding to an acceptance of 50% vs. distance to the beam center. Left: for nominal LHC center-of-mass energy. The corresponding σ^{beam} value for two emittances is also marked. Right: for different center-of-mass energies, the $-t$ value where $\sigma_{hadronic} = \sigma_{Coulomb}$ is also marked (square)

11.1.3 Resolution due to smearing effects

In order to study the accuracy of the t-measurement, different error sources have been studied separately. The smearing effects are added to the events, and the particles are tracked to the detector locations where the detector response is simulated.

For the 'two arms' measurement, the events are detected at two stations, ±220 m. The scattering angle is calculated from Eq. 11.2, averaged between two units on each side ($\langle\Theta^*\rangle_{1,2}$) and t is reconstructed as $-t_{rec} = p^2(\langle\Theta^*_x\rangle^2_{1,2} + \langle\Theta^*_y\rangle^2_{1,2})$. The 'one arm' measurement considers only the clockwise moving protons. The contributions of the different error sources to $\sigma(t)/t$, are summarized in Tab 11.1, for two t values and $\epsilon_N = 1\mu\text{m} \cdot \text{rad}$.

		$-t = 0.01$ GeV^2		$-t = 0.1$ GeV^2	
		two arms (%)	one arm (%)	two arms (%)	one arm (%)
Angular beam divergence	0.3 μrad	2.9	4.1	0.9	1.3
Detector resolution	20 μm	1.3	1.8	0.4	0.6
Vertex smearing x-dir	454 μm	0	1.25	0	0.4
Vertex smearing y-dir	454 μm	0	0.23	0	0.06
Beam position resolution	5 μm	0.32	0.45	0.1	0.15
Total		3.2	4.7	1	1.5

Table 11.1: Error sources and their contributions to $\sigma(t)/t$

For the smearing effects which are not correlated for the two forward protons, there is then an obvious $\sqrt{2}$ difference between the 'one' and 'two arms' case. The vertex smearing is an exception: the effect vanishes in the case of two arms because only the difference of the left-right coordinate is used for the reconstruction and the optical functions are symmetric. The angular beam divergence is by far the dominant error source on the t resolution, it is independent of the initial azimuthal angle φ and causes an offset on t_{rec} of about 0.2% for $-t > 4 \cdot 10^{-2}$ GeV^2, owing to the quadratic dependence of t on the detector coordinates. The effect due to the detector resolution shows a φ dependence, because of the different values of L^{eff} in the two projections x and y. The values given in Table 11.1 are averages over φ.

The smearing due to the beam divergence and vertex position depends on the emittance and can be rescaled with $\sqrt{\epsilon}$, while the detector and the beam position resolution are independent of the emittance and can be rescaled linearly with their value. The result with all the effects included for the two t-values in the table is shown in Fig. 11.3 as a function of φ. The t dependence, which behaves like $\sigma(t)/t \sim 1/\sqrt{-t}$, is shown in Fig. 11.4.

In order to be able to reconstruct elastic scattering events, the determination of the collinearity of the two tracks on either side is fundamental. One of the most important features of the present optics, with respect to the optics with $\beta^* = 1100$ m, is the improvement in the φ resolution as shown in Fig. 11.5: as a function of $-t$ on the left and versus φ for two t values on the right.

Measuring the angle between two RP units on each side makes it possible to reconstruct the position of the vertex in the transverse plane at the IP. The beam divergence, the detector resolution, and the small 4 m lever arm do not allow a precision better than $\sim$ 1 mm but still allow beam–beam events to be disentangled from beam–wall or beam–gas events (Fig. 11.6). It is not possible to determine the longitudinal position of the vertex because the angles involved are too small, but simulations show that the vertex smearing along the longitudinal direction has a negligible effect on the measurement. While the geometric alignment of the RP, for example, and the BPM can be guaranteed to a precision of 20–50 μm on each side of the IP, this precision might be worse by one order of magnitude when comparing one side of the IP with the opposite side. Low-t elastic scattering events will be used to study and eliminate these systematic effects [2].

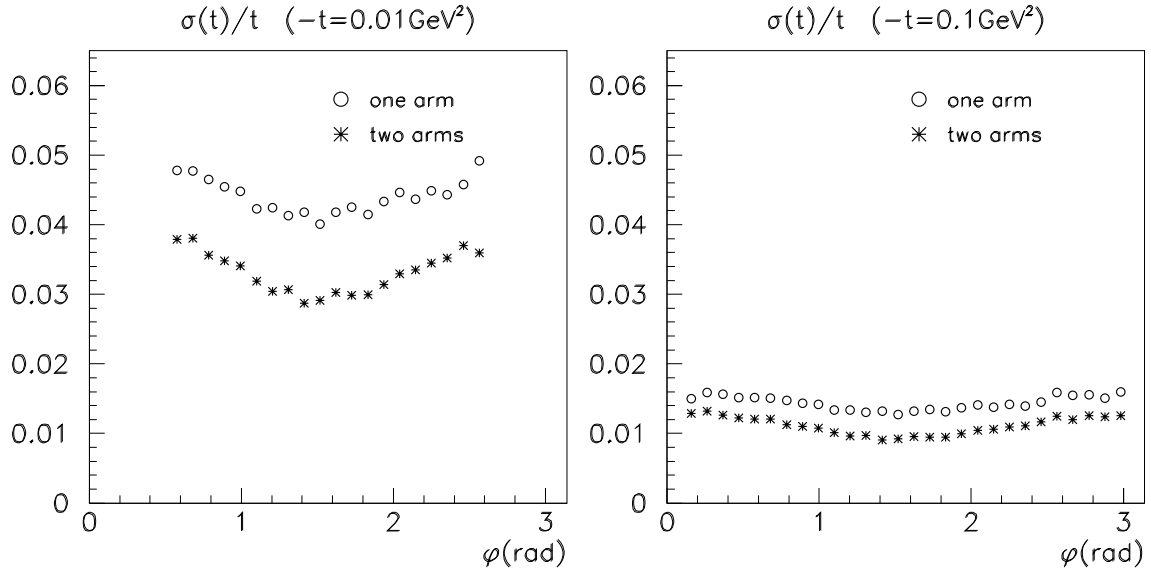

Figure 11.3: $\sigma(t)/t$ vs. φ for one and two arms measurement

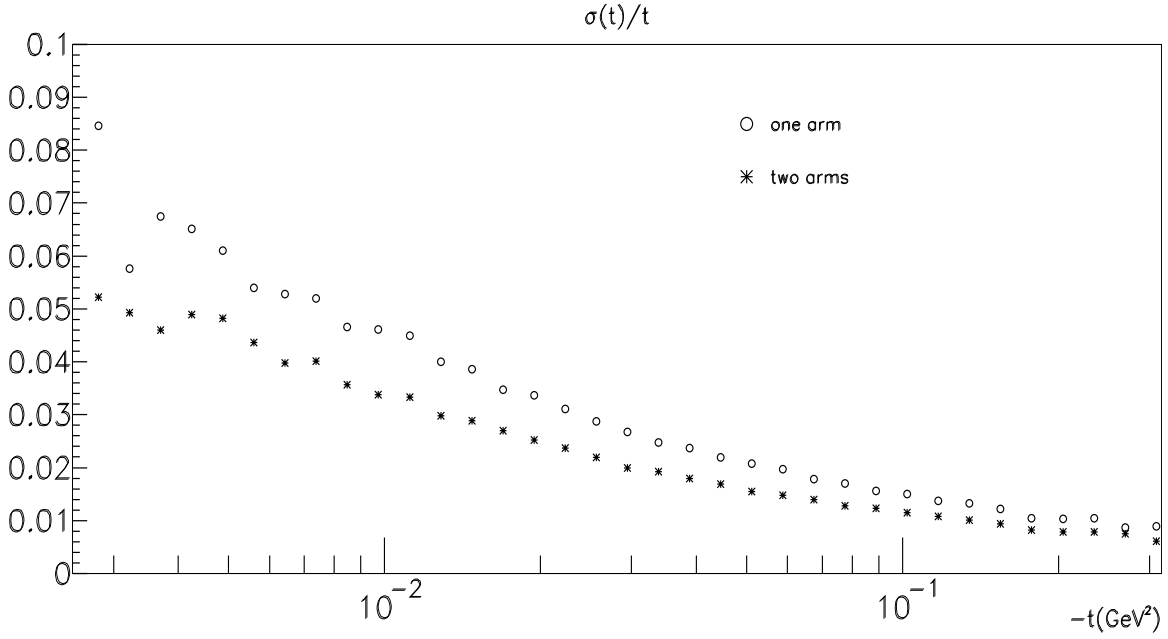

Figure 11.4: $\sigma(t)/t$ vs. t for one and two arms measurement

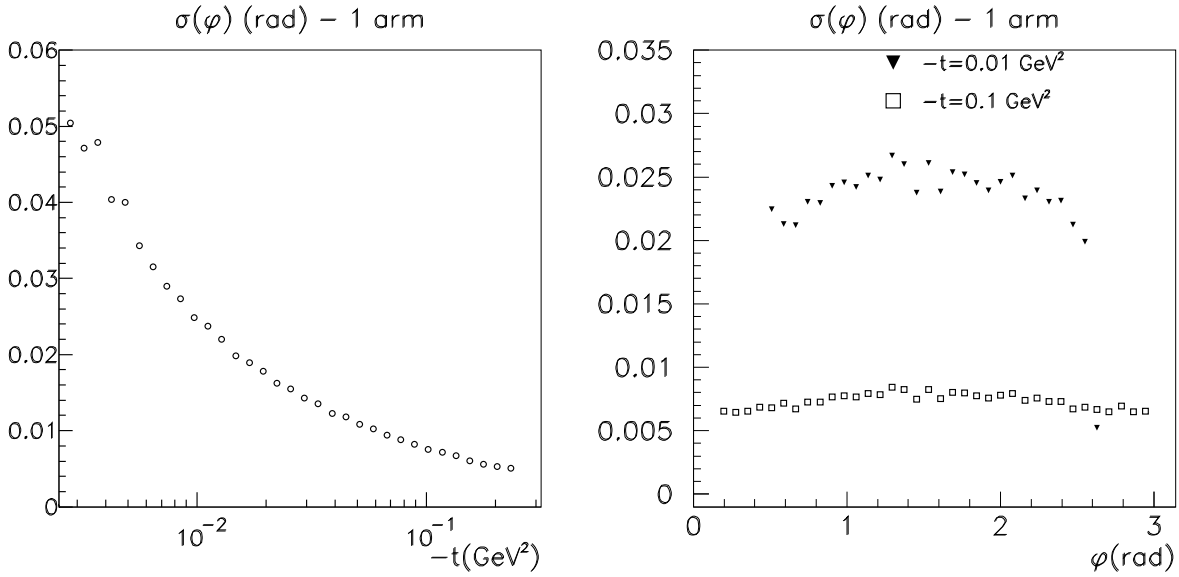

Figure 11.5: φ resolution vs. t (left) and vs. φ for two t values (right)

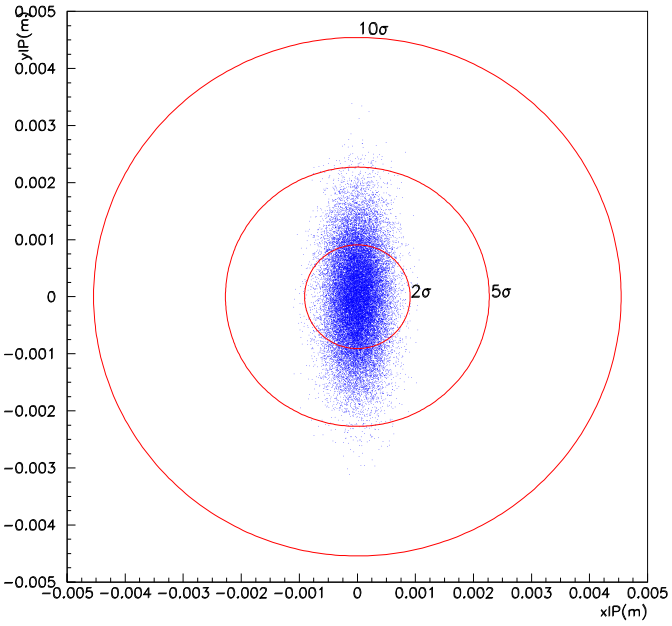

Figure 11.6: Distribution of the reconstructed vertex: the circles indicates the size of the transverse interaction region in units of the beam size σ

11.2 The extrapolation to $t = 0$

11.2.1 Experimental method

In order to measure the total cross-section, the extrapolation of the elastic scattering distribution dN/dt to $t = 0$ is required. The relative statistical uncertainty on the extrapolation is estimated to be ~ 0.1 % using $\sim 10^7$ reconstructed elastic events from 10 hours data taking at a LHC high-β^* fill with a luminosity of 10^{28} cm^{-2}s^{-1}.

The following study is performed by simulating elastic events, generated according to a distribution e^{-Bt} ($B = 20$ GeV^{-2}), with the high β^* optics at nominal emittance (see Chapter 3). The detectors are located at 220 m. They approach the beam at a distance $d = 1.6$ mm and their resolution is assumed to be 20 μm. The t-distribution of all reconstructed elastic events $(dN/dt)_{rec}$ (with both protons within the acceptance of the detectors) is corrected for acceptance and the $(dN/dt)_{t=0}$ is then determined by fitting an exponential function to this corrected distribution.

Two different criteria are used for the extrapolation. The first one ('without cut') contains all elastic events with both protons reconstructed and in the second one ('with cut') a special selection on the reconstructed elastic event sample has been introduced to reduce the influence of the uncertainties on the acceptance function. This cut consists in selecting events for which the averaged vertical displacement (between left and right side) fulfils: $|y_l + y_r|/2 > d + 3L_y^{eff}\sigma_\Theta^{beam}/\sqrt{2}$, where σ_Θ^{beam} is the beam divergence at the IP. The acceptance is then very close to the purely geometrical one: $(2/\pi)\arccos\sqrt{t_0/t}$, where t_0 is the lowest t-value at which the acceptance is non-zero. The acceptance function for the 'without cut' criteria is calculated from the simulation by a three-parameter fit to the ratio between the $(dN/dt)_{rec}$ and dN/dt distributions using the functional form $A\arccos(t_0/t)^\alpha$ (where A, t_0 and α are free parameters). The two acceptances and the corresponding fits are shown in Fig. 11.7 (left).

Next, systematic effects that can contribute to the accuracy of the extrapolation and the requirements to control these uncertainties are discussed. There are two main classes of systematic uncertainties on the extrapolation, one coming from experimental effects distorting the experimentally reconstructed t-distribution and the other one coming from the theoretically predicted t-distribution which might differ from a purely exponential form.

11.2.2 The extrapolation accuracy due to experimental effects

To study the influence of experimental effects, the t-distribution is assumed to be exponential: $dN/dt = C \cdot e^{-B\,t}$ and the accuracy of the extrapolation is reduced to the uncertainty of measuring the constant C.

No sizeable effect on the extrapolation result due to the finite t-resolution is observed when acceptance effects are not taken into account. Analytical calculations, based on the assumption that the t-uncertainty has a Gaussian distribution (see 11.1.3), show a contribution of $\sim 0.03\%$ on the extrapolated value.

The effect of changing the lowest $|t|$-bin in the fit while keeping the highest $|t|$-bin fixed at 0.1 GeV^2 was studied and showed no significant trend [see Fig. 11.7 (right)]. Note that in these studies, the elastic scattering event sample contains only $1.5 \cdot 10^6$ events, instead of the expected 10^7. The obtained statistical uncertainties of $\sim 0.3\%$ on the fitted parameters shown in the figures will in reality be reduced by about a factor 3. It should be noted that for the following studies of the impact of experimental uncertainties, always the same sample of elastic scattering events has been used. The apparent shift in the extrapolation (for nominal values of the simulation parameters), as shown in Fig. 11.7 (right) is thus due to statistics.

Possible uncertainties have been studied by varying each relevant parameter in the simulation at a time and keeping the acceptance correction unchanged. In order to observe significant effects, in most cases the parameter has to be varied beyond the expected accuracy.

Beam divergence The effect of a different beam divergence is shown in Fig. 11.8 (left). The reduced dependence of the extrapolation 'with cut' can clearly be seen. To keep the systematic effect from the beam divergence at a level of $\sim 0.05\%$, the size of the beam divergence should be known to $\sim 10\%$.

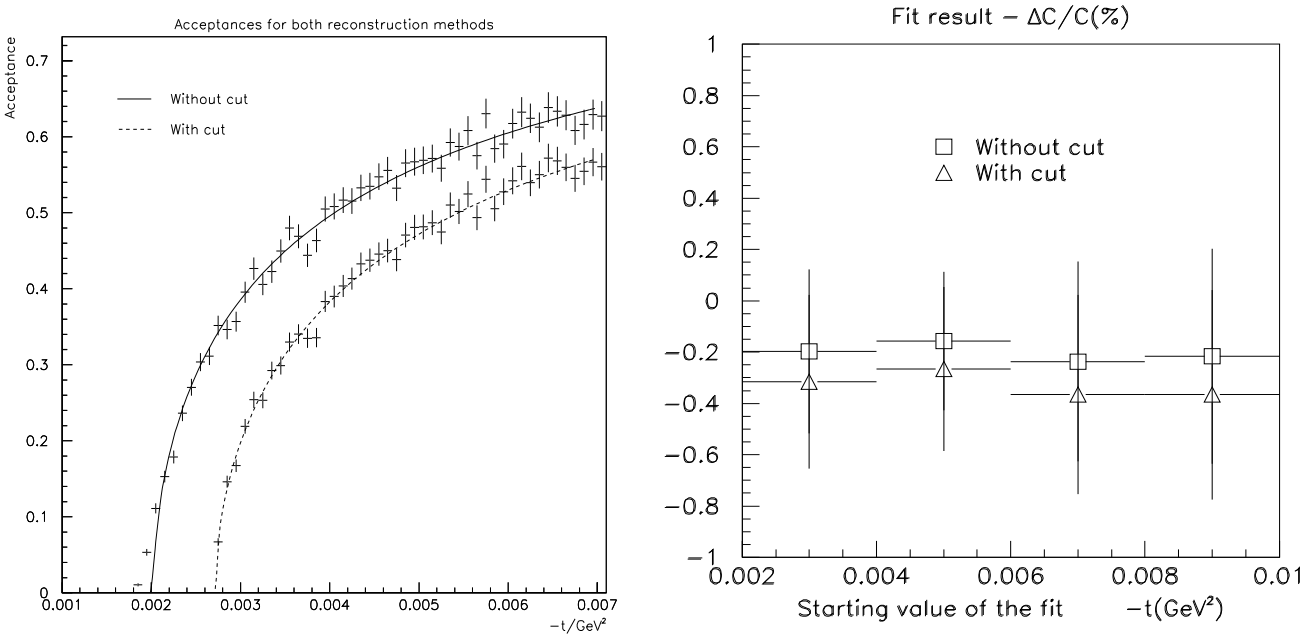

Figure 11.7: Acceptances for the two criteria with their corresponding fit (left). The relative systematic shift (in per cent) of $C = (dN/dt)_{t=0}$ as a function of the t-value of the first bin used in the fit (right). The 'cut' is described in the text

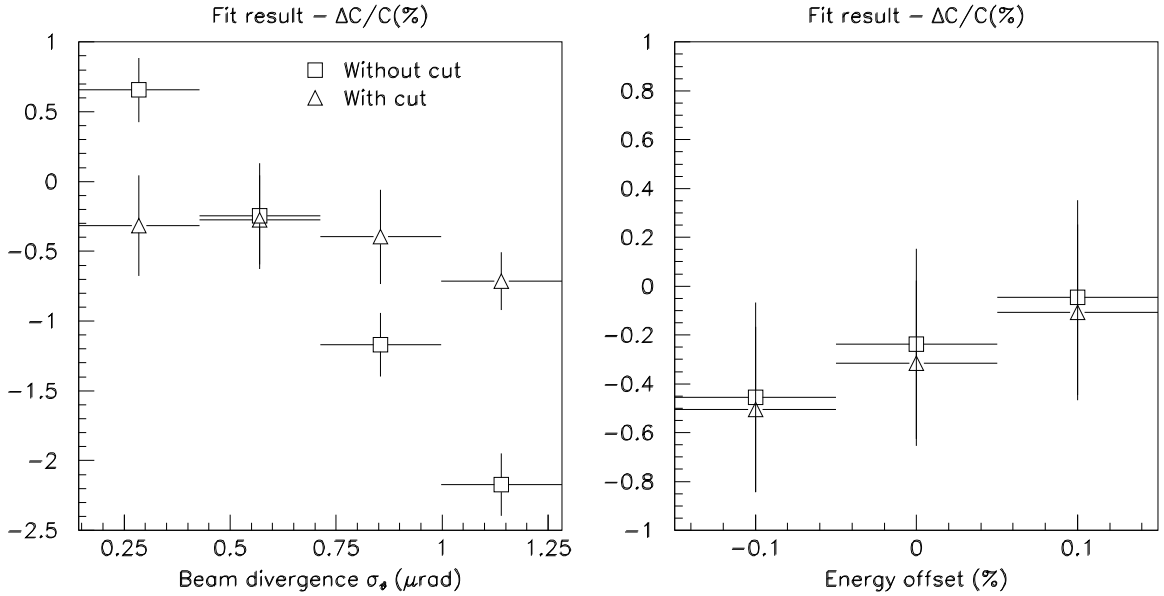

Figure 11.8: The relative systematic shift (in per cent) of $C = (dN/dt)_{t=0}$ for different beam divergences (nominal: 0.57 μrad) – (left) and for a beam energy offset (right). The lowest bin used in the fit is $-t = 0.003$ GeV^2 (with cut) and 0.007 GeV^2 (without cut). The 'cut' is described in the text

Beam energy offset The effect of a beam energy offset is shown in Fig. 11.8 (right). In this case there is no difference between the two samples: an energy offset introduces a shift of the t-scale which makes the extrapolation result very sensitive to it and the special treatment for the acceptance correction does not help. To keep the systematic effect from a beam energy offset at a level of ~ 0.1 %, the absolute beam energy should thus be known to ~ 0.05 %.

Beam/Detector position misalignment A displacement of either a detector or the beam relative to the respective nominal position can result in a change of the reconstructed t of the event as well as in a change of the acceptance. Both of these effects can then have an impact on the accuracy of the extrapolation.

Two scenarios have been considered; in both cases the distance between the upper (U) and lower (D) vertical detectors of each unit on both arms (Left, Right) is assumed to be known from the monitoring with the horizontal detector.

1. Upward shift by 100 μm of the detectors on the left arm, downward on the right arm ('+100/-100 μm').
2. Upward shift by 100 μm of the detectors on the left and right arm ('+100/+100 μm').

In scenario (1) the changes in t and in the acceptance cancel partially when averaging over the $U_L D_R$ and $D_L U_R$ tracks. As shown in Table 11.2, the extrapolation value does not differ very much from the nominal one and the special cut is not needed to reduce the sensitivity of the extrapolation to the detector shifts.

In contrast, for the scenario (2) there is no change in t for any event, whereas the changes in acceptance are not compensated. For both $U_L D_R$ and $D_L U_R$ tracks, the t–acceptance is shifted to larger $|t|$ values. As shown in Table 11.2, the cut helps to significantly reduce the sensitivity of the extrapolation.

Hence a precise monitoring of the beam position via the Beam Position Monitors is essential as the monitoring of the distance between the two vertical detectors of one unit.

Error on the crossing angle An error on the crossing angle of 0.2 μrad should be equivalent to a beam position offset of ~ 50 μm and has a small effect on the extrapolation result, in case the cut is used to define the event sample.

Knowledge of the effective length An uncertainty in the effective length leads to a possible additional displacement of the scattered proton at the detector location. For the minimum detectable scattering angle (reduced emittance), the displacement due to a shift of 2 % in L_y^{eff} amounts to about 25 μm. This is even smaller than the expected beam position offset in case of a non-zero crossing angle and furthermore such an effect should not be correlated between the two arms.

In Table 11.2 the uncertainty on the extrapolation accuracy is shown for the various experimental effects investigated with the simulation. A shift of $(-0.24 \pm 0.39)\%$ or $(-0.32 \pm 0.34)\%$ is obtained for the nominal conditions 'without' or 'with cut' respectively. This shift is consistent with zero and has not been subtracted from the values in Table 11.2.

11.2.3 Effect of non-exponential $\frac{d\sigma}{dt}$

As shown in Fig. 2.4, even at low $|t|$ there are considerable deviations of the hadronic cross-section from the exponential shape. Furthermore, for $|t| \leq 0.01\,\mathrm{GeV}^2$ the influence of Coulomb scattering becomes significant. To study the impact of these effects on the precision of the extrapolation of $\frac{d\sigma(hadronic)}{dt}$ to $t = 0$, an exponential function

$$f_{th}(t) = f_{th}(0)\mathrm{e}^{-B\,|t|} \tag{11.3}$$

was fitted to the expected total elastic cross-section $\frac{d\sigma(Coulomb+hadronic)}{dt}$. The upper limit of the fit interval was fixed to $0.1\,\mathrm{GeV}^2$ whereas the lower end was varied from $|t|_{min} = 0.0012\,\mathrm{GeV}^2$ to $0.1\,\mathrm{GeV}^2$.

Effect	Value	ΔC/C (%) without cut $-t_{min}$=7·10^{-3} GeV^2	ΔC/C (%) with cut $-t_{min}$=3·10^{-3} GeV^2
Beam divergence	$0.5 \cdot \sigma_\Theta$	0.65	−0.32
	$1.5 \cdot \sigma_\Theta$	−1.2	−0.4
Beam energy offset	−0.1%	-0.45	-0.5
Beam position offset	+100μm/+100μm	−1	−0.32
	+100μm/−100μm	−0.32	−0.41

Table 11.2: Summary of the extrapolation results

While the absolute scale of the statistical uncertainties of the individual measurements – defined by the integrated luminosity $\mathcal{L}_{int}$ – does not play any role for this systematic study, the t-dependence of these statistical errors has to be taken into account for χ^2 minimization:

$$\frac{\sigma^2(f(t))}{f^2(t)} = \frac{1 + \left[\frac{1}{a(t)}\frac{da}{dt} - B(t)\right]^2 \sigma^2(t)}{\mathcal{L}_{int}\, f_m(t)\, a(t)} \,, \tag{11.4}$$

where $\sigma(t)$ is the resolution of the t measurement (see Section 11.1.3), $a(t)$ is the acceptance, $f_m(t)$ is the measured differential cross-section, and $B(t) = -\frac{1}{f_m(t)}\frac{df_m}{dt}$.

The result is shown in Fig. 11.9. If the model for $\frac{d\sigma(Coulomb+hadronic)}{dt}$ on which the study was based is correct, a stable extrapolation requires the fit interval to begin below $|t| = 0.01\,\mathrm{GeV}^2$ while pushing the start point to values smaller than about $0.005\,\mathrm{GeV}^2$ does not yield any improvements but rather deteriorates the result because of the increasing importance of the Coulomb contribution. However, in order to have a sufficiently high acceptance in the relevant range $-t > 0.005\,\mathrm{GeV}^2$, the value of $-t_{min}$ has to be of the order $0.001\,\mathrm{GeV}^2$.

It should also be pointed out that this result – being based on a model for the elastic hadronic cross-section and its interference with Coulomb scattering in an experimentally unexplored domain – has theoretical uncertainties.

Conservatively, within the frame of this model, a systematic extrapolation uncertainty of 0.25% should be expected.

11.2.4 Summary on extrapolation uncertainty

The previous sections have investigated sources of systematic uncertainties which can influence the accuracy of the extrapolation of dN/dt towards $t = 0$.

For the experimental effects, an accuracy of less than 0.5 % should be achievable. This requires from the accelerator side the knowledge of the beam divergence to 10 % or better, of the beam energy to an accuracy of 0.05 %, of the crossing angle to better than 0.2 μrad and of the effective length to better than 2 %, as specified already as requirements in Chapter 3.

Furthermore the detector/beam position alignment has to be known to better than 20 μm.

Additional uncertainties can arise from the actual shape of the hadronic cross-section for elastic scattering, where for a certain model investigated in this report, a contribution of less than 0.25 % to the systematic uncertainty in the extrapolation is expected.

11.3 Inelastic measurement

The inelastic cross-section accounts for around 80% of σ_{tot}. The extrapolations from recent measurements foresee for the LHC energies the value $\sigma_{inel} \sim 79$ mb (see Chapter 8 for details and references). The

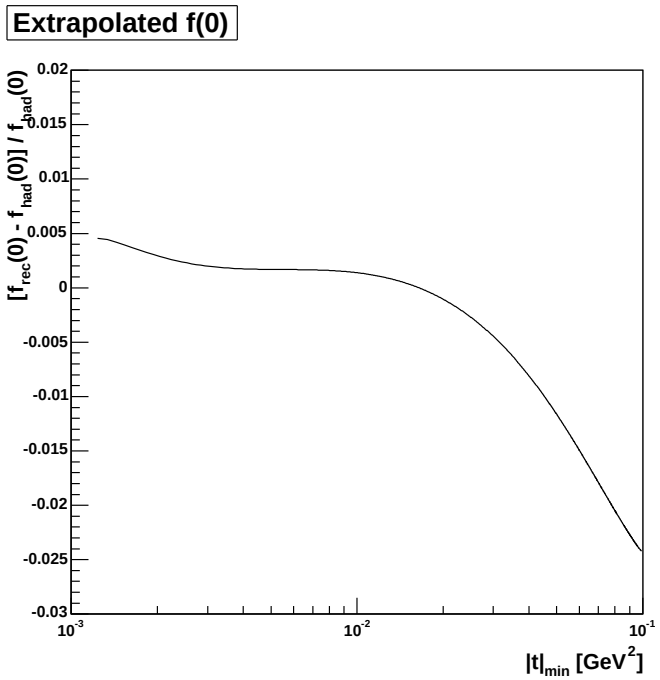

Figure 11.9: Relative deviation of the extrapolated value $\frac{d\sigma(\text{Coulomb+hadronic})}{dt}$ *from the true value* $\frac{d\sigma(\text{hadronic})}{dt}$ *as a function of the fit start value of* $|t|$*. The upper limit of the fit range was fixed to 0.1* GeV^2

inelastic processes can be divided into two categories: non-diffractive (minimum bias) with $\sigma_{mb} \sim 58$ mb and diffractive (single with $\sigma_{SD} \sim 14$ mb and double with $\sigma_{DD} \sim 7$ mb).

The measurement of the inelastic rate requires a trigger as inclusive as possible and a clear discrimination of beam-beam events from background interactions. The telescopes allow the following triggers to be used:

- double-arm trigger, which detects more than 99% of non-diffractive events;
- single-arm trigger, which detects the events escaping the double arm trigger, mostly diffractive interactions with all visible tracks in one arm only.

The trigger loss rates using the single- and double-arm trigger for the accounted physics processes are shown in Table 11.3.

Losses	Double arm		Single arm	
Process	%	mb	%	mb
Minimum bias	0.5	0.3	< 0.1	< 0.06
Double Diffractive	39.5	2.8	4.6	0.3
Single Diffractive	-	-	17.9	2.5

Table 11.3: Inelastic trigger losses for double-arm and single-arm trigger. In the double-arm trigger at least one particle per hemisphere has to be detected, while in the single-arm only at least one particle in either hemisphere

In order to discriminate beam–beam interactions from background, above all in the single-arm triggered events, a primary vertex reconstruction is required. The z vertex position is estimated determining the distance of minimum approach to the nominal z axis for each (at least two) track and then calculating the mean value: $z_{vertex} = \langle z_{track} \rangle$. This simple method allows the estimation of the primary vertex z

coordinate with a resolution achieved on minimum-bias events of $R_{vertex} = 4.5$ cm. The beam–beam events are selected by the requirement that the z position of the reconstructed primary vertex is within ± 50 cm from the nominal interaction point. With this selection the final yield of reconstructed events is more than 96%. The events lost are mainly diffractive ones where all charged tracks have angles smaller than the minimum angle covered by T2. The fraction of these events escaping detection can be estimated by extrapolation.

With the above selection a major fraction of the beam–gas events is rejected. Simulation studies have been performed, generating as first approximation, the interaction of a 7 TeV incoming proton with a proton at rest in different regions of the beam-pipe. The results show that, using the vertex reconstruction, only the beam-gas events generated near the interaction point contribute significantly to the background. The number of mis-identified beam-gas events is estimated to be $\sim 3\%$ of the interactions generated within ± 5 m from the nominal vertex. Thus, since the actual beam–gas rate is around 2 Hz/m at 1/20 of the nominal current, the trigger rate due to beam-gas interactions is negligible. Moreover, the tagging of a proton in the Roman Pots is a useful tool to discriminate single diffractive from beam–gas events. In fact, preliminary results show that $\sim$90% of the forward protons can be tagged in the Roman Pots. The condition of a leading proton trigger can be used in addition to the inelastic telescopes to make the single diffractive event selection more reliable.

The simulation of events with a double Pomeron exchange ($pp \rightarrow pXp$) is still in progress. Their contribution to the inelastic cross-section is expected to be $0.5 \div 1$ mb. Since the double Pomeron topology is given by two non-collinear very forward protons, these events can be detected using the leading proton trigger with a signature of the central system in the CMS detectors.

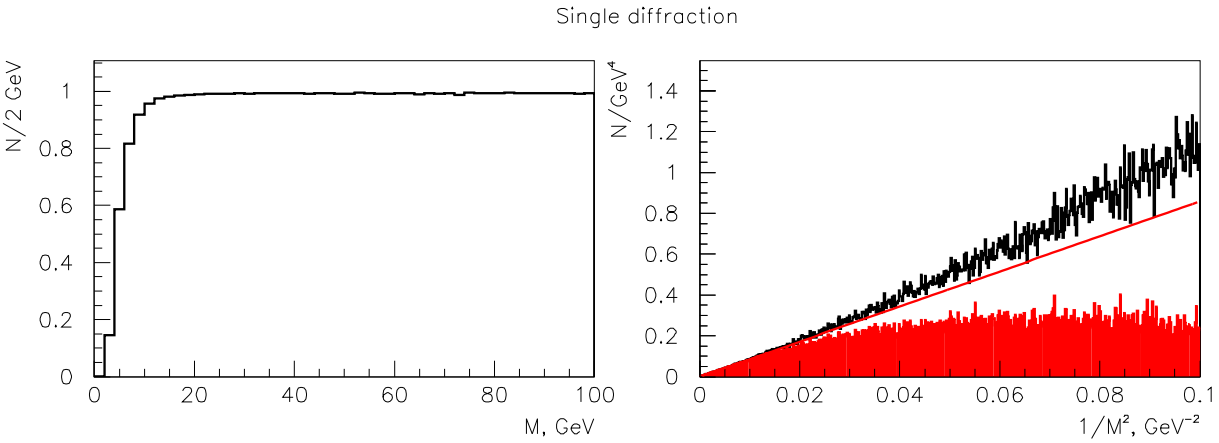

Figure 11.10: Left: ratio of detected single diffractive events as a function of M^2. Right: MC (unshaded) and acceptance corrected (shaded) single diffractive events. The line shows a linear fit of the acceptance corrected events in the mass region above 10 GeV

This last condition is necessary in order to limit the contamination due to halo protons because, in contrast to what happens in elastic scattering, with double Pomeron events the collinearity of the two detected protons cannot be imposed. Preliminary studies show a $\sim$80% efficiency in detecting double Pomeron events, which results in a loss of $0.1 \div 0.2$ mb.

The loss of single diffractive events is mainly due to events with a very low mass M, where all the particles have pseudo-rapidity above 7 and hence escape detection by the telescopes. In Fig. 11.10 (left) the detection rate is shown as a function of M. To obtain the total inelastic rate, the fraction of events escaping detection due to the incomplete angular coverage can be estimated by extrapolation. In the case of single diffraction, the reconstructed $1/M^2$ distribution has been linearly fitted for $M > 10$ GeV and the extrapolation to low masses have then been compared with the Monte Carlo, see Fig. 11.10 (right). For single diffraction, the extrapolated number of events differs from the Monte Carlo by 4% corresponding to a 0.6 mb uncertainty on the total cross-section. The same estimate for the double diffraction and double Pomeron exchange gives 0.1 mb and 0.02 mb of uncertainties respectively.

11.4 Expected accuracy on σ_{tot}

The measurement of the total cross-section is done in TOTEM with the luminosity independent method, which allows the determination of σ_{tot} by means of the optical theorem:

$$\sigma_{tot} = \frac{16\pi}{(1+\rho^2)} \frac{(dN_{el}/dt)_{t=0}}{N_{el}+N_{inel}} \tag{11.5}$$

where N_{inel} and N_{el} are the inelastic and elastic rate, $(dN_{el}/dt)_{t=0}$ is the elastic scattering t-distribution extrapolated to $t = 0$, and ρ is the ratio of the real to the imaginary part of the forward scattering amplitude.

The relative error on σ_{tot}, neglecting an uncertainty on ρ (see below), can be calculated by:

$$\left(\frac{d\sigma_{tot}}{\sigma_{tot}}\right)^2 = \left(\frac{d(dN_{el}/dt)_{t=0}}{(dN_{el}/dt)_{t=0}}\right)^2 + \left(\frac{d(N_{el}+N_{inel})}{N_{el}+N_{inel}}\right)^2 \tag{11.6}$$

The uncertainty on the inelastic cross-section has been estimated to be 0.78 mb (see table 11.4 for the contribution of each process). The elastic scattering is determinated within an error of 0.5%, corresponding to ~ 0.1 mb. However, since at very low $|t|$ the interference with the Coulomb scattering cannot be neglected, the 0.5% error on the elastic cross-section might be slightly underestimated. Nevertheless, the final error on the elastic cross-section is expected to remain below 1%.

Process	$\Delta\sigma$ (mb)
Minimum bias	0.06
Double Pomeron	0.02
Double Diffraction	0.1
Single Diffraction	0.6
Total inelastic	0.78
Elastic	0.1
$\sqrt{\Delta\sigma_{inel}^2 + \Delta\sigma_{el}^2}$	0.8

Table 11.4: Uncertainties on the cross-sections (mb) for the different processes. The uncertainties for single, double diffraction and double Pomeron are obtained by extrapolation (see the inelastic scattering section)

Adding in quadrature the uncertainty of 0.5% on the elastic scattering extrapolated to $t = 0$ yields an error on the total cross-section

$$\frac{\Delta\sigma_{tot}}{\sigma_{tot}} \sim 1\% \,.$$

Recent calculations [5] give an expected value of the ρ parameter at LHC energies of 0.12 ± 0.02, resulting in an additional error to σ_{tot} of 0.5%. It is expected that the contribution to the error from the uncertainty on the ρ parameter will be reduced when a direct measurement of ρ becomes available.

11.5 Large $|t|$ elastic scattering

The elastic scattering distribution at large $|t|$-values allows to discriminate between the various elastic scattering models. It is expected to fall steeply with t ($\sim t^{-8}$ at large $|t|$) and spans eleven orders of magnitude up to $t = 10$ GeV^2. Hence different optics have to be used to reach reasonable statistics at large values. Figure 11.11 shows the geometrical t-acceptance for two beta values: $\beta^* = 1540$ m ($\mathcal{L} \approx 10^{28}$ cm^{-2} s^{-1}) and $\beta^* = 18$ m ($\mathcal{L} \approx 10^{32}$ cm^{-2} s^{-1}) at two detector locations. The acceptance curves overlap if the station at 147 m is also used. Good statistics (see Fig. 2.2) can be obtained up to the highest observable t-value (10 GeV^2) within a few days running. The relative t-resolution is improving with increasing $|t|$ ($\sigma(t)/t \sim 1/\sqrt{-t}$) being 2% at $-t = 7$ GeV^2.

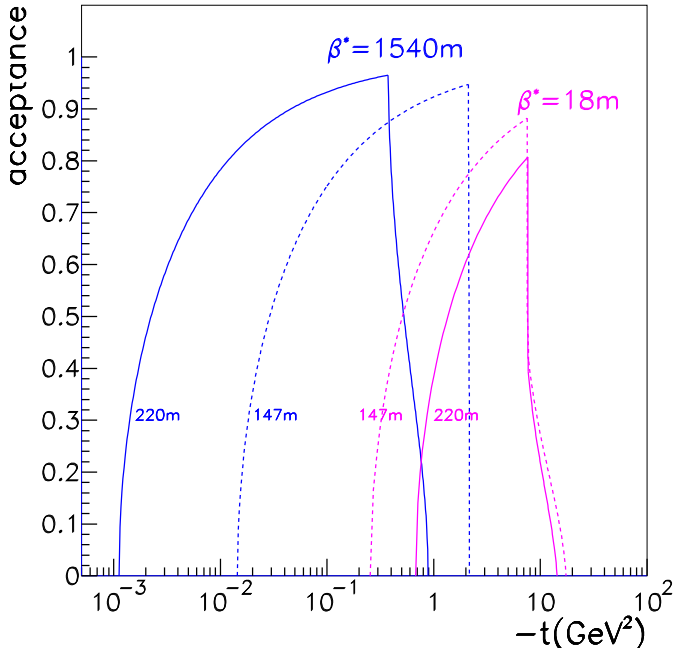

Figure 11.11: Geometrical acceptance of the detector at 147 m and 220m for medium optics, compared with the acceptance at high β^*

11.6 Diffractive proton measurement

11.6.1 Acceptance

The high β^* optics with the excellent acceptance down to small $|t|$-values also provides a very good coverage for diffractively scattered protons. Using the same approach as described earlier and taking into account both the two vertical and the one horizontal detector at the 220 m location, the acceptance for diffractively scattered protons has been determined for a detector approach of $10\sigma_{x,y} + 0.5$ mm and a reduced emittance of 1 μm·rad.

As shown in Fig. 11.12 (left), diffractively scattered protons can be observed in either one of the vertical or in the horizontal detector. For very small values of $|t|$, the proton is dominantly seen in the horizontal detector, due to its momentum loss (if this one is large enough). For larger values of $|t|$, the acceptance of the horizontal detector is reduced and the vertical detector recover a large part of it. When looking at the ξ ($= \Delta p/p$) dependence for fixed t [Fig. 11.12 (right)], this behaviour is confirmed. The horizontal detector observes all diffractively scattered protons in a limited range of ξ (< 0.04), for larger ξ values (> 0.14) the acceptance is reduced due to the beam screen apertures mostly in Q5. At smaller ξ values, protons will only be seen if they have a large enough $|t|$ and the appropriate azimuthal angle at production. In this kinematical region, the vertical detectors are important to achieve a good acceptance.

Figure 11.13 (left) shows for three ξ-values ($< 10^{-3}$, -0.01 and -0.06) the acceptance as a function of $\log(-t)$. The corresponding plot of the acceptance as a function of ξ is given in Fig.11.13 (right), for t=-0.01 and t=-0.1 GeV^2. As can be seen from both parts, the acceptance for diffractively scattered protons with a momentum loss of less than 10% is larger than 90% and thus provides TOTEM the opportunity to perform precise studies of diffractive scattering at $\sqrt{s} = 14$ TeV.

11.6.2 Resolution

The determination of the momentum loss of diffractively scattered protons can be made using two approaches:

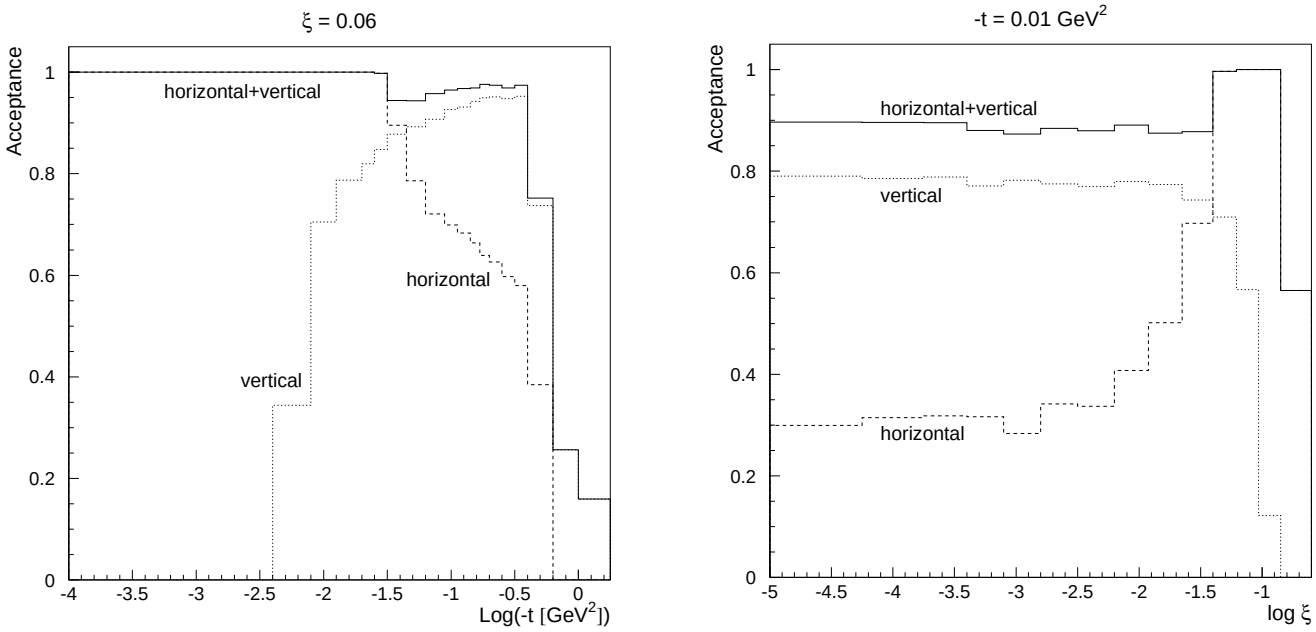

Figure 11.12: Acceptance for diffractive protons, showing the contributions of the horizontal and vertical detectors. Left: vs. $\log(-t)$ *for* ξ*=0.06. Right: vs.* $\log \xi$ *for* $t = -0.1$ *GeV*^{2}

- backtracking of the observed positions and angles of the protons through the accelerator optics elements,
- measurement of the bending of the protons in the beam separation dipole D2.

The measurement of the displacements x, y at the detector locations can be used to determine the initial kinematics of the proton. With RP units at $z = 145\,\text{m}$, 149 m, 216 m and 220 m the 3 kinematic variables ξ, x^*, θ_x^* are linked by 4 equations like (11.1). The optimum solution is then found by χ^2 minimisation. The achievable precision in ξ is $\sigma(\xi) = 5 \times 10^{-3}$.

Alternatively, the simultaneous observation and measurement of the proton displacements (and/or angles) before and after the bending dipole D2 allows one to obtain the momentum loss directly. In this case, the properties of only very few magnetic elements (predominantly the field of D2) will have to be known precisely.

Detailed simulation studies are underway to assess more quantitatively the expected accuracy on the measurement of the momentum loss for diffractively scattered protons.

11.7 Measurements at lower $\sqrt{s}$ values

The possibility to operate the LHC for lower values of the center-of-mass energy than the nominal one of $\sqrt{s} = 14$ TeV offers several additional interesting measurements which can be performed by TOTEM. These have not been studied in detail yet, but it is clear that the foreseen detector components with their planned coverage and resolution will allow to also make precise measurements under these conditions.

11.7.1 Energy dependence of total cross-section

With the luminosity independent method, it is expected that the total pp cross-section can be measured with comparable accuracy also at smaller values of $\sqrt{s}$. TOTEM could thus determine the energy dependence of the total cross-section for pp scattering within the same experiment over almost one order in magnitude (in $\sqrt{s}$) and thus contribute further to improved predictions at energies well beyond

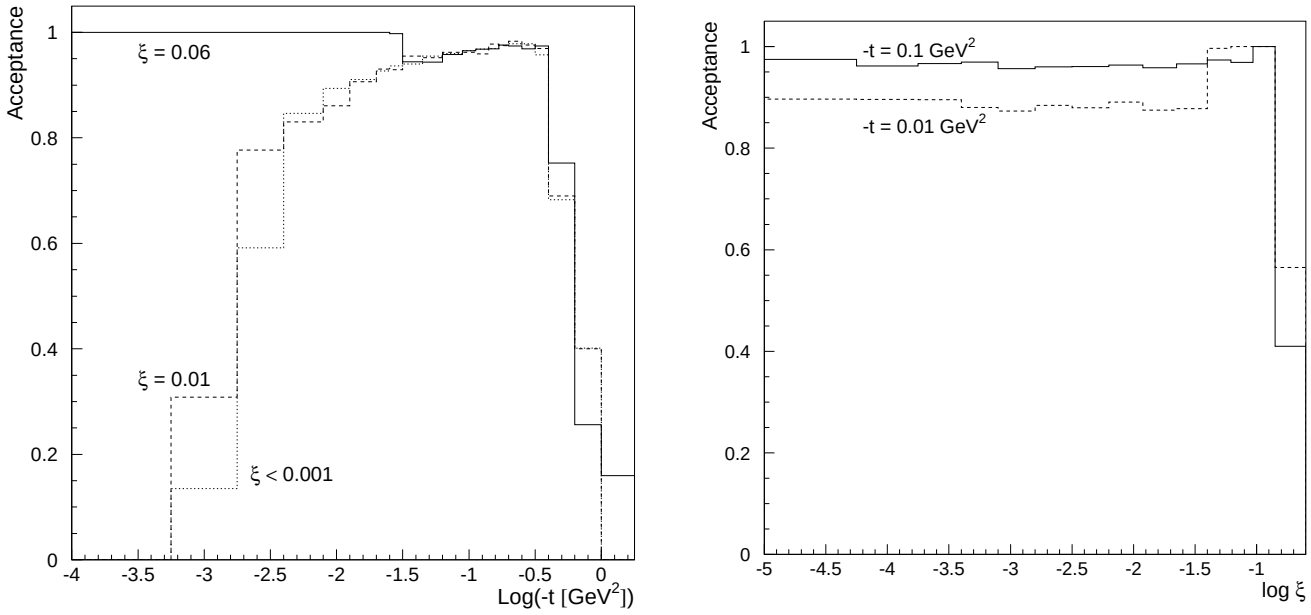

Figure 11.13: Acceptance for diffractive protons. Left: vs. $\log(-t)$*, for three* ξ *values. Right: vs.* $\log\xi$*, for two* $-t$ *values*

the LHC design value of 14 TeV. These data from LHC will also be very useful in the comparison with existing data from Tevatron on $p\bar{p}$ collisions at $\sqrt{s} = 1.8$ TeV, as the highest energies in pp collisions are/will be limited to 500 GeV only ([4]).

As described below in more detail, for values of $\sqrt{s}$ below 8 TeV it will be possible to determine the total cross-section also from the differential elastic scattering cross-section only, which will provide an important systematic cross-check of the measurement based on the luminosity independent method described in this report in great detail.

11.7.2 Energy dependence of elastic and diffractive scattering

Similarily to the case of the total cross-section, it is expected that running at lower center-of-mass energies will allow to perform various measurements of properties of elastic and diffractive scattering. This will then provide a determination of the energy dependence of relevant parameters, e.g. of the slope B of the elastic scattering cross-section and of the fraction of the total cross-section due to the contribution of the various diffractive processes.

The acceptance of TOTEM for these running conditions for elastic scattering will be (as shown in Fig. 11.2) reaching significantly smaller values of $|t|_{min}$ than for $\sqrt{s} = 14$ TeV, by up to one order of magnitude. In case of diffractive scattering, the loss of protons will be even smaller. The performance is expected to be quite similar to the one described in this report for 14 TeV.

11.7.3 Measurement of the ρ-parameter

As shown already in Section 11.1.2, lowering the center-of-mass energy allows to probe smaller values $|t|_{min}$ of the minimum momentum transfer squared, going down by one order of magnitude from $\sqrt{s} =$ 14 TeV to $\sqrt{s} = 1.8$ TeV. This will allow to probe the region where the interference between the nuclear interaction and the Coulomb interaction takes place and thus to have access to the ρ parameter. As shown in the right part of Fig. 11.2, for center-of-mass energies below 8 TeV it will be possible to probe this interference region.

As the cross-section for elastic scattering is determined by the nuclear scattering amplitude while the

Coulomb scattering amplitude is absolutely known, it is experimentally possible to obtain from a fit of the measured differential cross-section for elastic scattering simultaneously the ρ-parameter, the slope of the nuclear interaction, the total cross-section and the luminosity. As mentioned already above, for these energies an independent determination of the total pp cross-section will also be available, which will allow systematic cross-checks on the corresponding measurement via the luminosity independent method.

References

[1] The MAD-X Program, Methodical Accelerator Design, Version 2.00. http:www.cern.ch/mad

[2] TOTEM Memorandum: Additional Information to the referees (1999)
http://totem.web.cern.ch/Totem/memo.html

[3] UA4 Collaboration 'Measurement of the proton-antiproton total and elastic cross-sections at the CERN SPS collider', Physics Letters B, 147 (1984)

[4] S. L. Bueltmann et al., First measuremnt of proton proton elastic scattering at RHIC.
Preprint nucl-ex/0305012, May 2003. Submitted to Phys. Rev. Lett.

[5] Eur. Phys. J. C28, 97-105 (2003)

12 Luminosity and Luminosity Monitors

12.1 The Luminosity determination in TOTEM

The luminosity is an important parameter for any experiment, since it has to be known with precision to determine a cross-sections and should be known with the best possible precision.

The general purpose pp experiments at LHC, ATLAS and CMS, will provide high statistics data samples, and the accuracy of their measurements in many cases will be limited by the uncertainty on the knowledge of the luminosity $\mathcal{L}$. A precision of the order of a percent is considered sufficient for the LHC experiments.

The measurement of the luminosity at LHC has been discussed by many authors, see for example [1]. In general, there are two possibilities to determine the luminosity: either (i) measure a pair of cross-sections which are connected quadratically to each other, or (ii) measure a cross-section whose value is well known or which may be calculated with good accuracy.

Luminosity independent method

The well known example of the first possibility is the measurement of the total cross-section and the differential forward elastic cross-section, which are related by the optical theorem; this has been discussed in detail in Section 2. In principle, any process with a significant cross-section and which is straightforward to detect can be used to monitor the luminosity.

The total cross-section and the luminosity $\mathcal{L}$ can be expressed as:

$$\mathcal{L} \times \sigma_{tot} = \dot{N}_{el} + \dot{N}_{inel} \tag{12.1}$$

where $\dot{N}_{el}$ and $\dot{N}_{inel}$ are the observed rates of elastic and inelastic interactions, respectively. The measurement of the total inelastic rate is made by measuring with precision the rate in the tracking telescopes in the forward regions, whose efficiency and geometric acceptance then have to be determined precisely.

TOTEM will measure σ_{tot} with a precision of the order of 1% without knowing the luminosity and can thus provide the absolute calibration to luminosity monitors, as it will be explained in the next sections. This method has been used at the ISR [3] and later at the $Sp\overline{p}S$ Collider by UA4 [4].

Absolute luminosity - Coulomb and Nuclear Interference

When elastic scattering can be measured at t values where the Coulomb and the nuclear elastic cross-sections are of the same order of magnitude [3, 4], one obtains the absolute value of the total cross-section, since the electromagnetic Coulomb scattering is well known and can be calculated with very good accuracy. The present proposed optics ($\beta^* = 1540$ m) is such that this region is not yet accessible to TOTEM. Studies are continuing on the design of a suitable optics to allow TOTEM to extend the measurement of the elastic scattering down to values of $-t \approx 10^{-4}$ GeV^2.

Van der Meer method

The luminosity can also be measured directly, for example, with the method proposed by Van der Meer and used for the first time at the ISR [5]. The luminosity is calculated from the measured beam effective

dimensions. Here again, the limiting precision is the knowledge of the number of particles in each bunch or the beam current. A long and careful refinement at the ISR achieved an accuracy of ±1%. This method can be used to rapidly optimize the luminosity at the interaction point(s) and is a good candidate to be used for maximization at the beginning of each run.

Determination from the machine parameters.

The luminosity is an important parameter to describe the machine performance. The relative luminosity is *a quantity proportional in an unknown but constant way to the actual luminosity* [2] and has to be known from the very beginning of the LHC operations for the optimization and the monitoring of the circulating beams.

The luminosity of an accelerator can be calculated theoretically and for the LHC machine it can be written as:

$$\mathcal{L} \;=\; \frac{f_{rev}\;\gamma}{4\;\pi} \times \;F\; \times \;\frac{k\;N^2}{\epsilon_N\;\beta^*}, \tag{12.2}$$

where the term $f_{rev}\;\gamma/4\;\pi$ depends on well known machine parameters and has a value of $6.67634{\times}10^6\;Hz$, F describes the beam crossing angle and bunch length at the interaction point, k is the number of bunches, N is the number of particles per bunch, ϵ_N is the normalized emittance of the beams and β^* is the value of the betatron function at the crossing.

The uncertainty on the measurement of the luminosity using formula (12.2) is mainly due to the difficulty of measuring, with the necessary precision, some of the parameters and on their systematic uncertainties. The precision of the measurement will improve when detailed studies of the systematics become available.

The main sources of uncertainties are:

- the precise knowledge of N, the number of particles in the bunch/bunches. It is difficult to control the systematics for many bunches and to account properly for particles which may coast in the machine as *"un-allowed"* buckets or debunched particles;
- the crossing angle: the uncertainty from the machine beam dynamics and the precision of the BPM can already account for an overall uncertainty larger than 1% (for a 3% precision on the crossing angle); and
- β^*: when the value is small, for high luminosities, the uncertainty on the knowledge of β^* can become large.

It does not seem possible to reach the required precision of 1%, at least in the early stage of operation, directly from the machine parameters.

12.2 The absolute calibration of the luminosity in TOTEM

The total cross-section obtained by TOTEM with simultaneous measurements of the total inelastic rate and the elastic scattering provides the value of the luminosity. The precise determination of the total inelastic rate has been described previously in this document (Section 11.3).

Monte Carlo simulations incorporating the measured performance of the detectors are used to predict the data taken by the experiment. The trigger rate and the precise knowledge of the acceptance are then used to obtain the value of the total cross-section by applying appropriate corrections (See section 11.4).

The delicate part of the procedure is the estimate of the various sources of background and their influence on the uncertainty of the measurement. A systematic study of the background is performed for combinations of detectors which cover different η ranges. The efficiency of each combination, or the loss, is known with small uncertainties ($\leq 1\%$) after this procedure, and the correction to the measured inelastic rate gives the total cross-section.

Conversely, the precise measurement of the acceptance gives the *fraction* of the total cross-section seen by a particular trigger topology and defines an *effective monitor cross-section*, σ_{eff}.

Then the rate of events observed by the "monitor" is directly related to the luminosity via:

$$\mathcal{L} \;=\; N_{Monitor} \;\times \frac{\sigma_{tot}}{\sigma_{eff}}$$

,

This is the calibration of the specific luminosity monitor.

TOTEM trigger combinations as monitors

Each monitor rate is affected by background in a different way. The background depends highly on the running conditions and the beam quality may vary with the value of the luminosity or simply for different machine runs. It is important to check constantly the calibration factor from the rates of different monitors. The consistency and reproducibility check of the monitors is a reliable way to detect the variation of the background and to properly correct for it.

The best luminosity monitors are the ones that are least sensitive to background variations. Past experience from UA4 and the present simulations suggest that the double arm T1 combination is very good choice for a luminosity monitor, with little or no sensitivity to the known sources of background, as shown by the simulation discussed elsewhere in this document (see Section 8.2). CMS detector combinations (as discussed in the next section) will be part of the common luminosity monitoring.

The absolute calibration will be repeated at different luminosities for the different TOTEM running scenarios by obtaining again a value for σ_{tot}. The extrapolation of the luminosity measurement to higher luminosity values requires a continuous check of the linearity of the monitor rates. When the machine performance is such that TOTEM cannot measure any more, most likely for luminosities above 10^{32} cm^{-2} s^{-1}, the luminosity will be monitored only by CMS detectors.

12.3 CMS monitors

12.3.1 Overview

The task of measuring and monitoring the luminosity for the LHC experiments is very delicate, especially at the very high luminosity of 10^{34} cm^{-2} s^{-1}. For the first time in a storage ring the number of events/bunch crossing will be much larger than one and must be appropriately considered when designing a monitor. The calibration of the monitors for CMS will be made by running together with TOTEM during the total cross-section runs at a luminosity of 10^{28} cm^{-2} s^{-1}, a value which is much lower than the one expected during the standard LHC physics runs. The necessary extrapolation up to six orders of magnitude is a very delicate task.

First of all, it is necessary to identify possible monitors within CMS which are capable of following the evolution of the luminosity history. A good initial calibration for a range of low luminosity values will allow one to properly extend the measurement as the luminosity increases.

A brief description of the use of CMS detectors for the initial phase of luminosity monitoring, as discussed in a common CMS/TOTEM luminosity group, can be found in the following sections.

12.3.2 The CMS tracker

The CMS Tracker [6] ith its good vertex reconstruction capability is the ideal detector to identify and count beam-beam events with the same approach as employed in TOTEM, i.e. by counting minimum bias events with the reconstructed interaction vertex to be in the interaction region.

For this purpose, the use of only a part of the tracking capability of the detector will be sufficient, making the procedure faster and suitable for an automatic on-line usage. The simulation of the vertex reconstruction [7] in the tracker shows that, with the three layers of the tracker with z-measurement capability, one can reconstruct and identify beam-beam events with good efficiency.

This method works with good efficiency until the event rate per bunch crossing grows as high as 5 to 10 events per crossing, i.e. for luminosities up to a few 10^{33} cm^{-2} s^{-1}. Simulations also indicate that, for the very low luminosities of the TOTEM runs, the event rate in the tracker becomes statistically

significant for typical run times. This can then be a luminosity monitor which can be directly calibrated during TOTEM runs.

The fast and simple algorithm studied can be built into specific hardware boards and provide an on-line measurement of the luminosity, including a bunch-by-bunch measurement, as requested by CMS.

The integration over a few 100 events provides enough statistics for a stable measurement.

12.3.3 The forward calorimeter HF

Counting the number of hit sectors of the HF calorimeter [8], as a way to provide the value of the luminosity of the machine [9], was also discussed in the CMS/TOTEM luminosity study group. It has been suggested that this method can provide reliable measurements from the low values of the TOTEM runs up to luminosities of 10^{34} $\mathrm{cm}^{-2}\,\mathrm{s}^{-1}$. At very high luminosities, one would count "the zero's" (i.e. sectors that have not been hit) of the HF calorimeter. This procedure is used at present in the D0 experiment at FNAL. Although it needs more study, it may be a valid choice for CMS.

12.3.4 Monitors from specific processes

As the luminosity increases, it will be necessary to find monitors which can deal with the very high interaction rate without saturating. Specific processes with well measured cross-sections, such as isolated J/ψ or Υ production could provide a good monitor: this could easily be reconstructed in the e.m. calorimeter.

On-line monitoring can also be foreseen in this case by counting with a dedicated 'processor card' at the trigger level and calculating the correct isolated energy deposit [10].

W and Z^0 production are other good candidates for high luminosity monitoring. They will become available off-line for luminosity monitors once the performance of the detector for these processes has been determined.

Obviously, the uncertainties in the theoretical calculations of the cross-sections for the basic processes used to determine the luminosity should match the desired experimental accuracies.

12.3.5 Calibration runs and extrapolation

During the TOTEM low luminosity runs, the monitors involved will take data with the CMS minimum bias trigger. The counting rates (properly checked and corrected) will then be correlated with the value of the luminosity measured by the TOTEM main monitor.

The runs will be repeated with common runs foreseen at higher intermediate luminosities (2 to 3 orders of magnitude) when the TOTEM telescopes will still be able to provide a measurement for cross calibration.

CMS already foresees acquiring regularly a certain percentage of minimum bias triggers. The analysis of these minimum bias events provides the luminosity monitor. The time necessary to provide a statistically relevant value of the luminosity will depend (other than on the luminosity itself) on the fraction of minimum bias triggers taken.

The bunch by bunch luminosity, which is required by the experiment since strong variations have been observed in B-factories for long bunch trains, will also be available, but on a much longer time scale.

References

[1] V.A. Khoze et al., "Luminosity measuring processes at the LHC", Eur. Phys. J. C 19, (2001) 313.

[2] LHC project document, LHC-B-ES-0007 rev.4, EDMS doc. n. 347396 (2003)

[3] U. Amaldi et al., "Precision measurement of proton-proton total cross-section at the CERN Intersecting Storage Rings", Nucl. Phys., B145, (1978) 367.

[4] M. Bozzo et al., Phys. Lett. 147B, 4 (1984) 5.

[5] S. van der Meer, "Calibration of the effective beam height in the ISR", CERN-ISR-PO/68-31 (1968)

[6] The CMS Tracket TDR, CERN/LHCC 98-6, CMS TDR 5, 15 April 1998; Addendum to the Tracker TDR, CERN/LHCC 2000-016, CMS TDR 5 Addendum 1, 21 February 2000.

[7] A. Starodumov, https://edms.cern.ch/file/111912/1/starodumov-talk.pdf (2000)

[8] The HCAL Technical Design Report, CERN/LHCC 97-31, CMS TDR 2, 20 June 1997, chapter 5.

[9] G. Snow, https://edms.cern.ch/file/111912/1/snow-talk.pdf (2000)

[10] D. Cussan, https://edms.cern.ch/file/111912/1/cussans-talk.pdf (2000)

13 Responsibilities, cost and schedule

13.1 Introduction

A preliminary sharing of responsibilities for the different TOTEM activities discussed in the chapters of this TDR is described below. The sharing, based on technical and economical considerations, takes into account the expertise gained by the groups from their experience in similar projects and from the TOTEM specific R & D of the last three years together with the potential resources of each participating institute.

The responsibilities include all technical and financial aspects of the TOTEM experiment. The sharing as outlined below leaves ample possibilities in case new institutes decide to join the collaboration in the future.

13.2 Areas of responsibilities

The project is divided in two main parts:

- the detection of the protons scattered at very small angles, which includes the Roman pots, their installation in the machine, the detectors and related electronics, and

- the inelastic detectors, which include the two forward telescopes T1 and T2 with electronics, support and the installation in CMS.

Table 13.1 – TOTEM – Preliminary sharing of responsibilities

sub-system	preliminary responsibilities					
	Brunel	CERN	Helsinki	INFN (Bari)	INFN (Genoa)	Prague
Roman Pots		•	•			•
Supports and installation		•	•			•
Detectors	•	•				
FE electronics	•	•				
Proton Trigger		•		•		
DAQ electronics				•		
T1 Detectors					•	
T1 FE electronics					•	
T2 Detectors		•	•		•	
T2 FE electronics		•	•			
Inelastic Trigger			•	•	•	
T1, T2 DAQ electronics				•		
T1, T2 Supports and Installation		•	•		•	

13.3 Detector assembly and infrastructure

Detector construction and assembly will be carried out by the responsible institutions. CERN is responsible for the overall integration in the experimental area with particular emphasis on matters regarding safety. The detector groups are responsible for their detectors and will provide the equipment and material necessary for the installation. Provision of infrastructure is CERN's responsibility as a host laboratory. Special coordination with CMS is necessary at the time of installation.

13.4 Project schedule

The schedules for the different detectors parts are given in the following tables.

13.4.1 Roman Pots and Roman Pot detectors

The schedule for the construction of the Roman Pots, the detectors and the electronics to equip two stations on either side assumes that a decision on the final technology will be taken at the end of 2004 following the criteria described below.

Decision on the technology for the Roman Pot detectors

Assuming high detection efficiency ($> 98\,\%$) and a good production yield for all the candidate detectors, the decision on the technology for the detector of the Roman Pots will be taken on the basis of the following considerations at the end of 2004 after the tests of final size detectors in the test beam:

- Signal/Noise ratio: $\gtrsim 20:1$
- Spatial resolution: $\sigma \approx 15\ \mu m$
- Radiation hardness: good behaviour up to $> 10^{14}\ n/cm^2$ (leakage current not influencing the noise and efficiency >98%)
- operating temperature: $> -30\ ^{o}$C
- Insensitive edge region: $\lesssim 50 \div 60\ \mu m$
- Stability and reliability of the detector operation

13.4.2 Inelastic telescopes

The two parts T1 and T2 of the inelastic detector are at a different stage of design given the recent definition of the vacuum pipe in the very forward region of T2. For T1, technology was chosen, prototypes were built and successfully tested. The construction schedule is also completely defined. The location and the dimensions of the T2 telescope were recently reconsidered to take into account the presence of the CASTOR calorimeter. Two technologies are considered at the moment: GEM and silicon detector. Both fit the TOTEM requirements and are proven to work. The final choice will be taken at the end of 2004.

T1 Prototypes

A prototype of the largest CSC detector for T1 has been built in 2003 and tested, together with other pre-prototypes, with a pion/muon beam in the fall of 2003. Results from these tests have been discussed in a previous section. The prototype construction enabled the definition of most of the details of the detector and the construction procedure.

T1 construction schedule

The production schedule for T1 is prepared under the assumption that its installation in CMS will take place in the first months of 2007 after the closing of the end caps and before HF is brought to its final position.

By that date, the four half telescopes must be assembled, cabled on their transport platform and fully commissioned in a test beam. The schedule assumes that the tests will be done in 2006 before a presumed end of beam availability in September 2006.

Construction could start at the end of 2004 in the INFN Genoa laboratory where the infrastructure and tooling for assembly is being prepared. The final design of 10 similar detectors of various sizes and of the support and services is in an advanced phase and could be completed by the fall of 2004.

T2 with GEM detectors - Construction schedule

The detector will be designed in detail by the end of 2004, together with a complete definition of the system.

The geometry of TOTEM will require a special design of the GEM and of the anode boards. The production of the printed boards will then proceed rapidly considering that the GEM construction technology is by now fully understood. The development of boards with similar dimensions as required by TOTEM has been recently completed for COMPASS and TPG at CERN.

A *prototype* will be tested in a beam before starting production of the full system. The support mechanics design (support and services layout) should be completed by the end of 2004.

T2 with silicon detectors

The planning presented here is based on the assumption that the detectors, already developed for the CMS tracker, can be adapted to the T2 telescope and no further development will be needed. The readout electronics is based on the CMS APV25 chip.

Decision on the technology for the telescope is based on:

- Simplicity in the geometrical adaptation of the design
- Radiation hardness
- Adequate rate capability
- Cost and construction issues

DAQ planning

The TOTEM DAQ system should be able to run in stand alone mode and in common with CMS. Since we suggest to implement the DAQ and its interface to the trigger in CMS-like fashion, the system will be developed in collaboration with CMS experts and will benefit from their experience. Concerning the planning, the procurement of the material and the installation will be done in close contact with them.

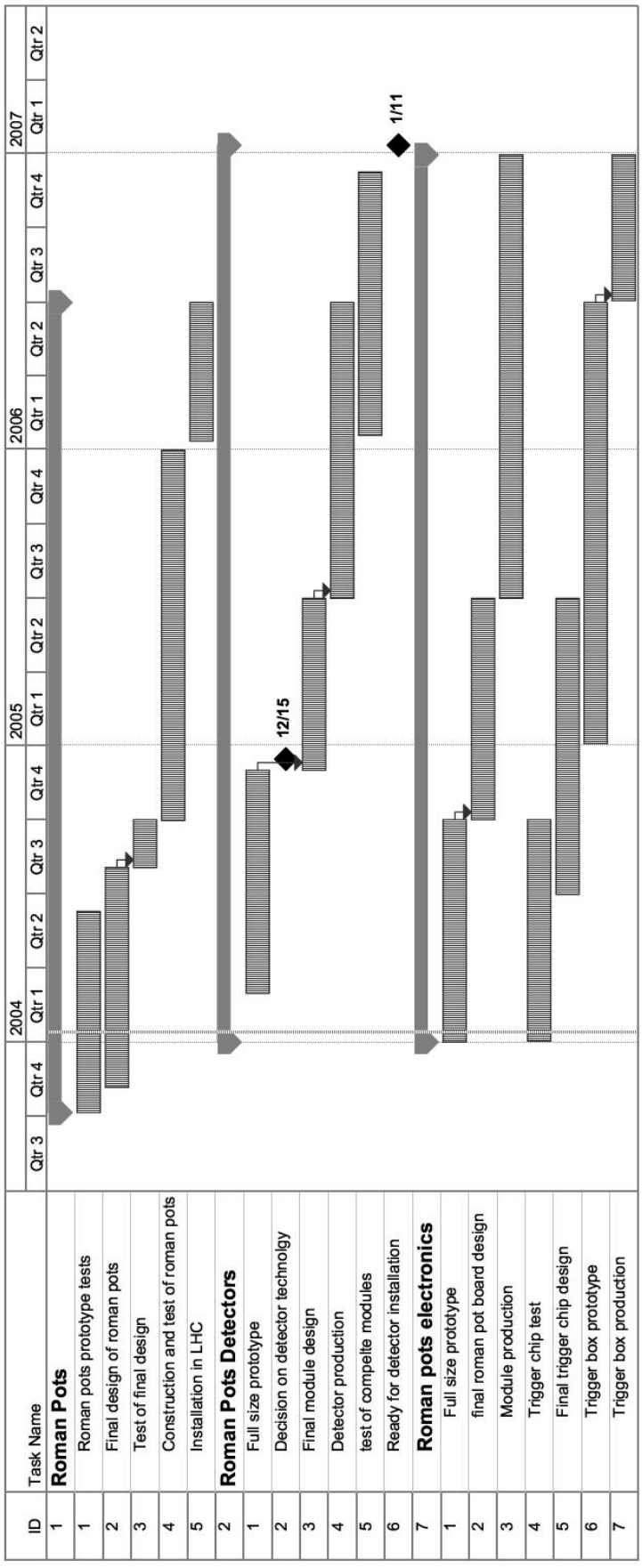
TOTEM planning - Roman Pots and Roman Pots detectors
ID
Task Name
2004
2005
2006
2007
Qtr 3
Qtr 4
Qtr 1
Qtr 2
Qtr 3
Qtr 4
Qtr 1
Qtr 2
Qtr 3
Qtr 4
Qtr 1
Qtr 2
1 Roman Pots
1 Roman pots prototype tests
2 Final design of roman pots
3 Test of final design
4 Construction and test of roman pots
5 Installation in LHC
2 Roman Pots Detectors
1 Full size prototype
2 Decision on detector technolgy
3 Final module design
4 Detector production
5 test of compelte modules
6 Ready for detector installation
7 Roman pots electronics
1 Full size prototype
2 final roman pot board design
3 Module production
4 Trigger chip test
5 Final trigger chip design
6 Trigger box prototype
7 Trigger box production
12/15
1/11

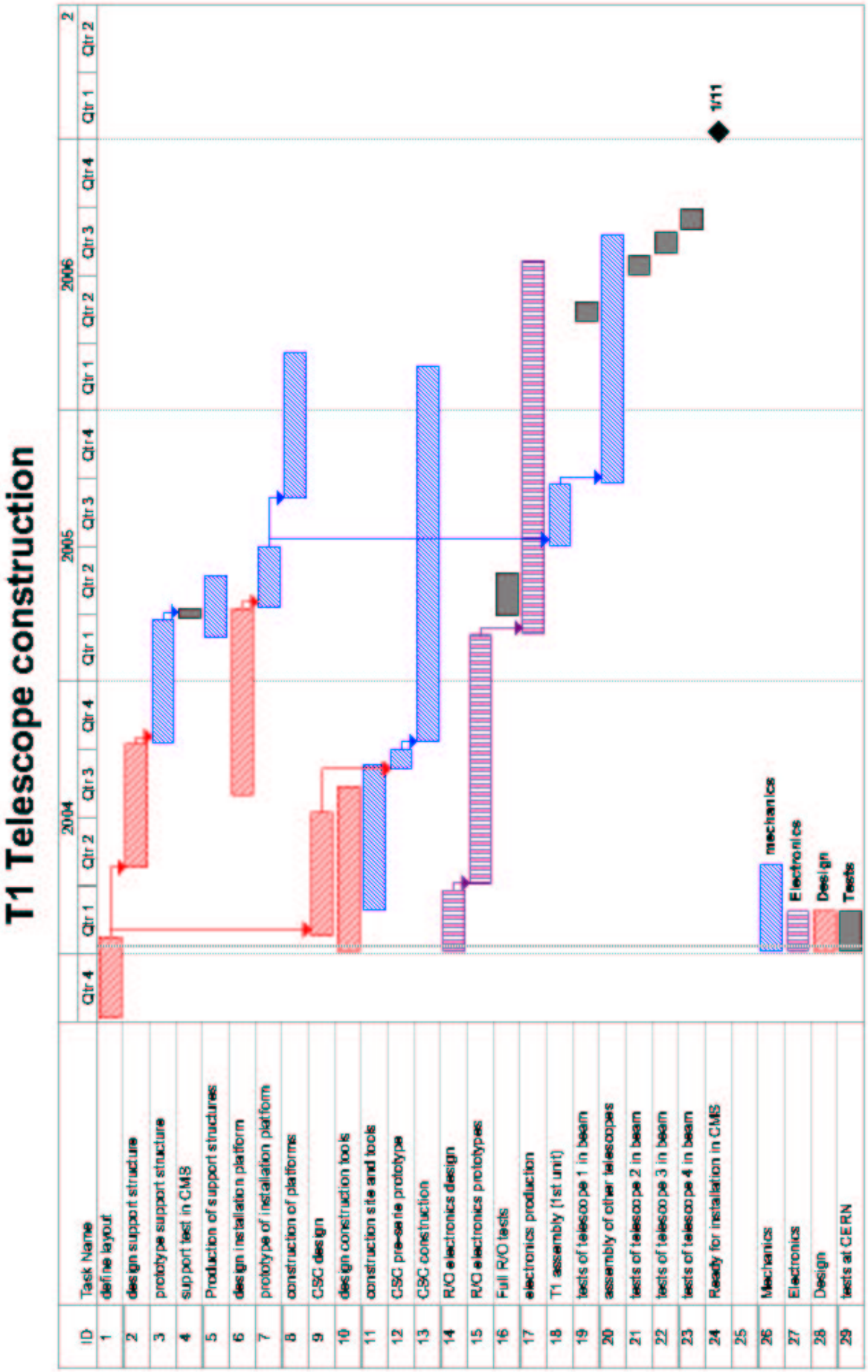
T1 Telescope construction
ID
Task Name
define layout
design support structure
prototype support structure
support test in CMS
Production of support structures
design installation platform
prototype of installation platform
construction of platforms
CSC design
design construction tools
construction site and tools
CSC pre-serie prototype
CSC construction
R/O electronics design
R/O electronics prototypes
Full R/O tests
electronics production
T1 assembly (1st unit)
tests of telescope 1 in beam
assembly of other telescopes
tests of telescope 2 in beam
tests of telescope 3 in beam
tests of telescope 4 in beam
Ready for installation in CMS
Mechanics
Electronics
Design
tests at CERN
2004
2005
2006
Qtr 4
Qtr 1
Qtr 2
Qtr 3
Qtr 4
Qtr 1
Qtr 2
Qtr 3
Qtr 4
Qtr 1
Qtr 2
1/11
mechanics
Electronics
Design
Tests

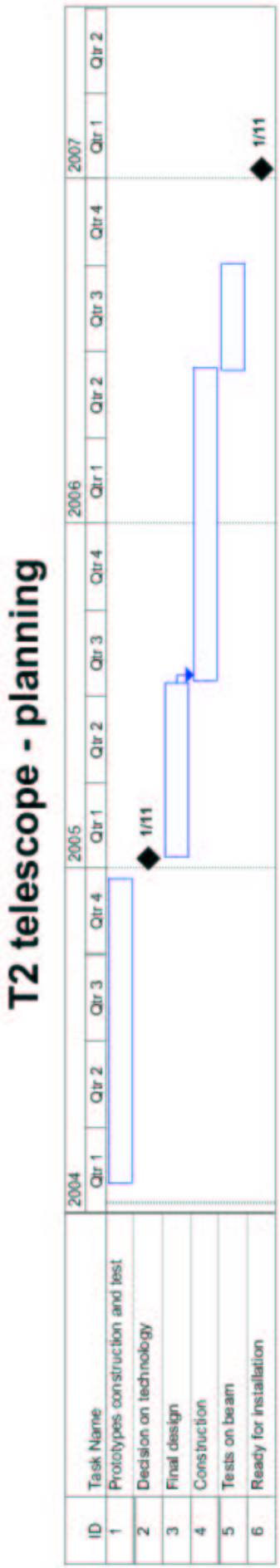
T2 telescope - planning
ID
Task Name
2004
2005
2006
2007
Qtr 1
Qtr 2
Qtr 3
Qtr 4
1 Prototypes construction and test
2 Decision on technology
3 Final design
4 Construction
5 Tests on beam
6 Ready for installation
1/11
1/11

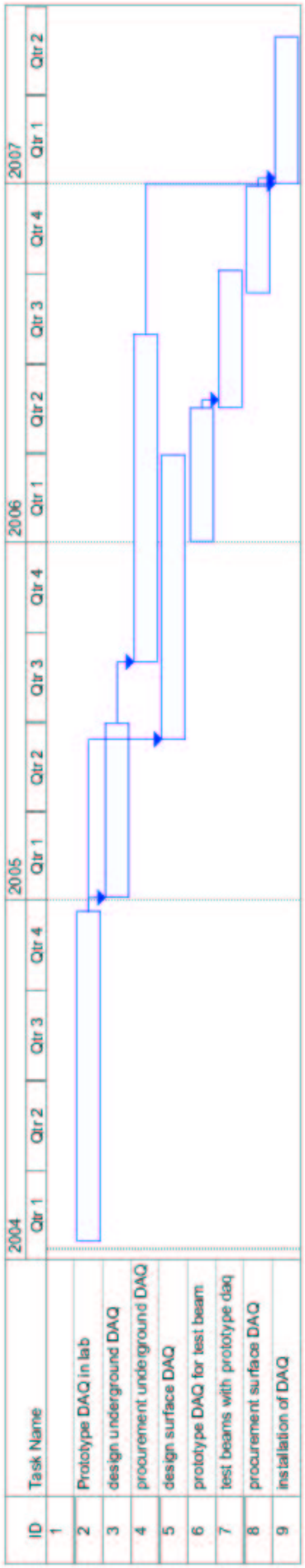
DAQ Planning
ID
Task Name
2004
2005
2006
2007
Qtr 1
Qtr 2
Qtr 3
Qtr 4
1
2 Prototype DAQ in lab
3 design underground DAQ
4 procurement underground DAQ
5 design surface DAQ
6 prototype DAQ for test beam
7 test beams with prototype daq
8 procurement surface DAQ
9 installation of DAQ

13.5 Project cost

The cost estimate for the different TOTEM detectors are summarized in the following tables. The two options for T2 have been estimated separately, the silicon detector option is 50% more expensive than the GEM option.

The cost of the Roman Pots and Roman Pot detectors is based on the case of two stations on each side of the Interaction Point.

The cost estimate contains a contingency of 10%. The data acquisition cost is detailed separately per detector and then summarized at the end.

Table 13.2 – Roman Pots and detector costs (in kCHF)

Table 13.5 – Roman Pots mechanics, motors and controls		560 kCHF
Roman Pot detectors		
detectors	324 kCHF	
mechanics	72 kCHF	
Si detectors TOTAL		396 kCHF
Electronics		
APV for det. (incl. hybrids)	120 kCHF	
Front End	246 kCHF	
Trigger	60kCHF	
Electronics TOTAL		426 kCHF
DAQ		222 kCHF
Infrastructure		
Cooling	200 kCHF	
Services (racks and cables)	160 kCHF	
Slow control	170 kCHF	
Infrastructure TOTAL		530 kCHF
TOTAL		2133 kCHF
Contingency		210 kCHF
TOTAL w. contingency		2343 kCHF

Table 13.3 – T1 estimated costs

T1 detectors		
Honeycomb	55.5 k CHF	
Printed boards	75.0 kCHF	
Assembly frames	22.5 kCHF	
Components	60.0 kCHF	
Detector TOTAL		213 kCHF
T1 Electronics		
Anodes FE (12k wires)	80 kCHF	
Cathodes FE (25k strips)	350 kCHF	
Local boards	60 kCHF	
Trigger	50 kCHF	
HV+LV	36 kCHF	
Electronics TOTAL		576 kCHF
DAQ		111 kCHF
Infrastructure		
Supports	96 kCHF	
Transport platforms	120 kCHF	
Services (cables, gas, cooling)	99 kCHF	
Slow Control	130 kCHF	
Infrastructure TOTAL		445 kCHF
TOTAL		1345 kCHF
Contingency		130 kCHF
TOTAL w. contingency		1475 kCHF

Table 13.4 – T2 estimated costs – GEM option

Detectors		
Position detector (GEM with strip board)	88 kCHF	
Trigger detector (GEM with pad board)	104 kCHF	
GEM detectors TOTAL		192 kCHF
T2 Electronics		
APV + FE for position det.	58 kCHF	
AD16 + FE for trigger det.	38 kCHF	
Trigger	40 kCHF	
HV+LV	25 kCHF	
Electronics TOTAL		161 kCHF
DAQ		111 kCHF
Infrastructure		
Supports	100 kCHF	
Electronics cooling	50 kCHF	
Services (racks and cables)	60 kCHF	
Slow control	63 kCHF	
Infrastructure TOTAL		273 kCHF
TOTAL		737 kCHF
Contingency		70 kCHF
TOTAL w. contingency		807 kCHF

Table 13.5 – T2 costs – Silicon option

detectors		
detectors	320 kCHF	
mechanics	64 kCHF	
Si detectors TOTAL		384 kCHF
T2 Electronics		
APV for det.	80 kCHF	
FE and trigger	164 kCHF	
Electronics TOTAL		244 kCHF
DAQ		166 kCHF
Infrastructure		
Supports	100 kCHF	
Electronics cooling	50 kCHF	
Services (racks and cables)	60 kCHF	
Slow control	100 kCHF	
Infrastructure TOTAL		340 kCHF
TOTAL		1134 kCHF
Contingency		110 kCHF
TOTAL w. contingency		1244 kCHF

Table 13.6 – Cost for the TOTEM DAQ

Item	**Cost in KCHF**
Roman Pots	222
T1	111
T2/GEMs	111
T2/Silicons	166
On-line computing	28
TTC partition	30
TOTAL with T2/GEMs	502
TOTAL with T2/Silicons	557

13.6 Overall Detector Cost

The overall cost for the construction and installation of the TOTEM detectors is summarized in Table 13.7.

The cost of the Slow Control is considered in the evaluation of each detector unit; a contingency of 10% is already included in the detector cost.

Table 13.7 – Summary of cost evaluation

Roman Pots and Roman Pot detectors			
Roman Pots	560 kCHF		
supports and installation	530 kCHF		
Detectors for the Roman Pots			
Planar Silicon detectors (planar or 3D)	396 kCHF		
Electronics (APV)	426 kCHF		
Contingency	210 kCHF		
Roman Pot TOTAL		2122 kCHF	
T1 Telescope			
Detectors	213 kCHF		
Electronics and trigger	576 kCHF		
Supports and installation	445 kCHF		
Contingency T1	140 kCHF		
T1 TOTAL		1364 kCHF	
T2 Telescope - GEM			
Detectors	192 kCHF		
Electronics	160 kCHF		
Supports and installation	273 kCHF		
Contingency T2-GEM	70 kCHF		
T2-GEM TOTAL		695 kCHF	
T2 Telescope - Silicon			
Detectors	384 kCHF		
Electronics	244 kCHF		
Supports and installation	340 kCHF		
Contingency T2-Si	110 kCHF		
T2-Si TOTAL			1077 kCHF
DAQ and trigger control		502 kCHF	557 kCHF
Computing		750 kCHF	
COST of Experiment		**5433 kCHF**	**5870 kCHF**
		w. T2-GEM	w. T2-Si

Based on preliminary discussion with some of the funding agencies of the TOTEM institutes, it is expected that sufficient funding can be provided for the construction of the detectors presented in this report.

Acknowledgements

We want to acknowledge first of all Giorgio Matthiae and Werner Kienzle who have proposed the experiment and followed it in its early stage, and the group of Rome 2 for their valuable and important contributions.

During the long time of the preparation of this document we have received the help of many colleagues that we want to acknowledge here. We may have forgotten some and we apologize. But to all of you our sincere "Thank you!".

G. Apollinari, R. Assmann, A. Ball, V. Bassetti, F. Bertarelli, N. Bondar, R. Breedon, R. Capra, L. Casagrande, F. Caspers, R. Cereseto, F. Cossey, R. De Oliveira, A. de Roeck, A. Dobrinov, L. Dufay, S. Durkin, N. Egorov, I. Eremin, V. Eremin, P. Fabbricatore, G. Faber, S. Farinon, L. Favre, T. Ferguson, S. Golubkov, J. Hauser, M. Hauschild, A. Honma, A. Inyakin, M.M. Islam, C. Joram, J. Kaplon, V. Khoze, J. Knaster Refolio, K. Konkov, T. Kurtyka, J. Lamsa, T.Y. Ling, G. Louvent, J. Lozano Bahilo, S. Lusin, G. Magazzu, A. Mardrino, P. Martinengo, I. McGill, L. Mirabito, N.V. Mokhov, M. Morel, L. Musa, M. Ottela, G. Passardi, B. Perea Solano, R. Perret, V. Polychronakos, K. Potter, J.L. Rakhno, C. Rathjen, J.M. Rieubland, A. Rossi, M. Ryynänen, M. Sanchez, J.C. Santiard, F. Sauli, P. Schlein, R. Sczygiel, A. Sidorov, P. Siegrist, R. Stampfli, A. Staude, M. Strikman, J. Troska, E. Van der Bij, F. Vasey, N. Wangnier, S. Weisz, B. Wittmer.